



SOUTH AFRICAN SOCIETY FOR ATMOSPHERIC SCIENCES



INNOVATION FOR INFORMATION
SASAS 2016

32nd Annual Conference of the South African Society for Atmospheric Sciences

31 October-1 November

Hosts: Climate System Analysis Group (University of Cape Town)

Lagoon Beach Hotel in Milnerton, Cape Town.

Sponsor:





32nd Annual Conference of the South African Society for Atmospheric Sciences

31 October-1 November

Cape Town, South Africa

SPONSORED BY
Future Climate for Africa (FCFA)

All rights reserved. No part of this publication may be reproduced or copied in any form – graphic, electronic, or mechanical, including photocopying, taping, or information storage and retrieval systems – without the prior written permission of the publisher. Contact SASAS for permission pertaining to the overall collection. Authors retain their individual rights and should be contacted directly for permission to use their material separately. The manuscripts reproduced herein are a collection of refereed and unrefereed papers presented at the 32nd Conference of the South African Society for Atmospheric Science. The peer reviewed conference proceeding in this collection constitute formal publication.

ISBN for peer reviewed conference proceedings: 978-0-620-72974-1

MESSAGE FROM THE PRESIDENT

Dear Delegates

I welcome you to the 32nd South African Society for Atmospheric Sciences Conference. After the successful 31th Conference held at Lanseria last year, it is a great pleasure to be in Cape Town in such a picturesque location and to be hosted by CSAG. I want to extend a special welcome to overseas delegates from Africa, Europe, USA, South America and Asia. This year, we are, for the second time, awarding the SASAS medal for excellence in science, education and technology. Last year the recipient was Professor Michael Savage. As usual, we will award the Stanley Jackson Award for the best peer reviewed paper in the preceding year. We also have an award for the best poster and oral. I remind you that SASAS aims to stimulate interest and support for all branches of atmospheric sciences, to encourage research and education in the atmospheric sciences and to promote collaboration between organisations and institutions interested in atmospheric science in Southern Africa. This includes meteorology, agro-meteorology, climatology, air quality, ocean-atmosphere interaction, troposphere-stratosphere interaction, physical oceanography, hydroclimatology, numerical modelling, and instrumentation. Proceedings of the conference include all peer reviewed extended abstracts and the document has an ISBN number. This publication qualifies for funding in most institutions (and looks good on your CV). Former conference papers and abstracts are available on the new SASAS web site at <http://www.sasas.org>.

Ultimately, we compete with one another for grants, for discoveries, for papers, for awards; and we may agree or disagree on how to run things, but SASAS unites us all and the conference is one of the longest running annual conferences in Africa. This is where we uncover the young talent. I encourage everybody to join SASAS by completing the membership form that you will find in on the website.

This year we will be electing a new executive committee during the conference including President and Vice President and results will be announced at the annual assembly at the end of the conference. So, this is my last mandate and we will have a new president by the end of the conference. (I am not leaving SASAS but cannot run for more than three mandates).

Finally, I remind you that we need to grow the society, and therefore welcome any suggestions for improvements. You can voice your idea or concerns at the assembly or ask the executive committee to bring it up. I also remind you that we do have a constitution that can be amended by a vote by the council. This is your opportunity to change things and help the society to progress.

Mathieu Rouault

SASAS President

Professor – Department of Oceanography UCT

COMMITTEES

EVENT ORGANISING COMMITTEE

Conference Co-Chairs -

- Prof Bruce Hewitson (Climate System Analysis Group, University of Cape Town)
- Dr Peter Johnston (Climate System Analysis Group, University of Cape Town)
- Mrs Kate Kloppers (Climate System Analysis Group, University of Cape Town)

Dr Chris Lennard (Climate System Analysis Group, University of Cape Town)

Mrs Melanie Rustin-Nefdt (Climate System Analysis Group, University of Cape Town)

Ms Carla Petersen (Climate System Analysis Group, University of Cape Town)

Ms Tania Williams (Climate System Analysis Group, University of Cape Town)

Conferecne proceedings edited and compiled by Mrs Kate Kloppers.

REVIEW PROCESSES

The South African Society for Atmospheric Sciences' annual meeting provides the opportunity for scientists to publish their work in the conference proceedings. All the papers in this proceedings underwent a blind review process in order to improve quality, performance and provide credibility to the research. Each paper was independently reviewed by two reviewers on the review panel. The reviewers were tasked to categorise the paper into; accept as is, accept with minor/major revisions, or reject. Based on the reviewers' comments, the convener made the final decision on acceptance. The reviewers' comments and decision on acceptance were sent to lead authors. Following this corrections were made by authors for final acceptance. A total of 37 conference proceedings were submitted, with only one paper rejected and one paper withdrawn by the author.

REVIEW PANEL MEMBERS

Review Convener - Prof Willem Landman (Council for Scientific and Industrial Research, SA)

Dr Babatunde Abiodun (University of Cape Town, SA)

Dr Asmerom Baraki (South African Weather Service, SA)

Dr Mary-Jane Bopape (University of Reading, UK)

Prof Natalie Burls (George Mason University, USA)

Dr Liesl Dyson (University of Pretoria)

Dr Gregor Feig (Council for Scientific and Industrial Research, SA)

Dr Rebecca Garland (Council for Scientific and Industrial Research, SA)

Prof Bruce Hewitson (Climate System Analysis Group, University of Cape Town, SA)

Dr Andries Kruger (South African Weather Service, SA)

Mr Mavhungu Muthige (Council for Scientific and Industrial Research, SA)

Prof Stuart Piketh (School of Geo and Spatial Science, University of North-West, SA)

Prof Mathieu Rouault (University of Cape Town, SA)

Dr Thando Ndarana (Council for Scientific and Industrial Research, SA)

Dr Warren Tennant (Met Office, UK)

Prof Sivakumar Venkataraman (University of KwaZulu-Natal, SA)

Prof Coleen Vogel (University of the Witwatersrand, SA)

Prof Sue Walker (Crops for the Future Research Centre, Malaysia)

Dr Caradee Wright (South African Council for Medical Research, SA)

SASAS MEDAL COMMITTEE

Chairman - Prof Willem Landman (Council for Scientific and Industrial Research, SA)

Dr Babatunde Abiodun (University of Cape Town, SA)

Prof Hassan Bencherif (Universite de La Reunion, Reunion, France)

Dr Simon Mason (International Research Institute for Climate and Society, USA)

Dr Thando Ndrana (Council for Scientific and Industrial Research, SA)

Prof Stuart Piketh (School of Geo and Spatial Science, University of North-West, SA)

Associate Prof, Marcello Vichi (Department of Oceanography, University of Cape Town, SA)

STANLEY JACKSON AWARD REVIEWERS

Prof Natalie Burls (George Mason University, USA)

Prof George Djolov (University of Pretoria, SA)

Prof Mike Harrison (Oxford University, UK)

Dr Neil Hart (Oxford University, UK)

Dr Andries Kruger (South African Weather Service, SA)

KEY NOTE SPEAKERS

PROF. WILLIAM J. GUTOWSKI, JR.



Associate Dean for Research and Graduate Education in the College of Liberal Arts and Sciences at Iowa State University

Dr. Gutowski is the Associate Dean for Research and Graduate Education in the College of Liberal Arts and Sciences at Iowa State University. His research concentrates on the role of atmospheric dynamics in climate. Central focuses are the dynamics of the hydrologic cycle, regional climate and weather and climate extremes. Because processes on a wide range of spatial and temporal scales are important for all of these, his research program entails a variety of modeling and data analysis approaches, from which he has authored or co-authored over 100 peer-reviewed publications. His work includes regional modeling of African, Arctic and East Asian (as well as North American) climates, and he has significant collaboration with scientists in these regions. Dr. Gutowski is currently Co-Chair of the Science Advisory Team for the WCRP's Coordinated Regional Downscaling Experiment (CORDEX). Prior to this, he helped lead earlier regional climate programs, most notably the Project to Intercompare Regional Climate Simulations and the North American Regional Climate Change Assessment Program. He has contributed assessment reports of the IPCC (including Lead Author, AR5), the U.S. National Academy of Sciences and the U.S. Climate Change Science Program. He has also served as an Editor for the Journal of Hydrometeorology. In light of his contributions to his field, he was recently elected a Fellow of the American Meteorological Society.

E-mail: gutowski@iastate.edu

Professor Timothy Carter



Research Professor at the Finnish Environment Institute (SYKE), Helsinki

Timothy Carter is a Research Professor at the Finnish Environment Institute (SYKE), Helsinki with over 35 years of research experience in the field of climate change impacts and adaptation. A geographer, he obtained a B.Sc. from the University of London and Ph.D. from the University of Birmingham, UK. He has worked on climate change and agriculture, methods of impact and adaptation assessment, including scenario development, and climate change adaptation. Based in Austria (International Institute for Applied Systems Analysis), the UK (Birmingham) and since 1990 in Finland, Carter has been a Lead Author for each of the five Intergovernmental Panel on Climate Change (IPCC) Assessment Reports as well as serving on the IPCC Task Group on Data and Scenario Support for Impacts and Climate Analysis (TGICA) since 1996. He has published 3 books and 120 refereed papers and reports.

E-mail: tim.carter@ymparisto.fi



INNOVATION FOR INFORMATION

SASAS 2016

**PROGRAMME
DAY 1: 31 OCTOBER**

KEY: *STUDENT

0800-0845	REGISTRATION
0845-0900	WELCOME (Dr Peter Johnston) AND HOUSEKEEPING (Mrs Kate Kloppers)
0900-0930	KEYNOTE ADDRESS
	Prof William Gutowski Water and Climate Change (WACC): Building Community Consensus for a Sustainable Future
0930-1000	INVITED SPEAKER
	Dr Yushi Morioka Role of Weddell Sea ice variability in southern African climate
1000-1030	TEA BREAK

1030-1230 SESSION 1 PARALLEL

1A		Climate Modelling and Development (Chairperson: Chris Lennard)	
1	1030-1045	Elelwani Phaduli	Evaluation of the Convective Scale Configurations of the Unified Model
2	1045-1100	Francois A. Engelbrecht	Dynamic core of the Variable-resolution Cubic Ocean Model (VCOM)
3	1100-1115	Magdel Erasmus*	Tropical Temperate Troughs over Southern Africa as Simulated by a Fully Coupled Model
4	1115-1130	Mary-Jane Bopape	Simulating the Convective Boundary Layer with a Dynamic Smagorinsky Model
5	1130-1145	Mavhungu S Muthige*	Impacts of spectral nudging on the simulation of present-day rainfall patterns over southern Africa
6	1145-1200	Rachel James	Representation of Tropical Temperate Troughs over southern Africa in coupled climate models

20 MIN DISCUSSION

1B		Ocean Dynamics and Atmosphere-Ocean Interactions (Chairperson: Marcello Vichi)	
1	1030-1045	Mathieu Rouault	Wind changes above warm Agulhas Current eddies

2	1045-1100	Marc de Vos	Towards understanding the impact of assimilating along-track SLA data on simulated eddy characteristics in the Agulhas System
3	1100-1115	Teboho Nchaba	Summer circulation trends over southern Africa and its adjacent oceans
4	1115-1130	Tharone Rapeti	Preliminary investigation into the impacts of assimilating SST and SLA on the surface velocities in a HYCOM of the Agulhas Current
5	1130-1145	Daneeja Mawren*	Variability of tropical cyclone heat potential and barrier layers in the South Indian Ocean
6	1145-1200	Fehmi Dilmahamod*	Investigating the regime of the South-West Indian Ocean Currents through a numerical model.

20 MIN DISCUSSION

1230-1330 LUNCH

1330-1410 POSTER PRESENTATIONS (1 MIN X 30)

PLENARY

1410-1550 SESSION 2

PARALLEL

2A		Climate Modelling and Development (Chairperson: Babatunde Abiodun)	
1	1410-1425	Stephanie Landman	Predictability of Rain-Bearing Systems over South Africa by Regional and Global Weather Prediction Models
2	1425-1440	Syamala Krishnannair	Comparative study of PCA and wavelet-PCA models for simulating monthly rainfall and temperature for Cape Point station
3	1440-1455	Willem Conradie*	Initial Conditions and Quantifying Model Climates: Does it Matter Where We Come from?
4	1455-1510	Georges-Noel T. Longandjo	How does well ECHAM simulate central Africa rainfall seasonal cycle?
5	1510-1525	Asmerom Beraki	Covariability of remote and local climate forcings and South African winter climate predictability

20 MIN DISCUSSION

2B		Atmosphere/Ocean Interaction, Aerosols and Atmospheric wave dynamics (Chairperson: Venkataraman Sivakumar)	
1	1410-1425	Kirodh Boodhraj*	An assessment of the role of vertical mixing schemes in the simulation of Southern Ocean upper dynamics
2	1425-1440	Neil Hart	Upper-level jets and eddies associated with tropical-extratropical cloud bands over southern Africa: The seasonal cycle
3	1440-1455	Xolile Nciphha*	Comparison of summer and spring carbon dioxide vertical and spatial distribution over the Southwest Indian Ocean Islands using TES data
4	1455-1510	Anzel Swart*	An Analysis of the Air Dispersion Potential over Uubvlei, Oranjemund, Namibia.

5	1510-1525	Majambo Gamoyo*	Mesoscale dynamics in the Western Indian Ocean (Focus on the Southern Gyre): A numerical investigation using ROMS
---	-----------	-----------------	-------------------------------------------------------------------------------------------------------------------

20 MIN DISCUSSION

1550-1610 TEA

1610-1730 SESSION 3 PARALLEL

3A	ENSO and seasonal impacts (Chairperson: Asmerom Baraki)		
1	1610-1625	Christien J. Engelbrecht	The 2015/16 Summer vs the Summers of the Last Decade
2	1625-1640	Willem A Landman	Decision-relevant information on seasonal time scales - the case of a farm in northern Namibia
3	1640-1655	Hector Chikoore	Evolution of the 2015/16 El Niño drought: circulation anomalies, heat waves and impacts on southern Africa
4	1655-1710	Takayoshi Ikeda	Linking malaria in Limpopo, South Africa to climate using self-organizing maps

20 MIN DISCUSSION

3B	Atmospheric Air Quality (Chairperson: Nkanyiso Mbatha)		
1	1610-1625	Maluta Pennington Mbedzi*	The potential use of CCAM as a meteorological driver to air quality mode over the Waterberg-Bojanala Priority Area
2	1625-1640	S.K. Sangeetha*	Comparative study of OMI BRD and PCA algorithm retrievals in relation to ground based measurements over a South African Site
3	1640-1655	Sewela Malaka*	Contribution of dairy farming on climate change through direct methane emissions to the atmosphere
4	1655-1710	Lynette V Schalkwyk	Warning South Africa when severe weather unfolds

20 MIN DISCUSSION

1730-1830 POSTER VIEWING (see poster presentation list below)

1730-1830 SASAS BOARD MEETING (by invitation only)

1900 GALA DINNER

DAY 2: 1 NOVEMBER

0830-0900	KEYNOTE ADDRESS
	Prof Tim Carter Modelling impacts of climate change: what are the information needs?
0900-0930	INVITED SPEAKER
	Prof Mike Savage Open water evaporation quo vadis?

0930-1030	SESSION 4	PLENARY
------------------	------------------	----------------

4		1.5 Degrees, Climate Services and application (Chairperson: Mark Tadross)	
1	0930-0945	Coleen Vogel	“END of END user!” – Transdisciplinary approaches in climate science.
2	0945-1000	Bruce Hewitson	The evolving landscape of Climate Information Websites
3	1000-1015	Piotr Wolski	Improving visualisations of climate projection information

15 MIN DISCUSSION

1030-1100	TEA
------------------	------------

1100-1300	SESSION 5	PARALLEL
------------------	------------------	-----------------

5A		Applications for water and agriculture (Chairperson: Piotr Wolski)	
1	1100-1115	Harold Weepener	Climate change related impact on avocado production areas in South Africa
2	1115-1130	Johan Malherbe	How would current advice benefit maize farmers with respect to historical associations with El Niño events
3	1130-1145	Shepherd Muchuru	Mitigating vulnerability to drought and enhancing livelihood resilience: A review of Southern Africa region
4	1145-1200	Teboho Masupha*	Temporal evolution of agricultural drought in the Luvuvhu River catchment of South Africa
5	1200-1215	Yao Télésphore Brou	Spatio-temporal variability of rainfall and impacts on vegetation in Reunion Island
6	1215-1230	Lisa van Aardenne	Climate and Tsetse: exploring the effect of climate variability and change on vector biology, population dynamics and distribution in the Zambezi Valley

20 MIN DISCUSSION

5B		Instrumentation and data collection (Chairperson: Mike Savage)	
1	1100-1115	Alexa Brown*	Time, space and vector relationships between historical ship log data and Cape Royal Astronomical Observatory wind data between 1834 and 1854

2	1115-1130	Yerdashin Padayachi	Anthropogenic Heat Flux in South African Cities: Initial estimates from the LUCY model
3	1130-1145	Morné Gijben	Recent improvements to the rapidly developing thunderstorm product - the addition of lightning data into the software
4	1145-1200	Erik Becker	Application of radar data at the South Africa Weather Service
5	1200-1215	Nkanyiso Mbatha	Stratosphere-troposphere exchange climatology over southern Africa using ERA-Interim data set and AIRS/Aqua satellite data
6	1215-1230	Zakhele Shabalala*	Development of a patching tool on recorded daily climate data

20 MIN DISCUSSION

1300-1400 LUNCH

1400-1530 SESSION 6

PARALLEL

6A		Climate & weather forecasting (Chairperson: Willem Landman)	
1	1400-1415	Henno Havenga*	High Resolution dBz simulation of some notable hailstorms that occurred in 2013 over the South-African Highveld using WRF
2	1415-1430	Melise du Toit*	The application of support vector regression (SVR) for stream flow prediction on the Amazon basin
3	1430-1445	Kelebogile Mathole	The climatology of the stratospheric zonal wind and its wave driving in the SAWS operation seasonal prediction system
4	1445-1500	Izidine Pinto*	Process-based assessment of two CORDEX climate models projections over southern Africa
5	1500-1515	Elizabeth Webster	Impact-based severe weather warning system

15 MIN DISCUSSION

6B		Dust - Southern African aerosols, sources pathways and impacts (Chairperson: Frank Eckhardt)	
1	1400-1415	Johanna von Holdt*	Aeolian dust emission from the Namib Desert: local-scale erodibility controls
2	1415-1430	Rebecca Garland	Representation of aerosol particles and associated transport pathways in regional climate modelling in Africa
3	1430-1445	Priyanka Singh*	Validation and comparison between Aerosol Optical Depth acquired from Sun Photometer and MODIS satellite over Durban
4	1445-1500	Thabo Makgoale*	The sensitivity of simulated temperatures in climate models to aerosols over southern Africa
5	1500-1515	Ruusa Gottlieb*	The contribution of fog to the biogeography of <i>Arthroerua leubnitziae</i> in the central Namib desert

15 MIN DISCUSSION

1530-1550 TEA

1550-1600 AWARDS AND CLOSING

1600-1700 AGM



TABLE OF CONTEXT

FIRST AUTHOR SURNAME	FIRST AUTHOR NAME	PEER REVIEWED CONFERENCE PROCEEDING TITLE	PAGE NUMBER
B			
Brown	Alexa	Time, space and vector relationships between historical ship log data and Cape Royal Astronomical Observatory wind data between 1834 and 1854.	1
Boodhraj	Kirodh	An assessment of the role of the k-ε vertical mixing scheme in the simulation of Southern Ocean upper dynamics.	6
Bopape	Mary-Jane	Simulating the Convective Boundary Layer with a Dynamic Smagorinsky Model.	11
C			
Conradie	Willem Stefaan	Initial Conditions and Quantifying Model Climates: Does it Matter Where We Come from?	16
D			
de Vos	Marc	Towards understanding the impact of assimilating along-track SLA data on simulated eddy characteristics in the Agulhas System.	21
du Toit	Melise	The application of support vector regression (SVR) for stream flow prediction on the Amazon basin.	25
E			
Engelbrecht	Christien J.	The 2015/16 Summer vs the Summers of the last decade.	29
Engelbrecht	Francois A.	Dynamic core of the Variable-resolution Cubic Ocean Model (VCOM).	32
Erasmus	Magdel	Tropical Temperate Troughs over Southern Africa as Simulated by a Fully Coupled Model.	36
G			
Garland	Rebecca	Representation of aerosol particles and associated transport pathways in regional climate modelling in Africa.	40

Gijben	Morné	Recent improvements to the Rapidly Developing Thunderstorm product – the addition of lightning data.	45
H			
Havenga	Henno	Evaluating WRF's dBZ diagnostic feature on the 28 November 2013 hailstorm over the South-African Highveld.	50
Hewitson	Bruce	The evolving landscape of Climate Information Websites.	55
K			
Krishnannair	Syamala	Comparative study of PCA and wavelet-PCA models for simulating monthly rainfall and temperature at Cape Point.	60
L			
Landman	Stephanie	Evaluation of the Predictability of Rainfall over South Africa by Regional and Global Weather Prediction Models.	64
Landman	Willem A	Decision-relevant information on seasonal time scales – the case of a farm in northern Namibia.	69
Longandjo	Georges-Noel T.	How does well ECHAM simulate central Africa rainfall seasonal cycle?	73
M			
Malherbe	Johan	How would current advice benefit maize farmers with respect to historical associations with El Niño events?	78
Mathole	Kelebogile	The climatology of the stratospheric zonal wind and its wave driving in the SAWS operation seasonal prediction system.	83
Mbedzi	Maluta	The potential use of CCAM as a meteorological driver to air quality models over the Waterberg-Bojanala Priority Area.	87
Muthige	Mavhungu S.	Impacts of spectral nudging on the simulation of present-day rainfall patterns over southern Africa.	92
N			
Nchaba	Teboho	Summer circulation trends over southern Africa and its adjacent oceans.	96
Ncipha	Xolile G.	Comparison of summer and spring carbon dioxide vertical and spatial distribution over the Southwest Indian Ocean Islands using TES data.	100
P			
Padayachi	Yerdashin	Anthropogenic Heat Flux in South African Cities: Initial Estimates from the LUCY model.	104
Phaduli	Elelwani	Evaluation of the Convective Scale Configurations of the Unified Model.	108
R			
Rapeti	Tharone	Preliminary investigation into the impacts of assimilating SST and SLA on the surface velocities in a HYCOM of the Agulhas Current.	112
Rouault	Mathieu	Wind changes above warm Agulhas Current eddies.	116

S			
Sangeetha	Sivakumar K	Comparative study of OMI BRD and PCA algorithm retrievals in relation to ground based measurements over a South African Site.	119
Savage	Michael J.	Open water evaporation – quo vadis?	123
Singh	Priyanka	Comparison between Aerosol Optical Depth acquired from Sun Photometer and MODIS satellite over Durban.	128
Swart	Anzel	An Analysis of the Air Dispersion Potential over Uubvlei, Oranjemund, Namibia.	132
W			
Weepener	Harold L.	Climate change related impact on avocado production areas in South Africa.	136
Wolski	Piotr	Improving visualizations of climate projection information.	140



INNOVATION FOR INFORMATION

SASAS 2016

PEER-REVIEWED CONFERENCE

PROCEEDINGS

Time, space and vector relationships between historical ship log data and Cape Royal Astronomical Observatory wind data between 1834 and 1854.

A. Brown (1), C. Lennard (2) and S. Grab (3)

(1) African Climate and Development Initiative, Department of Environmental and Geographical Sciences, University of Cape Town, Cape Town; (2) Climate System Analysis Group, Department of Environmental and Geographical Sciences, University of Cape Town, Cape Town; (3) School of Geography, Archaeology and Environmental Studies, University of the Witwatersrand, Johannesburg.

Abstract

This project assesses the extent to which Climatological Database for the World's Oceans (CLIWOC) data reflect recently digitized historical wind data from the Royal Astronomical Observatory in Cape Town, South Africa (1834 – 1854). This follows the precipitation reconstructions done by Hannaford *et al.* (2015) using CLIWOC ship log data. Temporal, spatial and vector relationships are established for each season using scatter plot graphs and Pearson correlation. No significant correlation or signal is evident over time, or with a difference in distance. However, seasonality is represented consistently in wind vector distribution. Thus, historical wind data used here are accurate but have no correlation over time and space. This project highlights the major inconsistencies and limitations in the CLIWOC data compared to land based historical data. Researchers in the future should use CLIWOC, or land based data, appropriately to suit the research question.

Keywords

Historical Climatology; South Africa; Cape Town Royal Astronomical Observatory; CLIWOC Ship Log Data

Introduction

South Africa, and much of the southern hemisphere lacks long-term historical climate data that is continuous and reliable (Neukom *et al.*, 2014). Neukom, *et al.* (2014), Nash (1990) and Vogel (1989) are some of the earlier authors who have engaged in data recovery and digitisation from available documentary and instrumental meteorological resources, specifically to perform long term historical studies on southern African climatology. Notably, much of the historical

climatology for the region is based on rainfall and temperature data. Added to which, the data are not consistent through time and are sparsely located over a very large spatial domain. This impedes the understanding of historical climatology for southern Africa, and therefore our current understanding of atmospheric dynamics and regional climate trends over time. For this reason, it is important to recover any known sources of data and analyse the data thoroughly.

Newer studies such as Brohan *et al.* (2009) and Wheeler and Suarez-Dominguez (2006) explain that barometric measurements and wind data, additional to temperature and precipitation, provide useful insight into historical surface climatology. The Climatological Database for the World's Oceans (CLIWOC) project (more info available at <http://pendientedemigracion.ucm.es/info/cliwoc/>) is an example of the extent to which the international community is collectively gathering and pre-processing historical atmospheric data for coupled analyses. This motivates the recovery, digitization and analysis of wind data from the Royal Astronomical Observatory (RAO) in Cape Town. A previously unknown observational data set.

Hannaford *et al.* (2015) presents an historical precipitation reconstruction for Southern Africa using CLIWOC ship log data. The knowledge of peer-authors using ocean based, ship log data further motivates the purpose of this study to assess the relationship between two of the oldest known sources of wind data for Southern Africa. There is a cross over period from 1834 – 1854 that allows for data comparison between the CLIWOC data and RAO data. This is a preliminary research opportunity to promote historical atmospheric sciences for Southern Africa.

This paper shall establish a general climatology for the RAO that will act as the reference data set. From this reference data set the CLIWOC data can be compared for temporal and spatial relationships.

This project will test the extent to which the data are equal on the same day, whether the data relationship deteriorates proportionately to distance between the data sources. Lastly this project assesses if the data has captured similar seasonal wind vectors.

Methodology and data

Manually digitising and pre-processing the wind data shows that the data were recorded in the same conventions despite the RAO being a 'scientific centre', and the ships recording wind for navigation and insurance purposes (Garcia *et al.*, 2003, Brown, 1977 and Sabine, 1851). Wind direction was recorded on a 32-point wind compass (converted to decimal degrees). Wind force was recorded on a scale of 0- 12 in Beaufort Force (converted to meters per second). Both data sets include noon readings only (00h00).

Data from the RAO (coordinates 33°56'7.30"S 18°28'39.34"E; 17m.a.s.l) provide consecutive daily noon readings from 1834 to the 1970s (7.4% of all noon readings missing). CLIWOC data recorded on board ships, provides noon readings from the 18th century until 1854. The data occurs sporadically

over space and time (i.e. it is not a consistent and consecutively recorded on a daily basis).

A combined qualitative and quantitative systems-based approach defined by Trenberth *et al.* (2002) is integral for identifying the limitations and inconsistencies in the data sets:

- i) Individually, the data sets are inconsistent over time.
- ii) Combined, the data values are variably spaced apart for the same date.
- iii) Seasonality and multi-scalar atmospheric conditions add noise to the data.

Therefore, days with complete wind vector (direction and force) are matched for the RAO using the available CLIWOC data from 1834 – 1854. These data may be compared in three geographically defined areas around the south west Cape of South Africa for each season (Fig. 1). Regionalisation minimises error associated with binning all regions of different prevailing wind directions caused by terrain/ topography effects and along-shore flow (i.e. A3 experiences east-west flow, A1 experiences SE-NW flow, RAO affected by complex Cape Peninsula terrain). Seasonal comparisons decrease error associated with seasonal wind shifts, linked with regional differences.

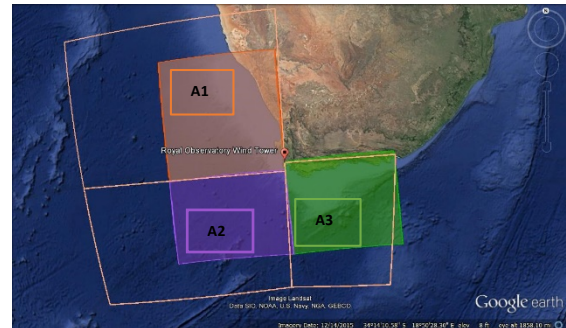


Figure 1: Map of demarcated regions: Area 1, Area 2 and Area 3.. CLIWOC data within each area will be analysed against the RAO (located at red pin). The orange lines indicate the original domain of data used by Hannaford *et al.* (2015).

This minimises the amount of error inherent in the data comparison, while still ensuring reliable and sufficient data integrity and density.

Results and discussion

The general climatology

The wind data from the RAO shows a general climatology consistent with the seasonal wind climate experienced at the south west Cape of South

Africa (Tyson and Preston-Whyte, 2004). Results show that 33.6% winds are from a southerly direction and 33.82% from a north westerly direction. The seasonal wind roses in Fig. 2 show seasonal prevailing winds that are consistent with the expected seasonal conditions.

Winter experiences predominantly north westerlies caused by approaching mid-latitude cyclones and frontal systems. Autumn and spring experience highly variable winds due to north-south shifting of planetary circulatory systems in the subpolar low pressure belt. Summer experiences southerly and south easterly winds due to the presence of the South Atlantic High Pressure cell. Additionally, a high frequency of north westerlies is recorded in summer at the RAO (17m.a.s.l), which can be attributed to station position below and to the east of Devil's Peak (970m.a.s.l) or localised micro-scale atmospheric conditions in the area of the RAO.

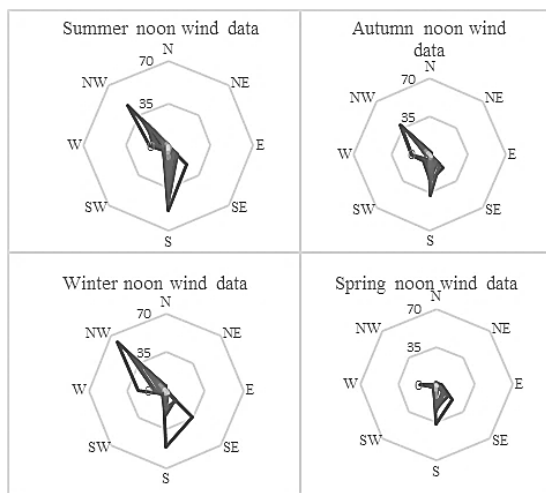


Figure 2: Wind roses for all recorded noon wind directions at the RAO, 1834 - 1854. Each seasonal wind rose represents expected prevailing wind directions.

Data relationships for the same date

There is no significant or strong correlation between the CLIWOC data from any of the three study areas and the RAO for wind direction ($r < 0.131437$ and $p > 0.05$ for all seasons) or wind speed ($r < 0.23964$ and $p > 0.05$ for all seasons). Throughout the time period being analysed, data value variability is random which shows no significant signal or relationship between the data over time. It is noticeable though that the ships record higher wind speeds, which is expected due to the effect of increased land surface drag effect on wind speed.

Determining the relationship between data based on distance away from the RAO

The value difference (delta wind direction/speed) plotted against the distance between the CLIWOC position of observation (given as latitude and longitude) and the RAO shows no clear signal in the data relationship. The data variability is random. That is to say that the distance between the RAO and the ships does not have any proportional effect on the standard of deviation in the data; all of the data has a high standard deviation. The percentage of data variability that is attributable to the relationship between the data is not significant ($R^2 \% < 2.43\%$ for wind direction and $R^2 \% < 6.77\%$ for wind speed). There is no significant signal in the differences between direction (and speed), and the distance from the RAO ($r = 0.117$ (and $r = 0.156$), $p > 0.05$).

The only exception is in the ships positioned within 100km from the RAO in Area 1 for the summer season. Fig. 3 shows that ships record less than 90° wind shifts (opposed to the high variability of small and larger differences in data further than 100km).

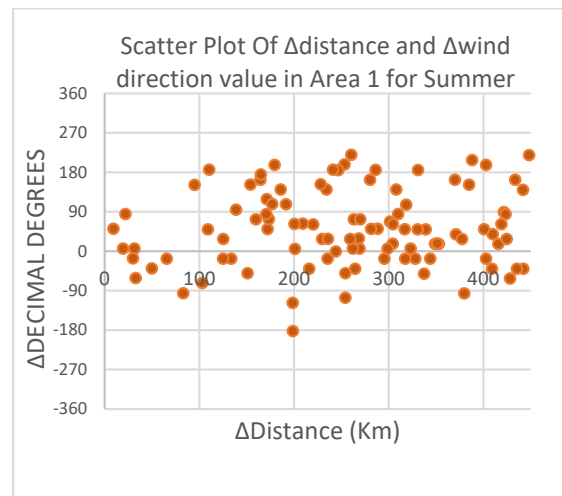


Figure 3 shows that within 100km, the difference between observed wind directions in the CLIWOC data and the RAO data are $\leq 90^\circ$. Despite a weak statistical correlation ($r = 0.116946$; $r > 0.05$), this shows an acceptable deviation.

Wind speed is mostly within a 10m/s difference, indicating a general agreement between observations taken up to 100km from the RAO. Wind data value differences occur within an acceptable range to denote a correlation between

wind data. The observers recorded similar conditions at the RAO and on board ships for the same days in summer in Area 1.

Dominant wind vector distributions for ship log data

The CLIWOC data shows typical seasonal prevailing wind directions and wind force frequencies given the study area. The heat map (colour coded distribution tables) in Table 1 shows the distinctive seasonality for Area 3 (see Fig. 1 for a map) where the distribution frequency shows predominantly (44.8%) south westerly winds. These winds follow the passing of winter mid-latitude cyclones over the region. The north westerlies are also dominant (31.2%) which is typical of approaching mid-latitude cyclones.

Table 1 shows the distribution of recorded wind directions and wind forces in Area 3 (south coast) for Winter from 1834 - 1854.

Winter	NE	SE	SW	NW	No. of events	% of events
0	1	0	2	2	5	1.15
0.1 to 1.5	14	5	12	12	43	9.93
1.6 to 3.3	5	9	22	14	50	11.55
3.4 to 5.4	15	8	22	27	72	16.63
5.5 to 7.9	11	1	22	11	45	10.39
8 to 10.7	7	5	14	9	35	8.08
10.8 to 13.8	7	7	21	13	48	11.09
13.9 to 17.1	1	2	18	10	31	7.16
17.2 to 20.7	2	2	21	5	30	6.93
20.8 to 24.4	0	1	25	12	38	8.78
24.5 to 28.4	0	1	11	13	25	5.77
28.5 to 32.6	0	0	4	7	11	2.54
32.7 +	0	0	0	0	0	0.00
No. of events					43	
% of events	14.6	9.47	44.8	31.2	3	

The summer, autumn and spring distribution tables (not shown in this report) show the domination of southerly winds with an easterly component. Whereas, the winter season shows northerly and southerly winds with a westerly component. The mid-latitude cyclones are cause for this winter variation between north and south, through west, due to the travelling cyclonic frontal systems. The wind vector distribution tables factor out time and space as a dependent variable and allow for the seasonal s=wind shifts to be shown for each area. Each area shows typical seasonal conditions which

suggests that the data is accurately capturing the winds over the oceans.

Conclusions

This project has successfully created a digital wind data set for the RAO that is compared to the only other known source of historical wind data for the time and region. Hannaford *et al.* (2015) uses CLIWOC wind data in order to do an historical precipitation reconstruction. This work motivated the research question of the extent to which CLIWOC data represents RAO data – land based data.

The results found that the data does not correlate well over space and time, and that only two clear signals exist in the data:

- i) Ship logs record expected higher wind speeds,
- ii) Only CLIWOC data within 100km from the RAO recorded similar wind observations (within acceptable deviations).

Data are not well correlated due to the limitations in the data integrity and the complexity of comparing a highly variable atmospheric variable over a large domain. However, despite the weak correlations (statistical and tested) over space and time, the expected seasonal signals in the wind vectors observed in each ocean region and at the RAO suggest that the ships' and RAO observers were capturing wind data accurately. That is to say, the wind vector distributions are consistent with expected seasonal trends and signals based on current knowledge of the atmospheric dynamics. It is because of limitations in space, time and data integrity that the cross correlations are weak. Therefore, although the data are reliable, appropriate means of analysing historical wind data from various sources should use multi-variate analyses, like a principal component analysis, for a better understanding of the correlations between different sources of historical data.

This study shows that there are many inconsistencies and limitations that have to be treated with caution when handling historical data of this nature. Furthermore, future research should use the data appropriately to suit the research question. Thus, it can be said that the CLIWOC data do not reflect RAO data well, but that the data are still correct in their absolute values.

Acknowledgements

This work was made possible by the financial support from the Climate Systems Analysis Group, UCT. Chris Lennard and Stefan Grab have motivated and supported this work for 18 months. Matthew Hannaford provided the CLIWOC data used in this project. Thank you to all who have helped me with data handling and editing.

References

Brown, A. C., 1977. *A History of Scientific Endeavour in South Africa*. (Editor), June 1977. The Rustica Press, Republic of South Africa.

Brohan, P., Allan, R., Freeman, J. E., Waple, A. M., Wheeler, D., Wilkinson, C. and Woodruff, S. (2009): Marine Observations of Old Weather. *Bulletin of the American Meteorological Society*. 90: 219–230.

Garcia-Herrera, R., Konnen, G. P., Wheeler, D. A., Prieto, M. R., Jones, P. D. and Koek, F. B. (2005): CLIWOC: A Climatological Database for the World's Oceans 1750 – 1854. *Climate Change*. 73: 1 – 12.

Hannaford, M. J., Jones, J. M. and Bigg, G. R. (2015): Early-Nineteenth-Century Southern African Precipitation Reconstructions from Ships' Logbooks. *The Holocene*. 25(2): 379 – 390.

Nash, M. D. (1990): *The Last Voyage of the Gaurdian, Lieutenant Riou, Commander: 1789 - 1791*, Van Riebeeck Society, Cape Town, Series no. 20.

Appendix: list of Figures and Tables

Figure 1: A Map of the study region (p. 2)

Figure 2: Wind roses for all recorded noon wind directions at the RAO from 1834 – 1854 (p. 2)

Figure 3: Scatter plot of Δ distance and Δ wind direction value in Area 1 for Summer (p. 3)

Table 1: distribution heat map of wind direction and force frequencies for Area 3 in winter

Neukom, R., Nash, D. J., Endfield, G. H., Grab, S. W., Grove, C. A., Kelso, C., Vogel, C. H. and Zinke, J. (2014): Multi- proxy summer and winter precipitation reconstructions for southern Africa over the last 200 years. *Climate Dynamics* 42: 2713–2726.

Sabine, E. (1851). “*Observation made at the Magnetic and Meteorological Observatory of the Cape of Good Hope*”, Vol I., Longman, Brown, Green and Longmans, London.

Trenberth, K. E., Karl, T. R. and Spence, T. W. (2002): The Need for a Systems Approach to Climate Observations. *Bulletin of the American Meteorological Society*. 83: 1593-1602.

Tyson, P. D. and Preston-Whyte, R. A. (2004): *The Weather and Climate of Southern Africa*, Oxford University Press, South Africa.

Vogel, C. H. (1989): A documentary derived climatic chronology for South Africa, 1820 – 1900. *Climate Change*. 14: 291 – 307.

Wheeler, D. and Suarez-Dominguez, J. (2006): Climatic reconstructions for the northeast Atlantic region ad 1685-1700: A new source of evidence from naval logbooks. *The Holocene*. 16: 39–49.

The Climatological Database for the World's Oceans 1750-1850, available at <<http://pendientedemigracion.ucm.es/info/cliwoc/>>; Accessed 2 August 2016, 10:25.

An assessment of the role of the k- ϵ vertical mixing scheme in the simulation of Southern Ocean upper dynamics

Kirodh Boodhraj^{1,2,*}, Marcello Vichi^{2,3} and Jacoba E. Smit¹

¹CSIR Modelling and Digital Science, Advanced Mathematical Modelling, Stellenbosch 7600, South Africa

²Dept. of Oceanography, University of Cape Town, Rondebosch 7701, Cape Town, South Africa

³Marine Research Institute, University of Cape Town, Rondebosch 7701, Cape Town, South Africa

Abstract

Following the work done by Reffrey, Calone and Bourdalle-Badie (2015) we implemented a one dimensional(1D) ocean physical model in the sub-Antarctic Southern Ocean using the Nucleus for the European Modelling of the Ocean(NEMO) model. The 1D model is a first attempt at studying sub-grid scale parameterizations in the region. It was used to test the effects of the k- ϵ turbulence closure scheme on the simulation of vertical mixing in the water column structure in the North Pacific and Southern Ocean, using the available scattered data as comparison. This analysis also gives indications for the choice of the grid's vertical levels.

Keywords: NEMO, Sub-mesoscale Parameterizations, Turbulence Closure Model, Vertical Mixing, Southern Ocean

Introduction

Currently the first African based Earth System model, the Variable Resolution Earth Systems Model (VRESM), is being developed at the CSIR and will greatly enhance understanding regional effects of climate change. Many components of the model that were optimized for other locations need to be adapted and optimized before the model can be implemented with focus on the African continent. One of the model components is the use of sub-grid scale parameterization techniques (Gent and McWilliams, 1990; Fox-Kemper et al., 2008) to resolve eddies.

The initial step to achieve this relies on vertical mixing processes. In a general model of the ocean, the choice of the vertical mixing model is essential to achieve more accurate modelling results. The vertical mixing will cause density differences that will result in the stratification of the water column which shifts the thermocline and halocline according to season. This physical process is important for marine species survival.

The objective of this paper is the use of vertical turbulence closure schemes to model vertical mixing processes similar to Reffrey et al. (2015). Furthermore, Southern Ocean (SO) conditions were

applied to find the temperature and salinity results for 75 and 51 vertical levels.

Instrumentation and Method

Reffrey et al. (2015) concentrated on comparing the results of using different vertical turbulence models that come with NEMO (<http://www.nemo-ocean.eu>; Madec et al., 2016) to observed data in the ocean. The k- ϵ turbulence model (Versteeg and Malalasekera, 2007) was used in this paper because Reffrey et al. (2015) concluded that this model produced the most accurate results in comparison to the other turbulence models.

Reffrey et al. (2015) used a 1-dimensional code referred to as the C1D_PAPA case to test the different turbulence schemes. The initial and boundary conditions files are included with C1D_PAPA. This case was later tailored to use SO conditions. C1D_PAPA uses an Arakawa A grid type consisting of a column composed of a 3 \times 3 horizontal grid (x- and y-directions) with an ideal resolution of 0.1 $^{\circ}$ \times 0.1 $^{\circ}$ with 75 vertical levels (z-direction). All the 9 water columns are identical and allow removing horizontal processes by zeroing the gradients while keeping the same computer code structure i.e. the 9 columns are needed only for the sound operation of NEMO but every level has the same temperature, salinity, velocity etc. values. The time step used was set to 360 s.

The observed data (needed for comparison with the calculated results) from PAPA Station was obtained

from the National Ocean Atmospheric Administration (NOAA, 2016) website. The PAPA Station is located in the North Pacific Ocean. The SO station was ideally located in the sub-Antarctic zone at 46S, 4W. The initial conditions were obtained from the World Ocean Atlas (Locarnini et al., 2013) and the forcing data from European Centre for Medium-Range Weather Forecasts (ECMWF) ERA-interim reanalysis (Dee et al., 2011).

Reffray et al. (2015) calculated the bias for the temperature by subtracting the calculated data from the observed data. All plots, for the North Pacific and SO, were plotted for the period 15 June 2010 to 14 June 2011 unless otherwise stated.

The following density model was chosen to calculate the density (Millero and Poisson, 1981) using the output from NEMO:

$$\rho(T, S) = AS + BS^{1.5} + CS^2 \quad (1)$$

,where

$$\begin{aligned} A(T) &= 8.24493 \times 10^{-1} \\ &- 4.0899 \times 10^{-3}T \\ &+ 7.6438 \times 10^{-5}T^2 \\ &- 8.2467 \times 10^{-7}T^3 \\ &+ 5.3875 \times 10^{-9}T^4 \end{aligned} \quad (2)$$

$$\begin{aligned} B(T) &= -5.72466 \times 10^{-3} \\ &+ 1.0227 \times 10^{-4}T \\ &- 1.6546 \times 10^{-6}T^2 \end{aligned} \quad (3)$$

$$C(T) = 4.8314 \times 10^{-4} \quad (4)$$

,where ρ is the density, T the temperature and S the salinity. Note that the density is a function of salinity and temperature only.

The Root Mean Square Error (RMSE) for the temperature was calculated using the standard formula:

$$RMSE = \sqrt{\frac{\sum_{i=1}^n (T_i^{Comp} - T_i^{Obs})^2}{n}} \quad (5)$$

Results and Discussion

Results following Reffray et al. (2015) work are shown in Figs. 1-3. Results following Figs. 4-7 were independent of Reffray et al. (2015).

Both the temperature data in Fig. 1 and the temperature bias in Fig. 2 show that within the first five months there was a large stratification with a

shallow Mixed Layer Depth (MLD) within a depth of 0 – 60 m. The high bias within the first five months indicated that the model could not represent the observed data accurately. The reason being that the MLD was shallower during the summer because of the surface heating. Seasonal surface cooling then destroyed the stratification for the rest of the year which deepened the MLD and caused the homogeneity. The bias (Fig. 2), found from the distribution of the calculated and observed temperature, followed the same trend as what Reffray et al. (2015) had found. The main difference was that the calculated temperature RMSE values (Fig. 3) were higher than what Reffray et al. (2015) had found.

The temperature RMSE values stabilized from midyear to the end of the year to 0.15 ± 0.05 °C. Reffray et al. (2015) RMSE values stabilized to 0.05 ± 0.3 °C. The discrepancy could have arisen from the averaging of data to obtain the biases as Reffray et al. (2015) had calculated the RMSE values up to 120 m whereas in this paper the RMSE's were calculated up to 300 m. The reason for calculating the RMSE up to 300 m was to take into account the MLD (homogeneous region) which extends lower than 120 m.

The results for the density (calculated using Eqs. 7–10) are shown in Figs. 4 and 5. The calculated densities lie within an error of ± 0.5 kg/m³ from the observed values. The overall form of the graphs for both September (during the mixing period) and October (the beginning of the mixing period) are similar to the observed data. The depth of the pycnocline suddenly increased in October, because of the seasonal change which started the mixing in autumn.

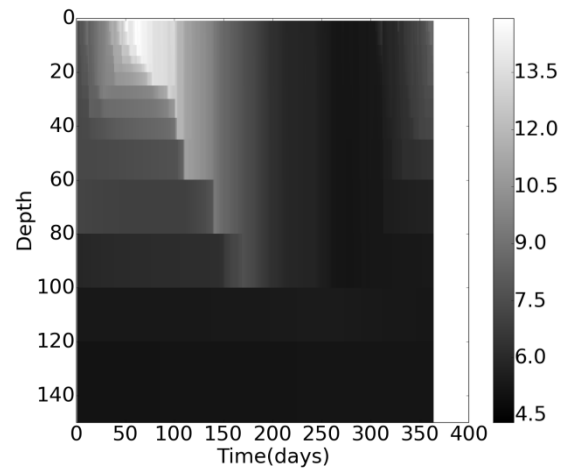


Figure 1: The calculated temperature for the period 15 June 2010 to 14 June 2011 using the NEMO C1D_PAPA case. The k-ε model was used with a time step of 360 s.

The results for temperature and salinity using SO conditions are shown in Figs. 6 and 7. In both the temperature and salinity calculated data the surface fluxes influenced the upper 300 m of the stratified water column. In the upper layer of Fig. 6, the temperature slowly increased and then decreased as time progressed. In the upper layer of Fig. 7, the salinity continually decreased as time progressed, indicating a drift likely due to the one-dimensional approximation.

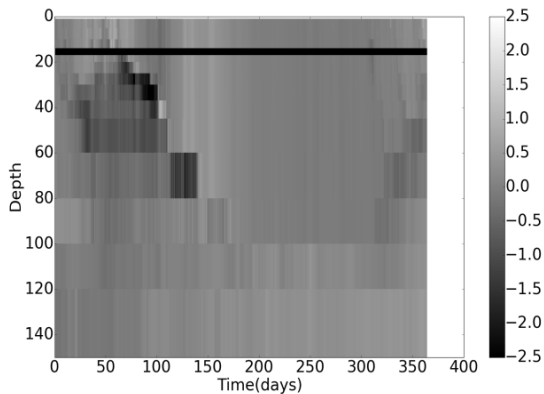


Figure 2: The temperature bias for the period 15 June 2010 to 14 June 2011 using the calculated data from NEMO C1D_PAPA case and the observed data from PAPA Station. The $k-\epsilon$ model was used with a time step of 360 s. There was no observed data for the horizontal band around 15 m.

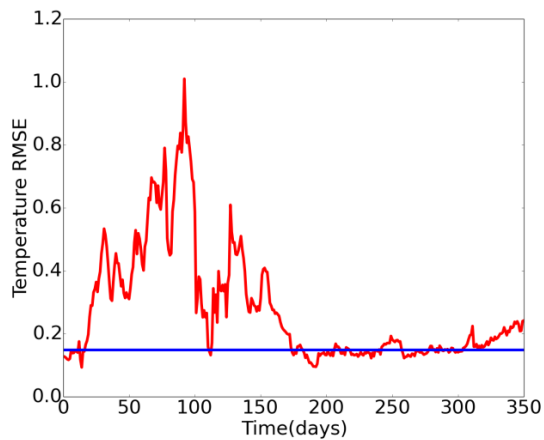


Figure 3: The temperature RMSE calculation for the period 15 June 2010 to 14 June 2011 using the calculated data from NEMO C1D_PAPA case and the observed data from PAPA Station. The horizontal line indicates that the RMSE stabilized to $0.15\text{ }^{\circ}\text{C}$. The $k-\epsilon$ model was used with a time step of 360 s.

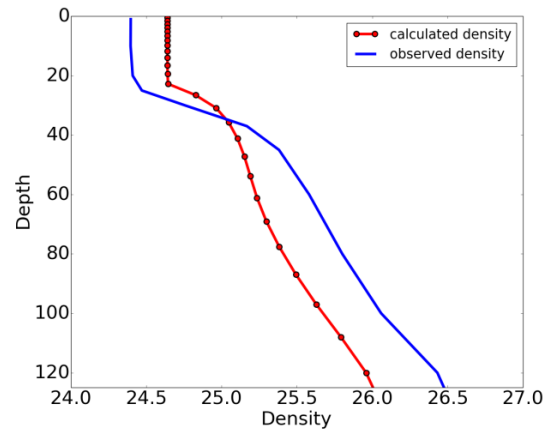


Figure 4: The density calculation for 12 September 2010 (during mixing period) using the calculated data from NEMO C1D_PAPA case compared to the observed data from PAPA Station.

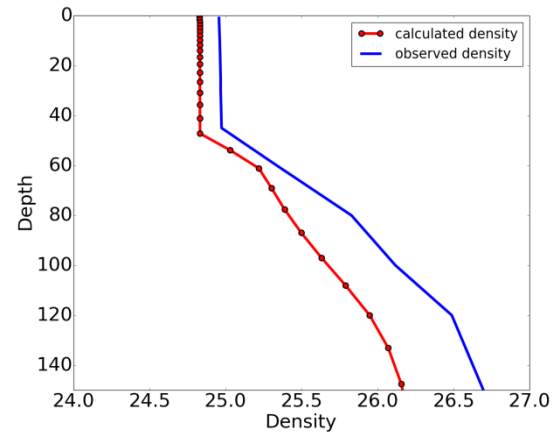


Figure 5: The density calculation for 12 October 2010 (beginning of mixing period) using the calculated data from NEMO C1D_PAPA case compared to the observed data from PAPA Station.

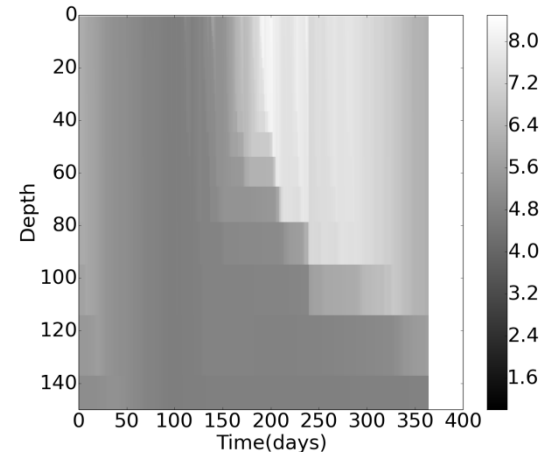


Figure 6: The calculated temperature for the period 15 June 2010 to 14 June 2011 using SO conditions produce the same result for 51 and 75 vertical levels. The $k-\epsilon$ model was used with a time step of 360 s.

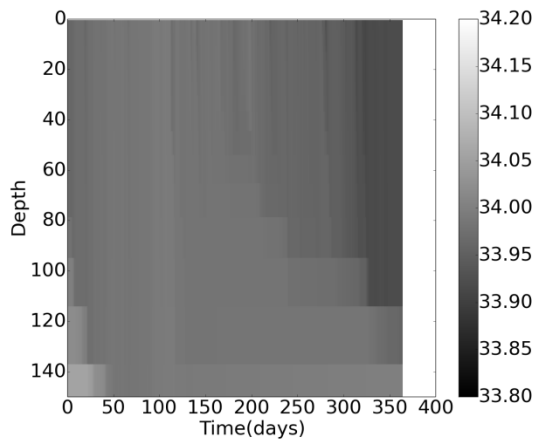


Figure 7: The calculated salinity for the period 15 June 2010 to 14 June 2011 using SO conditions produce the same result for 51 and 75 vertical levels. The k- ϵ model was used with a time step of 360 s.

A grid sensitivity test for the SO model was done by changing the number of vertical levels from 75 to 51. The temperature and salinity results were the same as Figs. 6 and 7 with no apparent changes in the structures.

Future work will include the modification of C1D_PAPA to verify the results of the other turbulence closure schemes (Turbulent Kinetic Energy (TKE), k-kl, k- ω and Generic). There is scope to test the vertical grid sensitivity further i.e. increase the number of vertical levels to assess whether vertical mixing is affected. Mixed layer depths in the region are usually deeper than 150 m and it is worth assessing whether a 1D model can reproduce them purely through local turbulence. The SO has a stronger horizontal advection which may influence the results and therefore it may also be necessary to consider restoration to avoid drifts as seen for salinity.

Conclusions

This paper highlights the first attempt to study the vertical mixing in the SO using NEMO. The results obtained from Figs. 1-3 were found from following Reffray et al. (2015) and the results from Figs 4-7 were found from applying SO conditions to the tailored C1D_PAPA case. The RMSE values converged within the time period however the value was approximately 0.1 °C bigger than what Reffray et al. (2015) had found. The density model (Eqs. 7-10) produced results within an error margin of 0.5 kg/m³ and also had a similar form to the observed data. Using SO conditions and changing the vertical levels to 51, it was found that the temperature and salinity results (Figs. 6 and 7) were identical compared to having 75 vertical levels. Scope lies within investigating the results of increasing the number of vertical levels and implementing other turbulence models using SO conditions.

Acknowledgements

The present work is funded by the CSIR Parliamentary Grant and the VRESM SRP project from Prof. Francois Engelbrecht. Acknowledgement is given to Dr Björn Backeberg for funding this extended abstract.

References

(i) Journals:

Reffray, G., Bourdalle-Badie, R. and Calone, C. (2015). Modelling turbulent vertical mixing sensitivity using a 1-D version of NEMO. *Geoscientific Model Development*. 8: 69-86

Gent, P.R. and McWilliams, J.C. (1990). Isopycnal mixing in ocean circulation models. *Journal of Physical Oceanography*. 20:150-155

Fox-Kemper, B., Ferrari, R. and Hallberg, R. (2008). Parameterization of mixed layer eddies. Part I: Theory and diagnosis. *Journal of Physical Oceanography*. 38(6): 1145-1165

Millero, F. J. and Poisson, A. (1981). International one-atmosphere equation of state of seawater. *Deep-Sea Research, Elsevier*. 6: 625-629

Dee, D. P., Uppala, S. M., Simmons, A. J., Berrisford, P., Poli, P., Kobayashi, S., Andrae, U., Balmaseda, M. A., Balsamo, G., Bauer, P., Bechtold, P., Beljaars, A. C. M., van de Berg, L., Bidlot, J., Bormann, N., Delsol, C., Dragani, R., Fuentes, M., Geer, A. J., Haimberger, L., Healy, S. B., Hersbach, H., Hólm, E. V., Isaksen, L., Kållberg, P., Köhler, M., Matricardi, M., McNally, A. P., Monge-Sanz, B.M., Morcrette, J. J., Park, B. K., Peubey, C., de Rosnay, P., Tavolato, C., Thépaut, J. N., Vitart, F., (2011). The ERA-Interim reanalysis: configuration and performance of the data assimilation system. *Quarterly Journal of the Royal Meteorological Society*. 137(656): 553-597

Locarnini, R. A., Mishonov, A. V., Antonov, J. I., Boyer, T. P., Garcia, H. E., Baranova, O. K., Zweng, M. M., Paver, C. R., Reagan, J. R., Johnson, D. R., Hamilton, M. and Seidov, D. (2013). World Ocean Atlas (2013). Volume 1: Temperature. Levitus, S. Ed., Mishonov, A. Technical Ed.; *NOAA Atlas NESDIS*. 73:40.

(ii) Books:

Madec, G. and the NEMO team (2016). *NEMO ocean engine*, Note du Pole de modelisation de l'Institut Pierre-Simon Laplace No 27.

Cushman-Rosin, B. and Beckers, J.-M. (2009). *Introduction to Geophysical Fluid Dynamics: Physical and Numerical Aspects*, Academic Press.

Versteeg, H. and Malalasekera, W. (2007). *An Introduction to Computational Fluid Dynamics: The Finite Volume Method*, Pearson.

(iii) Web references:

Arrigo, K. (2002). Lecture 3: Temperature, Salinity, Density and Ocean Circulation. http://ocean.stanford.edu/courses/bomc/chem/lecture_03.pdf. Last accessed July 2016.

NOAA, 2016, *Ocean Station Papa*, <http://www.pmel.noaa.gov/ocs/Papa>. Last accessed July 2016.

Simulating the Convective Boundary Layer with a Dynamic Smagorinsky Model

MM Bopape^{1,2}, RS Plant¹ and O Coceal¹

¹ Department of Meteorology, University of Reading, Reading, UK

² Centre for High Performance Computing, CSIR Meraka Institute, Pretoria, South Africa

Abstract

A convective boundary layer is simulated with the Smagorinsky model with different variations of the dynamic Smagorinsky model using different grid spacings. One variation of the dynamic model is scale dependent and is thought to be suitable for the grey zones where large eddies and the grid spacing are of similar size. Shortcomings in the Smagorinsky model at lower resolutions are found in all variations of the dynamic model, while at higher resolution all simulations are similar. The results suggest that the choice of the subgrid model is not important when simulating a convective boundary layer because large eddies dominate the flow.

Keywords: grey zone, dynamic model, atmospheric boundary layer, large eddy model

Introduction

The numerical modelling of the atmosphere at different time scales is based on the filtering of the Navier-Stokes equation (Bryan *et al.* (2003)). Scales that are larger than the filter length are simulated explicitly by the model, while the sub-filter scales must be parameterised. Most parameterisations are designed to be applicable for the specific resolution that they will be applied for. When modelling the atmosphere with grid spacings that are larger than 1km, the boundary layer is parameterised fully using column based models (Honnert *et al.* (2011)). Numerical Models used for predicting or projecting the future state of the atmosphere at different timescales, including Numerical Weather Prediction (NWP) have until recently used grid spacings that are much larger than 1km.

The grid spacing used in NWP by a number of meteorological organisations has decreased to around 1km, and below 1km in certain centres. That means the grid spacing is about the same as the size of energy containing large eddies in convective boundary layers (CBLs). The large eddies in CBLs have been found to scale with the boundary layer height which can be thought to be about 1km. That means the column based boundary layer parameterisations that assume that the filter scale is much larger than the large eddies in the boundary layer are no longer applicable for current NWP models (Bryan *et al.* (2003)). On the other end of the scales, large eddy models (LEMs) are run with grid spacing of about 5m to 200m, and they make an

assumption that the grid spacing is much smaller than the large eddies. They are therefore expected to simulate large eddies explicitly, and parameterise smaller eddies. They are also not designed to work well with grid spacings where the large eddies and the grid spacings are about the same size. There are therefore no suitable boundary layer parametrizations where the grid spacing and the large eddies are about the same, and as a result this regime has been termed the grey-zone or terra incognita (Bryan *et al.* (2003); Honnert *et al.* (2011)).

The Smagorinsky-Lilly method is a popular classic sub-filter scheme used in many large eddy models (Smagorinsky (1963); Lilly (1965)). The scheme is based on the concepts of eddy viscosity and mixing length, where the mixing length is representative of maximum size of the eddies that are parametrised. A number of enhancements have been introduced to the Smagorinsky-Lilly model, including one that is thought to make the scheme suitable for the greyzones. The particular scheme is called the lagrangian averaged scale dependent (LASD) dynamic Smagorinsky model (Bou-Zeid *et al.* (2004)). In this study we compare simulations made with the original Smagorinsky model to those made with variations of the dynamic model to determine whether or not the dynamic model makes improvements to the simulations of a CBL.

Model and Numerical Simulations

UK Met Office LEM

The UK Met Office LEM (MetLEM) is used in this study. MetLEM solves momentum, continuity and thermodynamic equations given by Equations 1 to 3 respectively. The letters and symbols have their usual meaning. The term on the left of Equation 1 is the total time-derivative of momentum, the first term on the right hand side is the pressure gradient force, the second term, buoyancy, is non-zero in the vertical, the third term is the divergence of the turbulent stress, and the final term is the Coriolis acceleration.

$$\frac{Du_i}{Dt} = -\frac{\partial}{\partial x_i} \left(\frac{p'}{\rho_s} \right) + \delta_{i3} B' + \frac{1}{\rho_s} \frac{\partial \tau_{ij}}{\partial x_i} - 2\epsilon_{ijk} \Omega_j u_k \quad (1)$$

$$\frac{\partial}{\partial x_i} (\rho_s u_i) = 0 \quad (2)$$

$$\frac{D\theta}{Dt} = \frac{1}{\rho_s} \frac{\partial h_i^\theta}{\partial x_i} + \left(\frac{\partial \theta}{\partial t} \right)_{\text{mpphys}} + \left(\frac{\partial \theta}{\partial t} \right)_{\text{rad}} \quad (3)$$

The left hand side of Equation (3) is the total derivative of potential temperature, while the first term on the right hand side is the divergence of the heat flux. The second and final terms represent the effect of latent heating or cooling due to phase changes, and the effect of radiation, respectively. The last two terms are zero in our study because we use dry simulations and a constant sensible surface heat flux.

Smagorinsky Model

The turbulent stress and sub-filter-scale heat flux in Equations 1 and 3 and parameterised using the Smagorinsky-Lilly scheme and are given by the equations 4 and 5 below, respectively.

$$\tau_{ij} = \rho_s \nu S_{ij} \quad (4)$$

$$h_i^\theta = -\rho_s \nu_h \frac{\partial \theta}{\partial x_i} \quad (5)$$

$$S_{ij} = \frac{\partial u_i}{\partial x_j} + \frac{\partial u_j}{\partial x_i} \quad (6)$$

$$\nu = \lambda^2 S f_m (Ri_p) \quad (7)$$

$$\nu_h = \lambda^2 S f_h (Ri_p) \quad (8)$$

$$S = \left(\frac{1}{2} \sum_{i,j=1,3} S_{ij}^2 \right)^{1/2} \quad (9)$$

The rate of the strain tensor is defined by Equation 6, while the eddy viscosity and diffusivity are prescribed as in equations 7 and 8 and they are functions of the Richardson number. S is the modulus given by Equation 9.

$$\frac{1}{\lambda^2} = \frac{1}{\lambda_0^2} + \frac{1}{[k(z+z_0)]^2} \quad (10)$$

$$\lambda_0 = c_s \Delta \quad (11)$$

The mixing length is given by equation 10, where the first term on the right determines the basic mixing length given in equation 11. The second term calculates the mixing length as a function of height and the roughness length. In the original Smagorinsky-Lilly model, c_s is a constant and was used as 0.23 in our study. A number of studies have shown that the suitability of the Smagorinsky constant depends on the flow and suitable values suggested for different stratifications include 0.1, 0.17, 0.2 and 0.23.

Dynamic Smagorinsky Model

The dynamic model was introduced by Germano (1991) and its aim is to determine a suitable value of c_s using the flow, by employing the grid scale filter (Equation 12), and a second test scale, usually with $\alpha=2$ (Equation 13).

$$\tau_{ij} = -2c_{s,\Delta}^2 \Delta^2 |\tilde{S}| \tilde{S}_{ij} \quad (12)$$

$$T_{ij} = -2c_{s,\alpha\Delta}^2 (\alpha\Delta)^2 |\overline{S}| \overline{S}_{ij} \quad (13)$$

$$L_{ij} = \overline{u_i u_j} - \tilde{u}_i \tilde{u}_j \quad (14)$$

$$L_{ij} - (\overline{T_{ij}} - \overline{\tau_{ij}}) = e = L_{ij} - c_{s,\Delta}^2 M_{ij} \quad (15)$$

$$M_{ij} = -2\Delta^2 \left(|\overline{S}| \overline{S}_{ij} - \alpha^2 \beta |\overline{S}| \overline{S}_{ij} \right) \quad (16)$$

$$\beta = c_{s,\alpha\Delta}^2 / c_{s,\Delta}^2 \quad (17)$$

Equation 14 uses the smallest resolved scale, and by taking its difference from the parametrized flow, we are able to get the value of the Smagorinsky coefficient. The calculated coefficient is averaged along a plane and is therefore suitable only for horizontally homogeneous flows over a plane. Meneveau et al. (1996) used a similar method to Germano, however used lagrangian averaging which makes the scheme suitable for inhomogeneous flows and complex geometries. Both the Germano and

Meneaveu scheme assume that the Smagorinsky coefficient is independent, that is β in equation 17 is 1. The Germano and Meneaveu models will be referred to as the Plane-Averaged Scale Invariant (PASI) and the Lagrangian-Averaged Scale Invariant (LASI), respectively.

The two schemes were designed for the inertial subranges, i.e. large eddy regimes and are therefore not designed for the grey-zones. Bou-Zeid et al. (2005) used lagrangian averaging similar to Meneaveu, however, he introduced scale dependence by using a second test scale which in our study is taken as $4 \times$ grid scale to determine a suitable value of β . The Bou-Zeid model is referred to as the Lagrangian-Averaged Scale-Dependent (LASD) Model.

Simulations

Simulations of a convective boundary layer were made using different grid spacings of 25m, 50m, 100m, 200m and 400m with the original Smagorinsky model as well the different variations of the dynamic model. The 25m resolution simulations is considered as the “truth run” because previous studies have shown that 25m is sufficient for simulating a CBL. The grid spacing in the vertical is take as $0.4 \times$ horizontal grid scale. A constant surface sensible heat flux of 241 Wm^{-2} and weak geostrophic winds of $(U_g, V_g) = (1, 0) \text{ ms}^{-1}$ are used following Sullivan and Patton (2011). The horizontal domain size for all the simulations is taken as $(9.6 \text{ km})^2$, while the model top is taken at a height of 2km.

Results and Discussion

The Smagorinsky coefficient calculated by all the dynamic models is comparable to all the Smagorinsky constant throughout the whole domain (Fig 1). PASI and LASD calculate larger values than the constant 0.23 of the original Smagorinsky model. LASI simulates the smallest values of the coefficient. c_s is below 0.23 above the boundary layer height. The calculated coefficients do not show an obvious reliance on grid spacing, so the 50m,

100m and 200m grid spacing lines almost fall on top of another.

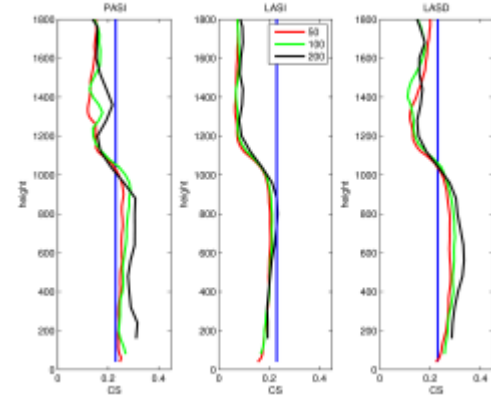


Figure 1: The vertical profile of averaged values of c_s for 50m, 100m and 200m grid spacing, and the line of the constant c_s for the original Smagorinsky model. The three columns are for different version of the dynamic Smagorinsky model.

Quadrant analysis was applied to the temperature flux of the original Smagorinsky-Lilly model simulations at different resolutions to determine what goes wrong when the grid spacing is increased to target what the dynamic models can possibly improve. Partitioning of a combination of vertical velocity perturbation (w') and potential temperature perturbation (Θ') was performed according to their signs as follows: quadrant 1 is given by $w' > 0; \Theta' > 0$ which represents warm air rising, quadrant 2 is given by $w' > 0; \Theta' < 0$ which represent cold air descending, quadrant 3 is given by $w' < 0; \Theta' < 0$ which gives cold air descending, and quadrant 4 is given by $w' < 0; \Theta' > 0$ which is warm air descending. For all the simulations the lower part of the boundary layer is dominated by thermals (i.e quadrant 1). In the upper troposphere, close to the inversion layer, the contribution of warm air descending is also significant which represent entrainment of warm air from the inversion layer into the boundary layer. The largest contribution is however from quadrant 2, which is cold air descending. The contribution of quadrant 2 in the vicinity of the boundary layer height increases with increased grid spacing (Figure 2).

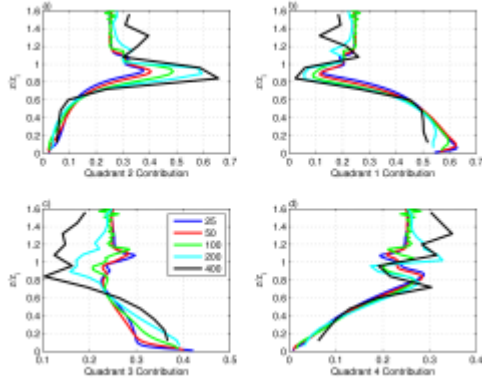


Figure 2: The contribution towards the total temperature flux by different quadrant using different grid spacings with the Smagorinsky Lilly model, using a Smagorinsky constant of 0.23. The quadrants are ordered according to their position on the cartesian plane.

Quadrant analysis was performed for different grid spacings using the Smagorinsky model, and different variations of the dynamic model using coarse grained 25m grid spacing simulation as the target simulation. At higher resolution, the lines with the different grid spacing fall on top of one another, which shows that the use of different subgrid models has little effect on the simulations (not shown).

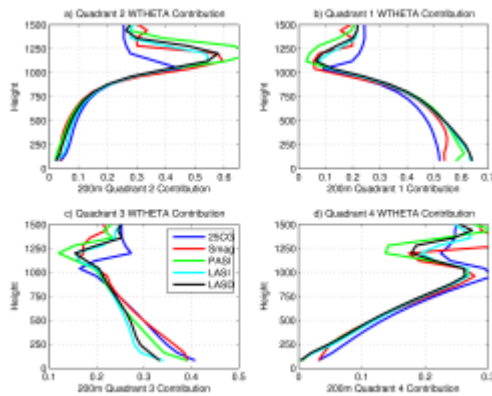


Figure 3: The contribution towards the total temperature flux by different quadrants using three versions of the dynamic model, the original Smagorinsky model, as well the coarse grained 25m grid spacing simulations with a 200m grid spacing.

With lower resolutions the lines start to diverge but the issues associated with the original Smagorinsky

model, are still found with all dynamic models. All the schemes underestimate entrainment of warm air into the boundary layer, and overestimate the contribution of cool air ascending close to the boundary layer height. The LASDcode, and advising on the implementation in the MetLEM.

Conclusions

Simulations of a convective boundary layer were performed using the Smagorinsky-Lilly model, and three different variations of the dynamic model using grid spacings of 25m, 50m, 100m, 200m and 400m. The dynamic models did not show a major improvement compared to the original Smagorinsky Lilly model. The Lagrangian averaged scale dependent model which is thought to be suitable for the greyzones also showed similar issues to the Smagorinsky model. This result is thought to be associated with the fact that large eddies dominate the flow in a convective boundary layer. Previous studies have shown an improvement by dynamic models when stable and neutral stratifications are simulated, but the same result is not found for a convective boundary layer. More tests are planned with the different dynamic models for different stratification, complex geometries, and for transitioning boundary layers where improvements are expected with the use of dynamic models.

Acknowledgements

This study was funded by a NERC grant (contract no.\ NE/K011502/1) under the GREYBLS project. O. C. gratefully acknowledges funding from NCAS (NERC contract no.\ R8/H12/83/002). We acknowledge use of the MONSooN system, a collaborative facility supplied under the Joint Weather and Climate Research Programme, which is a strategic partnership between the Met Office and the Natural Environment Research Council. The authors thank Bob Beare and George Efstathiou for useful discussions and for kindly helping with the setup of the convective boundary layer case. Elie Bouzeid is acknowledged for providing his LASD

code, and advising on the implementation in the MetLEM.

References

Bou-Zeid, E., Meneveau, C. and Parlange M. (2005). A scale-dependent Lagrangian dynamic model for large eddy simulation of complex turbulent flows. *Physics of Fluids*. 17: 025105.

Bryan, G.H., Wyngaard, J.C. and Fritsh J.M. (2003). Resolution requirements for the simulation of deep moist convection. *Monthly Weather Review*. 131: 2394-2416.

Germano, M., Piomelli, U., Moin, P. and Cabot, W.H. (1991). A dynamic subgrid-scale eddy viscosity model. *Physics Fluids* : 3, 1760-1765.

Honnert, R., Masson, V., and Couvreux F. (2011). A diagnostic for evaluating the representation of turbulence in atmospheric models at the kilometeric scale. *Journal of Atmospheric Science*. 68: 3112-3131.

Lilly, D.K. (1965). On the computational stability of numerical solutions of time-dependent non-linear geophysical fluid dynamics problems. *Monthly Weather Review*. 93: 11–25.

Meneveau, C., Lund, T. and Cabot, W. (2000). A Lagrangian dynamic subgrid-scale model of turbulence. *Annual Review of Fluid Mechanics*. 32: 1-32.

Smagorinsky, J. (1963). General circulation experiments with the primitive equations. *Monthly Weather Review*. 91: 99–164.

Sullivan, P.P. and Patton, E.G. (2011). The Effect of Mesh Resolution on Convective Boundary Layer Statistics and Structures generated by Large-Eddy Simulation. *Journal of the Atmospheric Sciences*. 68: 2395-2419.

Initial Conditions and Quantifying Model Climates: Does it Matter Where We Come from?

W. Stefaan Conradie, Babatunde J. Abiodun and Tristan P. Hauser

Climate System Analysis Group, University of Cape Town

Joseph D. Daron

UK Met Office

Abstract

There is no agreed-upon procedure to quantify model climates from their output. Here, we explore differences in characterisations of regional variable climatologies (expressed using probability distributions) that arise when three different climate quantification approaches are applied to the output of an initial condition (IC) ensemble experiment, using a climate system model. We find that that ensemble member trajectories, distinguished in set-up only by the round-off order differences in initial atmospheric temperature, can – over certain regional domains and for particular system ICs – give significantly ($p \ll 0.01$) different variable probability distributions. Further, using different quantification approaches to capture what might be presumed to be the same “climatic state” – which itself may be influenced by the initial climate system state – can yield significantly different distributions. We conclude that a multivariate distribution, sampled over both time and multiple ensemble members, together with measures of autocorrelation, may serve as a useful quantification approach for model climates.

Introduction

Uncertainty in climate system ICs is known to limit predictability of future atmospheric states. The influence of perturbations to slowly evolving climate system components on the evolution of model climates on longer time scales is, however, less well understood (Daron and Stainforth, 2013, 2015; Hawkins et al., 2015).

Many definitions have been proposed for climate in the literature (Lorenz, 1995; Werndl, 2015; Lovejoy, 2013; IPCC, 2013; WMO, 2010). For many of the central concepts in climate science, there do not appear to be any widely accepted definitions (Todorov, 1986; Daron, 2012; Werndl, 2015). One might argue that definitions used are broadly similar, that there appears to be consensus on the intuitive idea of climate (Leith, 1985) and that the descriptions used are generally “good enough” for the specific contexts in which they are applied. However, (Lorenz, 1995) notes that “certain questions regarding climate may be answered either affirmatively or negatively, according to the precise [definition of climate used]”. Furthermore, Lorenz (1995) suggests that definitions of climate which are applicable in observational studies, are not necessarily the most useful in theoretical or modelling studies (Lorenz, 1995; Schneider and Dickinson, 1974; Leith, 1978).

Of particular interest in this work are climate quantifications—definitions which, when applied,

provide a quantitative characterisation of a “model climate” (also referred to as a “model climatic state”). In an observational context, one must consider quantifications applicable to individual climate variable trajectories sampled over time; however, in ensemble modelling studies collections of such trajectories can either be sampled at a particular “instant” or over a period of time. In this work, ensembles considered are IC ensembles (the value of which is argued for in, e.g., Hawkins *et al.* (2015)), but definitions involving perturbed physics and multi-model ensemble output could also be proposed; in particular, it could be argued that the IPCC (2013) apply a multi-model ensemble definition in quantifying projected future climates.

Following Werndl (2015), we focus on probability distributions as a means of capturing the mean state, variability and extremes of a local, regional or global climatic state. For a particular variable, over a particular domain, three types of such quantifications – all previously applied – are considered here:

Climate Quantifications

Temporal (TCQs): the distribution sampled from a series of consecutive “points in time” of a single model trajectory. In this study, annual averages are considered as “points in time”, thus avoiding complexities involved with the diurnal and seasonal cycles. Note, furthermore, that in an observational

setting, rather than a model setting, only TCQs are applicable, as there is only one realisation of the planetary climate that occurs over a given period.

Ensemble (ECQs): the distribution sampled at a particular “point in time”, from all members of an IC ensemble at the n^{th} year of the ensemble duration.

Ensemble-temporal (ETCQs): the distribution sampled from all members of an IC ensemble over a series of consecutive points in time (in this case, thus, several years).

Understanding of the differences in climatic characterisations that could be produced by different approaches to defining climate, should be explored and considered in experimental design and interpretation of results. This study aims to contribute to the discussion on preferable future approaches to climate model experimental design, following Stainforth et al. (2007) and Daron and Stainforth (2013, 2015).

Methods

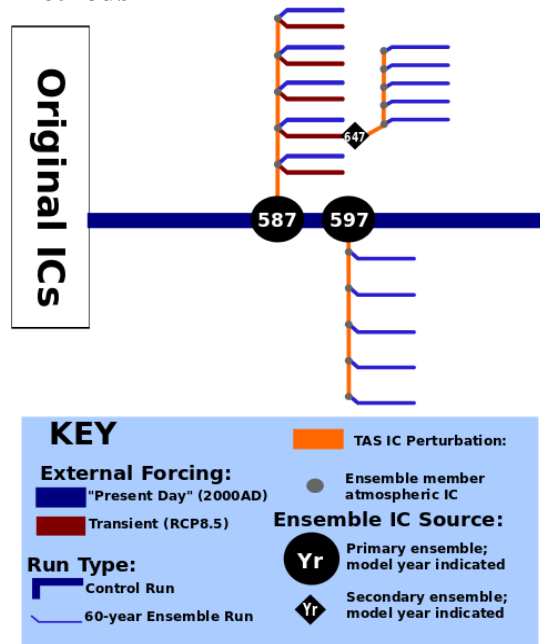


Figure 1: Conceptual schematic of ensemble experiments considered in this study. Primary ensembles are “branched” off from control run at selected model years. Secondary ensembles are started from ensemble member output. Note that all ensembles include 50 members, even though only 5 are shown. Each ensemble member is run under either present day (2000 AD) or projected transient RCP8.5 forcing for 2005–2064AD.

Results discussed here are obtained from the output of a large IC ensemble experiment documented in detail in Conradie (2015, ch. 3). For this experiment the Community Climate System Model, version 4 (Gent *et al.*, 2011) was run in a “fully coupled” configuration. This includes the following components: atmosphere, land, ocean, sea ice and river run-off. In order to minimise computational expense, the lowest resolution (f45gx3; implying that the atmospheric component is run with a $4 \times 5^\circ$ finite-volume dynamic core) on which the fully coupled model can be run, is used.

For simplicity, only four of the ensembles run for that study are considered here; their relation to one another is illustrated in Figure 1. These ensembles were all run at the South African Centre for High Performance Computing (CHPC), where a 1600-year present-day control run (PDC1) was performed, to serve as a basis for ensembles to be “branched” off from. Selection of model years to branch ensembles off from was partly strategic and partly arbitrary (see Conradie (2015, sect. 3.5.2)). The ICs for all model components of each new ensemble, are sourced from the output of a previous run. Atmospheric temperature is perturbed to distinguish individual ensemble members from one another. Ensembles are named according to corresponding control run model year (i.e. the number of years for which ocean circulation has been active) at their initialisation.

Differences between variable probability distributions are quantified using the Kolmogorov-Smirnov D -statistic. For illustrative purposes, in this work, annual-mean spatial-mean 2m air temperature (TAS) over a region denoted as the “Southern Ocean” (SO; the circumpolar domain defined by $-65^\circ \leq \phi \leq -40^\circ$, where ϕ denotes latitude) is used.

Results and Discussion

Figure 2 illustrates the evolution of SO TAS ensemble member trajectories for the four ensembles considered here. Sampling approaches to obtain each of the climate quantifications discussed in the introduction are illustrated. Notice that for the three constant forcing ensembles it appears to take a decade or more before they “settle” around a preferred temperature distribution and that this preferred distribution depends somewhat on the starting state.

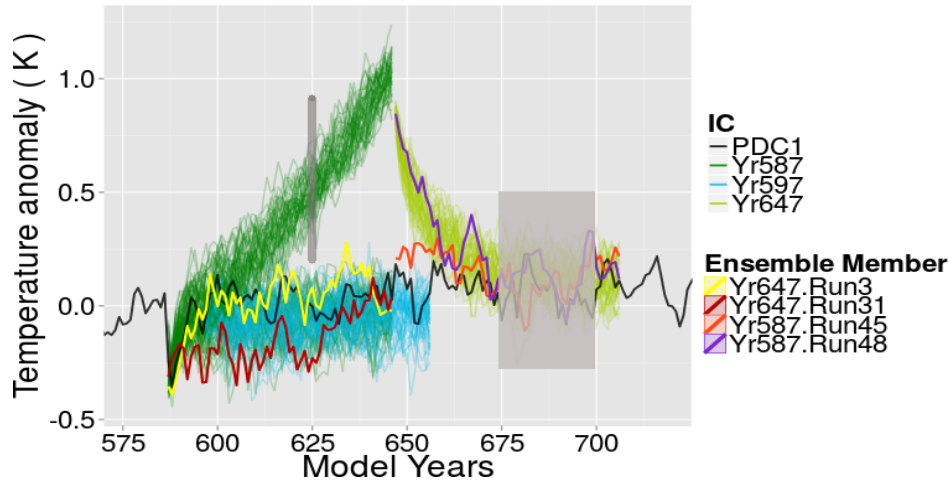


Figure 2: Illustration of the three types of climate quantification sampling considered for SO TAS. The black trajectory represents control run output. Shaded trajectories represent all 50 members of each of the three present day ensembles and one transient forcing ensemble shown. Individual coloured trajectories represent particular ensemble member runs, selected because their variable probability distributions (TCQs) are most different from one another and/or the overall distribution. The darker grey shaded line represents sampling for an ECQ at model year 625 for the Yr587 transient forcing ensemble, whereas the lighter grey shaded block represents sampling for an ETCQ between model years 675 and 700 applied to the Yr647 ensemble.

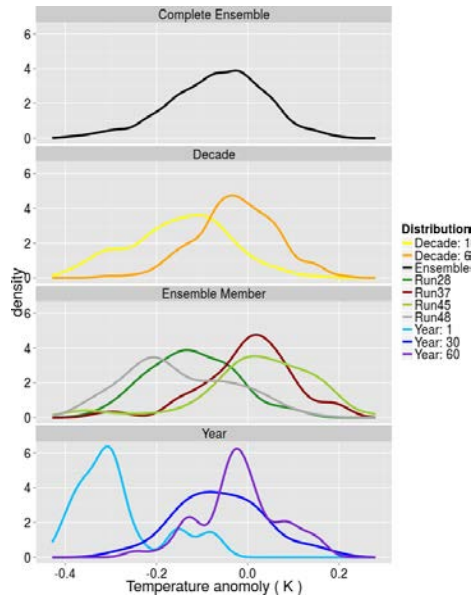


Figure 3: Comparison of SO TAS probability distributions obtained by applying each of the three climate quantifications listed in the Introduction. The complete ensemble (six decades over all members) and decade (one decade over all members) panels show ETCQs, the ensemble member panel TCQs (over 60 years, for various members) and the year panel shows ECQs for three different years.

In Figure 3 distributions obtained by applying each of the quantification approaches to the Yr587 ensemble

trajectories illustrated in Figure 2 are shown. Note that the trajectories from which were sampled to obtain the Run28 and Run45 distributions in Figure 3 are

highlighted in Figure 2. The distributions thus obtained are significantly different from one another ($D \approx 0.65, p < 10^{-10}$), i.e. these two TCQs differ very greatly from one another. The difference in distributions for the year 30 ECQ and the Run45 TCQ is also large ($D \approx 0.40, p < 0.001$), as is the differences between the Run48 TCQ and the decade 6 (“settled”) ETCQ ($D \approx 0.53, p < 10^{-10}$). For SO TAS, 60-year climate variable distributions often (in around $\sim 30\%$ of cases, depending on the system IC state used) are detectably different from one another and the overall ensemble distribution.

Based on these findings it is concluded that:

The time period required to capture a predictively useful TCQ may vary spatially, and depend on the spatial-scale of aggregation.

Centennial-order periods may, for certain regional variables, be required to adequately characterise the variable probability distribution from a single time series, in a system with similar characteristics to the one investigated here. Similar findings are reported by Daron and Stainforth (2013).

Conclusions

It is shown that round-off order changes in ICs can produce regional annual-mean climate variable trajectories differing significantly from one another, under constant forcing. Furthermore, ECQs for a particular ensemble year or ETCQs for a decade sometimes differ significantly from ensemble member TCQs. Similar findings are reported by. Hence, it is suggested that ETCQ multivariate distributions together with measures of autocorrelation, be used as quantification of model climates. A more detailed discussion of the merits and disadvantages of various climate quantifications can be found in Conradie (2015, ch. 6).

Acknowledgements

Our thanks go to Phillip Mukwenha, member of the Climate System Analysis Group (CSAG) software support team, without whose extensive and tireless help the model runs performed for this study would not have been possible. Significant help and support with running CESM1.2 and using NERSC was also provided by Karthik Kashinath, Travis O’Brien and Daithi Stone.

The financial assistance of the National Research Foundation (DAAD-NRF) towards this research is

hereby acknowledged. Opinions expressed and conclusions arrived at, are those of the author and are not necessarily to be attributed to the DAAD-NRF.

Computational resources were made available for this study by the South African Centre for High Performance Computing (CHPC)—operating as part of South Africa’s Centre for Scientific and Industrial Research (CSIR) under South Africa’s Department of Science and Technology (DST). CESM is freely available (<https://www2.cesm.ucar.edu/>) and is used here. The CESM project is supported by the National Science Foundation and the Office of Science (BER) of the U.S. Department of Energy.

References

Conradie, S. (2015). Conceptualising and quantifying the nonlinear, chaotic climate: Implications for climate model experimental design (Master’s thesis). University of Cape Town.

Daron, J. D. (2012). Examining the decision-relevance of climate model information for the insurance industry (PhD thesis). The London School of Economics and Political Science.

Daron, J. D. and Stainforth, D. A. (2013). On predicting climate under climate change. *Environ. Res. Lett.*, 8(3), 034021. <http://doi.org/10.1088/1748-9326/8/3/034021>

Gent, P. R. *et al.* (2011). The Community Climate System Model Version 4. *J. Clim.*, 24(19), 4973–4991. <http://doi.org/10.1175/2011jcli4083.1>

Hawkins, E., Smith, R., Gregory, J., and Stainforth, D. (2015). Irreducible uncertainty in near-term climate projections. *Clim Dyn*, 46(11-12), 3807–3819. <http://doi.org/10.1007/s00382-015-2806-8>

IPCC. (2013). Climate Change 2013: The Physical Science Basis. Contribution of Working Group I to the Fifth Assessment Report of the Intergovernmental Panel on Climate Change. (T. F. Stocker *et al.*, Eds.). Cambridge, United Kingdom and New York, NY, USA: Cambridge University Pres.

Leith, C. E. (1978). Predictability of climate. *Nature*, 276(5686), 352–355.

Leith, C. E. (1985). Global Climate Research. In J. T. Houghton (Ed.), *The Global Climate*. Cambridge University Press.

Lorenz, E. N. (1995). Climate is what you expect. online, available at <http://eaps4.mit.edu/research/Lorenz/publications.htm> [online 10 February 2013].

Lovejoy, S. (2013). What Is Climate?. *Eos Trans. AGU*, 94(1), 1–2.

Massey, F. J. (1951). The Kolmogorov-Smirnov Test for Goodness of Fit. *Journal of the American Statistical Association*, 46(253), 68–78. <http://doi.org/10.1080/01621459.1951.10500769>

Schneider, S. H. and Dickinson, R. E. (1974). Climate modeling. *Rev. Geophys.*, 12(3), 447.

Stainforth, D., M. Allen, E. Tredger, and L. Smith, 2007: Confidence, uncertainty and decision-support relevance in climate predictions. *Phil. Trans. R. Soc. A*, 365 (1857), 2145–2161.

WMO. (2010). WMO - No. 100: Guide to Climatological Practices (3rd Edition). World Meteorological Organisation.

Todorov, A. V. (1986). Reply. *J. Climate Appl. Meteor.*, 25(2), 258–259.

Werndl, C. (2015). On Defining Climate and Climate Change. *The British Journal for the Philosophy of Science*, 67(2), 337–364.

Towards understanding the impact of assimilating along-track SLA data on simulated eddy characteristics in the Agulhas System

Marc de Vos^{1,3}, Björn Backeberg^{2,3,4} and François Counillon⁴

Marine Research Unit, South African Weather Service, South Africa¹

Coastal Systems Research Group, Council for Scientific and Industrial Research, South Africa²

Nansen-Tutu Centre for Marine Environmental Research, Department of Oceanography, University of Cape Town, South Africa³

Nansen Environmental and Remote Sensing Center, Norway⁴

Abstract

The impact of assimilating along-track sea level anomaly (SLA) data into a regional Hybrid Coordinate Ocean Model (HYCOM) is investigated with regard to the simulation of mesoscale eddy characteristics in the Agulhas System. Eddy characteristics from an assimilated (*Assim*) and an unassimilated (*Free*) simulation experiment in HYCOM are compared with each other, using satellite altimetry derived eddy characteristics as a basis to evaluate accuracy. Overall, *Assim* yields improvements over *Free* in eddy density distribution and dynamics. South of Madagascar, the number of eddies simulated by both HYCOM experiments is too low, although *Assim* offers some improvements in this regard.

Keywords

Along-track SLA, HYCOM, mesoscale eddies, Agulhas System, data assimilation, satellite altimetry,

Introduction

The Agulhas Current is one of the most important currents in the global ocean-atmosphere system by virtue of its role in energy transport (Beal et al., 2011). An important transfer of warm, salty waters from the south-west Indian Ocean to the south Atlantic Ocean occurs in the region of the current's eastward retroflection which occurs south of South Africa. This is facilitated primarily by the periodic shedding of Agulhas Rings (mesoscale, anticyclonic eddies) (Lutjeharms & van Ballegooyen, 1988). An enhanced understanding and predictability of the Agulhas Current system would prove beneficial to industrial, commercial and recreational interests in the region, as well as in the event of oil spills and harmful algal blooms (Backeberg et al., 2014). Furthermore, Agulhas leakage has itself an important influence on the Atlantic Ocean Meridional Overturning Circulation (AMOC) and hence, on global ocean circulation (Beal et al., 2011) and climate.

The shedding of Agulhas Rings in the region of the Agulhas Current retroflection is thought to be linked to the propagation of eddies from the Mozambique Channel and East Madagascar Current. Eddies and dipoles reach the Agulhas Current frequently and on occasion propagate all the way to the retroflection, influencing its position and modulating ring shedding events there (Schouten et al., 2002; Ridderinkhof et al., 2013) potentially impacting the AMOC.

Mesoscale eddies are also important determinants of the marine ecology in the region, for example in the

western reaches of the Mozambique Channel seabirds have been observed to forage at the boundaries of eddies (Weimerskirch et al., 2004). Their impact probably extends further, given their associated high nutrient and low oxygen anomalies (Swart et al., 2010) and their tendency to advect phytoplankton-rich, coastal waters offshore (Omta et al., 2009). Mesoscale eddies may also boost primary production by raising nutrients from deep waters to upper ocean levels (e.g. Lathuiliere et al., 2010). Given the dearth of coherent monitoring systems in the Agulhas system (Backeberg et al., 2014), as well as lingering inaccuracies in model results due to the highly non-linear nature of the dynamics (Blastoch et al., 2008b), concrete conclusions about the magnitude of Agulhas leakage and the variability thereof remain elusive (Backeberg et al., 2014). Model simulations of the Agulhas system have been shown to be highly sensitive to subtle changes in the numerics (Backeberg et al., 2009; Barnier et al., 2006). Data assimilation processes seek to compute the most probable model state by strategically combining an accurate dynamical model with a set of observational data (Evenson, 2003). Continuous data assimilation constrains model solutions such that forecast accuracy is usefully enhanced (Backeberg et al., 2014).

In this study the impact of assimilating satellite altimetry data into a HYCOM simulation is investigated with respect to simulated eddy characteristics.

¹ Tel: +27 21 935 5764; Email: marc.devos@weathersa.co.za

Methodology

The HYCOM model configuration, satellite altimetry data for assimilation and EnOI data assimilation scheme are employed as in Backeberg et al. (2014). The satellite altimetry data used for validation with HYCOM were produced by Ssalto/Duacs and distributed by Aviso. Support for this product is provided by CNES (<http://www.aviso.oceanobs.com/duacs/>). They are distributed as merged daily gridded maps of global ocean gridded absolute dynamic topography (MADT), with a spatial resolution of 0.25° . Weekly means were created from the daily maps of MADT to coincide temporally with model results. The altimetry used for assimilation into HYCOM is the delayed-time, unfiltered, along-track SLA product.

The automated eddy detection algorithm used here is based on the work in Halo et al. (2014). Modifications were made to the algorithm code to account for spatial variability of the observational error..

Root mean squared errors for all eddy statistics were computed as per Eq. (1).

$$RMSE = \sqrt{\frac{\sum_{i=1}^n (y_o - y_e)^2}{n}} \quad \text{Eq. 1.}$$

where n is the number of estimations, y_o is the reference value (*Aviso*) and y_e is the estimated value (*Free* or *Assim*).

The difference in relative error (R.E.) between *Free* and *Assim* was then mapped on a grid (see Fig. 2d), with the difference shown in each grid cell computed as per Eqs. (2, 3).

$$R.E. \text{ Improvement } (\%) = \frac{y_e - y_o}{y_o} \times 100 \quad \text{Eq. 2.}$$

where y_o is the reference value (*Aviso*) and y_e is the estimated value (*Free* or *Assim*).

$$\text{Error Diff.} = \% R.E._{free} - \% R.E._{assim} \quad \text{Eq. 3.}$$

where $\% R.E._{free}$ and $\% R.E._{assim}$ are the *R.E. Improvements* (%) as calculated in Eq. 2.

A range of dynamical and geometric properties was computed for individual eddies by the detection and tracking algorithm, and used for comparison of *Free*, *Assim* and *Aviso*.

Results & Discussion

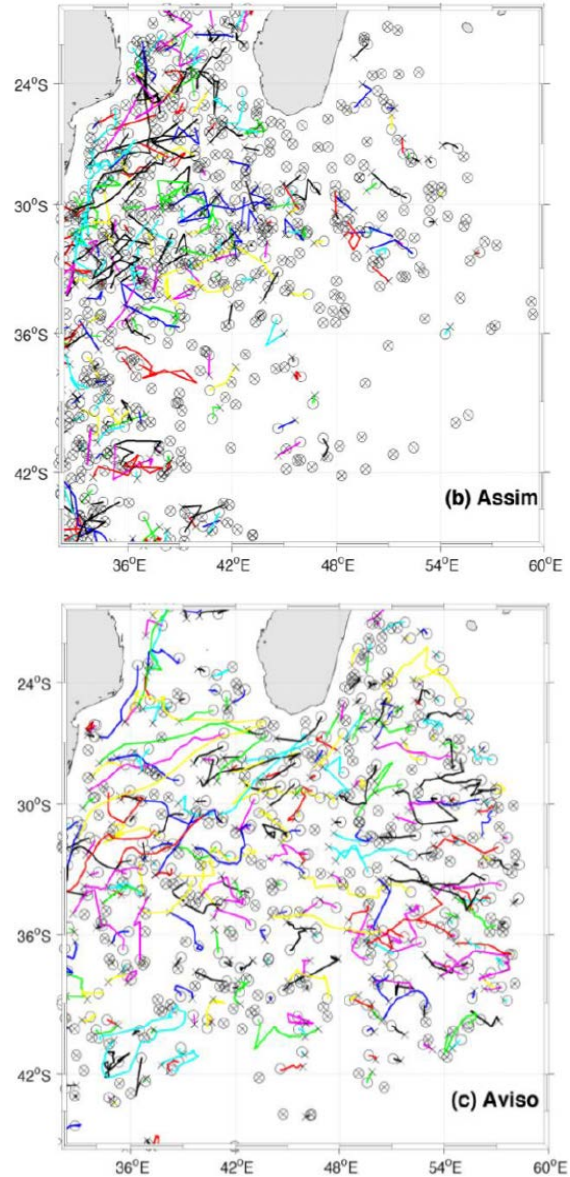


Figure 4. All eddy formation sites, dissipation sites and trajectories are shown for a) *Assim*. and b) *Aviso*, 2009 (*Free* not shown). Colours distinguish different eddies. Formation sites are marked 'O' whilst dissipation sites are marked 'X'. Eddies of all lifetimes are shown.

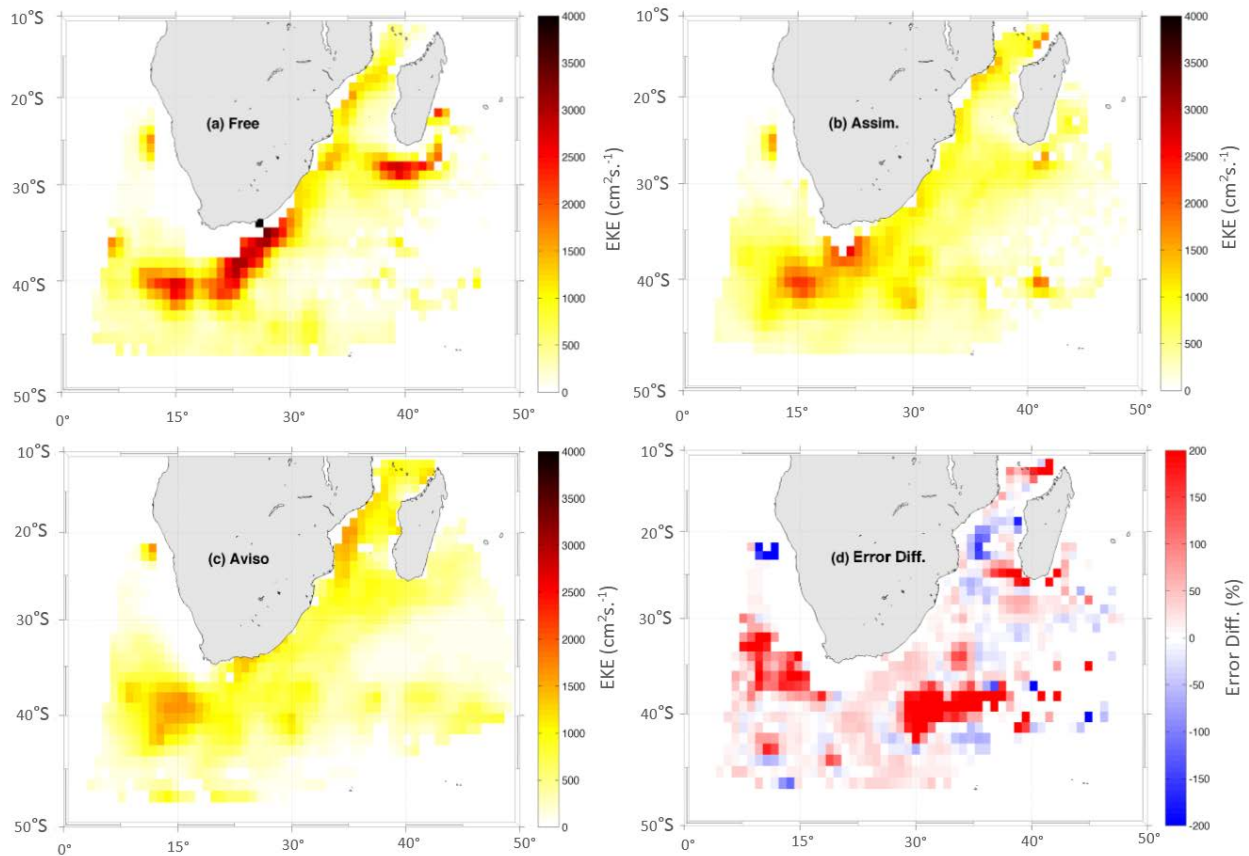


Figure 5. Eddy kinetic energy for a) *Free*, b) *Assim* and c) *Aviso* as computed by the detection and tracking algorithm. d) Shows difference in relative error as per Eq. 3, with redder tones indicating closer adherence of *Assim* to *Aviso*, and bluer areas indicating closer adherence of *Free* to *Aviso*.

Assim shows improvement across a range of derived dynamical eddy properties compared to *Free*, with the exception of cyclonic vorticity (figures not shown). Root mean squared errors (RMSE) for eddy amplitude and rotational speed are reduced in *Assim* by 36.5 %, and 27.5 % respectively. A slight degradation is also evident in eddy size (radii and area). Two results of particular interest are those of eddy density distribution (Fig. 1) and eddy kinetic energy (EKE) which shows an improvement of 13.7 % in RMSE in *Assim* (Fig. 2).

Whilst the number of eddies simulated by *Assim* is improved from that of *Free*, the eddy field remains deficient in the regions south and south east of Madagascar (Fig. 1). Analysis of eddy lifetimes revealed that HYCOM configurations initialise a number of eddies with coherent geometric and dynamical properties, but unrealistically short life times. As such, they do not appear in more than one frame (i.e. life time < 7 days), and therefore exhibit coincident birth and death sites (Fig. 1).

EKE is a proxy for mesoscale variability, including eddies (Backeberg et al., 2014). Previous studies (e.g. Backeberg et al., 2014) have shown EKE from HYCOM in this region to be, at times, exaggerated. In such studies, EKE is calculated from continuous velocity fields. As such, whilst it might sometimes be valid to do so, EKE cannot be explicitly linked to eddy

activity, and could be the result of meandering currents or other chaotic flow. In this study, computing EKE associated exclusively with eddies detected by the algorithm, allows EKE in the region to be attributed explicitly to mesoscale eddies, and highlights the importance of separating the eddy field from the continuous field. Further, this result suggests that, whilst the model appears to be simulating sufficient variability in the mean flow, it is not able to simulate and sustain eddies realistically.

Conclusions

Assimilating along-track SLA data in an eddy resolving HYCOM of the Agulhas system provides general improvement in eddy density distribution. Concerns remain however regarding the absence and lifespan of simulated eddies in the region south and south east of Madagascar. Eddies simulated here are unrealistically short lived. Derived statistics show improvement in *Assim* across a wide range of dynamical properties including amplitude, rotational speed and EKE. The accuracy of the eddy sizes simulated by *Assim* are somewhat degraded compared to *Free*. The study suggests that the strategy for the analysis of eddy properties should be carefully selected, for example, EKE calculated from a continuous velocity field is not a good proxy for eddy energy and validation.

References

- Backeberg, B.C., Bertino, L. and Johannessen, J.A., 2009. Evaluating two numerical advection schemes in HYCOM for eddy-resolving modelling of the Agulhas Current. *Ocean Science*, 5, pp.173-190.
- Backeberg, B.C., Counillon, F., Johannessen, J.A. and Pujol, M.I., 2014. Assimilating along-track SLA data using the EnOI in an eddy resolving model of the Agulhas system. *Ocean Dynamics*, 64(8), pp.1121-1136.
- Backeberg, B.C., Johannessen, J.A., Bertino, L. and Reason, C.J., 2008. The greater Agulhas Current system: An integrated study of its mesoscale variability. *Journal of Operational Oceanography*, 1(1), pp.29-44.
- Barnier, B., Madec, G., Penduff, T., Molines, J.M., Treguier, A.M., Le Sommer, J., Beckmann, A., Biastoch, A., Böning, C., Dengg, J. and Derval, C., 2006. Impact of partial steps and momentum advection schemes in a global ocean circulation model at eddy-permitting resolution. *Ocean dynamics*, 56(5-6), pp.543-567.
- Beal, L.M., de Ruijter, W.P., Biastoch, A. and Zahn, R., 2011. On the role of the Agulhas system in ocean circulation and climate. *Nature*, 472(7344), pp.429-436.
- Biastoch, A., Lutjeharms, J.R.E., Böning, C.W. and Scheinert, M., 2008b. Mesoscale perturbations control inter-ocean exchange south of Africa. *Geophysical Research Letters*, 35(20).
- Evensen, G., 2003. The ensemble Kalman filter: Theoretical formulation and practical implementation. *Ocean Dynamics*, 53(4), pp.343-367.
- Halo, I., Backeberg, B., Penven, P., Ansorge, I., Reason, C. and Ullgren, J.E., 2014. Eddy properties in the Mozambique Channel: A comparison between observations and two numerical ocean circulation models. *Deep Sea Research Part II: Topical Studies in Oceanography*, 100, pp.38-53.
- Lathuiliere, C., Levy, M. and Echevin, V., 2010. Impact of eddy-driven vertical fluxes on phytoplankton abundance in the euphotic layer. *Journal of plankton research*, 0(0) pp.1-5.
- Lutjeharms, J.R.E. and Van Ballegooyen, R.C., 1988. The retroflection of the Agulhas Current. *Journal of Physical Oceanography*, 18(11), pp.1570-1583.
- Omta, A.W., Llido, J., Garçon, V., Kooijman, S.A.L.M. and Dijkstra, H.A., 2009. The interpretation of satellite chlorophyll observations: The case of the Mozambique Channel. *Deep Sea Research Part I: Oceanographic Research Papers*, 56(6), pp.974-988.
- Ridderinkhof, W., Le Bars, D., Heydt, A.S. and Ruijter, W.P.M., 2013. Dipoles of the South East Madagascar Current. *Geophysical Research Letters*, 40(3), pp.558-562.
- Schouten, M.W., de Ruijter, W.P. and van Leeuwen, P.J., 2002. Upstream control of Agulhas Ring shedding. *Journal of Geophysical Research: Oceans*, 107(C8).
- Swart, N.C., Lutjeharms, J.R.E., Ridderinkhof, H. and De Ruijter, W.P.M., 2010. Observed characteristics of Mozambique Channel eddies. *Journal of Geophysical Research: Oceans* (1978–2012), 115(C9).
- Weimerskirch, H., Le Corre, M., Jaquemet, S., Potier, M. and Marsac, F., 2004. Foraging strategy of a top predator in tropical waters: great frigatebirds in the Mozambique Channel. *Marine Ecology Progress Series*, 275, pp. 297-308.

Acknowledgments. This work has been jointly supported by the Nansen-Tutu Centre for Marine Environmental Research, Cape Town, South Africa, the South African National Research Foundation (grant 87698), the Nansen Environmental and Remote Sensing Centre, Bergen, Norway. A grant for computing time from the Norwegian Program for supercomputing (NOTUR) was received through project number nn2993k.

The application of support vector regression (SVR) for stream flow prediction on the Amazon basin

Melise du Toit^{1,2}, Josefina M. Wilms², Gideon J.F. Smit¹ and Willie Brink¹

¹ *Department of Mathematical Sciences (Applied Mathematics), Stellenbosch University, South Africa*

² *Advanced Mathematical Modelling, Modelling and Digital Sciences, CSIR Stellenbosch, South Africa*

Long-term forecasting of river runoff is important for climate scientists and hydrologists. By analysing the processes of a river basin characterized by measurable variables, an empirical data-driven model can be constructed. The support vector regression technique is used in this study to analyse historical stream flow occurrences and predict stream flow values for the Amazon basin. Up to twelve month predictions are made and the coefficient of determination and root-mean-square error are used for accuracy assessment. Compared to previous studies, satisfactory results are obtained. Inclusion of environmental aspects such as precipitation and evaporation are suggested for more accurate predictions.

Keywords: Support vector machine, Support vector regression, Amazon basin, Stream flow prediction

1. Introduction

Research on model-generated river runoff is essential for climate scientists and hydrologists to predict and understand future changes in river runoff that may be associated with global climate change. The hydrologic cycle is closed by returning the correct amount of water to the river mouth with the appropriate timing and position (Miller *et al.*, 1993). River engineers and scientists use these results for the study of various hydro-environmental aspects, such as the increasing international concern of riverine pollution problems and the growing flood levels of rivers (Falconer *et al.*, 2005). Furthermore, sediment transport and salinity changes within the river basin can be examined and predicted (Falconer *et al.*, 2005; Miller *et al.*, 1993).

Numerous hydrological models have been implemented by researchers to analyse the behaviour of river basins and to model river flow in such basins by mapping the natural phenomena to a simulation program (Falconer *et al.*, 2005). These models are known as physically based or process models, since they are based on the physical behaviour of the specific river basin system as well as the mathematical description of the river flow (Falconer *et al.*, 2005; Solomatine and Ostfeld, 2008). A physically based model consists of a numerical process which involves the computation of an efficient and accurate solution to equations based on the physical laws obtained for the specific system. The accuracy of a process model is tested by comparing its results to past observations, and if a desired accuracy is obtained, such a model may be used to calculate and predict future changes in the particular system.

Even though various hydraulic and hydrologic process models have been constructed for river basin

systems, limited knowledge of the required modelling processes in a system may result in an unreliable model. However, such a system may consist of a process characterized by measurable variables and contain a sufficient amount of concurrent input and output data associated with the particular process (Solomatine and Ostfeld, 2008). By analysing the relationship between the input and output data an empirical mathematical model, known as a data-driven model, can be constructed to model and predict future output variables (Solomatine and Ostfeld, 2008).

A detailed understanding of the physical processes and behaviour of a river basin system is therefore not required for the construction of a data-driven model. Instead, data-driven modelling involves a study of the relationship between the system's state variables (Solomatine *et al.*, 2008). This may allow for the improvement of physically based models.

The objective of this study is the description and implementation of an empirically based (data-driven) model for river runoff. In particular, a supervised machine learning model known as support vector regression (SVR) will be considered. This model is used to analyse the stream flow history of gauging stations in a river basin in order to determine future stream flow. The Amazon River in South America is considered for the application of this data-driven model and an attempt to accurately predict stream flow is made.

2. Instrumentation and Method

2.1. Study area and available data

Stream flow data for the Amazon basin have been obtained from the Observation Service for the geodynamical, hydrological and biogeochemical control of erosion/alteration and material transport

(SO HYBAM). This association manages 20 gauging stations that are distributed in the Amazon. The stream flow records of three are considered for this study: the Obidos station in Rio Amazonas, the Manacapuru station in Rio Solimões, and the Lábrea station in Rio Purus, shown in Fig. 1.



Figure 1. Study area and location of the gauging stations.

2.2. Support vector regression: model formulation

In order to forecast an outcome $y(t + \Delta t)$ at an instant Δt from current time t , a regression method can be constructed. The purpose of such a method is to formulate a function $f(\mathbf{x})$ such that $f(\mathbf{x}) = y(t + \Delta t)$. The function f takes an input vector $\mathbf{x} = (x_1, x_2, \dots, x_m)$ of m known variables, including current and past data records $[y(t), y(t - 1), \dots, y(t - q)]$, where $q \leq m$. The input vector may also consist of any other available numerical variables.

An extension of the support vector machine (SVM), formulated by Cortes and Vapnik (1995), is known as the support vector regression (SVR) technique. A thorough description on the construction of the SVR technique, its optimization parameters (C and ϵ) and its applications in the field of hydrology can be found in Raghavendra and Deka (2014). An important concept of the SVR method is that it attempts to find a simple function that can fit all the data while minimizing the sum of prediction errors above a predefined margin (Callegari *et al.*, 2015).

For cases where the SVR model has to optimize nonlinear functions, the input vector \mathbf{x} is mapped to a feature space where its relationship with y is linearized. This mapping function is known as a kernel function. A detailed discussion on kernel functions is given by Raghavendra and Deka (2014).

2.3. Model training and testing

The process of formulating a function $f(\mathbf{x})$ on a given subset of the available data (known as the *training set*) is known as training. During training, the model is tested by fitting it to a second sample set (known as the *validation set*). Finally, the trained SVR model is verified by an accuracy measurement on a third subset of the given samples, known as the *test set* (Solomatine and Ostfeld, 2008).

For the Obidos gauging station, monthly stream flow data from 1970 to 2000 are considered. Furthermore, data from 1973 to 2003 and from 1968 to 1998 are available for the Manacapuru and Lábrea stations, respectively. For each station, data for the first 15 years are used as training sets. The following 10 years' data constitutes the validation set and the remaining 5 years' data are used for testing.

2.4. Feature and kernel function selection

Each input vector \mathbf{x} consists of 12 antecedent stream flow periods (months). The value of y represents the flow in the next period. One month predictions are made, where after forecasting is extended for up to 12 months. Evaluation is done by calculating the coefficient of determination (R^2) of the predicted and observed stream flow values. The purpose of R^2 is to give an estimation of how well observed models are replicated by the fitted model, based on the percentage of total variation of outcomes interpreted by the model. The R^2 percentage therefore represents the percentage of variation of predicted outcomes that are explained by the fitted model. Furthermore, the root-mean-square error (RMSE) percentage indicates residual variance between observed and forecasted outcomes, and will be used for evaluation in this study.

Linear, Polynomial (Poly) and Radial Basis (RBF) kernel functions are considered. These SVR formulations are expressed as follows:

$$\text{Linear: } k(x_i, x_j) = x_i^T x_j,$$

$$\text{Poly: } k(x_i, x_j) = (\gamma x_i^T x_j + r)^d, \text{ and}$$

$$\text{RBF: } k(x_i, x_j) = \exp(-\gamma \|x_i - x_j\|^2); \gamma > 0.$$

The mapping of features x_i and x_j to the feature space is represented by $k(x_i, x_j)$. An outline of the kernel functions and their hyperparameters are given by Granata *et al.* (2016). A built-in module in the Python programming language, known as Optunity, is used to optimize the parameters of each kernel.

3. Results and Discussion

3.1. Optimal hyperparameters and kernel functions

Historical stream flow records of the respective stations are examined. For each station, the optimal hyperparameters of the considered kernel functions are calculated in order to determine the best generalized model for the given data. The R^2 value for each optimized model is listed in Tables 1 to 3. For the training and validation sets, every kernel function provides an R^2 greater than 0.9, indicating

that at least 90% of the total variation of predicted outcomes are explained by the fitted models. The RBF and polynomial kernel functions provide the best results for each station. However, the RBF kernel is less complex in comparison to polynomial kernels, since it contains fewer parameters. Further investigation is therefore done by only considering the RBF kernel.

Table 1. Optimized kernel-specific hyperparameters and R^2 for one month predictions of river flow at the Obidos gauging station.

OBIDOS GAUGING STATION							
Kernel	Optimal Parameters					R^2	
	C	ϵ	γ	d	r	Trainin g set	Validatio n set
RBF	64 1	0.030 3	0.06 7	-	-	0.983	0.967
Linea r	30 4	0.026 2	-	-	-	0.976	0.965
Poly	38 1	0.030 7	0.1	2	0.3	0.981	0.966

Table 2. Optimized kernel-specific hyperparameters and R^2 for one month predictions of river flow at the Manacapuru gauging station.

MANACAPURU GAUGING STATION							
Kernel	Optimal Parameters					R^2	
	C	ϵ	γ	d	r	Trainin g set	Validatio n set
RBF	57 0	0.02	0.0 3	-	-	0.937	0.923
Linea r	38 5	0.048	-	-	-	0.912	0.904
Poly	78	0.005 6	0.1	3	0.5	0.942	0.925

Table 3. Optimized kernel-specific hyperparameters and R^2 for one month predictions of river flow at the Lábrea gauging station.

LABREA GAUGING STATION							
Kernel	Optimal Parameters					R^2	
	C	ϵ	γ	d	r	Trainin g set	Validatio n set
RBF	25 5	0.05	1. 7	-	-	0.985	0.965
Linea r	84	0.015	-	-	-	0.956	0.951
Poly	67 5	0.032 9	0. 1	5 1	0.1	0.984	0.959

3.2. Extended stream flow forecasting

The optimized RBF models are applied to the testing data for forecasting. At an instant (month) t , twelve antecedent observed flow values $\mathbf{x} = [y(t), y(t - 1), \dots, y(t - 11)]$ are used to predict flow $f(\mathbf{x})_{\{t+1\}}$ for month $t + 1$. This is known as *one month forecasting*. Similarly, for *two month forecasting*, an input vector $\mathbf{x} = [f(\mathbf{x})_{\{t+1\}}, y(t), \dots, y(t - 10)]$ is used to predict stream flow for month $t + 2$. Forecasting extending up to 12 months is done on the given test set of each station. The corresponding R^2 values and $RMSE$ percentages are determined and shown in Figs. 2 and 3, respectively.

For each gauging station the best results were obtained for one month forecasting. An R^2 of 0.973

is obtained for the Obidos station, whereas R^2 values of 0.94 and 0.95 are obtained for the Manacapuru and Lábrea stations, respectively. Furthermore, the $RMSE$ percentages are obtained respectively as 5.06%, 6.49% and 21.38%. R^2 is a relative error of fit, whereas $RMSE$ is an absolute measure of fit. Since $RMSE$ is the square root of a variance, it can be explained as the standard deviation of the unexplained variance. This clarifies the larger $RMSE$ values obtained for the Lábrea station. Compared to stream flow forecasting studies done by Veiga *et al.* (2015), Lin *et al.* (2006) and Callegari *et al.* (2015), these results are quite satisfactory.

Extended forecasting produces less accurate results. However, it should be taken into account that predicted stream flow values were used to make future predictions. Also, stream flow is the only environmental/hydrological variable considered.

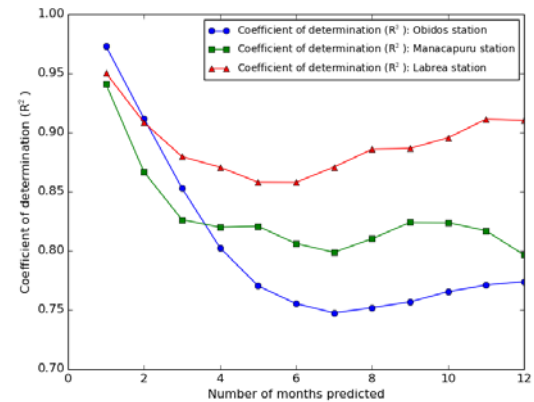


Figure 2. R^2 results for extended forecasting.

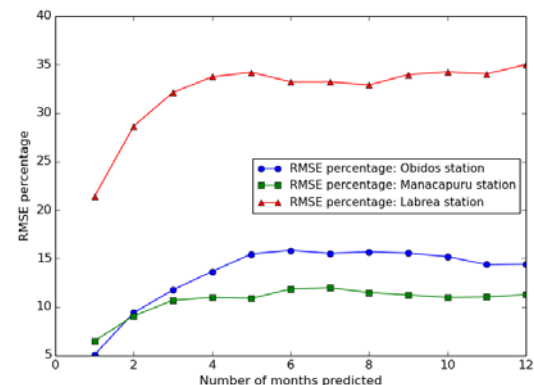


Figure 3. $RMSE$ percentages for extended forecasting.

3.3. Illustrations of stream flow predictions

Figure 4 is an illustration of one, six and twelve month extended stream flow forecasting compared to observed stream flow. The worst predictions are made at the minimum and maximum stream flow occurrences, whereas good results are obtained for the upward and downward flow tendencies.

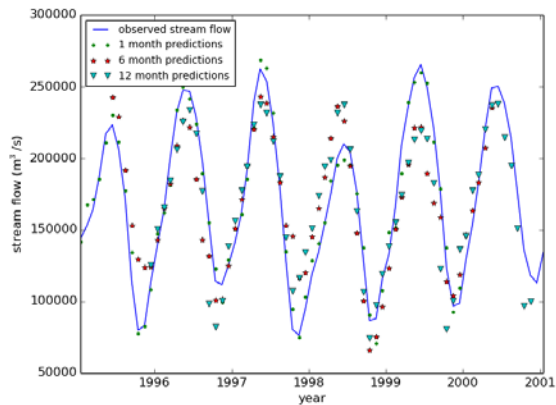


Figure 4: Stream flow discharge at the Obidos station for 1, 6, and 12 month predictions.

4. Conclusions

Research on long-term forecasting of river runoff predictions is important for climate scientists and hydrologists, since these results are used for the study of various hydro-environmental aspects. Numerous physically based hydrologic models have been implemented by researchers for this task, but due to limited knowledge of the necessary modelling processes in a river basin, inaccurate results have been obtained. Therefore, by analysing the processes of a river basin characterized by measurable variables, an empirical data-driven model can be constructed. The support vector regression (SVR) machine learning technique was used in this study to analyse historical stream flow occurrences in order to predict stream flow values. Predictions for up to twelve months were made and the coefficient of determination as well as the root-mean-square error were used as accuracy measurements. Satisfactory results were obtained and local stream flow data proved to be a trustworthy hydrological factor when predicting a specific river's stream flow. Even though the effects of precipitation may already be present in stream flow data, an understanding of the relationship between stream flow and precipitation may lead to a more accurate prediction of stream flow. Explicitly including precipitation and other environmental aspects such as temperature and evaporation when building an SVR model will therefore be addressed in further studies.

5. References

Callegari, M., Mazzoli, P., De Gregorio, L., Notarnicola, C., Pasolli, L., Petitta, M., Pistocchi, A. (2015). Seasonal river discharge forecasting using support vector regression: a case study in the Italian Alps. *Water*. 7: 2494-2515.

Cortes, C., Vapnik, V. (1995). Support-vector networks. *Machine Learning*. 20: 273-297.

Falconer, R., Lin, B., Harpin, R. (2005). Environmental modelling in river basin management. *International Journal of River Basin Management*. 3: 169-184.

Lin, J., Cheng, C., Chau, K. 2006. Using support vector machines for long-term discharge prediction. *Hydrological Sciences*. 51(4): 599-612.

Miller, J.R., Russel, G.L., Caliri, G. (1993). Continental-scale river flow in climate models. *Journal of Climate*. 7: 914-928.

Raghavendra, S., Deka, P.C. (2014). Support vector machine applications in the field of hydrology: a review. *Applied Soft Computing*. 19: 372-386.

Solomatine, D., Ostfeld, A. (2008). Data-driven modelling: some past experiences and new approaches. *Journal of Hydroinformatics*. 10: 3-22.

Veiga, V.B., Hassan, Q.K., He, J. (2015). Development of flow forecasting models in the Bow River at Calgary, Alberta, Canada. *Water*. 7: 99-115.

The 2015/16 Summer vs the Summers of the last decade

Christien J. Engelbrecht*, Agricultural Research Council, Pretoria

Stephanie Landman, South African Weather Service, Pretoria

Johan Malherbe, Agricultural Research Council, Pretoria

Abstract

Maximum temperature, minimum temperature and rainfall data of 248 weather stations across South Africa are used to assess the magnitude and spatial distribution of temperature and rainfall anomalies during the 2015/16 summer season relative to the previous 9 summer seasons. The 2015/2016 summer season was characterized by the presence of a very strong El Niño. The months of October and December were especially hot and dry, with 40% of the stations during December associated with maximum temperature anomalies exceeding 4°C. Rainfall conditions improved during the late summer, with exceptional rainfall anomalies over the western interior during January. Despite the improved rainfall conditions, January and February still experienced anomalously warm conditions over almost the entire country.

Keywords: South Africa, Temperature anomalies, Rainfall anomalies, El Niño

Introduction

Coupled climate models predicted a strong El Niño to develop during the latter half of 2015 and to peak during the austral mid-summer months (<http://www.iri.columbia.edu/our-expertise/climate/forecasts/enso/2015-September-quick-look>). The 2015/16 El Niño turned out to be one of the strongest El Niño events on record (http://www.cpc.noaa.gov/products/analysis_monitoring/ensostuff/ensoyears.shtml). Over South Africa, El Niño conditions are usually associated with below-normal rainfall and above-normal temperatures (Van Heerden and Terblanche, 1988). The impact of El Niño occurs usually during the mid-summer when the association between rainfall and ENSO is the strongest (Barnston et al., 1996; Landman and Beraki, 2012). The larger part of South Africa receives summer rainfall, and the mid-summer months (e.g. Landman and Beraki, 2012) are a crucial part of the growing season for summer crops. The drought associated with the 1991/92 El Niño had devastating impacts on agriculture in southern Africa (Vogel and Drummond, 1993). The prediction of a strong El Niño during the 2015/16 summer was therefore alarming, especially as parts of the central interior of the country suffered from drought conditions during 2012 and 2013 (Malherbe et al., 2015), continuing into 2014.

On top of the eminent 2015/16 El-Niño, the year 2015 was globally the warmest year recorded since surface temperature measurements commenced (<http://www.climate.nasa.gov>). This record high global average surface temperature is partly attributed to global warming, partly to El Niño. The past 15 years form all part of the warmest 16 years (average global surface temperature, land and ocean)

(<http://www.ncdc.noaa.gov/sotc/global/201513>).

The only year that forms part of the 16 warmest

years ever recorded, but that is not part of the last 15 years, is 1998. In this paper, temperature and rainfall anomalies over South Africa during the 2015/16 summer season are compared to the mean temperature and rainfall anomalies of the summers during the previous decade.

Data and Method

The summer season is defined as the months of October to March the following calendar year. Daily maximum temperature, minimum temperature and rainfall data for 248 weather stations across South Africa for 10 summer seasons (2006/07 to 2015/16) are used in this analysis. These 248 stations were chosen based on their continuous availability throughout these 10 summer seasons as well as passing minimum quality requirements. The geographical distribution of the 248 stations are representative of all the different climate regions over South Africa. Threshold value quality checks and missing value checks were employed on the daily data. Monthly means are only calculated if a station adhered to the minimum quality requirements for at least 90% of the days within a specific month. These calculated monthly means are then used to calculate temperature and rainfall anomalies for each of the months of the 2015/16 summer season relative to the monthly means of the remaining 9 summer seasons.

Results and Discussion

The range of maximum temperature and minimum temperature anomalies across South Africa for each of the 2015/16 summer months are shown in Fig. 1 and 2. With regard to maximum temperature anomalies, the median values were above 0°C during all the summer months. The months of October and December experienced the largest temperature anomalies (Fig. 1), reaching 6°C at a few stations over the western interior (Orange river valley) and

southern-central (Cradock, Grootfontein) to northeastern interior (Viljoenskroon, Alldays, Mokopani and Zebediela) respectively (Fig. 4).

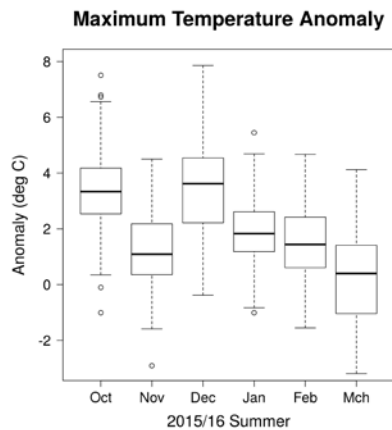


Figure 1: Box-plots of the 2015/16 summer maximum temperature anomalies ($^{\circ}\text{C}$) calculated at 248 stations across South Africa relative to the 2006/07-2014/15 maximum temperature monthly means.

More than 99% of the stations had positive maximum temperature anomalies during October and December, while 29% and 40% of the stations recorded anomalies exceeding 4°C during October and December respectively. During January and February, 98% and 87% of the stations recorded positive maximum temperature anomalies respectively. November and March had the smallest spatial distribution (expressed as percentage of the 248 weather stations) of positive maximum temperature anomalies (Fig. 4) with 82% and 60% of the stations that recorded anomalies $> 0^{\circ}\text{C}$ respectively.

Minimum temperature anomalies are generally smaller than that of the maximum temperature anomalies (Fig. 2). An interesting feature with regard to the minimum temperature anomalies is the $< 0^{\circ}\text{C}$ median value for the month of November.

The range of rainfall anomalies for the 2015/16 summer season at the 248 weather stations, expressed as a percentage, is shown in Fig. 3. The early summer months are characterized by a larger number of stations with negative rainfall anomaly percentages compared to the late summer months (96%, 87%, 88% vs 58%, 69%, 36%). The months of October and December, also the months with the most striking warm maximum temperature anomalies, were the months that suffered the largest rainfall deficits. During January, stations located over the western interior received very good rainfall (Fig. 5), with the rainfall anomaly percentage reaching 600% (Fig. 3). The northeastern interior received normal to above normal rainfall in

February continuing into March when good rainfall also fell over the southwestern part of the country (Fig. 5).

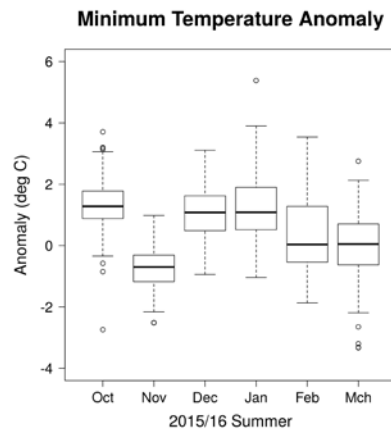


Figure 2: Box-plots of the 2015/16 summer minimum temperature anomalies ($^{\circ}\text{C}$) calculated at 248 stations across South Africa relative to the 2006/07-2014/15 minimum temperature monthly means.

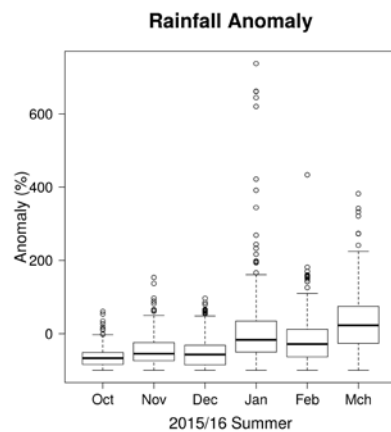


Figure 3: Box-plots of the 2015/16 summer rainfall anomalies (%) calculated at 248 stations across South Africa relative to the 2006/07-2014/15 monthly mean rainfall.

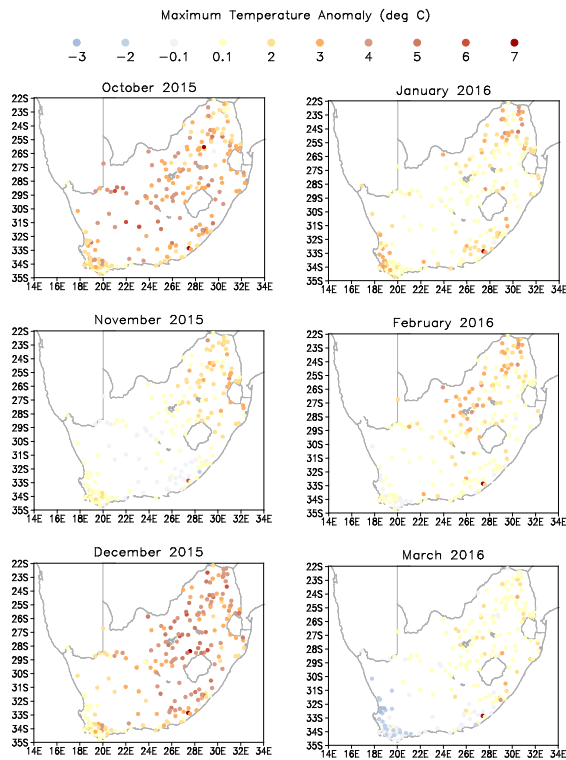


Figure 4: Maximum temperature anomalies for the 2015/16 summer season. Blue (red) shaded dots indicate negative (positive) anomalies (°C). The magnitude of the anomalies is shown at the top of the figure.

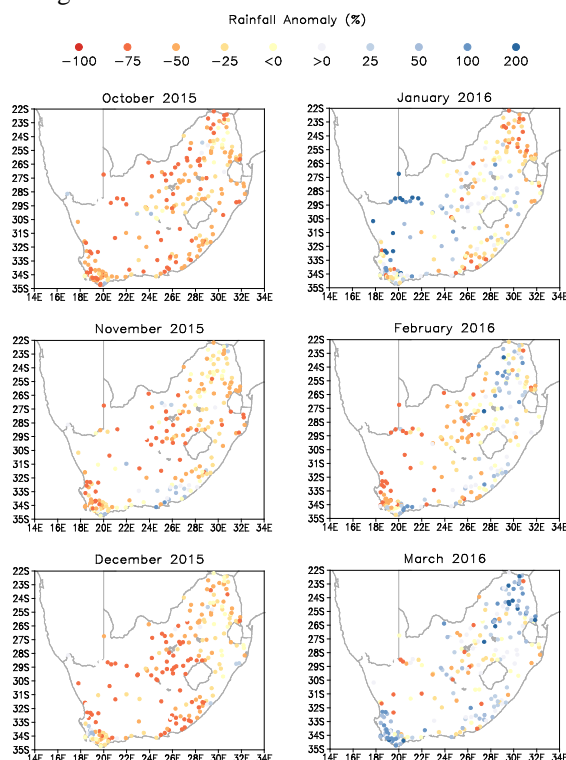


Figure 5: Rainfall anomalies for the 2015/16 summer season. Blue (red) shaded dots indicate positive (negative) anomalies (%). The magnitude of the anomalies is shown at the top of the figure.

Conclusions

Compared to the past decade, the 2015/16 summer season was warm and dry during the early summer, with somewhat wetter conditions during the late summer, although still anomalously warm over most of the country. The maximum temperature anomalies in the order of 4°C and higher during October and in particular during December when 40% of the stations are associated with anomalies of this magnitude are very noteworthy and might be a view into the future of projected temperatures for southern Africa (Engelbrecht et al., 2015).

References

- Barnston, A.G., Thiao, W. and Kumar, V. (1996). Long-lead forecasts of seasonal precipitation in Africa using CCA. *Journal of Climate*. 11: 506-520.
- Engelbrecht F. and co-authors. (2015). Projections of rapidly rising surface temperatures over Africa under low mitigation. *Environmental Research Letters*. 10: 085004.
- Landman, W.A. and Beraki, A. (2012) Multi-model forecast skill for mid-summer over southern Africa. *International Journal of Climatology*. 32: 303-314.
- Malherbe, J., Dieppois, B., Maluleke, P., Van Staden, M. and Pillay, D.L. (2015). South African droughts and decadal variability. *Natural Hazards*. DOI 10.1007/s11069-015-1989-y
- Van Heerden, J., Terblanche, D.E. and Schulze, G.C. (1988). The Southern Oscillation and South African summer rainfall. *Journal of Climatology*. 8: 577-597.
- Vogel, C.H. and Drummond, J. (1993). Dimensions of drought: South African case studies. *Geojournal*. 30: 93-98.

Dynamic core of the Variable-resolution Cubic Ocean Model (VCOM)

Francois A. Engelbrecht^{1,2,3}, Mary-Jane M. Bopape⁴, Mthetho Sovara⁴

Climate Studies, Modelling and Environmental Health; Natural Resources and the Environment; Council for Scientific and Industrial Research (CSIR); Pretoria, South Africa

Unit for Environmental Sciences and Management, North-West University, Potchefstroom, South Africa

School of Geography, Archaeology and Environmental Sciences, University of the Witwatersrand, Johannesburg, South Africa

Centre for High Performance Computing, Meraka Institute, Council for Scientific and Industrial Research, Pretoria, South Africa

Abstract

A new global ocean model is currently under development at the CSIR in South Africa, to serve as the ocean component of the Variable-resolution Earth System Model (VRESM). A novel aspect of VRESM is that both its ocean and atmospheric components employ the equi-angular gnomonic-cubic grid. A key computational advantage of this grid system is that it offers quasi-uniform resolution globally, even more so than in the case of the more widely used conformal-cubic grid, and significantly more so than in the case of the latitude-longitude grid. However, use of the equi-angular gnomonic-cubic projection results in a coordinate system that is non-orthogonal, which in turn implies that the primitive equations assume a more complicated form than in the case of orthogonal (e.g. conformal-cubic and latitude-longitude) coordinate systems. In this paper we derive the form that the hydrostatic primitive equations assume on the equi-angular gnomonic-cubic grid for an ocean that satisfies the Boussinesq assumption, thereby obtaining the dynamic core of the new ocean model. Given that the equi-angular gnomonic-cubic grid offers flexible options for high-resolution stretched-grid modelling through the Schmidt transformation, the new ocean model is termed the “Variable-resolution Cubic Ocean Model (VCOM)”.

Keywords: ocean model, equi-angular gnomonic-cubic-projection, quasi-uniform resolution, primitive equations, VCOM.

Introduction

The majority of global ocean models that are applied today, for example most of the models applied in the Coupled Model Intercomparison Project Phase Five (CMIP5) of the Intergovernmental Panel on Climate Change (IPCC), employ latitude-longitude based grid systems. A first problem associated with the use of the latitude-longitude grid in climate modelling are the polar singularities, although these can be avoided in ocean models (applied to Earth with its current configuration of continents) by rotating the grid so that both poles are located over the continents. A second problem is the convergence of longitudinal lines towards the poles and associated increases in horizontal resolution, which places a severe restriction on the Courant-Friedrichs-Lewy stability criterion across the entire integration domain. The use of tri-polar latitude-longitude grids has consequently become popular in ocean modelling. In these grid systems three different overlapping longitude-latitude grids are used to provide more uniform resolution. However, tri-polar grids are not an appealing option for global atmospheric modelling, which can't avoid the existence of the singularities inherent to these grids. This has resulted in the status quo in coupled climate modelling, namely the use of very different horizontal grid systems in global ocean and atmosphere models. Model couplers are needed to interpolate heat, mass and momentum fluxes between the different grid systems, with resulting complications towards avoiding model drift.

It is against this background that the CSIR in partnership with the Commonwealth Scientific and

Industrial Research Organisation (CSIRO) is developing a new coupled climate model with all component models using the same horizontal grid system. The equi-angular gnomonic-cubic grid (Sadourny, 1972) has been selected for this purpose, due to its appealing property of providing almost uniform resolution globally whilst at the same time avoiding the existence of singularities. This grid system is more uniform than the more widely used conformal-cubic grid, but is non-orthogonal, resulting in both the atmospheric and ocean equations assuming a more complicated form than in orthogonal coordinate systems (e.g. Rancic et al., 1996). This paper derives the form that the hydrostatic primitive equations assume on the equi-angular gnomonic-cubic grid, for an ocean that satisfies the Boussinesq assumption. The dynamic core of the new ocean model is thereby obtained, following on the recent development of a global atmospheric model cast on the same grid system at the CSIRO.

Hydrostatic primitive equations in general curvilinear coordinates

The hydrostatic primitive equations in general curvilinear coordinates applied to the ocean are (Tsugawa et al., 2008):

$$\frac{\partial u_\alpha}{\partial t} = (f + \zeta) E_{\alpha\beta} u^\beta - K_{;\alpha} - w \frac{\partial u_\alpha}{\partial z} - \frac{1}{\rho_0} p_{;\alpha} + F_\alpha, \quad (1)$$

$$\frac{\partial \theta}{\partial t} = -(\theta u^\alpha)_{;\alpha} - \frac{\partial w \theta}{\partial z} + D_\theta, \quad (2)$$

$$\frac{\partial s}{\partial t} = -(s u^\alpha)_{;\alpha} - \frac{\partial w s}{\partial z} + D_s, \quad (3)$$

$$\frac{\partial w}{\partial z} = -u_{;\alpha}^\alpha \quad (4)$$

$$\frac{\partial p}{\partial z} = -g\rho. \quad (5)$$

Here u_i and u^i are the covariant and contravariant wind components, respectively (Sadourny, 1972):

$$u_i = \bar{V} \cdot \bar{a}_i, \quad (6)$$

$$\bar{V} = u^i \bar{a}_i, \quad (7)$$

With \bar{V} the horizontal wind vector and \bar{a}_1 and \bar{a}_2 the horizontal unit base-vectors of the coordinate system. The Greek letter subscripts and superscripts express vector components 1 or 2, with the subscripts representing covariant components and superscripts contravariant components. w is the vertical velocity, ζ is the relative vorticity, f is the Coriolis parameter, K is the kinetic energy, θ is the potential temperature, p is the pressure, ρ is the density and ρ_0 is the constant reference density. The diffusion terms for potential temperature and salinity are D_θ and D_s , respectively. F_α is the viscous force. Note that the use of a reference density state in the horizontal momentum equations implies that the Boussinesq assumption has been made. The hydrostatic primitive equations are thought to only break down at length scales of 10 to 1 km in the horizontal, and are widely used for global and regional ocean modelling at resolutions of 10 km in the horizontal or coarser.

The contravariant component u^β of the horizontal velocity is related to the covariant component u_α by (Tsugawa et al., 2008)

$$u^\beta = g^{\alpha\beta} u_\alpha, \quad (8)$$

where $g^{\alpha\beta}$ is the contravariant component of the metric tensor with Jacobian

$$G = \sqrt{g_{11}g_{22} - g_{12}g_{21}}. \quad (9)$$

Furthermore (Tsugawa et al, 2008),

$$u_{;\beta}^\alpha = \frac{\partial u^\alpha}{\partial x^\beta} + \Gamma_{\gamma\beta}^\alpha u^\gamma, \quad (10)$$

$$u_{\alpha;\beta} = \frac{\partial u_\alpha}{\partial x^\beta} - \Gamma_{\alpha\beta}^\gamma u_\gamma, \quad (11)$$

$$K = \frac{1}{2} u_\alpha u^\alpha, \quad (12)$$

$$\zeta = E^{\alpha\beta} u_{\beta;\alpha}, \quad (13)$$

and

$$\begin{pmatrix} E_{11} & E_{12} \\ E_{21} & E_{22} \end{pmatrix} = \begin{pmatrix} 0 & \frac{1}{G} \\ -\frac{1}{G} & 0 \end{pmatrix}. \quad (14)$$

Here $T_{\alpha\beta}^\gamma$ is the Christoffel symbol which denotes changes of the basis vectors. Tsugawa et al. (2008) proceeded to develop a global ocean model using this equation set applied to the conformal-cubic grid and a related family of cubic grids more uniform than the conformal-cubic grid. The dynamic core developed in this paper is similar, but makes use of a different and possibly even more uniform projection of the cube onto the sphere, namely the equi-angular gnomonic-cubic projection.

Hydrostatic primitive equations on the equi-angular gnomonic-cubic grid

In order to construct the equi-angular gnomonic-cubic grid, a cube is set up to encompass the sphere and tangent to it. A line of grid points spaced equally in longitude is constructed on the cube, at the latitude of the equator. A grid is then set-up across the cube consistent with this construction. The equi-angular gnomonic grid on the sphere is subsequently obtained through a projection from the centre of the sphere (i.e. gnomonic) of the grid points on the cube onto the sphere. The area elements that are constructed in this way on the sphere are quasi-uniform. A G7 equi-angular gnomonic cubic-grid (7 x 7 grid points per panel of the cube) is displayed in Fig. 1.

To obtain the form that the curvilinear equations assume for the case of the coordinate system obtained from the equi-angular gnomonic-cubic projection, expressions for the base vectors \bar{a}_1 and \bar{a}_2 need to be derived for each of the faces of the cube. To this end, note that for a sphere of radius R half of the dimension of the cube is simply $a=R$. Let the cube be orientated so that the absolute centred coordinate axes (X_1, X_2, X_3) are normal to its faces. Note that x^1 and x^2 assume values from the interval $[-a; a]$.

For example, consider the face of the cube that is

looking in the $-X_2$ direction. The local coordinates are related to the absolute coordinates via the relation

$$\bar{M} = (X^1, X^2, X^3) = \frac{R}{r} (x^1, -R, x^2), \quad (15)$$

where r is defined as

$$r = \sqrt{(R^2 + (x^1)^2 + (x^2)^2)}. \quad (16)$$

Noting that $\frac{\partial r}{\partial x^1} = \frac{x^1}{r}$ and $\frac{\partial r}{\partial x^2} = \frac{x^2}{r}$, expressions for the base vectors follow:

$$\bar{a}_1 = \frac{\partial \bar{M}}{\partial x^1} = \frac{R}{r} \left[1 - \frac{(x^1)^2}{r^2}, \frac{x^1 R}{r^2}, -\frac{x^1 x^2}{r^2} \right]; \quad (17)$$

$$\bar{a}_2 = \frac{\partial \bar{M}}{\partial x^2} = \frac{R}{r} \left[-\frac{x^1 x^2}{r^2}, \frac{R x^2}{r^2}, 1 - \frac{(x^2)^2}{r^2} \right]. \quad (18)$$

These expressions may be used to calculate the terms that constitute the tensor g_{ij} , which describes the local geometry (the metric coefficients):

$$g_{ij} = \frac{\partial \bar{M}}{\partial x^i} \cdot \frac{\partial \bar{M}}{\partial x^j} = \bar{a}_i \cdot \bar{a}_j = \frac{R^2}{r^4} \begin{bmatrix} R^2 + (x^2)^2 & -x^1 x^2 \\ -x^1 x^2 & R^2 + (x^1)^2 \end{bmatrix}. \quad (19)$$

Eq. (19) above allows for the calculation of the Jacobian G in eq. (9) for the case of the equi-angular gnomonic-cubic derived coordinate system. The resulting hydrostatic primitive equations on the equi-angular grid are:

$$\frac{\partial u_1}{\partial t} = (f + \zeta) \frac{1}{G} u^2 - \frac{\partial K}{\partial x^1} - w \frac{\partial u_1}{\partial z} - \frac{1}{\rho_0} \frac{\partial p}{\partial x^1} + F_1, \quad (20)$$

$$\frac{\partial u_2}{\partial t} = -(f + \zeta) \frac{1}{G} u^1 - \frac{\partial K}{\partial x^2} - w \frac{\partial u_2}{\partial z} - \frac{1}{\rho_0} \frac{\partial p}{\partial x^2} + F_2, \quad (21)$$

$$\frac{\partial \theta}{\partial t} = -(\theta u^\alpha)_{;\alpha} - \frac{\partial w \theta}{\partial z} + D_\theta, \quad (22)$$

$$\frac{\partial s}{\partial t} = -(s u^\alpha)_{;\alpha} - \frac{\partial w s}{\partial z} + D_s, \quad (23)$$

$$\frac{\partial w}{\partial z} = -u_{;\alpha}^\alpha \quad (24)$$

$$\frac{\partial p}{\partial z} = -g\rho. \quad (25)$$

Here

$$K = \frac{1}{2} (u_1 u^1 + u_2 u^2) \quad (26)$$

and

$$\zeta = G \left(\frac{\partial u_2}{\partial x^1} - \frac{\partial u_1}{\partial x^2} \right). \quad (27)$$

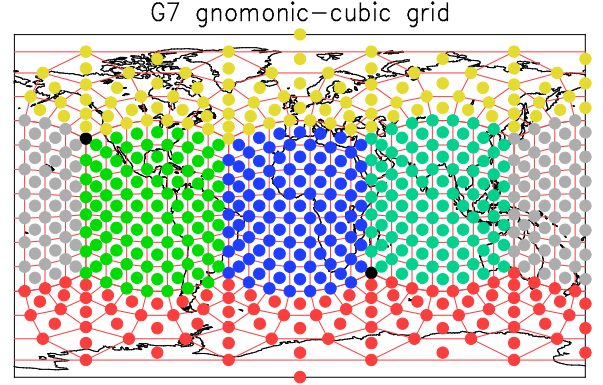


Figure 1: G7 equi-angular gnomonic-cubic grid on the sphere. Grid points at the centers of the grid boxes represent the Arakawa-A grid used in the numerical solution of the ocean equations. Different colors are used to indicate the six different panels of the cube that were projected.

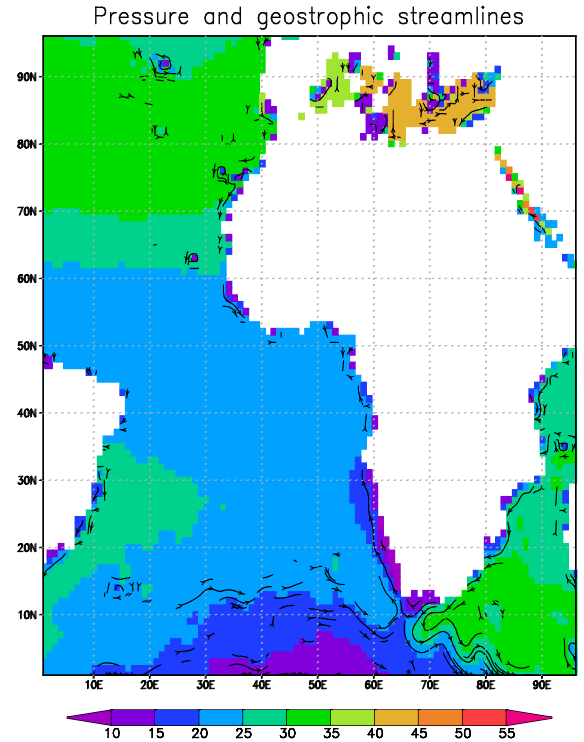


Figure 2: Model pressure (kPa) and geostrophic streamlines at $z=0$ at model initialization.

Note that towards the calculation of the horizontal derivatives in eqs. (22) to (24) above expressions for $\Gamma_{\alpha\beta}$ are needed. These expressions can be evaluated

by making use of eqs (17) and (18). Fig. 2 shows the VCOM calculated pressure at $z=0$ and associated geostrophic streamlines at model initialization, on the equi-angular gnomonic-cubic grid.

Conclusions

The form that the hydrostatic primitive equations assume on the equi-angular gnomonic-cubic grid for an ocean that satisfies the Boussinesq assumption has been derived. The resulting equation set is used as the dynamic core for the new ocean model under development at the CSIR. Since the equi-angular gnomonic-cubic grid also allows flexible stretched-grid options through the Schmidt transformation (McGregor, 1996), the new model has been termed the Variable-resolution Cubic Ocean Model (VCOM). VCOM compliments the Variable-resolution Atmospheric Model (VCAM) recently developed at CSIRO, and forms the ocean component of the new Variable-resolution Earth System Model (VRESM).

Acknowledgement

The research is funded through a CSIR Parliamentary Grant and CSIR thematic funds

References

McGregor J.L. (1996). Semi-Lagrangian advection on a cubic-gnomonic projection of the sphere. *Atmos. Ocean*.

Rancic, M. Purser, R.J. and Messinger F. (1996). A global shallow-water model using an expanded spherical cube: gnomonic versus conformal coordinates. *Q. J.R. Meteorol. Soc.* 124: 637-647.

Sadourny, R. (1972). Conservative finite-difference approximations of the primitive equations on quasi-uniform spherical grids. *Monthly Weather Review*. 100: 136-144.

Tsugawa M., Tanaka Y. and Matsuno T. (2008). An ocean general circulation model on a quasi-homogeneous cubic grid. *Ocean Modelling*. 22: 66-86.

Tropical Temperate Troughs over Southern Africa as Simulated by a Fully Coupled Model

Magdel Erasmus, University of Pretoria*

Willem A. Landman, University of Pretoria

Christien J. Engelbrecht, Agricultural Research Council

Abstract

The formation and development of tropical temperate troughs across southern Africa are investigated to determine the skill of a fully coupled model to simulate these tropical-temperate interactions. Hindcast outgoing long wave radiation data from the Global Seasonal Forecast System version 5 of the UK Met Office is compared to observed data for the months of November to February for the period 1996/1997 to 2009/2010. Overall, model data showed a smaller number of tropical temperate troughs than the observed data. The root mean square error revealed that on a monthly basis the model performs better at shorter lead times than at longer lead times. The monthly performance is also better than the overall seasonal performance.

Keywords: Cloud bands, GloSea5, Heavy rainfall, Metbot, Tropical-extratropical interactions

INTRODUCTION

Tropical-extratropical interactions exist in various parts of the world. Sometimes these weather phenomena are referred to as tropical plumes, but in southern Africa are more popularly known as tropical temperate troughs (TTT) (Hart *et al.*, 2010; Knippertz, 2007). TTT's represent an important mechanism for the poleward transportation of energy (heat), moisture and momentum. They consist of an area of enhanced convergence that can normally be identified as cloud bands on satellite imagery as regions of elongated clouds, stretching from the tropics south-eastward (north-eastward) towards the South Pole (North Pole) (Harangoza and Harrison, 1983; Harrison, 1984; Hart *et al.*, 2010; Macron *et al.*, 2014; Ratna *et al.*, 2013; Todd and Washington, 1999; Vigaud *et al.*, 2012). On either side of the cloud band there are areas of suppressed convection (Macron *et al.*, 2014), forming a ridge-trough-ridge like synoptic pattern (Ratna *et al.*, 2013). TTT's can form over the ocean and over a landmass, but usually the latter produces heavy rainfall along the full length of the TTT (Hart *et al.*, 2010).

TTT's usually last several days and can be tracked on satellite imagery by the cloud bands that move eastwards. Due to their longevity, these systems usually produce large amounts of rainfall and can contribute greatly towards a season's accumulative rainfall. These systems are one of the major contributors to summer rainfall over southern Africa (Harrison, 1984), and although the physical and dynamic characteristics of these systems are not fully understood at synoptic scale (Hart *et al.*, 2010; Ratna *et al.*, 2013; Vigaud *et al.*, 2012), a substantial amount of work has been done describing these significant rain-producing systems.

Three preferred regimes were discovered where TTT's tend to develop across southern Africa (Fauchereau *et al.*, 2009), which were confirmed by a later study (Vigaud *et al.*, 2012). These three regimes are bands of maximum convection that are rooted over the north-eastern parts of South Africa, Mozambique and Madagascar, stretching in a NW/SE direction and ends at longitudes between 40°E and 65°E (Fauchereau *et al.*, 2009). A precursory signal was also discovered of simulated zonal stretching deformation at the 200hPa level from about 5 days prior to a TTT event (Vigaud *et al.*, 2012). This discovery suggests that the mid-latitude westerly waves and especially their phasing play an important role during a TTT event (Vigaud *et al.*, 2012). Moreover, TTT's tend to develop most often and also the strongest in the southwest Indian Ocean (Cook, 2000; Hart *et al.*, 2010; Todd and Washington, 1999).

Several atmospheric circulation features of the southern African summer rainfall season play an important role in TTT development over southern Africa (Hart *et al.*, 2010). The following scenario typically can lead to the development of a TTT across southern Africa that will extend from the Angola Low, south-eastwards to an area in the southern Indian Ocean, just east of the ridging South Atlantic High (Hart *et al.*, 2010). A weak surface high developing over southern Mozambique and the adjacent ocean enhances the pressure gradient across Botswana and Zimbabwe towards the semi-permanent Angola Low (Hart *et al.*, 2010). The greater pressure gradient leads to stronger low-level north-easterly flow across the central parts, and brings tropical air into circulation across the subcontinent (Hart *et al.*, 2010; Todd and Washington, 1999). A continental heat low forming over the Kalahari Desert diverts the low-level north-easterlies further southwards (Hart *et al.*, 2010). If

the South Atlantic High ridges south of the subcontinent, onshore flow is induced and will bring the possibility of coastal showers (Hart *et al*, 2010; Ratna *et al*, 2013). Lastly, when the South Indian High extends north-westward an easterly wave is established over Mozambique and eastern South Africa (Hart *et al*, 2010; Ratna *et al*, 2013) (Fig. 1).

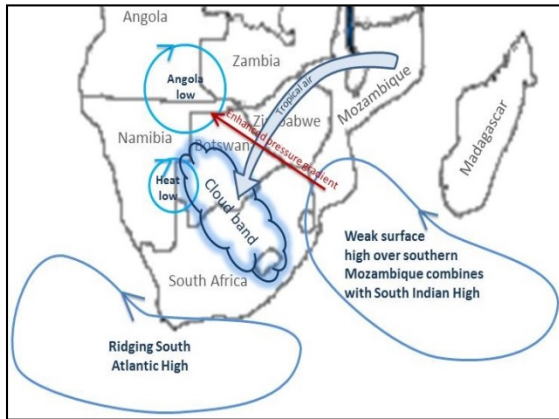


Figure 1: A schematic illustration of the various atmospheric circulation features playing a role during the development of TTTs across southern Africa.

Due to the great influence TTT's has on southern African rainfall, it is important to gain a better understanding as to how accurately models can reproduce these systems. During this study model output from a fully coupled ocean atmosphere general circulation model (OAGCM) is evaluated against the observations as discussed above.

DATA AND METHOD

The predictability of TTT events over southern Africa is investigated using hindcast data from a high resolution model, the Global Seasonal Forecast System version 5 (GloSea5) of the UK Met Office, over the summer rainfall period (November to February) for the years 1996/1997 to 2009/2010. The previous version of the GloSea model, GloSea4, was found to have the ability to predict seasonal to inter-annual variability over southern Africa (Landman *et al*, 2012). For the scope of this paper the data of three ensemble members are used with one start date, namely 1 November of each summer rainfall season. To achieve a spread between different ensemble members that are initialized on the same date, a stochastic physics scheme is utilized (MacLachlan *et al*, 2015).

Of all the atmospheric parameters available, only the results of daily OLR are considered for this paper. OLR represents cloud bands the best as it relates directly to tropical convection and therefore the characteristic cloud bands associated with TTT events. The modelled daily OLR data is compared to observed daily OLR values from the National

Environmental Satellite Data and Information Service (NESDIS) of the National Oceanic and Atmospheric Administration (NOAA). This observed data is archived onto a $2.5^\circ \times 2.5^\circ$ grid (Liebmann & Smith, 1996). Temporal and spatial interpolation has been used to overcome the problem of missing values (Liebmann & Smith, 1996).

The geographical domain for this investigation extends from 0° to 50°S and 20°W to 60°E in order to capture all aspects and characteristics associated with TTT events over southern Africa. This domain is consistent with previous studies on TTT's over southern Africa (e.g. Fauchereau *et al*, 2009; Vigaud *et al*, 2012). The resolution of the GloSea5 seasonal forecast model is as follows: For the atmosphere and over a landmass, the horizontal resolution is $0.833^\circ \times 0.556^\circ$ and for the oceans the grid spacing is $0.25^\circ \times 0.25^\circ$ (MacLachlan *et al*, 2015; Scaife *et al*, 2014). The vertical resolution of the GloSea5 is 85 quasi-horizontal atmospheric levels, with an upper boundary of 85km near the mesopause, and 75 quasi-horizontal levels for the ocean (Scaife *et al*, 2014).

The methodology developed by Hart *et al* (2012) is used to identify TTT events in both the observed and hindcast data. This methodology consists of a meteorological "robot" (MetBot) that identifies cloud band systems by plotting daily OLR data with the maxima threshold at 230W.m^{-2} and running it through a blob detection algorithm (Hart *et al*, 2013). When OLR blobs extend from the tropics south-eastward into the sub-tropics, the cloud bands are flagged (Hart *et al*, 2013). OLR data is then selected 48 hours before and after the flagged cloud bands, on which the process, with lower criteria, is repeated in order to establish a track for the cloud bands (Hart *et al*, 2013). From this arises a data object for each event describing the development of the cloud band (Hart *et al*, 2013).

RESULTS

Observed OLR data, as well as three different ensemble members of the GloSea5 model data with a start date of 1 November of each season, are analysed using the MetBot. Candidate cloud bands are then identified and as a result the Metbot produces two figures for each candidate cloud band, one showing raw OLR data and the other showing the OLR blob (Fig. 2 (a) and (b)).

For the observed dataset the MetBot identified 525 cloud bands in total for the months of November to February for the years 1996/1997 to 2009/2010, whereas for the three different ensemble members, model 001, model 002 and model 003 only totalled 389, 350 and 379 respectively. The reason for the great difference in number of TTT's between the observed data and modelled data has not yet been investigated, but it could be that TTT development is biased towards the east of the considered domain. It is also possible that the model will perform better if the threshold for candidate cloud bands is decreased. This can be considered in future studies.

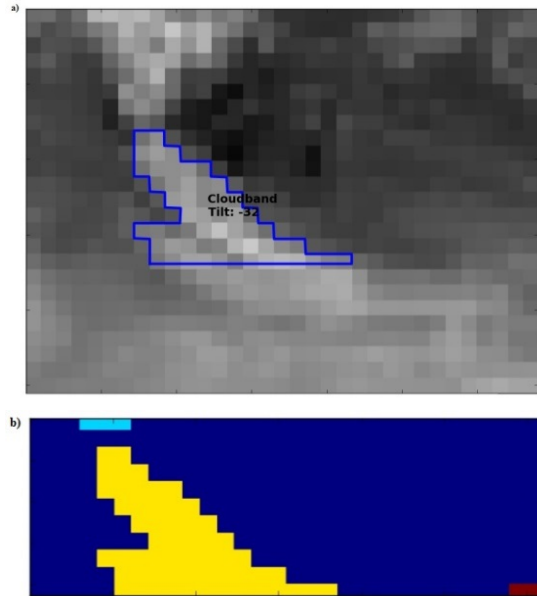


Figure 2: Figures produced by the MetBot for observed OLR on 12 November 1996. a) Raw OLR showing the cloud band (within the blue line) and the NW/SE tilt thereof. b) OLR blob (yellow) showing the candidate cloud band.

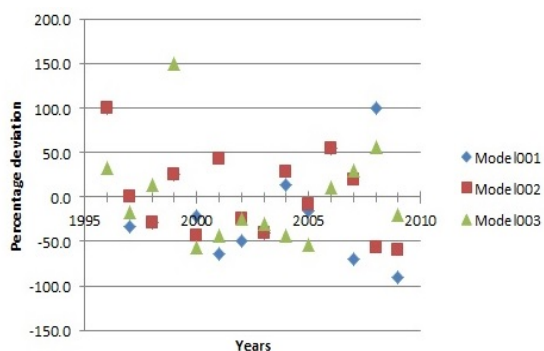


Figure 3: Percentage deviation of the modelled data from the observed data for December of each rainfall season. All three ensemble members are displayed (model1001, model1002 and model1003).

Candidate cloud bands are sometimes identified for a few consecutive days, but instead of considering these occurrences as one TTT event, candidate cloud bands were considered separately for both the observed and the model data. Sometimes more than

one candidate cloud band is identified for one specific day in which the one cloud band will lie in the eastern end of the region and the other one towards the west. In this case both of the candidate cloud bands are counted.

The total number of candidate clouds bands is considered on a monthly basis, as well as the total number of candidate cloud bands for the entire period from November to February of each rainfall season. The percentage deviation is then calculated for each month and the entire rainfall season using eq. 1, where CCC_M is the number of modelled candidate cloud bands and CCC_{Obs} is the number of observed candidate cloud bands (Fig.3).

$$\frac{CCC_M - CCC_{Obs}}{CCC_{Obs}} \times 100 \quad (1)$$

The root-mean square error (RMSE) is also calculated for each month of the entire period for each ensemble member, as well as for the entire rainfall season for each ensemble member. An average for the RMSE of each month is calculated as well to determine how each ensemble member performs for each month over the period from November to February (Table 1). To calculate the RMSE eq. 2 is used, where M is the number of years (14 in this case), y_m is the number of candidate cloud bands per ensemble member and o_m is the number of observed candidate cloud bands.

$$RMSE = \sqrt{\frac{1}{M} \sum_{m=1}^M (y_m - o_m)^2} \quad (2)$$

Table 1: RMSE values for each ensemble member (001, 002 and 003) for each month, the average of the four months per ensemble member, as well as for the entire rainfall season for the period 1996/1997 to 2009/2010.

	001	002	003
November	4.21	4.55	4.07
December	5.35	4.06	4.22
January	7.51	6.64	4.94
February	7.26	7.19	5.82
Average	6.08	5.61	4.76
Total period	15.35	16.57	13.75

DISCUSSION AND CONCLUSION

This study investigates the formation and development of TTT events across southern Africa as modelled by a fully coupled OAGCM, the GloSea5 of the UK Met Office. Modelled OLR data from three ensemble members is compared to observed OLR data to determine the capability of the

GloSea5 to predict TTT characteristics during the summer rainfall season of southern Africa. When considering the monthly performance of each ensemble member, one can conclude from the RMSE (table 1) that on average ensemble member 003 performs the best. On a monthly basis ensemble member 003 performs the best for November, January and February, while ensemble member 002 performs the best for December. When considering the entire rainfall season as a whole, ensemble member 003 also outperforms the other ensemble members. However, when looking at the total number of candidate cloud bands during the season, ensemble member 001 (389 candidate cloud bands) came closer to the observed number of candidate cloud bands (525). The different skill demonstrated by the different ensemble members adds to the uncertainty in the forecasts of TTT's.

A monthly outlook poses to be more promising, especially during the months of November and December with RMSE values below five for most of the ensemble members, but this is probably due to the shorter forecast lead time. Longer lead times will be considered in the investigation that follows this preliminary study to evaluate the predictability of TTT events over the summer rainfall season. It may also be worthwhile to separately determine whether there exist relationships between the modelled and observed number of TTT events during anomalously wet summer seasons, as well as during anomalously dry summer seasons.

ACKNOWLEDGEMENTS

The authors kindly thank Neil Hart for providing the MetBot software, the UK Met Office for supplying the data and Bernard Erasmus for software support.

REFERENCES

Cook, K.H. (2000). The south Indian Ocean convergence zone and interannual rainfall variability over southern Africa. *Journal of Climate*, 13: 3789-3804.

Fauchereau, N., Pohl, B., Reason, C., Rouault, M. and Richard, Y. (2009). Recurrent daily OLR patterns in the southern Africa / southwest Indian Ocean region, implications for South African rainfall and teleconnections. *Climate Dynamics*. 32: 575-591.

Harangozo, S. and Harrison, M.S.J. (1983). On the use of synoptic data indicating the presence of cloud bands over southern Africa. *South African Journal of Science*. 79: 413-414.

Harrison, M.S.J. (1984). A generalized classification of South African summer rain-bearing synoptic systems. *International Journal of Climatology*. 4: 547-560.

Hart, N.C.G., Reason, C.J.C. and Fauchereau, N. (2010). Tropical-extratropical interactions over

southern Africa: Three cases of heavy summer season rainfall. *Monthly Weather Review*. 138: 2608-2609.

Hart, N.C.G., Reason, C.J.C. and Fauchereau, N. (2012). Building a tropical-extratropical cloud band metbot. *Monthly Weather Review*. 140: 4005-4016.

Hart, N.C.G., Reason, C.J.C. and Fauchereau, N. (2013). Cloud bands over southern Africa: seasonality, contribution to rainfall variability and modulation by the MJO. *Climate Dynamics*. 41: 1199-1212.

Knippertz, P. (2007). Tropical-extratropical interactions related to upper-level troughs at low latitudes. *Dynamics of Atmospheres and Oceans*. 43: 36-62.

Landman, W.A., Graham, R., Knight, J., Engelbrecht, C. and Olivier, C., 2012: Assessment of GloSea4 seasonal forecasts for SADC and the global oceans, SASAS, 26-27 September 2012, p. 102-103.

Liebmann, B. and Smith, C.A. (1996). Description of a complete (interpolated) outgoing long wave radiation dataset. *Bulletin of the American Meteorological Society*. 77: 1275-1277.

MacLachlan, C., Arribas, A., Peterson, K.A., Maidens, A., Fereday, D., Scaife, A.A., Gordon, M., Vellinga, M., Williams, A., Comer, R.E., Camp, J., Xavier, P. and Madec, G. (2015). Global seasonal forecast system version 5 (GloSea5): a high-resolution seasonal forecast system. *Quarterly Journal of the Royal Meteorological Society*, 141: 1072-1084.

Macron, C., Pohl, B., Richard, Y. and Bessafi, M., (2014). How do tropical temperate troughs form and develop over southern Africa? *Journal of Climate*. 27: 1633-1647.

Ratna, B.S., Behera, S., Ratnam, J.V., Takahashi, K. and Yamagata, T. (2013). An index for tropical temperate troughs over southern Africa. *Climate Dynamics*. 41: 421-441.

Scaife, A.A., Arribas, A., Blockley, E., Brookshaw, A., Clark, R.T., Dunstone, N., Eade, R., Fereday, D., Folland, C.K., Gordon, M., Hermanson, L., Knight, J.R., Lea, D.J., MacLachlan, C., Maidens, A., Martin, M., Peterson, A.K., Smith, D., Vellinga, M., Wallace, E., Waters, J. and Williams, A. (2014). Skilful long-range prediction of European and North American winters. *Geophysical Research Letters*. 41: 2514-2519.

Todd, M. and Washington, R. (1999). Circulation anomalies associated with TTT in southern Africa and the southwest Indian Ocean. *Climate Dynamics*. 15: 937-951.

Vigaud, N., Pohl, B. and Cr  tat, J. (2012). Tropical-temperate interactions over southern Africa simulated by regional climate model. *Climate Dynamics*. 39: 2895-2916.

Representation of aerosol particles and associated transport pathways in regional climate modelling in Africa

Rebecca M. Garland^{1,2,*}, Hannah M. Horowitz³, Christien J. Engelbrecht⁴, Zane Dedkind¹, Mary-Jane M. Bopape⁵, Stuart J Piketh², and Francois A. Engelbrecht^{1,5}

¹ *Natural Resources and the Environment Unit, CSIR, Pretoria, South Africa*

² *Climatology Research Group, North West University, Potchefstroom, South Africa*

³ *Department of Earth & Planetary Sciences, Harvard University, Cambridge, MA, USA*

⁴ *Agricultural Research Council, Pretoria, South Africa*

⁵ *Centre for High Performance Computing, CSIR, Pretoria, South Africa*

School of Geography, Archaeology and Environmental Studies, University of the Witwatersrand, South Africa

Aerosol particles can have large impacts on air quality and on the climate system. Regional climate models for Africa have not been well-tested and validated for their representation and simulation of aerosol particles. This study aimed to validate the current representation of aerosol particles in the Conformal Cubic Atmospheric Model (CCAM), using the CMIP5 historical emissions inventory, to monitored data over Africa. In this study, CCAM was used to produce historical regional climate model simulations at 50 km horizontal resolution, globally, through the dynamical downscaling of ERA Interim reanalysis data. CCAM has a prognostic aerosol scheme for organic carbon, black carbon, sulphate, and dust, and non-prognostic sea salt. The aerosol optical depth (AOD) at 550nm from CCAM was compared to the AOD values (observed at 440nm and adjusted to 550nm using the Ångström exponent) from AERONET stations across Africa for 1999-2012. For this validation with AERONET, sites that are strongly impacted by aerosols from natural sources were prioritized. In general, the model captures well the monthly trends of the AERONET data. In addition, a climatology of simulated aerosol transport during the southern African biomass burning season was developed using self-organizing maps. This presentation will provide, through comparisons to monitored data, a basis for understanding how well aerosol particles are represented over Africa in regional climate modelling using the emissions inventory from the latest Intergovernmental Panel on Climate Change assessment report.

*corresponding author: RGarland@csir.co.za

Keywords: *Aerosol optical depth, CMIP5 emissions, CCAM, AERONET*

Introduction

Aerosol particles can impact the climate directly, through scattering and/or absorbing radiation, indirectly through modifying clouds. Currently, the largest uncertainty in climate models comes from the impacts of aerosols on the radiative balance of the Earth (Boucher et al., 2013). Africa contains the largest single sources of biomass-burning emissions and dust globally, which are large sources of aerosol particles (Crutzen and Andreae, 1990; Schütz et al., 1981). Dust aerosols, along with carbonaceous aerosols produced from biomass burning, are known to impact climate through direct scattering and absorption of radiation, and indirectly through their effects on cloud formation and properties. When considering anthropogenic emissions, black carbon is estimated to be second only to CO₂ in contributing to warming globally (Bond et al., 2013).

Meteorology plays a key role in the seasonality of emissions and transport in Africa. Changes in the large-scale circulation shift the location of maximum dust activity and transport of dust northward (~5°N to ~20°N) from winter through summer (e.g. Prospero et al., 2002). The seasonality of the dry season influences the seasonality of biomass burning in Africa, with the maximum biomass burning activity shifting from June-September in southern Africa, to December-

February in sub-Saharan northern Africa (e.g. Liousse et al., 2010).

Biomass burning emissions in southern Africa contribute greatly to the region's aerosol burden and in many places dominate the seasonal cycle of the column of aerosol particles in the region (e.g. Tesfaye et al., 2011; Queface et al., 2011;), which in turn can have a significant impact on the regional climate (Tummon et al., 2010).

In addition to local impacts, aerosols particles from African can be transported long distances and thus have far-reaching impacts. For example, over southern Africa, massive aerosol plumes during peak biomass burning are exported off the southeastern coast of southern Africa to the Indian Ocean (i.e. "River of Smoke"), as well as over the southwestern coast out to the Atlantic Ocean (Garstang et al., 1996; Swap et al., 2003). This latter exit pathway aligns with the stratocumulus cloud deck that forms off of the southwestern coast, and is an area of large uncertainty in modelling aerosol radiative forcing (Stier et al., 2013).

As Africa is a large source of aerosol particles, an accurate representation of African aerosols and their transport in climate models is needed to understand the regional and global radiative forcing and climate impacts of dust and biomass burning aerosols, at

present and under future climate change. However, regional climate models for Africa have not been well-tested and validated for their representation and simulation of aerosol particles (Tesfaye et al., 2013).

This study aimed to validate the current representation of aerosol particles in the Conformal Cubic Atmospheric Model (CCAM) to monitored data over Africa. In addition, a climatology of simulated aerosol transport during the southern African biomass burning season was developed using self-organizing maps.

Methods

Regional Climate Modelling

CCAM (McGregor, 2005) was used to provide historical regional simulations at 50 km horizontal resolution, globally, through the dynamical downscaling of ERA Interim data reanalysis data (Dee et al., 2011). The Coupled Model Intercomparison Project Phase 5 (CMIP5) emissions inventory was used in the simulations under a scenario of RCP8.5 (Representative Concentration Pathway 8.5; i.e. low mitigation scenario) from the Intergovernmental Panel on Climate Change (IPCC) Assessment Report 5 report (Moss et al., 2010). CCAM modelled outputs for 1999-2012 were used in the analysis as that was the time period of the available monitored data. CCAM 6-hourly outputs were used in this analysis.

CCAM has a prognostic aerosol scheme for organic carbon, black carbon, sulphate, and dust, and non-prognostic sea salt (Rotstayn et al., 2007). In CCAM, dust is emitted into the atmosphere through mechanical action by the wind. In the CMIP5 emissions inventory each month has a constant emissions rate of the particulate organic carbon, black carbon and sulphate emissions, and these emission rates are held constant for multiple years. Thus, when using this inventory, the changes in the aerosol loading on temporal scales smaller than monthly are not due to changes in emissions, nor are some of the inter-annual variability.

In order to compare to observations, the focus of was to investigate the monthly cycle of aerosol particles from CCAM to understand if that cycle is captured correctly. Multi-year monthly averages of the CCAM modelled and the Aerosol Robotic Network (AERONET) measured aerosol optical depth (AOD) were compared.

Aerosol Optical Depth

The AOD describes the attenuation of light through the atmosphere due to aerosol particles based on the Beer-Lambert Law. The AOD is the integral of the extinction coefficient at a specific wavelength (i.e.,

the sum of the light at that wavelength that is scattered or absorbed by the aerosol particles) in a column of air from the surface to the top of the atmosphere (TOA). Equation (1) describes the basic equation for AOD where τ_λ is the AOD at wavelength λ , z is the height, and σ_{ext} is the aerosol extinction coefficient.

$$\tau_\lambda = \int_{z=0}^{z=TOA} \sigma_{ext}(\lambda, z) dz \quad (1)$$

Monitored Data

The monitored data were AOD values from AERONET stations across Africa (Holben et al., 1998). For this validation, sites that are strongly impacted by natural sources (i.e. biomass burning and dust) were prioritized. As they are large sources of aerosol particles for the continent and globally, with Africa having the largest emissions in the world of dust and biomass burning aerosols (Crutzen and Andreae, 1990; Schütz et al, 1981). Thus, it is critical to understand if CCAM using the CMIP5 emissions inventory from the IPCC assessment can capture the monthly cycle of these large emission sources.

In addition, only sites that had a multi-year dataset were selected, and those sites that had continuous sampling were prioritized. Figure 1 highlights the AERONET sites that were used in this comparison. The sites are color-coded by geography and the AOD trends seen at the sites (as described in the Results and Discussion section).

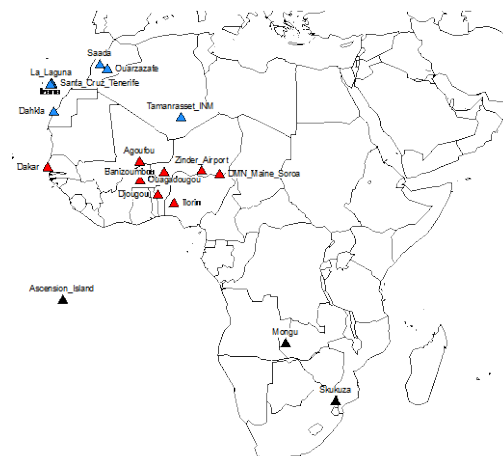


Figure 1: Map of AERONET sites used in the model-observed comparison

The modelled and monitored AOD were compared for 1999-2012. The aerosol optical depth (AOD) at 550nm from CCAM was compared to the AOD values (observed at 440nm and adjusted to 550nm using the Ångström exponent) from AERONET stations across Africa.

AERONET daily data were used, and the monthly averages were calculated using a 70% data completeness rule. In other words, if more than 30% of the daily values were missing, then a monthly average could not be calculated.

Aerosol Particle Transport

An aerosol climatology and associated transport patterns were analysed through Self Organizing Maps (SOMs) (Hewitson and Crane, 2012). CCAM simulated AOD and the geopotential heights of 700-850 hPa were extracted for July to October for 1979-2012. It was observed in the SAFARI campaign that during the biomass burning period, aerosol particles are transported aloft (peaks between ~600-800 hPa) (Haywood et al., 2004). The SOM analysis for geopotential height was performed for 35 nodes, and the AOD associated with each synoptic type were mapped onto the nodes. This analysis focused on southern Africa (20°W – 35°E, 40°S-0°S) during the biomass burning period to understand the simulated aerosol climatology and transport patterns.

Results

Figure 2 displays the multi-year monthly mean for the studied sites for both the observed data (in pink) and the CCAM data (in blue). The dark blue line in Figure 2 are when all CCAM data are used, the light blue line are when the CCAM data from only those months where there was monitoring data are used. The shaded region is one standard deviation of the dark blue line, and is shown to highlight the spread of the monthly means from CCAM.

The panels in the figure are ordered with the northern Africa sites first, then the western Africa sites, and then the southern.

The northern Africa sites have generally low AOD values Africa sites. Note that the scales are not the same in all the panels to aid in viewing of the trends. (<~0.5), with peaks in June-August. The western sites (red in Figure 1) are strongly influenced by dust and have highest AOD values of the African sites studied. At these sites, the AOD peaks generally around March and/or June, though there is variety in the timing of peak across the sites. The southern-most western Africa sites (i.e. Djougou and Ilorin) have an earlier peak in January and February. The southern African sites have peaks during the biomass burning period in the austral late winter and spring, generally peaking in September.

Figure 2 highlights that the monthly trends in the CCAM data, and the comparison of the modelled and monitored data, are similar using either all the CCAM data or only those that align to the available monitoring data. The differences in only including those CCAM outputs where AERONET data were available that are seen are within one standard deviation of the monthly averages for the dark blue line (i.e. all CCAM data) for all sites except Ouazazate.

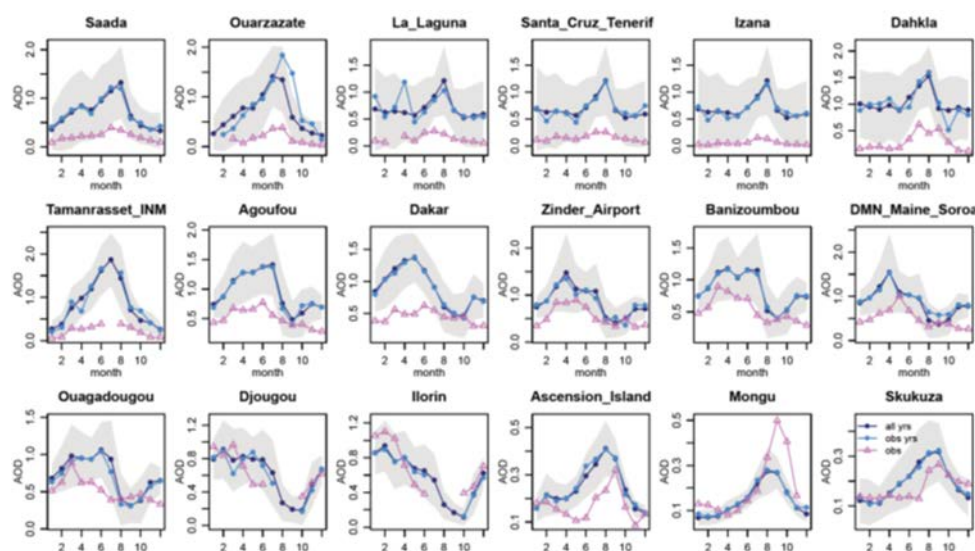


Figure 2: AOD at 550nm for observed (pink) and modelled with all CCAM outputs (dark blue) and only those months with AERONET data (light blue). The shaded areas is one standard deviation from the monthly averages of the dark blue line

For most sites, the monthly cycle (i.e. timing of peak and minimum AOD values) is well-captured by CCAM using CMIP5 emissions. Additionally, the magnitude of multi-year monthly average of the observed AOD are within one standard deviation of the model for at least half of the observed monthly averages for all sites, with the except seven sites (Ascension Island, Mongu, Dakar, Agoufou, Tamanrasset_INM, Ourzazate, Dahkla). The reasons for these differences are currently under investigation; it is interesting to note that these sites are not in only one region, but are from all three regions studied (i.e. western, northern and southern Africa).

These results suggest that the model is overestimating the AOD for the northern-most sites due to an overestimation of dust. Preliminary analysis of the southern Africa aerosol climatology and associated transport patterns through SOMs, suggest that CCAM does represent the two major pathways of biomass burning aerosol exit off of the continent.

Conclusions

In general, CCAM captures well the monthly trends of the AERONET data across the continent. Additionally, the magnitude of the multi-year monthly averages of the observed AOD are within one standard deviation of the model for at least half of the observed monthly averages for 11 of the 18 studied sites. These are important first findings of the use of CCAM with the CMIP5 emissions inventory for simulating aerosol particles over Africa, as the CMIP5 emissions inventory is currently the inventory widely used globally to project climate futures. In addition, preliminary analyses indicate that the model does capture the spatial trends in the transport of aerosol particles from southern Africa during the biomass burning season.

This study is the first step in validating the aerosol output from CCAM over Africa. Future work will focus on understanding the causes for the discrepancies between the modelled and monitored values, including additional African AERONET sites, as possible, and understanding the sensitivity of the southern African climate (e.g. surface temperature) to the presence and characterization of aerosol particles.

Acknowledgments

This work was supported by NRF CSUR Grant Number 9157 and a CSIR PG Grant. HH was funded through the NSF GROW with USAID RI

Fellowship. We thank the PIs and their staff for establishing and maintaining the 18 AERONET sites used in this study.

References

- Bo-nnd T et al., 2013, 'Bounding the role of black carbon in the climate system: A scientific assessment', *J. Geophys. Res.*, 118.
- Boucher O et al., 2013, 'Clouds and aerosols' IPCC AR5.
- Crutzen, PJ and Andreae, MO. 1990, 'Biomass burning in the tropics: Impact on atmospheric chemistry and biogeochemical cycles' *Science*, 250:1669-1678.
- Dee, DP et al. 2011, 'The ERA-Interim reanalysis: Configuration and performance of the data assimilation system' *Quart. J. R. Meteorol. Soc.*, 137:553-597.
- Garstang et al. 1996 'Horizontal and vertical transport of air over southern Africa', *J. Geophys. Res.*, 101:23721-23736.
- Haywood JM, Osborne SR and Anel SJ. 2004. 'The effect of overlaying absorbing aerosol layers on remote sensing retrievals of cloud effective radius and cloud optical depth' *Q.J.R. Meteorol. Soc.*, 130:779-800
- Hewitson BC and Crane RG, 2002, 'Self-organizing maps: applications to synoptic climatology,' *Clim Res*, 22:13-26.
- Holben BN et al., 1998, 'AERONET - A federated instrument network and data archive for aerosol characterization', *Rem. Sens. Environ.*, 66:1-16.
- Liousse C et al. 2010, 'Updated African biomass burning emission inventories in the framework AMM-IDAF program, with an evaluation of combustion aerosols, *ACP*, 10.
- McGregor JL. 2005, CSIRO Atmospheric Research Tech. Paper, No 70, 43 pp.

Moss, RH et al. 2010. 'The next generation of scenarios for climate change research and assessment,' *Nature*, 463.

Prospero JM et al., 2002 'Environmental characterization of global sources of atmospheric soil dust identified with NIMBUS 7 TOMS absorbing aerosol product,' *Reviews of Geophysics*.

Rotstayn, LD *et al.* 2007, 'Have Australian rainfall and cloudiness increased due to the remote effects of Asian anthropogenic aerosols?' *J. Geophys. Res.*, 112.

Schütz L. et al, 1981, 'Saharan dust transport over the North Atlantic Ocean', *Spec. Pap. Geol. Soc. Am.*, 186:87–100.

Stier P. et al, 2013, 'Host model uncertainties in aerosol radiative forcing estimates: results from the AeroCom Prescribed intercomparison study,' *ACP*, 13.

Swap R et al. 2003 'Africa burning: A thematic analysis of Southern African Regional Science Initiative (SAFARI 2000),' *J. Geophys. Res.*, 108.
Tesfaye M et al. 2011, 'Aerosol climatology over South Africa based on 10 years of MISR data,' *J. Geophys. Res.*, 116.

Tesfaye M et al. 2013, 'Evaluation of regional climate model simulated aerosol optical properties over South Africa using ground-based and satellite observations.' *ISRN Atmospheric Science*, 2013.

Tummon F et al., 2010, 'Simulation of the direct and semidirect aerosol effects on the southern African regional climate during the biomass burning season,' *J. Geophys. Res.*, 115

Queface AJ et al., 2011, 'Climatology of aerosol optical properties in Southern Africa,' *Atmos Env.*, 45.

Recent improvements to the Rapidly Developing Thunderstorm product – the addition of lightning data

Morné Gijben^{*1}, Bathobile Maseko¹, Louis van Hemert¹, and Estelle de Coning²

¹ South African Weather Service, Private Bag X097, Pretoria, 0001, South Africa

² World Meteorological Organization, PO Box 18, Geneva, CH-1211, Switzerland

The Rapidly Developing Thunderstorms (RDT) product has been operational at the South African Weather Service since 2014, and has proved to be a very useful tool for nowcasting purposes, especially where radar systems are not available or operational. The aim of this work was to test the effect of including lightning data as auxiliary data into the RDT product and to verify this against radar reflectivity over South Africa. The results of 25 cases over South Africa show that the inclusion of lightning data on average improves the POD by 6.6%, the HSS by 4.6% and the FAR by 0.1%.

Keywords: nowcasting, satellite, numerical weather prediction, lightning, data sparse regions

Introduction

Remote sensing tools like radars, lightning detectors, and satellites play an important role in the nowcasting of thunderstorms (de Coning *et al.*, 2011). Nowcasting is the science of predicting ordinary and severe weather events in the next few hours. Many sectors of society need to be prepared for these events and it is the mandate of the South African Weather Service (SAWS) to issue timely weather-related warnings. Radar systems offer the most useful information on the characteristics, intensity, and movement of thunderstorms, but radars are expensive to maintain and they require extensive maintenance. In South Africa, the radar coverage do not extend over the entire country, while in other southern African countries very few operational radars exist. Despite these shortcomings, weather services still need to warn the public of inclement weather as to ensure the safety of people and properties.

The Meteosat Second Generation (MSG) satellite has proved to be particularly useful for the nowcasting of thunderstorms in data sparse regions. It provides coverage over all African countries every 15 minutes with a horizontal resolution of 3 km for most of the 12 channels. Using numerical weather prediction (NWP) model data in conjunction with satellite data adds additional value for nowcasting in the areas where radars are not available (de Coning *et al.*, 2015).

In order to optimise the use of satellite data, centres of excellence, called Satellite Application Facilities (SAF), were established in European countries to develop products for different applications,

including nowcasting. One of the products developed within the Nowcasting SAF (NWC SAF, 2016) framework is the so-called “Rapidly Developing Thunderstorms (RDT)” product. The aim of the RDT product is to identify, monitor and track intense cloud systems and to detect rapidly developing storm systems (NWC SAF <http://www.nwcsaf.org>).

The 2013 version of the NWC SAF software was installed at SAWS in 2014. For the southern African region, the software uses the local version of the UK Meteorological Office (UKMO) Unified Model (UM) as input. Aside from using MSG (mandatory) and UM (optional) data, the RDT product can be used with an auxiliary data set from local lightning detection networks. Initial tests were done to validate the RDT (without using lightning data as input) against the occurrence of lightning (de Coning *et al.*, 2015). The results were very encouraging and showed that the RDT product can be very useful for the identification and tracking of the intense parts of thunderstorms using MSG and NWP data.

The developers of the RDT product recommends that lightning data be used as input dataset to characterize electrical activity in order to force the identification of convective systems. The aim of this work was to test the effect of including lightning as an auxiliary dataset into the RDT product and to verify this against radar reflectivity over South Africa.

Instrumentation and Method

In this study, 25 random cases were analysed between September and March over the period from 2011 to 2015. This is the time of year where most convective activity occurs over South Africa (de Coning *et al.*, 2015). On each of the 25 days, the hours between 11:00 to 18:00 UTC were isolated and only those parts of South Africa with lightning and radar coverage were considered.

The RDT product requires the use of the VIS 0.6, WV 6.2, WV 7.3, IR 8.7, IR 10.8 and IR 12.0. MSG satellite channels, which are updated every 15 minutes. NWP prognosis are surface pressure and geopotential, temperature of the tropopause, 2m temperature, relative humidity and dew point temperature, land/sea mask, altitude model, as well as temperature and humidity at all the pressure levels of the NWP. The local version of the UM used for the case studies was available once a day at a horizontal resolution of 12 km, with hourly output for 48 hours ahead. Similar to the satellite data, the RDT product updates every 15 minutes and is available during day and night time (during the night the VIS channel is not used).

Lightning data supplied by the southern African lightning detection network was included into the processing for RDT. Two settings are made in the RDT configuration files (NWC SAF, 2013a). 600 seconds (10 min) before and after each RDT time step are used as the time window for lightning data to be included and 3 satellite pixels (approximately 9 kms) are set as the distance between the satellite cell and the lightning flash with which it is associated.

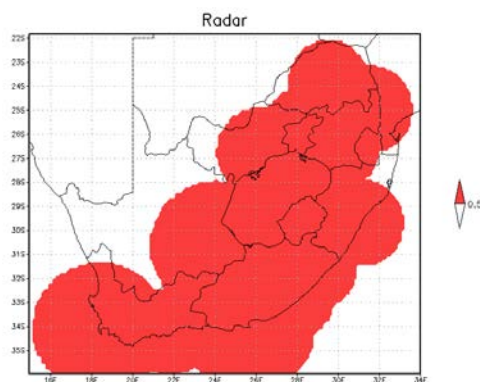


Figure 1. Red areas shows the domain of the study when all radars were available.

Radar data are used as ground truth for the RDT polygons. Fig. 1 shows a map of the radar system mosaic over South Africa if all radars are operational. A challenge with the use of radar data is the availability of the data. The radar coverage varied from day-to-day and even from time to time, during any day. To deal with these variations, the first step was to identify which radars were operational between 1100 and 1800 UTC on each of the case days. A problem arises when comparing radar data from the SAWS network with MSG data. For the older (2011, 2012 and 2013) case days, the interval of radar mosaic data was 5-minutes, while the interval of the 2015 cases was 6-minutes. The availability of RDT data – derived from MSG – is 15-minutes. For the cases prior to 2014, the maximum radar reflectivity in the 10 minutes before and after the RDT timestamp was used for the evaluation. For the March 2015 cases, the 6-minute interval radar data does not correspond so well with the RDT time stamps. MSG data is available at 00 (on the hour), 15, 30 and 45 minutes after the hour (red numbers on Fig. 2). The 6-minute radar data is available at 00 (on the hour), 6, 12, 18, 24, 30, 36, 42, 48 and 54 minutes past the hour (blue numbers on Fig. 2). As a result, the RDT times of 15 and 45 minutes past the hour do not match up with radar times. To solve this dilemma different time intervals had to be used. When the RDT timestamp was 00 (on the hour) or 30 minutes past the hour, the radar data for the 6 minutes following the RDT time were used (blue zone on Fig. 2). When the RDT timestamp was 15 and 45 minutes past the hour, the radar data for the 6 minutes surrounding the RDT time (3 minutes before and after RDT) were used (red zone on Fig 2). If an extra radar timestamp were added it would have meant that the RDT times of 00 and 30 minutes past the hours would have used radar data for a 12-minute period (2 radar timestamps). The RDT times of 15 and 45 minutes past the hour would have used radar data for an 18-minute period (3 radar time steps). In 17 out of the 25 cases this approach was used where only one radar time-step was considered compared to the 8 older cases where the maximum reflectivity of four radar time steps were considered.

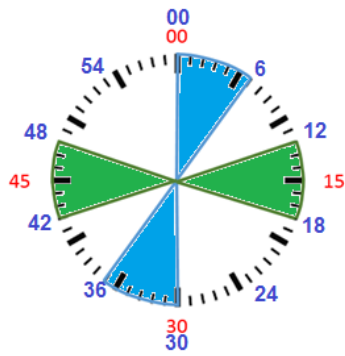


Figure 2. Graphical representation of the radar periods (blue numbers) considered in relation to the RDT times (red numbers) for the March 2015 cases. The blue zones shows the radar period considered for 00 and 30 minutes past the hour while the green zones show the periods for 15 and 30 minutes past the hour.

A reflectivity value of 30 dBZ in radar data is usually seen as a threshold to start tracking thunderstorms and indicates light rain or drizzle. 40 dBZ indicates moderate rain and 50 dBZ heavy rain. At reflectivity values above 50 dBZ, hail is likely. (NCAR, 2016). Using an object approach, cell-tracking algorithms define an object as an area where the reflectivity exceeds a specified threshold such as 35, 40 or 45 dBZ (Dixon and Weiner, 1993). In order to consider all the phases of the storms in the evaluation of the RDT product, radar reflectivity ≥ 35 dBZ were used, to exclude less significant storms and align with the RDT principle of rapidly developing and/or intense parts of thunderstorms.

The RDT algorithm is a methodology to identify and track thunderstorms by means of polygons for different phases of convective storms. These phases are the initial triggering of the storm, the growing of the storm and the maturing of the storm. To validate these objects against radar reflectivity requires an object-orientated methodology (NWC SAF, 2013b). An overview of the research done on spatial validation methodology is provided by Ebert (2008) and statistical modules are available in “R” software (R development core team, 2015). Based on objects or features, new definitions for hits, misses and false alarms can be calculated according to the identified objects. This package was used to do an object-orientated validation of the RDT polygons against the radar reflectivity polygons.

Results and Discussion

Twenty-five cases were considered during the southern hemisphere spring and summer seasons. As an example of the value of including lightning data, results for 21 March 2015 are shown in Figs. 3 (a-c). More storms were identified when lightning data were included in the input and some of the phases of the storms were different. An intense storm (>50 dBZ) over the central parts of the country, as indicated by the arrow, was absent when light data was not included but was identified when lightning data was included.

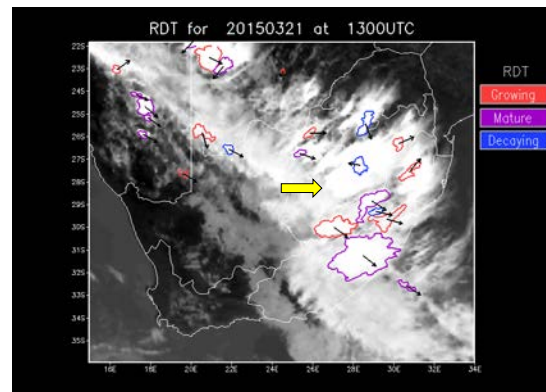


Figure 3. a) RDT without lightning data included for 21 March 2015 at 13:00 UTC.

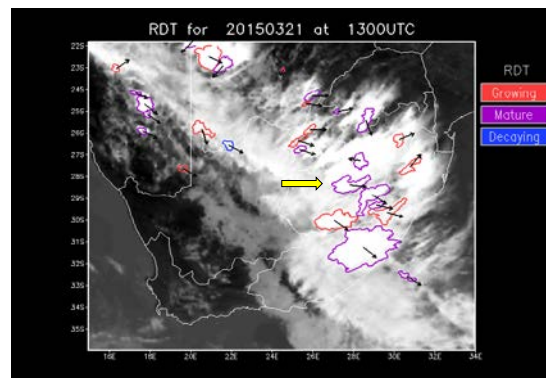


Figure 3. b) RDT with lightning data included for 21 March 2015 at 13:00 UTC.

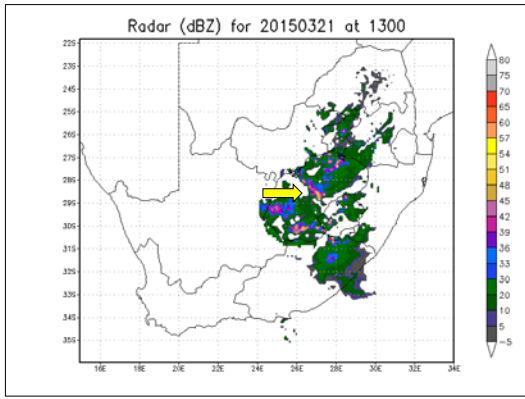


Figure 3. c) Radar reflectivity's for 21 March 2015 at 13:00 UTC

A few statistical scores were calculated for all time steps on this day for when no lightning data was included and when lightning data was included. The POD improved by 5% (from 0.76 to 0.81), the FAR increased slightly (from 0.062 to 0.067) and the HSS improved by 2% (from 0.83 to 0.85) when lightning data was added.

Fig. 4 (cases prior to 2014) and Fig. 5 (cases for March 2015) shows the average HSS, POD and FAR for different times of the day. The HSS and POD scores show that the inclusion of lightning data as input improves the RDT product for all times of the day in Fig. 4 and almost all of the times in Fig. 5. The FAR remained similar with the addition of lightning data.

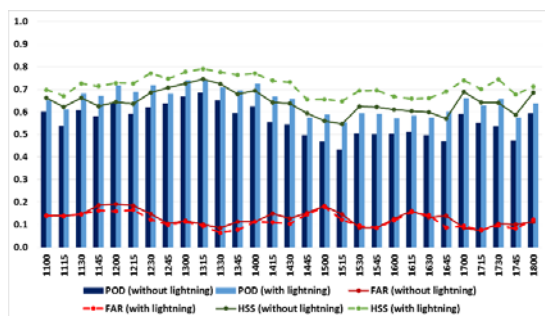


Figure 4. The POD, FAR and HSS for cases prior to 2014. Darker colours and solid lines depict the RDT without lightning data added, while the lighter colours and dashed lines show the RDT with lightning data added.

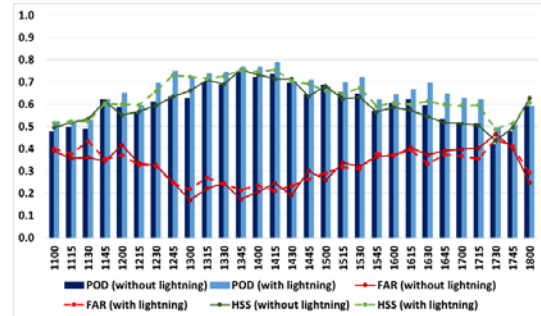


Figure 5. Same as for Fig. 4 but for March 2015 cases.

In the majority of the cases, the inclusion of lightning data was beneficial to the RDT product. On average, for these twenty-five cases, the POD improved by 6.6%, the HSS by 4.6% and the FAR by 0.1%. Differences could be seen when images for individual times were compared: in many cases, the inclusion of lightning data in the input data set led to the identification of convective storms that were missed based on MSG data alone. The inclusion of lightning data also resulted in some of the storm phases being adjusted based on the amount of lightning activity.

Conclusions

Radar systems are the ideal tools for identification and tracking of convective storms. In many countries, however, these powerful tools are not available. The NWC SAF developed various satellite-based tools, which can address some of the nowcasting needs. The RDT is used for thunderstorm identification and tracking. The aim of this work was to test the effect of including lightning data as auxiliary dataset into the RDT product and to verify this against radar reflectivity over South Africa. The results of twenty-five case studies over the South African domain showed that the inclusion of lightning data had a positive effect on the RDT product. However, even without the inclusion of lightning data the RDT product shows promise to provide information on possible severe or intense convective storms in regions that are not covered by radar systems.

Acknowledgements

The authors would like to thank the Water Research Commission for funding this project and the South

African Weather Service for the data.

<http://www.nwcsaf.org/HD/MainNS.jsp>.

References

De Coning, E., Koenig, M. and Olivier, J. (2011). The combined instability index: a new very-short range convection forecasting technique for southern Africa. *Meteorol. Appl.* 18: 421–439.

De Coning, E., Gijben, M., Maseko, B. and van Hemert, L. (2015). Using satellite data to identify and track intense thunderstorms in south and southern Africa. *South African Journal of Science*, <http://dx.doi.org/10.17159/sajs.2015/20140402>.

Dixon, M. and Wiener, G. (1993) TITAN: Thunderstorm Identification, Tracking, Analysis, and Nowcasting—A Radar-based Methodology. *J. Atmos. Oceanic Technol.* 10, 785–797

Ebert, E.E. (2008) Fuzzy verification of high resolution gridded forecasts: A review and proposed framework. *Meteorol. Appl.*,15, 51–64.

NCAR (2016) TITAN - Thunderstorm Identification Tracking Analysis and Nowcasting. [online]. Available at: http://www.rap.ucar.edu/projects/titan/home/storm_identification.php

NWC SAF (2016) Rapidly Developing Thunderstorm (PGE11 v3.0) v2013. Available at: <http://www.nwcsaf.org/HD/MainNS.jsp>

NWC SAF Documentation (2013a) Interface control document for the external and internal interfaces of the SAF NWC/MSG. SAF/NWC/CDOP2/INM/SW/ICD/1. Issue 7, Rev. 0. 15 July 2013. Applicable to SAFNWC/MSG version 2013. Available at: <http://www.nwcsaf.org/HD/MainNS.jsp>.

NWC SAF Documentation (2013b) Validation report for “Rapid Development Thunderstorms” (RDT-PGE11 v3.0) SAF/NWC/CDOP/MFT/SCI/VR/11, Issue 3, Rev. 4, 15 July 2013 Applicable to SAFNWC/MSG version 2013. Available at:

R development core team (2015) R: A language and environment for statistical computing. ISBN 3-900051-07-0. Vienna, Austria: R Foundation for Statistical Computing.

Evaluating WRF's dBZ diagnostic feature on the 28 November 2013 hailstorm over the South-African Highveld

Henno Havenga^{1*}, Roelof P. Burger¹, Stuart J. Piketh¹ & Cindy Bruyere²

¹NWU-Potchefstroom, Potchefstroom North-West. School for Environmental Science, Climatology Research Group
22743529@nwu.ac.za, roelof.burger@nwu.ac.za, stuart.piketh@nwu.ac.za

²University Centre For Atmospheric Research (UCAR), Boulder, CO. Mesoscale and Microscale Meteorology Laboratory (MMM) bruyerec@ucar.edu

Abstract

The Weather research and Forecasting model (WRF) is used to simulate a severe storm that occurred in 2013 over the Highveld region, a particular storm on 28 November resulted in over ZAR1,6 billion insurance loss, the most expensive catastrophe in South-Africa to date. A WRF domain of 4km and a nested domain of 1.3km is set-up over the Highveld. ERA-Interim (0.75°x0.75°) is used to initialize the model. WRF radar reflectivity diagnostic (dBZ) was used as the main evaluation tool of WRF's ability to simulate the occurrence the severe storm. The model was successful in simulating the spatial and temporal presence of high dBZ value for the case study. WRF also simulated to larger scale formation of the storm reasonably well when compared with satellite imagery.

Keywords: Numerical Weather Prediction, dBZ, Hailstorms, Highveld

Introduction

Severe hailstorms are one of nature's most devastating phenomena's. Over the South-African Highveld these storms are a dreaded occurrence. In 2013 several hailstorms in the region of Johannesburg, Pretoria caused devastation on an unprecedented economical scale. The 28 November hailstorm resulted in an estimated damage of over R1.6 billion, the storm was described as "*one of the most catastrophic events experienced in South Africa to date*" (Barry, 2014). Parts of the Tshwane Metro Area had been declared a disaster area with more than R100 million allocated to support families in the affected area (Eliseev, 2013)

The Weather Research and Forecasting Model (WRF) has yet to be implemented on a high resolution over South-Africa, this offers an opportunity to evaluate the model on spatially and temporally rare hail events. In this study WRF is used to simulate dBZ, a common observation method to identify hail. Other similar studies have been conducted before with reasonable success (Rezacova, and Sokol, 2003; Done, *et al.*, 2004; Vel'tishchev and Zhupanov, 2012).

Values of > 50 dBZ has been identified as a measure for the potential hail development (Mader, *et al.*, 1968; Visser, and van Heerden, 2000; Hohl, *et al.*, 2002).

The paper will only evaluate WRF and not the synoptic and observational aspects of the storms. Although the observations form a critical part of the evaluations, it will only be briefly mentioned. Radar data from the Irene weather radar is used as a comparison to simulations.

Background

Hailstorms over the South-African Highveld are a

frequent occurrence during the summer months from October to December. These events usually characterised by a trough or low pressure system over the interior of the country and the conditions are not much different than days with normal thunderstorm activity. Line storms along squall lines can also cause severe hail damage (Carte and Held, 1978; Olivier, 1990).

WRF is a next generation mesoscale numerical weather prediction (NWP) model, it was developed by the National Centre for Atmospheric Research (NCAR) and the University Cooperation for Atmospheric research (UCAR). It is a community model available for anyone to download (Skamarock, *et al.*, 2008).

WRF has been successfully used in high resolution simulations of severe thunderstorms and floods (Schwartz, 2014; Kumar, *et al.*, 2010) hurricanes (Khain, *et al.*, 2016) hail events (Chevuturi, *et al.*, 2016; García-Ortega, *et al.*, 2007), tornadoes (Matsangouras, *et al.*, 2016) and other convective weather events (Trapp, *et al.*, 2011; Litta, *et al.*, 2012).

Methodology

Access to WRF and the Research Data Archive (RDA) was provided by NCAR through the Yellowstone Supercomputer. WRF and WPS (WRF pre-processing system) Version 3.8 was used in this study together with ERA-Interim Data from the RDA to initialize the model.

WRF was set-up with two domains, one parent domain with a horizontal grid-spacing of 4km and a nested domain with a horizontal grid-spacing of 1.3km, see Fig 1. Both parent domain and the nested domain's center point was Johannesburg (28.047 E, 26.204 S), the nested domain covered the major area

affected. The model was initialized at 12:00 the day before the storm-day and ran for a total of 48 hours (eg 12:00, 27 November – 12:00, 29 November). Visualizations are only shown for time steps correlating with radar data observed from the Irene Radar.

The model setup is indicated in Table 1. A two-way nest was used, allowing the nested domain to provide feedback to the parent domain and the cumulus parametrization was turned off to permit convection in the nested domain.

Computational power provided by Yellowstone made this study possible, WRF was run on NCAR's 1.5-petaflops high-performance IBM iDataPlex cluster, which features 72,576 Intel Sandy Bridge processors and 144.6 TB of memory (CISL. 2012). The simulations were carried out with the main purpose to evaluate WRF's radar diagnostic feature although other diagnostics exist, this will form the basis of the study.

Table 2: WRF Setup

High-Resolution WRFV3.8 Case studies Setup	
Grid Spacing	4km, 1.3km
Data	ERA-Interim
Geographical data	USGS (WRF Default)
Map Projection	Mercator
Centre Point	28.04 S, -26.20 E (JHB)
Run Time	48h
Time Step	20s
Radar Reflectivity Diagnostics	On
Microphysics Scheme	New Thomsom, <i>et al</i>
Long Wave Radiation	RRTMG Scheme
Short Wave Radiation	Dudhia Scheme
Land Surface Model	Noah Land Surface Model
Planetary Boundary layer	Yonsei University scheme
Cumulus Parametrization	4km – Kain Fritsch Scheme, 1.3km – None

WRF High-Resolution Hail Case Study Domains

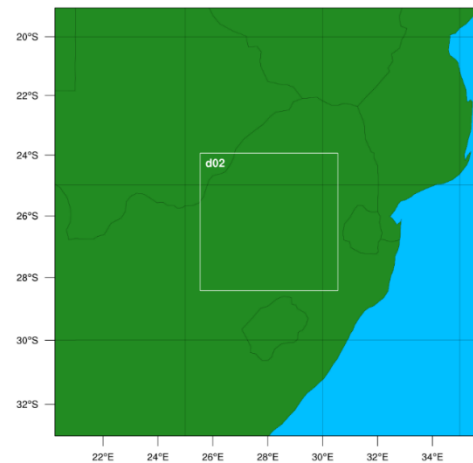


Figure 6: WRF Domains

Results

The WRF radar diagnostics was the main indicator used to evaluate the potential for hailstorm to occur, dBZ values of >50 dBZ in clouds have shown a high potential for hailstones to fall to the surface level. It is also a widely used indicator by weather services and news agencies across the world to communicate daily weather to the public.

Figure 2 shows the results of the WRF simulations over South Africa in both the inner and outer WRF domain, times shown are from 15:00 local time to 20:00 local time.

Figure 3 shows the observed reflectivity from the Irene weather from 15:00 to 19:00. When examining the output files WRF simulated a maximum of 71dBZ during the storm, the observed reflectivity from the SAWS Irene radar on the storm day was also above 70dBZ (Thema, 2013).

Figure 4 highlights the simulated reflectivity compared to the observed data from the Irene weather station. Areas of high reflectivity from the enlarged image of the nested WRF domain is well correlated with the observed radar reflectivity.

Satellite images taken from Meteosat-10 on 28 November that WRF simulated the storm formation on a larger scale with good accuracy, various features in the simulation correlates with the satellite imagery (Figure 5).

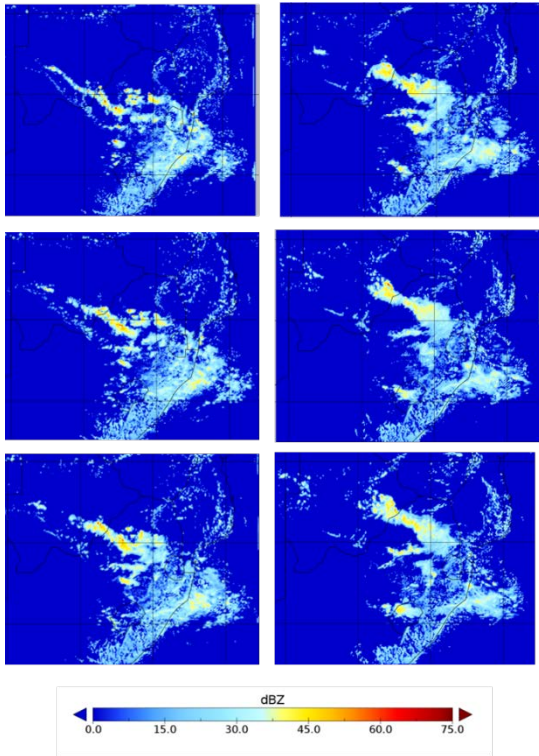


Figure 7: WRF Simulated dBZ of the 28 November 2013 Hailstorm. Column 1, left, top to bottom (15:00, 16:00, 17:00). Column 2, right, top to bottom (18:00, 19:00, 20:00).

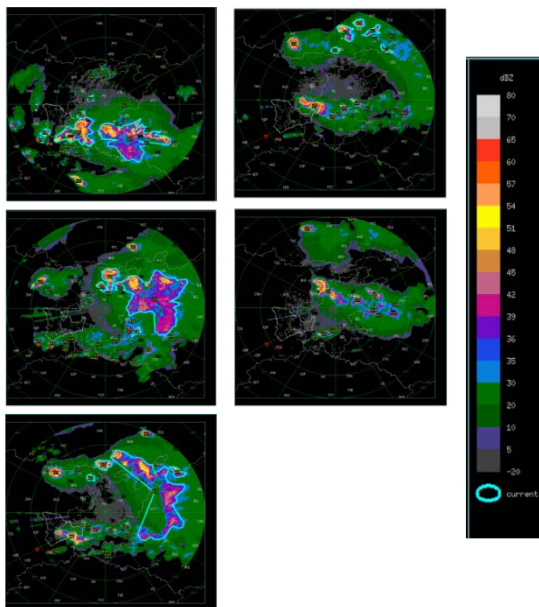


Figure 8: Observed dBZ from the Irene weather station on 28 November 2013. Column 1, left, top to bottom (15:00, 16:00, 17:00). Column 2, top to bottom (18:00, 19:00)

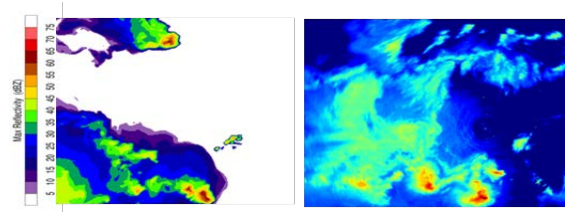


Figure 9: Enlarged WRF dBZ reflectivity (left) vs Observed Radar Reflectivity (right).

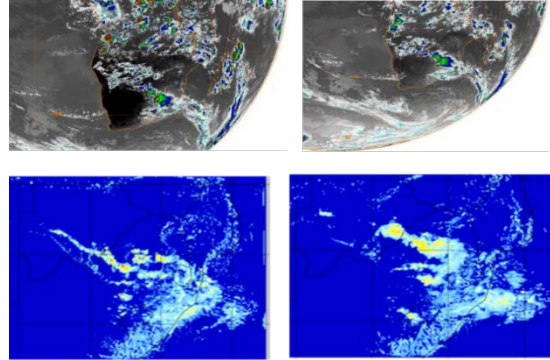


Figure 10: Top, Satellite Imagery from Meteosat-10 taken on 28 November 2013. Bottom, WRF simulations from 28 November 2013.

Conclusions

Hailstorms are difficult to predict with even the most sophisticated of models. WRF was effective in simulating potential hailstorms by using dBZ as an indicator, various other indices are examinable within the WRF model to further expand the capabilities of WRF.

The 28 November storm simulation showed correlation with that observed by the Irene Radar, WRF was able to simulate areas of high dBZ with reasonable accuracy. Maximum values of 71 dBZ was observed in the simulation correlating with the 70+ dBZ recorded at the Irene station.

WRF also simulated the larger formation of the storm well when comparing the simulation with satellite images taken on the storm day.

Examining the various parametrisation schemes also offer opportunity for further investigation into improving the model results.

WRF is a powerful NWP model and although the methods used in this study only scratched the surface in terms of WRF's capabilities it provided valuable results for future use of WRF in high resolution case studies.

References

Barry, H. (2014). Short-term insurers take a R1.6bn hammering. Moneyweb. <http://www.moneyweb.co.za/moneyweb-insurance/shortterm-insurers-take-a-r16bn-hammering>

Carte, A. E., & Held, G. (1978). Variability of

- hailstorms on the South African Plateau. *Journal of Applied Meteorology*, 17(3), 365-373
- Chevuturi, A., Dimri, A.P. and Gunturu, U.B., 2014. Numerical simulation of a rare winter hailstorm event over Delhi, India on 17 January 2013. *Nat Hazards Earth Syst Sci*, 14(12), pp.3331-3344.
- CISL. Computational and Information Systems Laboratory. 2012. Yellowstone: IBM iDataPlex System (Climate Simulation Laboratory). Boulder, CO: National Center for Atmospheric Research. <http://n2t.net/ark:/85065/d7wd3xhc>.
- Done, J., Davis, C.A. and Weisman, M., 2004. The next generation of NWP: Explicit forecasts of convection using the Weather Research and Forecasting (WRF) model. *Atmospheric Science Letters*, 5(6), pp.110-117.
- Eliseev, A. (2013). Parts of Tshwane declared 'disaster areas'. *Eye Witness News*. <http://ewn.co.za/2013/12/04/Parts-of-Tshwane-declared-disaster-areas>
- García-Ortega, E., Fita, L., Romero, R., López, L., Ramis, C. and Sánchez, J.L., 2007. Numerical simulation and sensitivity study of a severe hailstorm in northeast Spain. *Atmospheric Research*, 83(2), pp.225-241.
- Hohl, R., Schiesser, H.H. and Aller, D., 2002. Hailfall: the relationship between radar-derived hail kinetic energy and hail damage to buildings. *Atmospheric Research*, 63(3), pp.177-207.
- Khain, A., Lynn, B. and Shpund, J., 2016. High resolution WRF simulations of Hurricane Irene: Sensitivity to aerosols and choice of microphysical schemes. *Atmospheric Research*, 167, pp.129-145.
- Kumar, A.R., Dudhia, J. and Bhowmik, S.R., 2010. Evaluation of physics options of the weather research and forecasting (wrf) model to simulate high impact heavy rainfall events over indian monsoon region. *Geofizika*, 27(2), pp.101-126.
- Litta, A.J., Mohanty, U.C., Das, S. and Idicula, S.M., 2012. Numerical simulation of severe local storms over east India using WRF-NMM mesoscale model. *Atmospheric Research*, 116, pp.161-184.
- Mader, G.N., Neishlos, H., Saunders, M.M. and Carte, A.E., 1986. Some characteristics of storms on the Transvaal Highveld. *Journal of climatology*, 6(2), pp.173-182.
- Matsangouras, I.T., Nastos, P.T. and Pytharoulis, I., 2016. Study of the tornado event in Greece on March 25, 2009: Synoptic analysis and numerical modeling using modified topography. *Atmospheric Research*, 169, pp.566-583.
- National Centers for Environmental Prediction/National Weather Service/NOAA/U.S. Department of Commerce. 2000, updated daily. *NCEP FNL Operational Model Global Tropospheric Analyses, continuing from July 1999*. Research Data Archive at the National Center for Atmospheric Research, Computational and Information Systems Laboratory. <http://dx.doi.org/10.5065/D6M043C6>.
- Olivier, J. 1990. Some temporal aspects of hail in the Transvaal. PhD (Geography). University of Johannesburg. <https://ujdigispace.uj.ac.za/handle/10210/11151>
- Rezacova, D. and Sokol, Z., 2003. A diagnostic study of a summer convective precipitation event in the Czech Republic using a nonhydrostatic NWP model. *Atmospheric research*, 67, pp.559-572.
- Schwartz, C.S., 2014. Reproducing the September 2013 record-breaking rainfall over the Colorado front range with high-resolution WRF forecasts. *Weather and forecasting*, 29(2), pp.393-402.
- Secunda Weather Blog. Secunda – Hail Storm: 2013/10/28. <http://secundaweather.co.za/blog/?p=1678>
- Skamarock, W. C., J. B. Klemp, J. Dudhia, D. O. Gill, D. M. Barker, M. G Duda, X.-Y. Huang, W. Wang, and J. G. Powers, 2008: A Description of the Advanced Research WRF Version 3. NCAR Tech. Note NCAR/TN-475+STR, 113 pp. doi:10.5065/D68S4MVH
- Thema, E. 2013. Severe thunderstorms with golf ball size hail and flash floods hit Gauteng province of South Africa in late November. EUMETSAT. http://www.eumetsat.int/website/home/Images/ImageLibrary/DAT_2716642.html
- Trapp, R.J., Robinson, E.D., Baldwin, M.E., Diffenbaugh, N.S. and Schwedler, B.R., 2011. Regional climate of hazardous convective weather through high-resolution dynamical downscaling. *Climate dynamics*, 37(3-4), pp.677-688.
- Vel'tishchev, N.F. and Zhupanov, V.D., 2012. Experiments on the radar reflectivity data assimilation in the WRF-ARW model. *Russian*

Meteorology and Hydrology, 37(3), pp.149-158.

Visser, P.J. and van Heerden, J., 2000. Comparisons of hail kinetic energy derived from radar reflectivity with crop damage reports over the eastern Free State. *WATER SA-PRETORIA*, 26(1), pp.91-96.

Acknowledgements

Special thanks to UCAR and NCAR for access to Yellowstone Supercomputer and their Research Data Archive (<ark:/85065/d7wd3xhc>). Also special thanks Roelof, for always welcoming me into his office, and the countless hours we spend figuring out problems and finding new ones, Cindy Bruyere for the Skype sessions and help from the other side of world and finally Prof. Piketh, this project wouldn't have been possible by the funding provided by the NWU Climate Research Group under his leadership.

The evolving landscape of Climate Information Websites

Bruce Hewitson (Climate System Analysis Group (CSAG)), Katinka Lund Waagsaether (CSAG),² Jan Wohland (Potsdam Institute for Climate Impact Research/CSAG), Kate Kloppers (CSAG) and Teizeen Kara (CSAG)

Abstract

Climate Information Websites (CIWs), online platforms providing a variety of climate data and information, have seen a rapid and organic growth, yet with variable content and quality, while unfettered by any code of practice. This builds an ethical-epistemic dilemma (value choices predicated on understanding how we know something) that warrants assessment, since the presence of CIWs contribute to real-world consequences and commitment. We consider the context of CIW growth, and review a representative sample of CIWs to draw out key issues for consideration in CIW development. The net conclusion is that few CIWs approach the standards of robust information, many present substantial hurdles to the user, and in some cases there are clear examples of indefensible and inappropriate practices.

Key words: Climate change, Next-users, Climate services, Climate portals and Value judgements

Introduction

The availability of Climate Information Websites (CIWs) has expanded rapidly as global awareness of systemic climate risks is mainstreamed into decision and policy-making. The 2015 agreement of COP21 was a milestone in this regard, and established challenging yet necessary targets (Schellnhuber et al. 2016), which is being matched by an accelerating demand for scale-relevant climate information.

The ways in which CIWs have tackled the task differ widely, and value judgements are made by a community of scientists and boundary organizations (Hoppe et al. 2013) on what and how to deliver to user communities. CIWs provide everything from the simple delivery of maps and numbers based on different generations of Global Climate Models (GCMs), through to an eclectic mix of spatial disaggregation methods and downscaling techniques. The concept of “uncertainty” is critical in this context, and where addressed it often conflates multiple sources of error and bias with a time-evolving and irreducible component of natural variability (Fischer et al. 2013; Hawkins et al. 2016). Uncertainty, as presented in most CIWs, typically receives a mixed treatment, and may draw on a number of approaches that include simply assessing the spread of data (Brown & Wilby 2012; Calel et al. 2015; Clark et al. 2016), else attempt to constrain these to a likelihood outcome (Collins et al. 2012; Katz et al. 2013).

Likewise, on the side of the next-user value judgements on adaptation are made by non-scientists holding presumptions about the robustness of climate information. This raises a critical ethical-epistemic dilemma (Tuana 2013); the combined result of value judgements creates a heightened potential that adaptation measures may be poorly aligned with actual defensible information, with the possibility that they may contribute to maladaptation and increased rather than decreased risk, under a future climate. This potential for negative outcomes places a notable ethical responsibility on CIWs to consider the consequences of their presence and of their formulation of information in the context of society’s accelerating agenda for climate change action.

Because of the potential real-world consequences, there is a strong need to establish principles of practice and principles of product. There is an emerging discussion on this particular topic (Adams et al. 2015; Lacey et al. 2015), but given the absence of any governing authority or enforceable code of conduct for CIWs, the responsible provision of online disseminated information will necessarily remain subject to self-recognition of the issues by the CIW community.

The activities of online resources is nominally encompassed by the broader term “climate services” which remains an evolving concept (Brasseur &

² katinka@csag.uct.ac.za

Gallardo 2016). Historically the development of climate services has been dominated by a developed country perspective due to resources and capacity, yet it is continually challenged by shifting epistemologies (Carr & Owusu-Daaku 2016) – approaches to knowledge and belief that are rooted in the diverse experiences of the decision community (Steynor et al. 2016).

Herein lays the challenge: how to assess the appropriateness of generic online services for an individualized application?

We assess characteristics of a representative sample of CIWs in the context of their applicability to the information needs for climate change adaptation. This is not an exhaustive treatment of the CIW landscape but surveys a selection of CIWs that represent a range of implementation designs, content and geographic coverage. A dual approach of metrics and narrative experience is used to provide a review of the dominant nature of current online offerings.

An approach to assessing the CIW landscape

There is no canonical solution for how climate change information should be disseminated. This complicates the design of any assessment framework for CIWs.

Here we take a combined approach with a typology of classifications based on metrics of CIW characteristics, and lessons learned from use-case narratives. This offers some measure of objectivity and a sense of the subjective ‘real-life’ experience of accessing CIWs by which the diverse landscape of CIWs can be better understood, and exposes key lessons and messages for the evolution of future CIWs.

A total of 42 CIWs are assessed; by intention the list was constructed around those CIWs that have good visibility and would likely be encountered in a user’s search for data and information on climate change, and are considered to provide a fair sampling of English-based CIWs at the time of the assessment (See Fig 1 for overview of the CIWs).

A typology approach

The applied typology of classifications is comprised of criteria aimed at addressing the overarching questions of who is providing the service, who are the target users, what is the content being delivered, and how is the content communicated. These criteria evolved through a number of assessment trials. For criteria that are not simple yes/no answers or where the answer is simply a number, a static set of ‘option’ categories are established. The scope of these

categories needs to cover the entirety of possible answers and inevitably leaves a tension between being specific enough to say something of value, and general enough to apply across the diversity of CIWs. The classification of CIWs thus requires a delicate and necessarily subjective balancing between specificity and genericity. The adopted typology approach is the authors’ selection of criteria based on the experience of many hours working with the diversity of CIWs.

Two researchers accessed the 42 sites between September 2015 and May 2016. This was first undertaken independently, but given the often ambiguous nature of categorizing CIWs then did so again collectively to resolve any discrepancies. A third researcher, with a climate science and modelling background, undertook an additional assessment of the types of data included in CIWs.

A narrative approach

The next-user experience is, of course, paramount to the added value of a CIW, and complements the more objective typology which is not able to capture user experience. The narrative approach explores a limited set of websites through the lens of use-case scenarios. Four junior researchers, each with different disciplinary backgrounds and varying levels of experience, took on the role of different next-users. The four accessed the same set of CIWs and spent on average 1½ to 2 hours per CIW applying the use-case scenarios to five selected CIWs. The written narratives were then collated and summarised into a single narrative per CIW to represent the key aspects which emerged. One additional CIW, a commercial service, was only assessed by one researcher due to licensing issues.

The typology of websites

The geographic spread of the institutions hosting CIWs illustrates dominance by the economically developed world, with North America accounting for the largest share, followed by Europe, Australia and New Zealand.

The main providers of CIWs are governments, researchers and multi-national entities, with commercial and not-for-profit entities playing a smaller role. The limited role of commercial actors is further reflected in the accessibility of data and information, with 40 of the services assessed offering their data and information free of charge. A large portion of the services do not explicitly specify the next-user, a puzzling aspect if presuming that CIW content and presentation is linked to the provider’s perceptions of the target next-user(s).

The majority of the assessed CIWs (32) allow for access to raw data downloads (for example in ACSII

or NetCDF files) that are generally most appropriate to other researchers. However, approximately ¾ of the CIWs also contain, or solely focus on, visualized data in the form of maps, graphs or tables. Among them, more of the CIWs are designed to be interactive (19), i.e. next-users can navigate the data by making input choices (e.g. emission scenarios, GCMs), compared to those with static content (13) where next-users have to select from a pre-developed set of maps, graphs and tables.

Approximately a quarter of the CIWs focuses on historical climate information and do not include any model projections. Among the remaining services, 15 out of 32 with model data include an extensive set of GCMs (more than 15). In contrast, five climate services offer only a single GCM.

The number of CIWs offering SRES³ and/or RCP-based⁴ output indicates a focus on the more recent RCP-based results. 36% of the CIWs use both SRES and RCP scenarios, 19% only RCP, 19% only SRES, and the remainder only have historical data.

The breakdown between dynamical and statistical downscaling (pattern scaling and bias correction techniques are included under statistical methods) reflects a clear tendency for CIWs to favour either Regional Climate Models (RCMs) or statistical methods, but not both. This result reflects the fact that, unlike for GCMs, downscaling has as yet no comprehensive archive equivalent to CMIP⁵. For those CIWs explicitly providing individual downscaled data (24 in total), just over half (13) were judged to be transparent with respect to explaining how the modelling chain is constructed.

Narratives – the next-user experience

From a practical perspective the overall message is that all the CIW grossly over-estimate the ease of use, as illustrated by the experience summary from one of the narratives: *“Having located the non-apparent climate information section, one is overwhelmed by options, and without substantial reading time the extensive supportive material does not make for easy manoeuvring the jargon-laden landscape of options. Technical challenges and unfamiliar data file formats further alienate the user.”*

³ The Special Report on Emission Scenarios (SRES) details greenhouse gas emission scenarios developed in 2000, and form the basis on which the climate projections developed for the Intergovernmental Panel on Climate Change’s (IPCC) Second (2000) and Third (2007) Assessment Reports are based.

⁴ The Representative Concentration Pathways (RCPs) superseded the SRES scenarios, and are the greenhouse gas concentration

In terms of appropriateness, the issues are more subtle, and perhaps of significantly more concern in some cases. The issues revolve around the question of what may be inferred from the data, and what is left unsaid or unaddressed. Leading points of concern include: potential over-interpretation (*“Despite clear messages regarding data being non applicable at a local scale, the site tempts one to extract local scale messages with relative confidence simply because it is possible”*); major challenges for the user to subjectively constrain the options to something manageable (*“Repetitive text and endless mouse-clicking providing pathways to a multitude of pdf file maps, discouraging the narrator from considering multiple lines of evidence.”*)

Discussion & Conclusion

The overarching impression is that all CIWs present substantial hurdles that hinder next-users from completing a process of exploration through to a defensible conclusion.

Two core issues emerge. First, the dangers and implicit ethical questions from the use of CIWs, even when developed with the best of intentions. The provision of climate information without clearly communicated qualifiers, guidance, and explanations to enable reasonable checks and balances, is an ethical-epistemic problem which the CIW community needs to seriously consider. Second, the question of what this means for building capacity to use climate information as part of adaptation planning. Hewitson (Hewitson 2015) argues that developing skills is not enough, but that experiential learning that leverages foundational skills is required. This poses the key challenge of deciding how far CIW’s need to extend their support to meet the capacity of users, versus the degree to which users need to develop skills to use CIWs.

To consider which framing considerations will help to advance CIW developments (Adams et al. 2015), three areas can be identified:

a) *The ethics of information:* With no binding authority to mandate a code of conduct, how the CIWs evolve depends on community agreement and on user awareness of responsible practice.

trajectories adopted by the latest IPCC report, the Fifth Assessment Report (2014).

⁵ The Coupled Model Intercomparison Project (CMIP) was established in order to provide standard frameworks for systematically analysing GCMs.

b) *The interface to the information*: With current interfaces maximising options of choice and data sets with no structured approach to filtering – simplification is needed. Distillation, as well as the evolution of methods to identify problems in data and interface structure to guide next-users towards choices that credibly serves their needs, is key to achieve this.

c) *The defensibility of the information*. This is predicated on the CIW evolving the capacity to identify and understand the information limits of the data and to use this understanding to design their delivery and communication.

While the CIW landscape is prolific and makes a substantial contribution to closing the gap between science and the decision maker, there are deep issues embedded in current practices that raise concerns about real-world consequences.

References

Adams, P. et al., 2015. Call for an Ethical Framework for Climate Services. *Bulletin of the World Meteorological Society*, 64(2).

Brasseur, G.P. & Gallardo, L., 2016. Climate services: Lessons learned and future prospects. *Earth's Future*, 4(3), pp.79–89.

Brown, C. & Wilby, R.L., 2012. An alternate approach to assessing climate risks. *Eos, Transactions American Geophysical Union*, 93(41), pp.401–402.

Calel, R., Stainforth, D.A. & Dietz, S., 2015. Tall tales and fat tails: the science and economics of extreme warming. *Climatic Change*, 132(1), pp.127–141.

Carr, E.R. & Owusu-Daaku, K.N., 2016. The shifting epistemologies of vulnerability in climate services for development: the case of Mali's agrometeorological advisory programme. *Area*, 48(1), pp.7–17.

Clark, M.P. et al., 2016. Characterizing Uncertainty of the Hydrologic Impacts of Climate Change. *Current Climate Change Reports*, 2(2), pp.55–64.
Collins, M. et al., 2012. Quantifying future climate change. *Nature Climate Change*, 2(6), pp.403–409.

Fischer, E.M., Beyerle, U. & Knutti, R., 2013. Robust spatially aggregated projections of climate extremes. *Nature Climate Change*, 3(12), pp.1033–1038.

Hawkins, E. et al., 2016. Irreducible uncertainty in near-term climate projections. *Climate Dynamics*,

46(11-12), pp.3807–3819.

Hewitson, B., 2015. To build capacity, build confidence. *Nature Geoscience*, 8(7), pp.497–499.

Hoppe, R., Wesselink, A. & Cairns, R., 2013. Lost in the problem: the role of boundary organisations in the governance of climate change. *Wiley Interdisciplinary Reviews: Climate Change*, 4(4), pp.283–300.

Katz, R.W. et al., 2013. Uncertainty analysis in climate change assessments. *Nature Climate Change*, 3(9), pp.769–771.

Lacey, J. et al., 2015. Informed adaptation: Ethical considerations for adaptation researchers and decision-makers. *Global Environmental Change*, 32, pp.200–210.

Schellnhuber, H.J., Rahmstorf, S. & Winkelmann, R., 2016. Why the right climate target was agreed in Paris. *Nature Climate Change*, 6(7), pp.649–653.

Steynor, A. et al., 2016. Co-exploratory climate risk workshops: Experiences from urban Africa. *Climate Risk Management*.

Tuana, N., 2013. Embedding philosophers in the practices of science: bringing humanities to the sciences. *Synthese*, 190(11), pp.1955–1973.

Climate Information Website	Link
Arctic Climate Research at the University of Illinois	http://arctic.atmos.uiuc.edu/
aWhere	http://www.awhere.com/
Canada Centre for Climate Modelling and Analysis	http://www.ec.gc.ca/ccmac-cccma/
CCAFS Downscaled GCM Data Portal*	http://ccafs.cgiar.org/
Centre for Climate Change Research (CCCR)	http://cccr.tropmet.res.in/
Climate Change in Australia	http://www.climatechangeinaustralia.gov.au/
Climate Change Knowledge Portal *	http://sdwebx.worldbank.org/
Climate CHIP	http://www.climatechip.org/
Climate Data Online	http://reg.bom.gov.au/climate/data/
Climate Information Portal (CIP)	http://cip.csag.uct.ac.za/
Climate Wizard	http://www.climatewizard.org/
Climatic Research Unit	http://www.cru.uea.ac.uk/
CliMond	https://www.climond.org/
CLIMsystems*	http://www.climsystems.com/
CORDEX East Asia	https://cordex-ea.climate.go.kr/
Downscaled CMIP3 and CMIP5 Climate & Hydrological Projections archive	http://gdo-dcp.ucllnl.org/
Earth System Grid Federation	http://esgf.llnl.gov/
EDENext Data Portal	http://www.edenextdata.com

European Climate Assessment & Dataset (ECA&D)	http://www.ecad.eu/
European Space Agency Climate Change Initiative (esa cci) open data portal	http://cci.esa.int/
Giovanni	http://giovanni.sci.gsfc.nasa.gov/
IPCC Data Distribution Centre (DDC)	http://www.ipcc-data.org/
IRI/LDEO Climate Data Library	http://iridl.ldeo.columbia.edu/
IS-ENES Climate4impact portal	https://climate4impact.eu/impactportal/
KlimafolgenOnline	http://www.klimafolgenonline.com/
KMNI Data Centre	https://data.knmi.nl/
KNMI Climate Explorer	http://climexp.knmi.nl/
Med CORDEX	https://www.medcordex.eu/
NCAR's GIS Program Climate Change Scenarios GIS data portal	https://gisclimatechange.ucar.edu/
Nevada Climate Change Portal	http://sensor.nevada.edu/NCCP/
NOAA Climate.gov	https://www.climate.gov/
NOAA Geophysical fluid dynamics laboratory	http://www.gfdl.noaa.gov/
Ontario Climate Change Data Portal	http://www.ontarioccdp.ca/
Pacific Climate Futures	http://www.pacificclimatefutures.net/
Pacific Climate Impacts Consortium Data Portal	https://www.pacificclimate.org/
Regional Clearinghouse Database*	http://clearinghouse.caribbeanclimate.bz
South African Risk & Vulnerability Atlas*	http://sarva.dirisa.org/
Global and Regional Adaptation Support Platform (ci-grasp)*	http://pik-potsdam.de/cigrasp-2/
The Satellite Application Facility on Climate Monitoring (CM SAF)	http://www.cmsaf.eu/
USGS Geo Data Portal	http://cida.usgs.gov/gdp/
Wisconsin Initiative on Climate Change Impacts	http://www.wicci.wisc.edu/
WoodForTrees.org	http://woodfortrees.org/

Table 1: Overview of the 42 CIWs reviewed in the typology, with the six included in the narratives highlighted with an as

Comparative study of PCA and wavelet-PCA models for simulating monthly rainfall and temperature at Cape Point

Syamala Krishnannair^{6*}, Venkataraman. Sivakumar² and Raven Jimmy²

¹University of Zululand, Private Bag X1001, Kwadlangezwa, 3886, South Africa

²School of Chemistry and Physics, University of Kwazulu Natal, Private Bag X54001, Durban, South Africa

Abstract

31 years of long-term time series analysis of rainfall and temperature data are used for simulating or reconstructing temperature variations and the estimation of rainfall for a weather station at Cape Point. This paper aims at studying the relationship among climatic variables using multivariate techniques such as principal component analysis (PCA) and wavelet-PCA. In this study, we have tested the simulations by dividing the data into two parts, the first 21 years of data were used to train/simulate the model and the rest of 10 years for comparison purpose to test the performance of the simulation. Model performance was evaluated using Correlation Coefficient (R), Root mean square error (RMSE) and Accuracy and Prediction error (PE). The results show that the wavelet-PCA model is comparable with the PCA model which may be attributed to the regularity in the seasonal patterns.

Keywords: rainfall predictions, temperature variations, wavelet analysis, multivariate methods

Introduction

The study of climatological and meteorological variability of surface fields such as precipitation and temperature at a regional scale is one of the challenging tasks in the prediction of climatic behaviour. It has been found by the Intergovernmental Panel on Climate Change (IPCC) that the global temperatures have been increasing by a rate of 0.13 degrees Celsius per decade (IPCC, 2007). Recently, temperature variations due to climate change have become a major concern in Southern Africa (Kuhn, 2012). Variations in temperature have caused severe disruptions in agricultural activities, hydroelectric power generation and drinking water supplies in South Africa. Previous studies on temperature variations over South Africa, indicated that there is a maximum increase of 0.11°C per decade between 1960 and 1990 (Hughes and Balling, 1996). There was also a substantial increase in temperature over three weather stations in Limpopo in South Africa between 1960 and 2003 (Kruger and Shongwe, 2004). Food production in South Africa is particularly sensitive to climate change because crop yields are directly dependent on climate conditions such as rainfall patterns and temperature. In South Africa, even a small amount of warming may lead to a large decline in the production of wine (Kuhn, 2012). Thus the time-series analysis of temperature and rainfall data are important for investigating temperature

variations, predicting temperature changes and the estimation of rainfall.

Over the past years, PCA models have been widely used in simulating geophysical as well as hydrological time series (Botai et al., 2010 and Petr, 2005). However, it assumes that data are stationary and has a limited ability to capture non-stationarities and non-linearities in hydro-climatic data. Recently, wavelet transformation has shown excellent performance in hydrological modelling as well as in multiple atmospheric and environmental applications by decomposing the time series into subcomponents. Decomposed data improves the performance of the prediction model by capturing useful information at various resolution levels (Nury et al., 2015). The present study proposes an alternative method for analysis of temperature and rainfall data recorded at Cape Point, where wavelet transform is used to decompose the non-stationary signal into several stationary signals. Then, PCA is applied to the decomposed signal to improve the accuracy in simulation. Model performance between PCA and wavelet-PCA is evaluated using correlation coefficient, prediction error, root mean square error and accuracy. A comparison between wavelet-PCA and PCA is done to find out the best-fitted model.

*krishnannairs@unizulu.ac.za, Tel:035-9026235, Fax:035-9026078

2. Data and Method

2.1 Data

The data was collected from South African Weather Service (SAWS) for the period from March 1980 to November 2011. The data comprises of minimum and maximum surface temperature and rainfall which was generally obtained from ground based Automatic Weather Stations (AWSs). The obtained daily data sets are averaged for each month in the time series and used for the present study.

2.2 Method

2.2.1. Principal component analysis (PCA)

PCA is a useful statistical technique that has been used in many applications for extracting features in data of high dimension to a reduced dimension by arranging the features in the PCA domain in the order of their variance. These uncorrelated features in the transformed domain are obtained by the linear combination of the original features and carries significant amount of information from the data (Fowdur et al., 2014).

2.2.2. Wavelet Analysis

Among several mathematical transformation techniques, wavelet analysis is the most popular method that can be used to analyze the non-stationary time series data. Wavelets are a set of basis functions, which is defined as

$$\varphi_{a,b}(t) = \frac{1}{\sqrt{a}} \varphi\left(\frac{t-b}{a}\right)$$

where φ is the mother wavelet function, a and b are the dilation and translation parameters, respectively. The basis function provides a mapping from the time domain to the time-frequency domain (Mallat, 1989).

2.3. Wavelet coupled with PCA (wavelet-PCA) model

The procedure for wavelet-PCA model is described as follows:

Step1: The wavelet transformation, which is a Daubechies -1 type and a decomposition level 3, is applied to the time series X_t ($t = 1, 2, \dots, T$) results in 4 series, which are denoted by $WT(X_t) = \{A3_t, D3_t, D2_t, D1_t; t = 1, 2, \dots, T\}$, where $A3_t$ is the coarse approximation and $D1_t$, $D2_t$, and $D3_t$ are the detailed information.

Step 2: The wavelet denoising method reconstruct the time series by removing the high frequency components by $WT^{-1}\{A3_t, D3_t, D2_t; t = 1, 2, \dots, T\} = X'_t; t = 1, 2, \dots, T$.

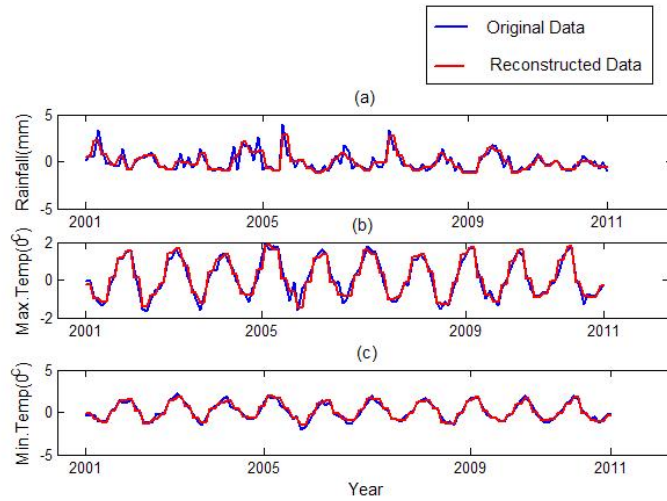
Step 3: The PCA model is applied to the reconstructed series to predict the test series.

$$\left\{ \begin{aligned} X'_t; t = 1, 2, \dots, T &\xrightarrow{PCA\ model} X_t^p; t \\ &= T + 1, \dots, T + n \end{aligned} \right\}$$

Model performance was estimated by measuring the prediction accuracy between the predicted and observed according to correlation coefficient (R), root mean square error (RMSE), prediction error (PE) and accuracy.

3. Results and Discussion

To simulate the monthly rainfall at the Cape-Point station, monthly average rainfall as well as maximum and minimum temperature data of 31 years from March 1980 to November 2011 were used. The first 21 years' data from March 1980 to March 2001 was used for calibration of the model, and the remaining 10 years' data from April 2001 to November 2011 were used for validation of the model. Fig.1 shows the obtained original and reconstructed monthly mean rainfall and the maximum and minimum temperature data by the wavelet-PCA method for Cape Point.



Figs. 1(a-b). Temporal evaluation of original and reconstructed rainfall (a), maximum temperature (b) and minimum temperature (c) for the period from 1980 to 2011 using wavelet-PCA for Cape Point.

The statistical properties of the calibration, validation and total data for monthly rainfall, maximum and minimum temperatures are shown in Table 1. The observed monthly maximum rainfall is 168 mm, while the mean rainfall was 29 mm. The

recorded monthly rainfall data shows low positive skewness (1.5) and indicates that data points are scattered closer to the mean value or have less scattered distribution. The minimum of the maximum temperature is 13.92°C, while the maximum of the maximum temperature is 17.45°C

Table 1: Statistics of rainfall, maximum and minimum temperatures

Variable	Data	Minimum	Maximum	Mean	Standard Deviation	Skewness
Rainfall (mm)	Total	0.00	168.60	29.33	26.37	1.52
	Calibration	0.00	168.60	29.36	26.53	1.51
	Validation	0.00	135.40	29.27	26.15	1.53
Maximum temperature (°C)	Total	13.92	23.93	19.17	2.48	0.02
	Calibration	13.92	23.93	19.08	2.53	-0.03
	Validation	15.04	23.78	19.35	2.48	0.12
Minimum temperature (°C)	Total	8.32	17.45	13.14	2.07	0.07
	Calibration	8.32	17.27	13.03	2.07	0.02
	Validation	8.75	17.45	13.34	2.09	0.15

Wavelet analysis decomposed the time series into four Details and Approximations sub-time series $\{D1_t, D2_t, D3_t, A3_t\}$. The data is reconstructed using the low frequency detail wavelet components $D2_t, D3_t$ and $A3_t$ using the inverse wavelet transform. Thus the outliers and noise are removed from the denoised signal while the trend remained the same as in the original data. The PCA model of reconstructed series is developed for comparing the prediction accuracy of the proposed

model over the PCA model. The performance of PCA and wavelet-PCA models estimated to forecast the rainfall is listed in Table2. The results show that for the denoised maximum and minimum temperature, the RMSE of both calibration and validation are lower than that of the PCA approach. The accuracy value for the denoised maximum and minimum temperature for both calibration and validation is higher than that of PCA approach. This indicates capability of wavelet-PCA approach.in

simulation. However, the model estimated the temperature to be 99 % in agreement with the actual measurements. The RMSE of the denoised rainfall of both validation and calibration models in PCA is higher than that of wavelet-PCA while all other

results remain the same for both models. From the overall performance wavelet-PCA is found to be capable for the simulation purposes in general while it was comparable with PCA model in the analysis of rainfall data.

Table 2: Statistical parameters of calibration and validation for the simulated/forecasted rainfall, maximum and minimum temperatures.

Model	Data	Calibration				Validation			
		RMSE	R	PE	Accuracy %	RMSE	R	PE	Accuracy %
Wavelet-PCA	Rainfall	0.15	0.99	0.13	99.84	0.13	0.99	0.16	99.86
	Max.Temperature	0.19	0.97	0.32	99.80	0.14	0.99	0.02	99.85
	Min.Temperature	0.18	0.98	0.01	99.81	0.13	0.99	0.18	99.86
PCA	Rainfall	0.03	0.99	0.06	99.97	0.02	0.99	-0.07	99.97
	Max.Temperature	0.22	0.98	-0.30	99.78	0.17	0.98	0.34	99.83
	Min.Temperature	0.20	0.98	-0.26	99.79	0.16	0.98	-0.11	99.84

4. Conclusion

We have used the rainfall, surface minimum and maximum temperature datasets collected from 1980 to 2011 (31 years) over a Cape Point AWS. Based on RMSE and accuracy, the wavelet-PCA model is found to be comparable in rainfall forecasting to the conventional models. The future plan is to extend the study for other South African Weather Service stations and different parameters (including ozone, rainfall and humidity). However, this will be highly dependent on the availability of valid data.

References

Botai, O. J., Sivakumar, V., Combrinck, C.L., and Rautenbach, C. J. D. (2010). Multi-Scale organization of water vapor over low and mid-tropical Africa. *Advances in Geosciences*. 16: 241-251.

Fowdur, S.C., Rughooputh, S.D.D.V., Cheneebash, J., Boojhawon, R., and Gopaul, A. (2014). Rainfall Analysis over Mauritius using PCA. *Environmental management and Sustainable Development*. 3:94-108.

Hughes, S. H., and Balling, R. C. (1996). Urban influences on South African temperature trends. *International Journal of Climatology*. 16: 935-940.

IPCC ,(2007): Climate Change 2007: Fourth Assessment Report of the Intergovernmental Panel on Climate Change Cambridge University Press, Cambridge.

Kruger, A. C., and Shongwe, S. (2004). Temperature trends in South Africa: 1960-2003. *South Africa. International Journal of climatology*.24: 1929-1945.

Kuhn, M. -L. (2012). VinIntell (????) March 2012- Social Media in the Wine Industry, Annual report, IBIS Business and Information, Stellenbosch: SAWIS

Mallat, S.G. (1989). A theory for Multiresolution Signal Decomposition: The Wavelet Representation. *IEEE Transaction on Pattern Analysis and Machine Intelligence*. 11: 674-693.

Nury, A.H., Hasan, K., and Alam, J.B. (2015). Comparative study of wavelet-ARIMA and wavelet-ANN models for temperature time series in northeastern Bangladesh. *Journal of King Saud University-Science*. Article in Press.

Praus,P. (2005). Water quality assessment using SVD-based principal component analysis of hydrological data. *Water SA*.31:417-422.

Evaluation of the Predictability of Rainfall over South Africa by Regional and Global Weather Prediction Models

Stephanie Landman^{1,4}, Christien J. Engelbrecht², Simon J. Mason³ and Geoffrey G.S. Pegram⁴

¹South African Weather Service, Pretoria, 0001, South Africa

²Agricultural Research Council-Institute for Soil, Climate and Water, Pretoria, 0001, South Africa

³International Research Institute for Climate and Society, Palisades, New York, United States of America

⁴University of KwaZulu-Natal, Durban, 4041, South Africa

Abstract

Five different numerical model forecasts were used to predict daily rainfall totals, with lead times of day 1 and day 2 for the period of January 2011 to March 2015. ERA-Interim daily 12 UTC 850 hPa circulation and African Rainfall Climatology rainfall fields were used to cluster the days into 35 nodes, each assigned to one of 8 identified rain-bearing systems. This identification was done in order to determine the skill in rainfall forecasts per rain-bearing system. Results showed that for all rain-bearing systems and all lead-times the ensemble mean outperforms the individual model forecasts. It was also shown that the forecasts overall had more skill in predicting daily rainfall totals associated with ridging highs and tropical temperate troughs.

Keywords: Rainfall Predictability, Rain-bearing systems, Numerical Weather Prediction, Ensemble Forecasts, SOM

Introduction

Rainfall forecasts are arguably the most notable parameter from weather forecasts since rainfall is a tangible and visible event. South Africa is considered a semi-arid country with most of the country's annual rainfall totals are below 500 mm/year (Taljaard, 1996). Across most of South Africa the rainfall occurs during the austral summer months (October to March) resulting from large synoptic scale rain-bearing systems like Tropical Temperate Troughs (TTT; Hart *et al.*, 2010) to smaller convective-scale heat-induced thunderstorms. The southern coast of South Africa is recognized as an all-year rainfall region (Engelbrecht *et al.*, 2014) and the south-western region receives the majority of its rainfall during the winter months due to passing mid-latitude low pressure systems.

A clustering system was used to group the daily atmospheric circulation into recognizable rain-bearing circulation patterns. Clustering of data has a tendency to expose groups within a dataset and each group will result in distinct classification of the clustering variable (Tambouratzis and Tambouratzis, 2008). The technique used to cluster the forecasts was the Self-Organising Maps (SOM; Kohonen, 2001) since it has been used extensively in atmospheric sciences (Tennant and Hewitson, 2002, Engelbrecht *et al.*, 2014, Lennard and Hegerl, 2015).

Furthermore, in this study, the rain-bearing systems identified by Taljaard (1996) and some summer systems identified by Harrison (1983) were used as guidance to determine the predictability of daily rainfall totals associated with these systems from different numerical weather prediction models. The forecast models used range from high resolution regional short-range weather models (12 km, t+48 hr forecasts) to global circulation medium-range weather models (~17 km, t+144 hr forecasts).

Data and Methodology

SOM was used to do a synoptic classification for the period of 1 January 2011 to 31 March 2015 based on daily 850hPa circulation and rainfall patterns. ERA-Interim data (ERA-Int; Dee *et al.*, 2011) were used to determine the daily 12 UTC circulation patterns at the 850 hPa pressure level together with the accompanying African Rainfall Climatology, based on satellite estimated and rainfall observed data (ARC2; Novella and Thiaw, 2013). The dual data set, after being normalized, was ingested into the SOM software to create a 5×7 node matrix. Each of the nodes in the matrix consists of a regular two-dimensional structure, based on the two variables being clustered. The 850 hPa heights were chosen to develop the SOM together with the ARC2 estimated daily rainfall totals as this low-level atmospheric circulation is influential in rainfall over the region. The SOM was then able to determine the

accompanying 850 hPa circulation patterns with associated daily rainfall totals. The 35 nodes were then clustered into 8 possible rain-bearing systems as identified by Taljaard (1996; Fig. 1).

Numerical weather models were then used to determine the skill in forecasting daily rainfall totals from each of the 8 identified rain-bearing systems. The regional weather prediction model used was the United Kingdom's (UK) Met Office's Unified Model (UM) configured in three different ways; two with different science versions and one with data assimilation. The UM covers the area of 0° to 45° S and 10° W to 56° E at a horizontal resolution of 12 km (Davies *et al*, 2005, Landman *et al*, 2012).

Also available from the Met Office is the UM Global Atmosphere (GA) with a horizontal resolution of ~ 17 km (Walters *et al*, 2014). The second global model forecast used was from the European Centre for Medium Range Weather Forecasting (ECMWF) with a resolution of 16 km (Wedi *et al*, 2015).

All the data sets were rescaled to the ARC2 resolution of 0.1° × 0.1° and the daily rainfall forecasts were accumulated to 24-hr totals to correspond with ARC2 estimated rainfall. The lead times under investigation in this paper are days 1 (24-hr) and 2 (48-hr). The original SOM covered the domain of -10° to -40° S and 0° to 54° E in order to capture the influences of both the tropical and mid-latitude systems. However, for the rainfall verification the domain only covered South Africa; -22° to -35° S and 16° to 34° E.

Verification of the model forecasts was done by calculating the daily bias (Eq. 1) and the Brier skill score (BSS) for rainfall greater than 1 mm/day (Eq. 2) per grid point (Wilks, 2011). The area average for the South African domain of both the bias and BSS is calculated to summarise the results and for ease of interpretation.

$$Bias = \frac{1}{n} \sum_{i=1}^n (f_i - o_i) \quad \text{Eq. 1}$$

$$BSS = 1 - \frac{\frac{1}{n} \sum_{i=1}^n (f_i - o_i)^2}{\frac{1}{n} \sum_{i=1}^n (o_{i-1} - o_i)^2} \quad \text{Eq. 2}$$

In Eqs. (1) and (2) the f_i term is referring to the forecast value, the o_i to the corresponding observation and in Eq. (2) the o_{i-1} is the persistence used as reference forecast for calculating the skill score.

Each of the 5 model forecasts were evaluated individually, but for summary only the ensemble mean spatial maps will be shown. The multi-model ensemble (MME) mean was calculated by only taking the average of the 5 individual daily rainfall forecasts, as indicated in Eq. (3):

$$MME = \frac{(EC+GA+NT+NA+NG)}{5} \quad \text{Eq. 3}$$

Results and Discussion

The dual parameter 5 × 7 SOM matrix is shown in Fig. 1 indicating the 8 identified clusters of the different dominant weather systems covering both summer and winter rainfall events. Notably, the continental high (CH) is not identified as a rain bearing system by Taljaard (1996), but for numerical forecasting it is important to determine if the weather models are able to capture the circulation and the accompanying limited rainfall. In Fig.2 the seasonal distribution of the contribution of each day to each node is shown.

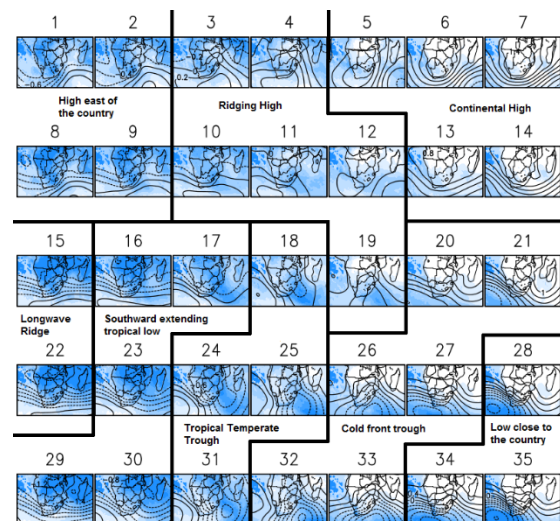


Figure 11: The 35 matrix SOM and rain-bearing systems. Shaded blue background indicate the ARC2 normalised rainfall anomalies and black contours the corresponding 850 hPa circulation anomalies.

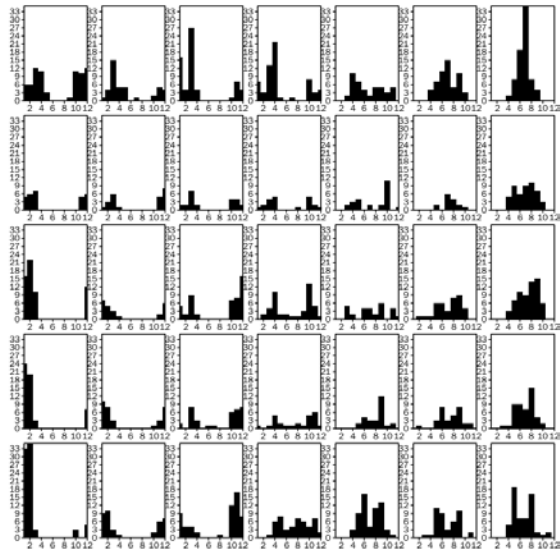


Figure 2: The accompanying 35 nodes indicating the seasonal distribution of the cases within each node (x-axis is the 12 months and y-axis indicates number of cases per month per node)

The corresponding daily average MME mean rainfall forecast (mm/day) is mapped to each node (as identified in Fig. 1) in Fig.3 where it is shown that the greatest spatial scale of rainfall forecasts occur in nodes associated with summer rain-bearing system; ridging highs (RH), TTT's and tropical lows (SETL).

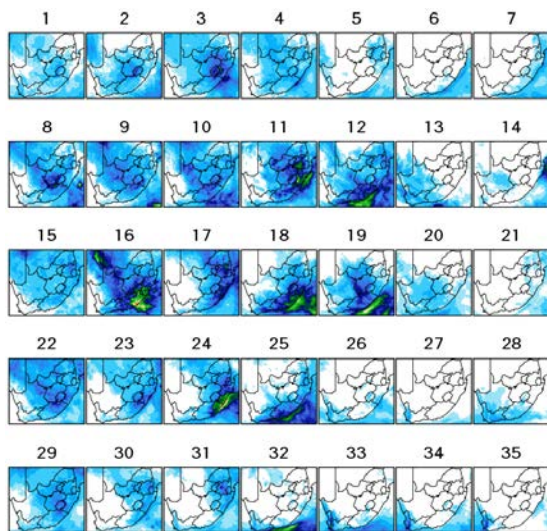


Figure 3: Daily average MME mean rainfall forecasts mapped to nodes in Fig.1 (scale is 0 to 15 mm/day)

In Fig. 4 the MME mean bias (Eq. 1) mapped per node from Fig.1 matrix is shown. The highest positive bias is seen in nodes 15 and 22 (longwave ridge; LR) and the lowest overall bias with the continental high (CH) nodes and some of the nodes associated with cold-fronts (CF; 21 and 27). The highest negative bias is mostly in nodes 18, 19 and

25. Mostly it is seen that the bias of the MME mean is ~ 2 mm per day. Details of the individual ensemble members and system average bias for day 1 lead time is shown in Fig. 5.

The solid black line in Fig. 5 is the MME mean area average bias and the red bar indicates the average bias per circulation pattern. It is seen that UM global forecasts (GA) has the largest and mostly negative bias for all nodes, whereas the UM regional forecasts (NA and NT) have almost similar, but positive biases. The UM data assimilation (NG) and ECMWF (EC) have the smallest area averaged biases. Looking at the average bias per circulation pattern it is also seen that the LR and southward extending tropical low (SETL) nodes have the highest biases and nodes associated with the high east of the country (RE) the lowest. Similar results were found with the day 2 lead time.

Similar to the bias in Fig. 4, the BSS is also spatially calculated and presented in Fig. 6. When comparing the spatial maps in Fig. 6 with the MME area average graph in Fig. 7 it is seen that the nodes clustered for RH have the highest overall skill for both day 1 and day 2 lead times. For nodes 1, 2, 8 and 9 (associated RE) the spatial BSS maps indicate the greatest variability of skill over the domain compared to the other nodes. However, if the focus is for example only to the north-eastern parts of the country the forecasts do seem to be mostly skilful for the nodes associated with summer rainfall (i.e. excluding CH and CF).

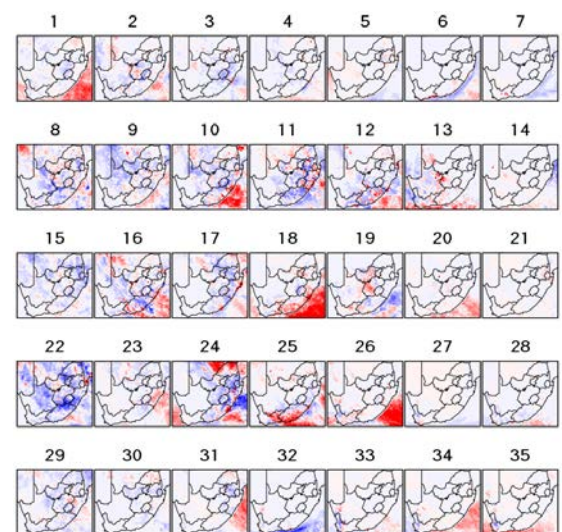


Figure 4: Daily average bias of the ensemble mean forecasts (scale is -10, red to 10, blue) for day 1.

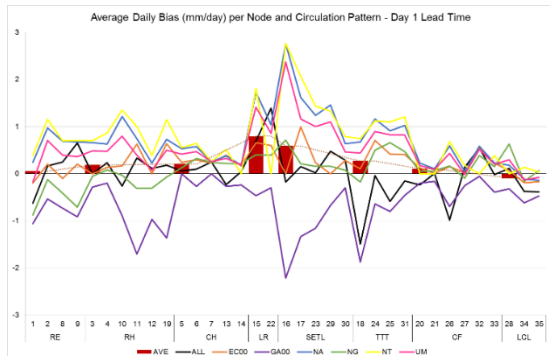


Figure 5: Area average daily bias for each of the 35 nodes for each of the 5 models as well the MME (solid black line) for day 1 forecasts.

Conclusions

As shown by previous research (e.g. Landman 2012) it is again seen that an ensemble mean (even if it is a small ensemble size) does outperform a single model forecast. Furthermore it is also shown that under different rain-bearing circulation patterns, the forecasts have different biases and skill. This result is important in contributing to further research in order to bias correct model forecasts per region and per circulation patterns.

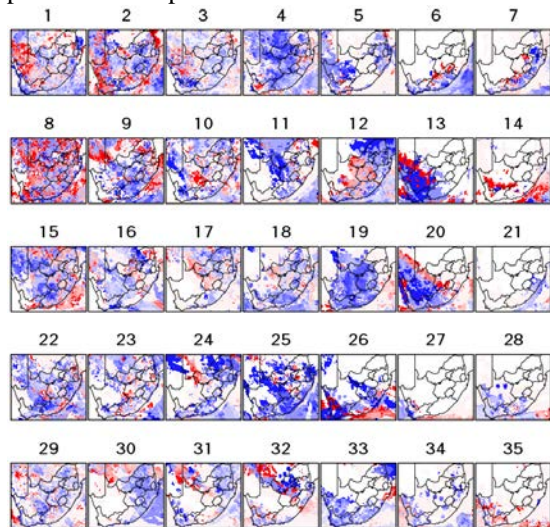


Figure 6: Brier skill score of the ensemble mean forecasts (scale is -1, red to 1, blue) for day 1.

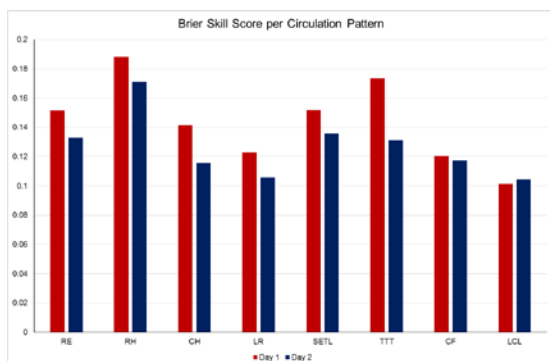


Figure 7: Area average daily Bier skill score for daily ensemble mean precipitation forecast per circulation

pattern (similar to horizontal axis of Fig. 5) for day 1 and day 2 lead times.

Results for cut-off lows and lead times for 3 to 5 days are not discussed in this paper but will be presented. Cut-off lows are evaluated separately from the other circulation patterns due to their small scale and low frequency of occurrence.

Acknowledgment

The authors would like to thank ACCESS for the scholarship funding of the research. The authors are also thankful for Prof. F. Pappenberger for making available the ECMWF deterministic forecasts for inclusion in this research as well as Dr. B. Fock (UK Met Office) for extracting the necessary UM Global archive data.

References

- Davies, T., Cullen, M.J.P., Malcolm, A.J., Mawson, M.H., Staniforth, A., White, A.A., Wood, N. (2005) A new dynamical core for the Met Office's global and regional modelling of the atmosphere. *Q. J. R. Meteorol. Soc.* **131**, 1759–1782.
- Dee D.P. and Co-authors, 2011: The ERA-Interim reanalysis: configuration and performance of the data assimilation system. *Q. J. R. Meteorol. Soc.* **137**: 553–597
- Engelbrecht, C. J., Landman, W. A., Engelbrecht, F. A. and Malherbe, J. 2014, 'A synoptic decomposition of rainfall over the Cape south coast of South Africa', *Clim. Dyn.* **44**: 2589-2607
- Favre, A., Hewitson, B.C., Lennard, C., Cerezo-Mota, R. and Tadross, M. 2013: Cut-off lows in the South Africa region and their contribution to precipitation. *Clim Dyn* **41**:2331–2351.
- Hart, N.C.G., Reason, C.J.C. and Fauchereau, N. 2010: Tropical–Extratropical Interactions over Southern Africa: Three Cases of Heavy Summer Season Rainfall. *Mont. Wea. Rev.* **138**; 2608-2623
- Harrison, M.S.J. 1983: A Generalized Classification of South African Summer Rain-Bearing Synoptic Systems. *J. Climatol.* **4**: 547-560
- Kohonen T. 2001, 'Self-organizing maps'. 3rd ed. Springer
- Landman, S., Engelbrecht, F.A., Engelbrecht, C.J., Dyson, L.L., Landman, W.A. (2012). A short-range weather prediction system for South Africa based on a multi-model approach. *WaterSA*, **38**, 765-773
- Lennard, C. and Hegerl, G. 2015: Relating changes in synoptic circulation to the surface rainfall response using self-organising maps. *Clim. Dyn.* **44**: 861-879
- Novella N.S. and W.M. Thiaw, 2013: African Rainfall Climatology Version 2 for Famine Early Warning Systems. *J. App. Met. Clim*, **52**: 588-606

Tennant, W.J., and Hewitson, B.C. 2002: Intra-seasonal rainfall characteristics and their importance to the seasonal prediction problem. *Int J Climatol* **22**:1033–1048.

Taljaard, J.J. 1996: Atmospheric circulation systems, synoptic climatology and weather phenomena of South Africa. Part 6: Rainfall in South Africa. South African Weather Bureau, Technical paper 32

Tambouratzis, T. and Tambouratzis G., 2008: Meteorological Data Analysis Using Self-Organizing Maps, *Int. J. Intel. Sys*, **23**, pp. 735-759

Walters, D.N. and Co-authors, 2014: The Met Office Unified Model Global Atmosphere 4.0 and JULES Global Land 4.0 configurations. *Geosci. Model Dev.*, **7**, 361–386

Wedi, N.P. and Co-authors, 2015: The modelling infrastructure of the Integrated Forecasting System: Recent advances and future challenges. *Technical Memorandum*, 760, ECMWF

Wilks, D.S. (2011). *Statistical Methods in the Atmospheric Sciences*. Third Edition. Elsevier Academic Press. California, USA.

Decision-relevant information on seasonal time scales – the case of a farm in northern Namibia

Willem A Landman¹, Emma Archer² and Mark Tadross³

¹*Department of Geography, Geoinformatics and Meteorology, University of Pretoria, Pretoria, South Africa*

²*Council for Scientific and Industrial Research, Natural Resources and the Environment, Johannesburg, South Africa*

³*Climate Systems Analysis Group, University of Cape Town, Cape Town, South Africa*

Abstract

The potential advantage for a farmer to use seasonal forecasts from models is demonstrated in this case study. The farm is located in the northern regions of Namibia near Grootfontein, where El Niño and La Niña events have in the past been associated with respectively drought and wet seasons. Two forecasting approaches are evaluated: The use of climatological rainfall data collected at the farm over 50 years to provide insight into what a coming summer rainfall season might be like, and the use of robust seasonal forecasting models of varying complexity (statistical and dynamical) to predict seasonal rainfall totals. For both approaches, skill is assessed for three categories that represent the 25th and 75th percentile of the climatological records, i.e. extreme rainfall seasons. Forecasts of the most recent 5 years for the 4-month season of December to March are compared through the use of the Ranked Probability Skill Score (RPSS). It is shown that both the forecast models outscore the use of estimates based on the climatological data of the farm as well as forecasts of climatology, and hence we propose that the farmer may derive greater benefit from using forecasts from models.

Key words: ENSO, seasonal climate modelling, skill

INTRODUCTION

Seasonal forecasts, including forecasts of the evolution of ENSO events and forecasts of seasonal rainfall and temperature variations over land often have skill. The recent very strong El Niño event of 2015/16 was successfully predicted several months in advance of its peak, and the associated drought over large parts of southern Africa was also captured by forecast models. Although the predictability of seasonal rainfall totals over southern Africa ranks modestly against other areas of the globe also affected by ENSO (Landman et al., 2015), forecast skill has improved over the years (Landman, 2014) in accordance with the increase of the complexity of forecast models (Beraki et al., 2015). Notwithstanding all the efforts to improve on forecast skill and on our understanding of the Earth system, as a modelling community we need to provide stronger evidence that potential users can derive some benefits from using seasonal forecasts.

DATA AND METHOD

Three data sets are considered; 50 years of monthly rainfall data of the farm Poolmanskloof near Grootfontein in Namibia provided by the farmer from 1966/67 to 2015/16; Aug-Sep-Oct (ASO) sea-surface temperatures (SSTs) of NOAA's Extended Reconstructed Sea Surface Temperature Dataset, Version 3b (Smith et al., 2008); and hindcasts from the GFDL-CM2.5-FLOR-B01 fully coupled model of the North American Multi-model Ensemble (Kirtman et al., 2014). Monthly global hindcast data from March 1980 to the present are available at a

1°x1° latitude-longitude resolution for 12 ensemble members and for lead-times up to 11 months. We are using only 1-month lead-time hindcasts for both the statistical model and for the coupled model in order to produce forecasts near the beginning of November for the 4-month rainfall season of December to March (DJFM).

A Principal Component Regression (PCR) statistical model is developed that uses ASO SSTs over the equatorial Pacific Ocean (10° N to 10° S; dateline to 90° W) as predictors of DJFM rainfall at Poolmanskloof in order to constitute a 1-month forecast lead-time. Nine EOF modes of central equatorial Pacific SST are considered, but the best results, determined through a 5-year-out cross-validation approach, uses only the first EOF mode as a predictor. EOF1 represents ENSO. The PCR model, based on 31-years of training data (1980 to 2010), is subsequently used to make independent DJFM rainfall predictions for 2011/12 to 2015/16. Probabilistic forecasts for these 5 years are obtained from the error variance of the cross-validated predictions (Troccoli et al., 2008).

DJFM total precipitation ensemble mean hindcasts from the coupled model are interpolated to the location of the farm, after which the mean and variance biases of the model data are corrected statistically. The interpolation and corrections of forecasts are performed over the same 31 years over which the statistical model is developed, and are subsequently used to determine independent probabilistic forecasts for the 5 years stated above. This forecast process has already been done for gridded rainfall fields (Landman et al., 2016) and is

similarly used here for a single location. The decision to obtain only 5 years of independent forecasts for the purpose of verification is due to the fact that we wanted to determine the potential usefulness of forecasts over a very recent period of past extreme events.

We next develop scenarios on which the farmer himself could have produced a rainfall forecast or estimate for those 5 years without having access to any model forecasts. The simplest type of such a scenario would be to adopt forecasts of climatology. In this case a forecast for each of the 5 years would be a 25% chance for both below- and above-normal rainfall totals and a 50% chance for near-normal rainfall totals to occur over the farm.

Since some farmers actually do prefer undertaking their own climate analysis, we are also proposing a forecasting approach here that such a farmer can use to estimate what a coming DJFM rainfall season might be like. One way in which the farmer could have produced a forecast for his farm is to consider how it rained in the past on the farm during El Niño, La Niña and ENSO-neutral seasons (the classification used here of such seasons over the equatorial Pacific Ocean is that of the Oceanic Niño Index). He/she could have counted the number of seasons it was wet ($> 75^{\text{th}}$ percentile of the records), dry ($< 25^{\text{th}}$ percentile of the records), or near-normal during El Niño, La Niña and ENSO-neutral seasons. For 45 years (last 5 years of the 50 not included) it is found to have been dry (below-normal = B) for 9 years, wet (above-normal = A) for 2 years and near normal (=N) for 5 when there was an El Niño, and so the probabilities are 56, 31 and 13 % (=B, N, A) when there is an El Niño. La Niña related rainfall probabilities are 14, 36 and 50% (=B, N, A), while ENSO-neutral probabilities are 7, 73 and 20% (=B, N, A). So for the 5 test years we had a La Niña (2011/12), three ENSO-neutral (2012/13 to 2014/15) and an El Niño year (2015/16). For a rainfall forecast when, say, a La Niña event is developing the farmer would then use the La Niña related rainfall forecast of 14, 36 and 50 % (=B, N, A). This "model" is what a farmer could use without having any forecasts to consider and if he/she would assume that such a "home-made" forecast system based on historical events could be an improvement over just climatology as a forecast (i.e. 25, 50, 25 = B, N, A).

RESULTS

First it is determined which multi-month period of the summer the various forecast models need to be developed for. Fig. 1 shows the annual cycle of rainfall over the farm as well as the occurrence of rainfall per month over the 5-year test period. The 25th and 75th percentile values of the 50 years are also presented. The three wettest months are January to March, but December (the fourth wettest month) is also included in the analysis since it has already

been shown that the inclusion of December months in seasonal forecasts can enhance seasonal forecast skill over the region (Landman et al., 2012). Moreover, the rainfall during the December months of the 5-year test period were associated with anomalous rainfall totals for 4 of the 5 years (Fig. 1).

The seasonal-to-interannual DJFM rainfall variations over the farm are shown in Fig. 2. In addition to the rainfall time series, the median, 25th and 75th percentile values of the rainfall records are also shown. Seasons above the 75th percentile line are considered to be above-normal seasons and those below the 25th percentile line to be below-normal seasons. The seasons in between these line are considered to be near-normal seasons.

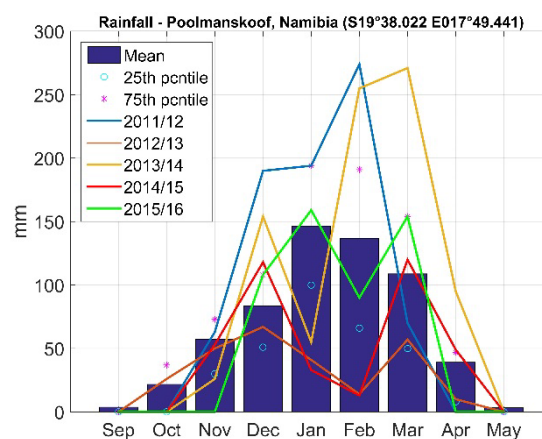


Fig. 1. Summer rainfall seasonal cycle (blue bars) at the farm Poolmanskoof near Grootfontein, Namibia. The 25th (open circles) and 75th (asterisks) percentile values of the monthly climatological records are also presented, together with the rainfall totals per month for each year of the 5-year test period.

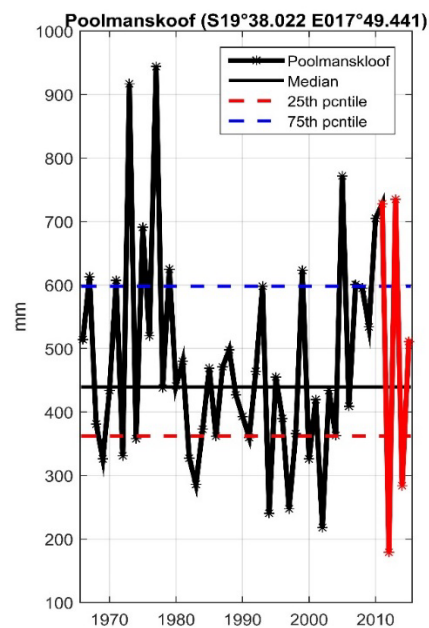


Fig. 2. DJFM rainfall totals per year at the farm Poolmanskoof, including the mean, 25th and 75th percentile lines. The red part of the time series represents the 5-year test period.

We next verified the forecasts from the various models over the 5-year test period. Fig. 3 shows the accumulated probabilities over the three categories, for three forecast models (excluding forecasts of climatology) over the 5 test years. The verification measure used here is the Ranked Probability Score (RPS), which produces a verification statistic capable of penalizing forecasts if more probability is assigned to event categories further removed from the actual outcome (Wilks, 2011). The RPS per season is calculated for each model as well as for forecasts of climatology, from which Ranked Probability Skill Scores (RPSS) are calculated where the “home-made” forecasts and the forecasts of climatology are respectively used as reference forecasts. Consequently, RPSS values are calculated only for the statistical model that uses SSTs as predictor, as well as for the coupled forecast model. Positive RPSS values indicate that the forecasts from these two models are outperforming the two reference forecasts.

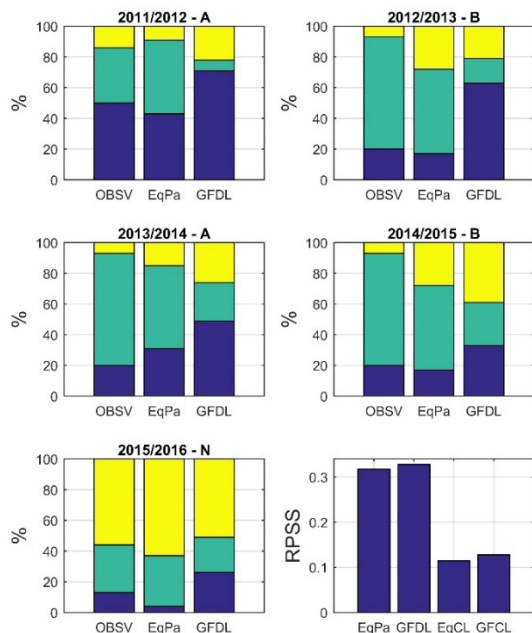


Fig. 3. Probabilistic DJFM rainfall forecasts at a 1-month lead-time for the three categories explained in the text, and RPSS values calculated over the 5-year test period. The heading of each forecast graph includes the year and the observed rainfall outcome of A, N or B for that year. Yellow bars represent probabilities for below-normal rainfall totals, green for near-normal totals and blue for above-normal totals to occur [OBSV = “home-made” model; EqPa = statistical model; GFDL = coupled model]. For RPSS values, the two bars on the left show how the two models are outperforming the “home-made” model (RPSS>0), and the two bars on the right show how the two models are outperforming forecasts of climatology (RPSS>0).

The graph on the bottom right of Fig. 3 shows the RPSS that use the forecasts from the “home-made” model as reference (two bars on the left) and RPSS values when using forecast of climatology as reference. The four positive RPSS values imply that

the two models are respectively far superior than the “home-made” model and slightly superior to forecasts of climatology. These positive skill scores provide evidence that using robust physically based seasonal forecast models for predicting seasonal rainfall outcomes should be more advantageous to the farmer of Poolmanskloof than not using forecasts (the two models outscore climatology) or using seasonal rainfall estimates based on observed rainfall outcomes of the past (the two models outscore the “home-made” model). If the RPSS values were all negative then the “home-made” forecasts and forecasts of climatology provide better forecasts than the two models presented here. As it turns out, RPSS values are positive and the “home-made” model is even worse than using forecasts of climatology (RPSS = -0.2973).

DISCUSSION AND CONCLUSION

In this study, we wanted to find evidence that a farmer could derive more benefit from using forecasts produced by robust physically-based models as opposed to not using any forecasts at all (and as a result assume that each season will be equally likely to experience drought, wet or near-normal rainfall conditions), or using information related to his/her own rainfall records and how these relate to ENSO events. Although there is a range of factors that could be beneficial to farmers, such as improved agricultural practices, here we selectively equate benefit to forecast skill, as has already been demonstrated for southern Africa before (Lazenby et al., 2014; Muchuru et al., 2014).

The main conclusion from verifying the models of various complexity presented here is that greater benefit could potentially be derived when using the physically-based models as opposed to not using them. The farmer at Poolmanskloof may thus have benefitted from using the model forecasts over the 5-year test period presented here. Although physically based climate models should be considered as incrementally more skillful than climatology techniques, the value to the decision-scale requires, however, contextual assessment. We need to provide additional evidence to farmers that forecasts can impact positively on their farming decision support systems and that the use of forecasts can lead to financial gains. Such an endeavor requires forecast producers and farmers to work together to understand the decisions that farmers will undertake, the financial implications of those decisions, as well as co-producing tailored forecasts and data analysis for the farm.

ACKNOWLEDGEMENT

The work was funded by the National Research Foundation through their financial support of rated researchers.

REFERENCES

- Beraki, A.F., Landman, W.A. and DeWitt, D. (2015). On the comparison between seasonal predictive skill of global circulation models: coupled versus uncoupled. *Journal of Geophysical Research – Atmospheres*. 120: 11151-11172, DOI:10.1002/2015JD023839
- Harris, I., Jones, P. D., Osborn, T. J., and Lister, D. H. (2014). Updated high-resolution grids of monthly climatic observations - the CRU TS3.10 Dataset. *International Journal of Climatology*. 34: 623-642. doi: 10.1002/joc.3711
- Kirtman, B.P., and Coauthors. (2014). The North American Multimodel Ensemble: Phase-1 seasonal-to-interannual prediction; Phase-2 toward developing intraseasonal prediction. *Bulletin of the American Meteorological Society*. 95: 585-601. DOI: <http://dx.doi.org/10.1175/BAMS-D-12-00050.1>
- Landman, W.A. (2014). How the International Research Institute for Climate and Society has contributed towards seasonal climate forecast modelling and operations in South Africa. *Earth Perspectives*. 1: 22.
- Landman, W.A., DeWitt, D. Lee, D.-E., Beraki, A. and Lötter, D. (2012). Seasonal rainfall prediction skill over South Africa: 1- vs. 2-tiered forecasting systems. *Weather and Forecasting*, 27: 489-501. DOI: 10.1175/WAF-D-11-00078.1.
- Landman, W.A., Barnston, A.G. and Vogel, C. (2015). Ranking seasonal rainfall forecast skill of emerging and developing economies. Peer review abstracts, 31st Annual conference of the South African Society for Atmospheric Science, Pretoria, 21-22 September 2015, pp 112-116 ISBN 978-0-620-67825-4.
- Lazenby, M., Landman, W.A., Garland, R. and DeWitt, D. (2014). Seasonal temperature prediction skill over southern Africa and human health. *Meteorological Applications*. 21: 963-974. DOI: 10.1002/met.1449.
- Muchuru, S., Landman, W.A., DeWitt, D. and Lötter, D. (2014). Seasonal rainfall predictability over the Lake Kariba catchment area. *Water SA*. 40 (3): 461-469. <http://dx.doi.org/10.4314/wsa.v40i3.9>.
- Smith, T.M., Reynolds, R.W., Peterson, T.C. and Lawrimore, J. (2008) Improvements to NOAA's Historical Merged Land-Ocean Surface Temperature Analysis (1880-2006). *Journal of Climate*. 21: 2283-2296.
- Troccoli, A., Harrison, M., Anderson, D.L.T. and Mason, S.J. (2008). *Seasonal Climate: Forecasting and managing risk*. NATO Science Series. Earth and Environmental Sciences Vol 82. Springer: Dordrecht, The Netherlands.
- Wilks, D.S. (2011) *Statistical Methods in the Atmospheric Sciences*, 3rd edition. Academic Press, San Diego

How does well ECHAM simulate central Africa rainfall seasonal cycle?

Georges-Noel T. Longandjo^{1,2*} and Mathieu Rouault^{1,2}

¹*Nansen-Tutu centre for Marine Environmental Research, University of Cape Town*

²*Department of Oceanography, University of Cape Town*

**Corresponding author e-mail address: gntiers@gmail.com*

Due to poor meteorological observations network over central Africa, water resources are not well evaluated yet. In this paper, we used a state-of-art atmospheric climate model forced by SST (ECHAM version 5.3) to figure out what are mechanisms and how central Africa rainfall are represented in observations in term of spatial distribution, seasonality and intensity. So ECHAM5.3 does well capture the westward (eastward) migration of central Africa rainfall annual cycle as well as its spatial distribution, but it fails to simulate its intensity. However, the seasonal variation of ITCZ location of the thermally-driven central Africa rainfall is controlled either by local and remote latent heat or by low level convergence during strong rainy and dry seasons respectively.

Keywords: Bias; Guinea Gulf; ITCZ location; Latent heat; Moist Static Energy

Introduction

According to Intergovernmental Panel on Climate Change (IPCC, 2012), precipitation patterns over Africa would change in a warmer climate. But due to sparsity of observational datasets over central Africa, the understanding of spatio-temporal variability of rainfall – which is substantial to evaluate water resources availability – is limited and requires reliable and controlled data. In this situation, the use of alternative sources of rainfall rates such as satellite information or numerical weather prediction (NWP) may be useful. Various rainfall datasets have been utilized widely to study inter-annual variability of central Africa rainfall (Balas et al. 2007; Nicholson and Grist, 2003; Todd and Washington, 2004; etc.) and their use is arbitrary. However over central Africa, few studies tried to evaluate rainfall in observations, reanalysis and climate models (McCollum et al. 1999; Asadullah et al. 2008; Washington et al 2013; Siam et al. 2014). Washington et al (2013) found that over central Africa, the zonal rainfall distribution within observational datasets illustrates high rainfall either over Guinea Gulf (CMAP, ERA-40, ERA-Interim, TRMM) or in the east of central Africa (TAMSAT, NCEP, CMORPH). However, all observational datasets reproduce the bimodal annual cycle of rainfall over central Africa, but almost all general circulation models (GCMs) in the Coupled Model Intercomparison Project Phases 3 and 5 (CMIP3/5) were deficient by overestimating rainfall and runoffs, which depend deeply on their respective spatial resolution (Siam et al. 2014). The above results outlined that there is no consistent rainfall distribution pattern in climate models, reanalysis and observations products. This leads us to infer that sources of central Africa rainfall inadequacies within observations and, biases in climate models remain unclear. Many studies focused on inter-annual variability compared to the annual cycle where the big challenge is. In addition, this paper will try to unfold the zonal migration of central

Africa rainfall annual cycle in using state-of-art climate model – the ECHAM version 5.3 – as well as how the observational central Africa rainfall is simulated in term of spatial distribution, seasonality and intensity.

Data

a) Observations and reanalysis

As ground-based data (in situ measurements), we choose only two gridded-gauge only data, the Climatic Research Unit, CRU TS3.10 (merely referred as CRU, Harris et al. 2013) and the Global Precipitation Climatology Centre dataset (hereafter GPCC, Schneider et al. 2013; Becker et al. 2013). But GPCC and CRU cover only land areas at monthly temporal resolution (1901 to present). In addition, we used also essentially the Climate Prediction Center Merged Analysis of Precipitation dataset (CMAP, Xie and Arkin 1997) and the Global Precipitation Climatology Project monthly precipitation dataset (GPCP, Huffman et al. 2009), available at monthly temporal resolution (1979 to present). CMAP and GPCP datasets are compiled from merged satellite precipitation data and bias-corrected over land through continental rain-gauge observations (Bolvin et al. 2009). These datasets cover the whole globe, including the oceans. We add TAMSAT African Rainfall Climatology and Time-series (TARCAT) (Tarnavsky et al., 2014; Maidment et al., 2014), which combines satellite thermal infrared measurements with other data sources such as microwave retrievals and rain gauge measurements (Maidment et al. 2014). Its temporal resolution spans from 1983 to present. As Reanalysis, NCEP–NCAR reanalysis product (hereafter NCEP, Kalnay et al. 1996) and ERA-Interim product (hereafter ERA-I, Dee et al. 2011) are used in this study. Meanwhile the time spans from 1948 to present and 1979 to present respectively. For ERA-I, rainfall is a sum of convective precipitation and large scale precipitation available daily at time of 6-hours. But beside rainfall, we used atmospheric variables of

ERA-I, which include among others air temperature, geopotential, specific humidity, zonal and meridional wind components at 2 pressure levels (1000 and 700) at monthly time steps, are used to compute the moist static energy.

b) SST-forced atmospheric climate model

The European Centre Hamburg Model (ECHAM) version v5.3 is an atmospheric general circulation model forced by SST (Roeckner et al. 2003) at monthly time steps spanned from 1870 to 2009, while the spatial resolution is gridded at $1.125^{\circ} \times 1.125^{\circ}$. The total precipitation is obtained as sum of convective and large scale precipitation respectively. We also used air temperature, geopotential, specific humidity, zonal and meridional wind components at 2 pressure levels (1000 and 700- hPa). Hence, in this study, rainfall and all atmospheric variables based on all these datasets have been interpolated onto the same $1.125^{\circ} \times 1.125^{\circ}$ grids to eliminate potential influence of the horizontal resolution.

Zonal evolution and distribution of central Africa rainfall seasonal cycle: intercomparison and bias

Firstly, we want to figure out how the central Africa rainfall is associated with Walker circulation. Thus, the longitude vs. time Hovmöller plot of meridional mean rainfall averaged between 10°N and 15°S is portrayed in Fig. 1.

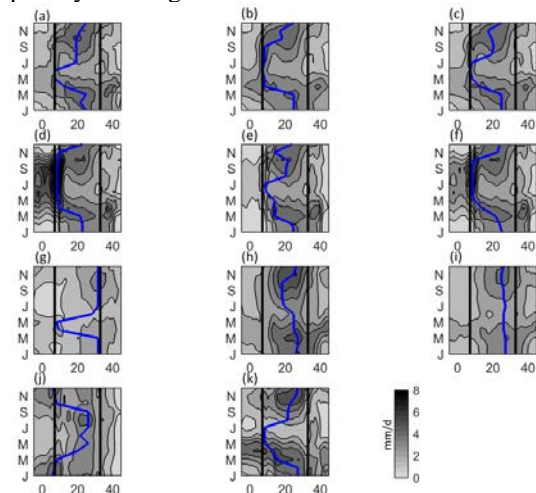


Figure 1. Hovmöller (longitude-time) of observed and modelled central Africa seasonal rainfall mean: (a) GPCP; (b) CMAP; (c) GPCP+CMAP; (d) CRU; (e) GPCC; (f) CRU+GPCC; (g) ERAI; (h) NCEP; (i) ERAI+NCEP; (j) TAMSAT and (k) ECHAM5.3. The bold blue line on all panels follows the zonal propagation of rainfall maximum (unit: mm/day).

So in DJF, rainfall develops between 20° - 30°E and peaks in MAM ($>5\text{mm/d}$), while ITCZ location propagates westward toward Guinea Gulf. ITCZ location is defined as meridional-mean rainfall maximum over central Africa (10°N - 15°S). In JJA, rainfall weakened abruptly ($< 2\text{mm/d}$) over entire

central Africa, but it is higher over Guinea Gulf. This is related to the northward propagation of rainfall over Gulf of Guinea. In August/September, rainfall increases and matures ($>5\text{mm/d}$) in SON. This rainfall intensification is associated with a westward migration of ITCZ towards highlands in east central Africa. In DJF, rainfall decreased, but remains high, while confined west of 30°E . However, CRU shows high rainfall bands ($>8\text{mm/d}$) at $\sim 10^{\circ}\text{E}$ in JJA, but less rainfall is found in ERAI. NCEP does not reproduce westward (eastward) migration of rainfall bands during transitional seasons. Whereas both GPCP and ERAI capture the westward rainfall migration in MAM, but by June, rainfall bands return to their initial position between 20° - 30°E . However, the migration in ERAI seems to be faster (Fig. 1j). Noteworthy, ECHAM5.3 does reasonably represent not only the westward rainfall migration, but also the bimodal characteristic of zonal central Africa rainfall annual cycle, even though with slight larger amplitudes during strong rainy seasons (Fig. 1k). This leads us to be confident while using ECHAM5.3 to represent central Africa rainfall, consistent with the findings of Yang et al. (2015) over east central Africa.

Another helpful diagnose of rainfall datasets is the seasonal rainfall probability density function (PDF, Botev et al. 2008) as shown in Fig. 2. The area-averaged rainfall index over central Africa has been binned at 0.005 mm/d . All rainfall datasets show positive skew unimodal rainfall intensity ranged between 2 and 6 mm/day – except TAMSAT (Fig. 2j), which presents bimodal rainfall intensity and negative skewness. However, much and less rainfall occurred in SON and in JJA (DJF for CRU) respectively. But ECHAM5.3 shows three rainfall intensities peaking at 2, 3 and 4 mm/day, with less and much rainfall in JJA and MAM respectively (Fig. 2k). However, each rainfall dataset describes a bit different spatial pattern and rainfall intensity. Thus, the inconsistency between rainfall datasets could be due either to the intrinsic technique used for estimation of rainfall rate or to the quality of the gauge observations used (McCollum et al. 2000). This is more evident when we carried out the temporal correlation of central Africa rainfall based on respective datasets used (not shown). The result indicates substantial dissimilarity of central Africa inter-annual rainfall variability among the datasets. However, whether the rainfall products are grouped with respect to their retrieved technique e.g., satellite- rainfall gauge (CMAP and GPCP) or stations based (CRU and GPCC) or reanalysis (ERA-I and NCEP), the mean-rainfall between each of the grouped datasets improves not only the correlation coefficient comparatively to their respective dataset taken alone, but reduce the discrepancy between them.

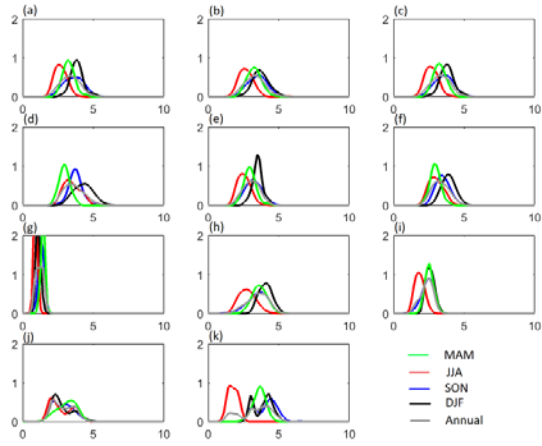


Figure 2. Probability density functions (PDF; Botev et al. 2010) (a) GPCP; (b) CMAP; (c) GPCP+CMAP; (d) CRU; (e) GPCC; (f) CRU+GPCC; (g) ERAI; (h) NCEP; (i) ERAI+NCEP; (j) TAMSAT and (k) ECHAM5.3. Unit: mm/day.

On the role of local environment on central Africa rainfall

We further understand how central Africa rainfall arises seasonally – in term of location and strength, atmospheric energy budget and circulation to highlight the physical mechanisms underlying the rainfall representation. The moist static energy (MSE, Neelin and Held, 1987) is defined by as follow:

$$h = DSE + Lq \quad (1)$$

$$DSE = c_p T + \Phi \quad (2)$$

Where DSE is dry static energy, with contribution of both internal and potential energy ($c_p T$) and Φ respectively; c_p is specific heat capacity of dry air at constant pressure; T is temperature; L is the latent heat of vaporization; q is specific humidity; Φ is geopotential. To compute saturated MSE (MSE*), saturated specific humidity q^* is used in equation (1). Moist static stability is defined as difference between MSE at surface and MSE* at 700- hPa, and the air column is unstable if this is positive. The seasonal evolution of meridional-mean of MSE averaged over 10°N - 15°S of latitude is plotted in Fig. 3. The MSE shows, at surface, a similar “lung-like” pattern of zonal propagation of central Africa rainfall annual cycle (cfr Fig. 1), with warmer and moister air ($h > 345$ K) at 20°E during strong rainy seasons, essentially in MAM, with a tail extending westwards towards Guinea Gulf and in SON respectively (Fig. 3a).

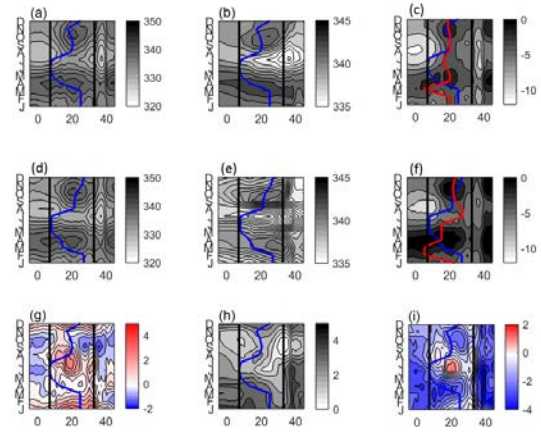


Figure 3. Hoerl (longitude-time) of (left column) MSE at surface; (middle column) MSE* at 700- hPa; (right column) Moist static stability over central Africa. (a-c) observations; (d-f) ECHAM5.3: (g-i) biases. The bold blue line on all panels follows the zonal propagation of rainfall maximum in observations (combined of GPCP and CMAP. Unit: mm/day) and red line in (c and f) indicates the moist static stability maximum

In dry seasons (JJAS), MSE ($h < 330$ K) weakened, with minima located over east Africa (33° - 40°E) and tropical Atlantic (including the Guinea Gulf, 07° - 12°E) respectively. At 700- hPa, MSE* produced similar feature, but with stronger amplitudes (Fig. 3b). In comparison with Figs. 1 and 3c, it emerges that intensification of rainfall is associated with strengthened convective instability, as moist static stability become close to zero or slightly positive (Fig. 3c). But during weak rainy (dry) season (JJAS), low troposphere is more stable, particularly over tropical Atlantic where cold tongue is maturing (Richter et al. 2012, Tokinaga and Xie, 2011). This leads us to infer that convective instability is associated with rising motions of warm and moist air at 20°E year round and stable low-troposphere is associated with subsidence, which in turn, suppressed convection over offshore regions (including Guinea Gulf). In addition, it is relevant to note strong seasonal change of MSE at surface and MSE* at 700- hPa. However the presence of warm and moist air is likely to destabilize the low-level troposphere, particularly during wet seasons. During dry seasons, the absence of low-level humidity leads to opposite. Significant relation is noted between the ITCZ location and moist static stability location (0.50). However, during strong rainy season, ITCZ and moist static stability collocate at $\sim 20^\circ\text{E}$, while during JJAS, ITCZ location seems to be linked low level convergence. We do posit that year-round, ITCZ location does primarily co-occur with moist static stability during strong rainy seasons, but seems to be more related to

⁷ In reference to the chest X-ray showing two black lungs separated by a white trachea.

low-level convergence in JJAS. ECHAM5.3 does fail to reproduce the collocation of ITCZ and moist static stability. However, a quantitative role of thermodynamics and dynamics of central Africa rainfall/convection is beyond the scope of this paper.

Conclusions

Noteworthy in this paper that ECHAM5.3 does well represent the westward (eastward) propagation of central Africa rainfall annual cycle and its spatial distribution as well, but fails to capture its distribution. However, the seasonal variation of ITCZ location of the thermally-driven central Africa rainfall is strongly connected to moist static stability. Nevertheless the central Africa rainfall variability seems to be controlled either by local and/or remote latent heat.

Acknowledgements

ERA-Interim reanalysis data were obtained from ECMWF through their website at <http://ecmwf.int/>. The research leading to these results received funding from EU FP7/2007-2013 under grant agreement no. 603521. First author thanks Noel Keenlyside for discussion and S. Gleixner for providing some data used in this paper.

References

- Asadullah A., N. McIntyre and M. Kigobe (2008) Evaluation of five satellite products for estimation of rainfall over Uganda / Evaluation de cinq produits satellitaires pour l'estimation des précipitations en Ouganda, *Hydrological Sciences Journal*, **53:6**, 1137-1150, DOI: 10.1623/hysj.53.6.1137
- Balas et al. 2007; The relationship of rainfall variability in West Central Africa to sea-surface temperature fluctuations, *Int. J. Clim* DOI: 10.1002/joc.1456
- Becker, A., P. Finger, A. Meyer-Christoffer, B. Rudolf, K. Schamm, U. Schneider, and M. Ziese (2013), A description of the global land-surface precipitation data products of the Global Precipitation Climatology Centre with sample applications including centennial (trend) analysis from 1901–present, *Earth Syst. Sci. Data*, **5**, 71–99, doi:10.5676/DWD.
- Dee et al. 2011 The ERA-Interim reanalysis: Configuration and performance of the data assimilation system. *Quart. J. R. Met. Soc.*, **137 (656)**, 553-597.
- Harris, I., Jones, P.D., Osborn, T.J. and Lister, D.H. (2014), Updated high-resolution grids of monthly climatic observations - the CRU TS3.10 Dataset. *International Journal of Climatology* **34**, 623-642 doi:10.1002/joc.3711
- Huffman GJ, Adler RF, Bolvin DT, Gu G (2009) Improving the global precipitation record: GPCP Version 2.1. *Geophys Res Letters* **36**: L17808, 5 pp
- IPCC. 2012. Managing the risks of extreme events and disasters to advance climate change adaptation. C. B. Field, V. Barros, T. F. Stocker, D. Qin, D. Dokken, K. Ebi, M. Mastrandrea, K. Mach, G. Plattner, and S. Allen, editors, Cambridge University Press, Cambridge, UK, and New York, NY, USA.
- Kalnay E, Kanamitsu M, Kistler R, Collins W, Deaven D, Gandin L, Iredell M, Saha S, White G, Woollen J, Zhu Y, Chelliah M, Ebisuzaki W, Higgins W, Janowiak J, Mo KC, Ropelewski C, Wang J, Leetmaa A, Reynolds R, Jenne R, Joseph D (1996) The NCEP/NCAR 40-year reanalysis project. *Bull Am Meteor Soc* **77**:437–470
- Maidment, R. I., D. I. F. Grimes, R. P. Allan, H. Greatrex, O. Rojas, and O. Leo (2013), Evaluation of satellite-based and model re-analysis rainfall estimates for Uganda, *Meteorol. Appl.*, **20(3)**, 308–317, doi:10.1002/met.1283.
- McCollum, J. R., A. Gruber, and M. B. Ba, 2000: Discrepancy between gauges and satellite estimates of rainfall in equatorial Africa. *J. Appl. Meteor.*, **39**, 666-679.
- Nicholson, S. E., and J. P. Grist, 2003: On the seasonal evolution of atmospheric circulation over West Africa and Equatorial Africa. *J. Climate*, **16**, 1013-1030.
- Schneider, U., Becker, A., Finger, P. et al. *Theor Appl Climatol* (2014) **115**: 15. doi: 10.1007/s00704-013-0860-x
- Siam SM, Demory ME, Eltahir EAB Hydrological cycles over the Congo and upper Blue Nile basins: evaluation of general circulation models simulations and reanalysis data products. *J Clim.* doi:10.1175/JCLI-D-12-00404.1
- Tarnavsky, E., D. Grimes, R. I. Maidment, M. Stringer, R. Chadwick, R. P. Allan, E. Black, and F. Kayitakire (2014), Extension of the TAMSAT Satellite-based Rainfall Monitoring over Africa and from 1983 to present, *J. Appl. Meteorol. Climatol.*, doi:10.1175/JAMC-D-14-0016.1.
- Todd MC, Washington R. 2004. Climate variability in central equatorial Africa: influence from the Atlantic sector. *Geophys. Res. Lett.* **31**, 2–5 (doi:10.1029/2004GL020975)
- Roeckner, E., G. Bäuml, L. Bonaventura, R. Brokopf, M. Esch, M.

- Giorgetta, S. Hagemann, I. Kirchner, L. Kornblueh, E. Manzini, A. Rhodin, U. Schlese, U. Schulzweida, and A. Tompkins, 2003: The atmospheric general circulation model ECHAM5. Part I: Model description. Max Planck Institute for Meteorology Rep. 349, 127 pp.
- Washington R, James R, Pearce H, Pokam WM, Moufouma-Okia
W (2013) Congo Basin rainfall climatology: Can we believe the climate models? Phil Trans R Soc S Biol Sci 368:20120296
- Xie P and Arkin PA, (1997) Global monthly precipitation estimates from satellite-observed outgoing longwave radiation. J Clim 9:840–858
- Yang, W., R. Seager, M. A. Cane, and B. Lyon, 2014: The East African long rains in observations and models. *J. Climate*, **27**, 7185–7202, doi:[10.1175/JCLI-D-13-00447.1](https://doi.org/10.1175/JCLI-D-13-00447.1).

How would current advice benefit maize farmers with respect to historical associations with El Niño events?

Johan Malherbe, Wiltrud Durand – Agricultural Research Council

e-mail: johan@arc.agric.za

We evaluate the potential effect of a range of management decisions that can be taken by maize farmers in the western maize production region of South Africa in response to forecasts of dry conditions founded on the ENSO signal. Recommendations are based on crop simulation results for the period 1953 – 2016. Current typical advice, such as early planting and conservative practices, are evaluated focusing on El Niño years relative to the rest. Findings will contribute to the advice given during fora such as the National Agrometeorological Committee Meetings, aimed at informing best practices before and during growing seasons.

KEYWORDS: El Niño, Maize production, South Africa, Seasonal forecast, Crop modelling

Introduction

The ENSO signal in South African climate anomalies (Ropelewski and Halpert, 1987) provides much of the seasonal forecast skill of coupled climate models for southern Africa (Landman and Beraki, 2012). The well-established teleconnection results in the greatest skill, for both rainfall and maximum temperature, in mid-to-late summer (Landman and Beraki, 2012; Lazenby et al. 2014). ENSO-related crop reduction over part of the western maize producing region of South Africa has been observed to be related to both lower seasonal total rainfall as well as a shorter growing season (Moeletsi et al. 2011), specifically due to an earlier cessation of the rainy season. Adverse weather conditions during the recent summer (2015/16) were associated with a strong El Niño event and resulted in a total maize production being down 40% from the average for the 2010/11 – 2014/15 summers (CEC 2016).

The western maize production region of South Africa produces most of the country's white maize, used for human consumption. Average annual rainfall over the region ranges between 400 and 600 mm and negative climate impacts related to ENSO have caused significant reductions in production in the region in 1992, 2007 and 2016 (CEC 2016). Current advice, such as distributed by the National Agrometeorological Committee (NAC), provides some guidance early in a growing season. For example, the NAC advisory given in October 2015, called for a conservative approach with relation to planting density, soil (avoid marginal soils) and cultivar choice as well as a

conservative fertilizer strategy, whilst also advising to plant as early as possible during the normal planting window. These recommendations were made, based on the expectation of hot and dry conditions over the summer rainfall region towards mid- and late summer as indicated by the seasonal outlooks from a multitude of coupled climate models (<http://iri.columbia.edu/our-expertise/climate/forecasts/seasonal-climate-forecasts/>).

It eventually turned out that specifically the early part of summer was unfavorable for cultivation whilst cooler, wetter conditions since January together with a late onset of winter frost supported late planting or cultivation of alternative cash crops. It therefore follows that most of the advice given for maize production would not have benefitted farmers, except for supporting conservative approaches. Over the same region, planting later also resulted in higher yields during the 2014/15 season (Malherbe et al. 2015), which was also forecasted to be dry towards the end by seasonal forecast systems, based on weak El Niño conditions (<http://iri.columbia.edu/our-expertise/climate/forecasts/seasonal-climate-forecasts/>).

In the current study we consider the above elements of past growing seasons, associated with El Niño, as assimilated by a crop model, to understand the benefits of the advice given during El Niño years.

Instrumentation and Method

Daily weather data and soil profile information from the Agricultural Research Council – Institute for Soil, Climate and Water (ARC-ISCW) climate and

soil databanks respectively were used as input data to a crop model to test for the sensitivity of potential yields to a change in management decisions taken. Finding a continuous dataset of daily rainfall, temperatures and solar radiation for a specific area presents some challenges, and the research presented here focused on one specific area in the western maize production region, located near Potchefstroom (26.75°S, 27.05°E).

The DSSAT Crop System Model (previously known as CERES-maize - Jones et al. 2003; Hoogenboom et al. 2010) was used to simulate the effect of various management interventions such as different planting dates and planting density on yield, with respect to the occurrence of El Niño. Table 1 represents the crop management considerations of which all combinations were simulated for each of 6 planting dates within the normal planting window. Application of fertilizers was assumed to 60 kg Ha⁻¹ Nitrogen, a typical fertilizer strategy for dryland cultivation in the area.

Table 1 Variables considered during modeling

Variable	Experiment
Soil Type	Hutton Makatini, Hutton Msinga, Pinedene Klerksdorp
Row Width (m)	0.9, 1.0, 1.2, 1.5, 1.8
Plant Population (plants m ⁻²)	1, 1.5, 2.0, 2.5
Planting date	15 Oct, 31 Oct, 15 Nov, 30 Nov, 15 Dec, 31 Dec
Cultivar type	Short growing-season, Medium growing-season, Long growing-season

The sum total of combinations considered is 1080 – resulting in a total of 68040 experiments when executed for each year in the time series (1953 – 2016). The soil types are some of the common types found in the area of interest, as indicated by the land type inventories of the dominant land types (ARC-ISCW Land Type Inventory and soil descriptions). All these have reddish fine sandy loam to sandy clay loam textured upper horizons. The main difference between the soil types, relevant for cultivation, is the depth of the upper horizons, being relatively shallow in the case of the Hutton Makatini (± 440 mm) to fairly deep (± 760 mm) for the Hutton Msinga and 520 mm for the Pinedene Klerksdorp soil type. The

6 planting dates are considered to represent the full range of early-to-late planting periods within the planting window in the area.

Model simulations started 150 days before planting with a soil moisture content of 50% of field capacity at end April/May in order to stabilize soil moisture content by the beginning of planting. Results were subdivided for the 22 El Niño, 18 La Niña and 23 Neutral summers during the period of 63 years, based on the value of the Oceanic Niño Index (http://www.cpc.ncep.noaa.gov/products/analysis_monitoring/ensostuff/ensoyears.shtml).

Results and Discussion

To demonstrate the effect of soil type (as represented by the 3 soil types considered) and climate variability as related to ENSO, Fig. 1 shows the box plot of modeled yields per soil type and type of summer related to ENSO (El Niño, Neutral or La Niña year). These results are representative of yields simulated for planting dates ranging from mid-November to mid-December, considered to be the main planting period within the larger potential planting window indicated earlier. Examination of results indicates sensitivity rather to plant population than row width. So the results shown are for the relatively high plant population of 2.0 – 2.5 plants m⁻² which also, in the majority of cases, resulted in the largest simulated yields.

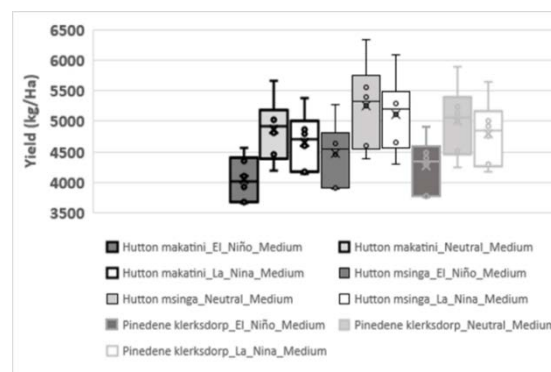


Figure 1 Box plot, showing the yields obtained during El Niño (dark grey), Neutral (light grey) and La Niña (white) summers per each of the soil types as indicated.

From the subset of modeling results, it is clear that the soil type as well as the association with ENSO (and resultant weather conditions) play an important role in determining yield. Yields are, in accordance with observations, lower during El Niño summers than the other years, but they are not significantly

different. Interestingly, simulations suggest higher yields during neutral summers than during La Niña events, related to excessive cloudiness and wet weather towards the middle and end of summer often occurring during La Niña years (not shown). The importance of soil depth is also indicated, with consistently higher yields simulated for all 3 types of summer seasons for the deeper Hutton Msinga soil type (e.g. median yield of 4512 kg Ha⁻¹ during El Niño summers) than for the shallower Hutton Makatini (median yield of 4007 kg Ha⁻¹ during El Niño summers).

Results pertaining to planting date, between the different soil types, are consistent (not shown), whilst a higher planting density leads to a higher yield simulated for all three types of summers. To demonstrate these results, Figs. 2 (a) and (b) show for short-growing-season and long-growing-season maize cultivars respectively the average yields simulated during El Niño year per planting date and plant population.

Higher plant densities have consistently yielded better results than lower densities for both short and long-growing-season cultivars during El Niño years (and the rest). There is a gradual increase (resulting in a total of 20%) for the mean yields from the earliest to latest planting dates (see also the numbers indicated on the bars representing a plant population of 2 m⁻²). Even though the largest reductions relative to La Niña summers are also found in the latter part of the planting window, mean actual yields are still simulated to be higher than for maize planted earlier.

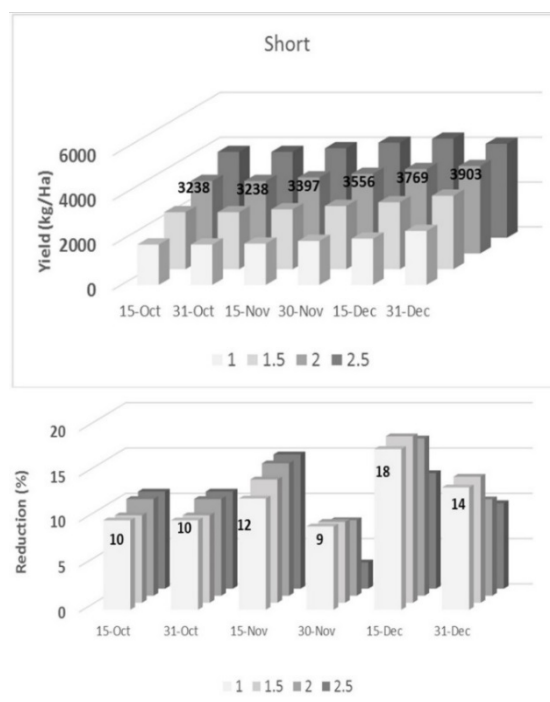


Figure 2a Mean yield (top) simulated for the short growing-season maize cultivar on the Hutton Makatini soil type per planting date (left to right) and plant population as indicated. The percent decrease from the mean simulated during La Niña years, is similarly indicated in lower graph.

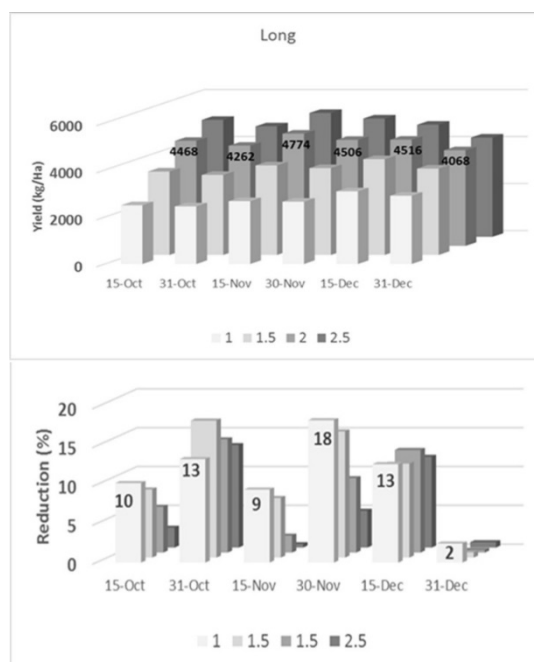


Figure 2b Same as Figure 2a, but for a long growing season cultivar.

For the long-growing-season cultivar, higher planting densities also consistently result in higher yields on average, but the most favored planting date becomes earlier with progressively higher planting

densities. This may indicate a larger tendency for stressors to affect yield negatively due to conditions towards the end of summer and early autumn. The highest mean yields are simulated for the mid-planting dates of 15 November and 30 November. Moreover, the later planting date of 15 December results in higher yields for all planting densities than the earlier dates of 15 and 31 October (e.g. 4516 kg Ha⁻¹ vs. 4468 and 4262 kg Ha⁻¹ for a plant population of 2 m⁻²

This finding is further demonstrated, for medium growing season cultivars on the same (Hutton Makatini) soil type, for high (2.5 plants m⁻²) and low (1 plant m⁻²) populations. The number of El-Niño summers during which the highest yields were obtained at each planting date is shown in Fig. 3.

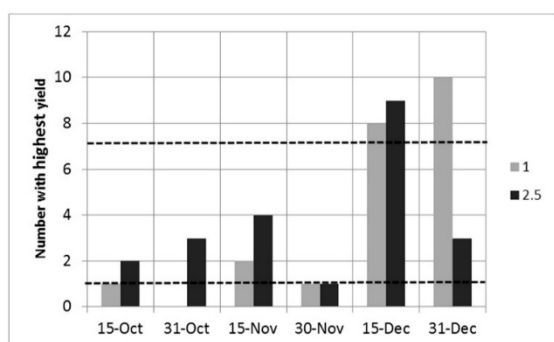


Figure 3 Simulated number of El Niño summers (from a total of 22) during which the highest yield was obtained per planting date, for low (grey bars) and high (black bars) plant populations of medium growing-season maize on Hutton Makatini soil type. Broken lines indicate the 95% upper and lower significance levels.

The low yields for earlier planting relative to late planting, is related to the extreme maximum temperatures experienced especially during the month of January in El Niño years, relative to the other years. Fig. 4 is a box plot for 10-daily maximum temperatures, during January and February, for El Niño and La Niña summers respectively.

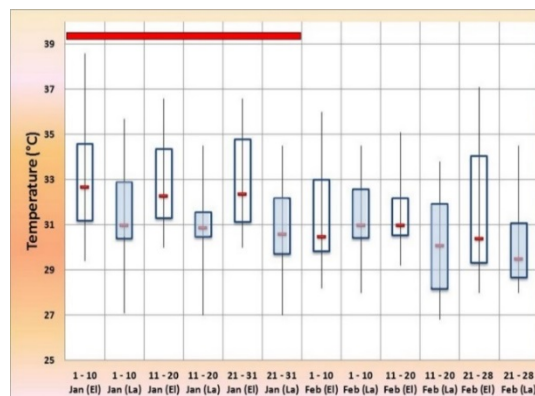


Figure 4 Box plot of maximum temperatures, at ten day intervals, during January and February, for El Niño and La Niña (blue) summers as indicated. The period during which the median temperature difference between El Niño and La Niña summers exceeds 1.5° C, is indicated by a horizontal red bar.

Whilst the difference in median of the maximum temperatures between El Niño and La Niña summers per 10-day period exceeds 1.5°C for each 10-day period in January, it is never higher than 0.5°C during February. The larger difference during January is indicative of the much more unfavorable conditions associated with El Niño during January specifically.

Conclusions

Considering the typical advice prior to El Niño summers, the model simulation have demonstrated that certain recommendations for maize production over the western maize production region would not have contributed to higher yields if followed during the previous 22 El Niño years since 1953. While relatively marginal soils do result in lower yields (even though not to a greater extent than during other years), later planting dates have been shown, especially for short to medium-growing season cultivars, to favour production. The tendency for better yields through mid-to late planting window planting is related to the high maximum temperatures experienced in El Niño years, mostly during January, relative to the other months. With early planting (as recommended), these temperatures are experienced during the more sensitive reproductive phenological stages whilst vegetative phases still dominate during this period if the planting occurred only during December. Therefore, the crop model shows that following the strategy to plant earlier would ultimately have led to lower yields.

References

CEC (2016) Crop Estimates Committee, Department of Agriculture, Forestry and Fisheries, Pretoria.

Hoogenboom G, Jones JW, Wilkens PW, Porter CH, Boote KJ, Hunt LA, Singh U, Lizaso JL, White JW, Urusev O, Royce FS, Ogoshi R, Gijsman AJ and Tsuji GY (2010) Decision Support System for Agrotechnology Transfer (DSSAT) Version 4.5 [CD-ROM]. University of Hawaii, Honolulu, Hawaii.

Jones JW, Hoogenboom G, Porter CH, Boote KJ, Batchelor WD, Hunt LA, Wilkens PW, Singh U, Gijsman AJ and Ritchie JT (2003) DSSAT Cropping System Model. *European Journal of Agronomy*, 18, 235-265.

Landman WA and Beraki A (2012) Multi-model forecast skill for midsummer rainfall over southern Africa. *International Journal of Climatology*, 32, 303-314. DOI: 10.1002/joc.2273

Lazenby MJ, Landman WA, Garland RM and DeWitt DG (2014) Seasonal temperature prediction skill over Southern Africa and human health. *Meteorological Applications*, 21, 963-974. DOI: 10.1002/met.1449

Malherbe J, Durand W and Engelbrecht CJ (2015) Acknowledging decadal to intraseasonal variability in support of agriculture – the 2014/15 maize production season. 31st Annual Conference of the South African Society for Atmospheric Sciences, Potchefstroom, 21–22 September 2015. ISBN 978-0-620-67825-4.

Moeletsi ME, Walker S and Landman WA (2011) ENSO and implications on rainfall characteristics with C for each 10-day period in January, reference to maize production in the Free State Province of South Africa. *Physics and Chemistry of the Earth*, 36, 715-726.

Ropelewski CF and Halpert MS (1987) Global and regional scale precipitation patterns associated with the El Niño–Southern Oscillation. *Monthly Weather Review*, 115, 1606-1626

The climatology of the stratospheric zonal wind and its wave driving in the SAWS operation seasonal prediction system

Kelebogile Mathole¹, Thando Ndarana², Willem A. Landman³ and Asmerom F. Beraki¹

¹South African Weather Service, Research, Pretoria

²Council for Scientific and Industrial Research – Natural Resources and the Environment, Pretoria

³Department of Geography, Geoinformatics and Meteorology,
University of Pretoria, Pretoria,

Abstract

Stratospheric circulation during winter and spring is mostly determined by wave activity forcing which propagates from the troposphere to the stratosphere. Eddy-heat fluxes, which contributes to wave activity forcing are to some extent proxy for coupling the troposphere and the stratosphere. This process occurs as heat fluxes propagates from the upper troposphere up into the stratosphere and interact with the stratospheric mean flow. Using eddy diagnostic method, the study reveals that wave forcing is an important mechanism for defining the proper stratosphere and the dynamical coupling thereof. However, this mechanism seems to be absent in the South African Weather Service - SAWS-ECHAM4.5-MOM coupled model. The result shown by the model's wave forcing suggests inconsistencies with regards to the Charney-Drazin wave propagation theory. This shortcoming also affects important stratospheric circulation and dynamics of the model during winter and spring.

Keywords: wave activity, eddy-heat flux, stratosphere, dynamical mechanism,

INTRODUCTION

On shorter to inter-annual timescale, variations in the stratospheric circulation can influence the troposphere as well as surface climate (Baldwin and Dunkerton, 2001; Charlton *et al.*, 2004). This influence occurs as stratospheric anomalies propagate down into the troposphere by means of a dynamical mechanism, but as to how this coupling really occurs still remains a research question (Wallace, 2000; Plumb and Semeniuk, 2003; Waugh and Polvani, 2010). Notwithstanding, suggestions as to under which dynamical mechanism does this downward influence occur have been raised by several studies (e.g. Polvani and Kushner, 2002; Song and Robinson, 2004; Perlwitz and Harnik, 2004), with mainly wave propagation stated to be the main possible fundamental mechanism (Perlwitz and Harnik, 2004). However, not only is there a one-way downward influence, but also a two-way interaction between the two atmospheres (i.e. from the troposphere to the stratosphere) is also possible. In fact, Perlwitz and Harnik (2004) stressed the troposphere to be the main source of this downward propagation as waves get generated first in the troposphere and then propagate up into the stratosphere where they perturb its circulation. These perturbed stratospheric anomalies also have a tendency of propagating slowly with time into the troposphere on time scales of a few weeks. Since wave driving in the upper troposphere maintains the stratospheric circulation and coupling thereof, the study here aims to try and quantify the current state

of the stratospheric circulation of the model at SAWS using a simple wave driving diagnostic.

DATA AND METHODS

The National Center for Environmental Prediction/ Department of Energy (NCEP/DOE) Reanalysis II (Kanamitsu *et al.* 2002) and SAWS-ECHAM4.5-MOM coupled model datasets from 1982 to 2009 are used. To estimate the propagation of wave activity into the stratosphere (Waugh *et al.*, 1999; Polvani and Waugh, 2004), meridional eddy-heat flux statistics as well as climatologies are calculated. Defined by the vertical component of (E-P) flux (Eq. (2.2)), the meridional eddy-heat fluxes ($v'T'$) are derived from the components of both eddy temperature (T') and meridional wind (v'). Newman and Nash (2000) analysed the wave activity of the stratosphere by classifying it into its different wave types /numbers. However, the study showed that eddy-heat fluxes in the lower and upper stratosphere (at least 100hPa and above) during winter are dominated by large-scale waves such as Rossby-planetary waves (i.e. waves of type 1 to 3) in the middle-latitude regions. Therefore, the analysis here focuses thus on eddy heat-fluxes of the larger planetary scale rather than the smaller scale ones during winter-spring season. The Eliassen-Palm (E-P) flux divergence is also calculated (later in the study) in order to estimate the forcing on the zonal flow. To diagnose stratospheric wave driving, we use Eliassen-Palm (E-P) flux theorem (Edmon *et al.*, 1980; Andrews *et al.*, 1983) which estimates the

divergence of a vector \mathbf{F} in spherical (φ denotes latitude) co-ordinates such that :

$$\nabla \cdot \mathbf{F} \equiv \frac{1}{a \cos \varphi} \frac{\partial}{\partial \varphi} (F_{(\varphi)} \cos \varphi) + \frac{\partial F_{(p)}}{\partial p} \quad (1)$$

Where, $\mathbf{F} = \{F_{(y)}, F_{(p)}\}$ (2)

$$F_{(y)} = -\overline{v'w'} \quad (2.1)$$

$$F_{(p)} = f \frac{\overline{v'\theta'}}{\partial p} \quad (2.2)$$

The quantity \mathbf{F} (Eq. (2)) comprises both the vertical eddy-heat flux (Eq. (2.2)) and the angular momentum. Over bars and primes denotes zonal mean and departure from the zonal means, respectively. Lastly, u and v are the zonal and meridional winds while f and θ are Coriolis parameter and potential temperature, respectively. The divergence of this E-P flux is used to estimate the forcing on stratospheric mean flow.

RESULTS AND DISCUSSIONS

The climatological structure of the middle stratospheric zonal wind as well as its wave driving in the southern hemisphere (SH) is presented (Fig. 1). Here, observed stratospheric winds (Fig. 1a) and heat-fluxes in the lower stratosphere (Fig. 1b) are used as proxy for representing the relationship between stratospheric circulation and wave forcing, which is assumed to be under specialized dynamical mechanisms (Waugh and Polvani, 2010). This association is shown by the general structure of the stratospheric zonal wind as a function of months, together with its associated eddy-heat fluxes in the SH. The zonal wind structure (Fig. 1a) as depicted by the reanalysis data, agrees well with structures seen in other studies (e.g. Andrews *et al.*, 1987; Randel and Newman, 1998 and Waugh and Polvani, 2010).

A somewhat stronger westerly flow in the high latitudes, with wind speed reaching as high as 80m/s can be clearly seen, which on average confirms the strength of the polar vortex during winter/spring months. Associated with this stratospheric flow, is its underlying wave activity (Fig. 1b). It can be seen that eddy-heat flux is generally stronger during mid-late winter when the flow is strong and westerly. This result is in good agreement with the Charney-Drazin theory of wave propagation which explains that larger scale waves can only propagate into a stronger westerly flow. (Charney and Drazin, 1961). The model also captures the general structure of

stratospheric winds even though biased towards a weaker wind. This is confirmed by the negative difference in the zonal wind which also occurs during mid-winter months (Fig. 1c). However, the model's underlying wave activity seems to be extremely weaker than observed as shown by the positive difference (Fig. 1d).

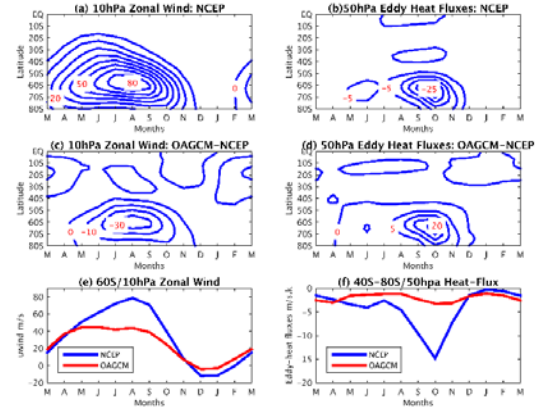


FIG. 1: Monthly annual cycles of 10hPa zonal-mean zonal wind averaged over 27 year climatology period (1983-2009) as well as the corresponding Eddy-heat fluxes at 50hPa also averaged over the same period (a and b, respectively) for NCEP-Reanalysis. Differences between OAGCM-SA and NCEP-Reanalysis climatological zonal wind and eddy-heat fluxes (c and d respectively). Lastly, the climatology of the stratospheric polar vortex and heat-fluxes averaged over the middle-latitudes (e and f, respectively). Contour intervals are 10m/s and 5K.m/s for zonal wind and heat-fluxes, respectively.

This type of wave activity cannot be expected to propagate up into the modelled stratospheric westerly flow in order to satisfy the Charney-Drazin relation. In fact such weaker waves are mostly seen during the summer as the stratospheric flow is easterly (Newman and Nash, 2000). To quantify this relationship further, the strength of the polar night jet confirms the propagation of wave activity into the stratosphere in the NCEP data. This is shown by the deceleration of the polar vortex (Fig 1e, blue line), which occurs a month (late November) after an enhanced wave activity takes place in October (Fig 1f, blue line). As expected, the relationship is not observed in the model as there seem to be little/no wave activity throughout the seasons (Fig. 1e and f, red line).

Furthermore, Fig. 2 shows the response of the stratospheric circulation under extreme wave activity conditions such as the so-called Sudden Stratospheric Warming (SSW). This warming event is one of the major extreme stratospheric events to ever occur in the SH and has been discussed extensively in the literature in order to quantify the dynamical connection between the troposphere and the stratosphere (e.g. Baldwin and Dunkerton, 2001; Polvani and Waugh, 2004) as a result of wave

activity during winter-spring season of the year 2002. Here, the 120-days period before the final break-down of the polar vortex covers the winter-spring season and also ensures that the SSW event is captured during that year of 2002. Observed heat-fluxes confirm this anomalous wave activity, which is indicated by strong heat fluxes of values of about 80K/s (Fig. 2b, blue line). It can also be seen how heat-fluxes fluctuated from earlier days (i.e. from 120th day) prior to the large anomalous wave activity event.

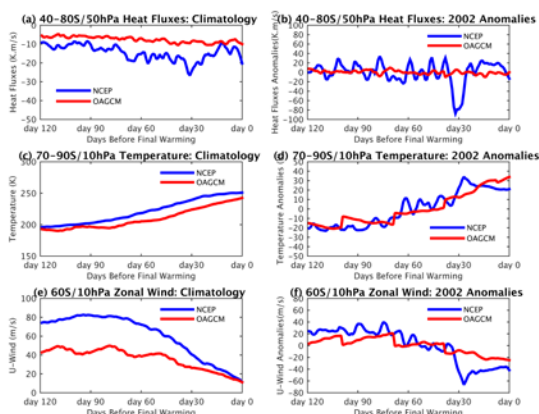


FIG. 2: Daily values of 10hPa zonal-mean wind (at 60°S) and the associated daily eddy-heat fluxes calculated 120 days before the final warming/breaking of polar vortex for both (a). NCEP and (b). Coupled model. Contour intervals are 10K.m/s and 50K.m/s for climatology and year 2002, respectively. Daily climatologies are determined from 1982-2009 period.

The dramatic warming follows few days after this major wave activity, which is also accompanied by the sudden drop in polar vortex speed (Fig. 2d and f respectively, blue line). It is also important to note that this temporary reversal of polar winds coincides exactly with the time when the major warming occurs which is also a few days prior to the final break-down of the vortex. This demonstration is one indication that the coupling mechanism manifests even more under extreme wave activity events. On the contrary, the model seems not to capture any of these stratospheric extreme events (i.e. sudden warming and drop in winds, Fig. 2d and f, red line). This shortcoming is a result of the absence of strong wave activity which was seen in observations (Fig. 2b, red line).

CONCLUSIONS AND FUTURE WORK

The results presented above suggests that wave activity could be an important mechanism for maintaining the proper stratospheric circulation as well as coupling the troposphere and the stratosphere. Using the vertical component of Eliassen-Palm flux, the study has shown that wave activity is absent in the SAWS-ECHAM4.5-MOM coupled model and therefore compromised the

climatological representation of both the stratosphere and its dynamics during winter-spring seasons. This result also reveals that there exist no dynamical coupling in the upward direction. However, to confirm these arguments the study is currently looking at the divergence of E-P flux (using Eq. (1)) in order to examine the entire dynamic wave forcing on the mean flow in the model. And the result will be presented in the future.

ACKNOWLEDGEMENTS

Applied Centre for Climate and Earth Systems Science (ACCESS) is gratefully acknowledged for financially supporting this study. The authors would like express their eternal gratitude to the South African Weather Service for offering its computation and data resources. The National Oceanic and Atmospheric Administration (NOAA) - National Centre for Environmental Prediction (NCEP) is also gratefully acknowledged for making their reanalyses data freely available, which have been utilized intensively in this study.

REFERENCES

- Andrews DG, Holton JR., and Leovy, C.B. (1987). Middle Atmosphere Dynamics. *Academic Press*.
- Andrews, D. G., Mahlman, J. D., and Sinclair, R. W. (1983). Eliassen-palm diagnostics of wave-mean flow interaction in the GFDL "SKYHI" general circulation model. *J. Atmos. Sci.* **40**, 2768-2784.
- Baldwin, M. P., and Dunkerton, T. J. (2001). Stratospheric Harbingers of Anomalous Weather Regimes. *Science*, **294**, 581-584.
- Charney, J. G., and Drazin, P. G. (1961). Propagation of planetary-scale disturbances from the lower into the upper atmosphere. *J. Geophys. Res.* **66**, 83-109.
- Charlton, A. J., O'Neill, A., Lahoz, W. A., and Massacand, A. C. (2004). Sensitivity of tropospheric forecasts to stratospheric initial conditions. *Quart. J. Roy. Meteor. Soc.* **130**, 1771-1792.
- Edmon, H. J., Hoskins, B. J. and McIntyre, M. E. (1980). Eliassen-Palm cross section for the troposphere. *J. Atmos. Sci.* **37**, 2600-2616.
- Kanamitsu, M., Ebisuzaki, W., Woollen, J., Yang, S.-K., Hnilo, J. J., Fiorino, M., and Potter, G. L. (2002). NCEP-DOE AMIP-II Reanalysis (R-2). *Bull. Amer. Meteor. Soc.* **83**, 1631-1643.
- Newman, P. A., and Nash, E. R. (2000). Quantifying the wave driving of the stratosphere. *J. Geophys. Res.* **105**, 12485-12497.

Polvani, L.M., and Kushner, P.J. (2002). Tropospheric response to stratospheric perturbations in a relatively simple general circulation model. *J. Geophys. Res.*, **29**, 14284–14287.

Polvani, L. M., and Waugh, D. W. (2004). Upward Wave Activity Flux as a Precursor to Extreme Stratospheric Events and Subsequent Anomalous Surface Weather Regimes. *J. Clim.*, **17**, 3548-3554.

Perlwitz, J., and Harnik, N. (2004). Downward Coupling between the Stratosphere and Troposphere: The Relative Roles of Wave and Zonal Mean Processes. *J. Clim.*, **17**, 4902-4909.

Plumb, R. A., and Semeniuk, K. (2003). Downward migration of extratropical zonal wind anomalies. *J. Geophys. Res.*, **108**, pp. doi:10.1029/2002JD002773, D7.

Randel, W., and Newman, P.A. (1998). The stratosphere in the Southern Hemisphere. In: Meteorology of the Southern Hemisphere. Washington, D. C: *Meteorol. Monogr*, pp. 243–28

Song, Y., and Robinson, W. A. (2004). Dynamical Mechanisms for Stratospheric Influences on the Troposphere. *J. Atmos. Sci.*, **61**, 1711-1725.

Waugh, D. W., Randel, W. J., Pawson, S., Newman, P. A., and Nash, E. R. (1999). Persistence of the lower stratospheric polar vortices. *J. Geophys. Res.*, **104**, 27191-27201.

Wallace, J. M. (2000). North Atlantic oscillation annular mode: Two paradigms—one phenomenon. *Q. J. R. Meteorol. Soc.*, **126**, 791-805.

Waugh, D. W., and Polvani, L. M. (2010). Stratospheric Polar Vortices. *Geophys. Mon. Ser.*, p. doi10.1029/2009GM000887.

The potential use of CCAM as a meteorological driver to air quality models over the Waterberg-Bojanala Priority Area

M.P Mbedzi^{*1,2}, F. Engelbrecht^{2,3}, S. Grab², J. van der Merwe³ and C. J. Engelbrecht⁴

¹*Eskom Holdings SOC Limited: Research Testing and Development, Lower Germiston Road, Green Route 18, Cleveland, Johannesburg, 2022, South Africa, mbedzim@eskom.co.za*

²*School of Geography, Archaeology and Environmental Studies, University of the Witwatersrand, Private Bag X3, WITS, 2050, South Africa, Stefan.Grab@wits.ac.za*

³*CSIR Natural Resources and the Environment: Climate Studies and Modelling, PO BOX 395, Pretoria, 0001, South Africa, fengelbrecht@csir.co.za and JHvdMerwe@csir.co.za*

⁴*Agricultural Research Council - Institute for Soil, Climate and Water, Private Bag X79, Pretoria, 0001, South Africa, EngelbrechtC@arc.agric.za*

Abstract

This study seeks to assess the ability of the Conformal-Cubic Atmospheric Model (CCAM) in predicting meteorological parameters relevant to air quality studies. CCAM is evaluated against observations from a variety of sources at eight locations in the study area. The variables of interest include temperature, wind speed and rainfall. The CCAM simulations have been performed at a resolution of 8 km. The results show that the model realistically simulated the diurnal cycle in temperature and the onset of stronger winds at most of the locations. The model also realistically portray the seasonal cycle in rainfall over the Waterberg-Bojanala region, although rainfall amounts are overestimated.

Keywords: Meteorological models, Air quality models, Rainfall, Temperature, Wind speed.

Introduction

The promulgation of the National Environmental Management: Air Quality Act (Act No. 39 of 2004) has increased the need for using air quality models in the air quality management in South Africa (DEA, 2010). These models require several input data types, including meteorological fields. Meteorological conditions control the transport, transformation and deposition of air pollutants emitted into the atmosphere from a multitude of both natural and anthropogenic sources.

It is well-recognized in the atmospheric science community that meteorological data used as input to air quality models are insufficient in many areas of the world, in terms of both spatial and temporal resolutions (e.g. Segal *et al.*, 1982; Segal *et al.*, 1982; Lyons *et al.*, 1995). This is more so in developing countries such as South Africa. Both the number and spatial distribution of surface and upper air weather observing stations are also limited in South Africa. In addition, not all the required parameters (e.g. boundary layer height) are observed by the existing observation network. Furthermore, even at the few locations where balloon soundings are made, the boundary layer is often inadequately sampled because of the fast rate of ascent. Moreover, upper air data are only available twice daily, whereas air quality models require such data on an hourly basis or less. The above-mentioned problems,

among others, present a number of problems for air quality modelling and air quality management.

Prognostic meteorological models can provide the aforementioned data. Meteorological models have some advantages over the measurements. For instance, prognostic models have the ability to construct meteorological fields in areas where little or no observations exist. A number of such models have been developed across the world and their sophistication varies from one model to the other. In addition, their predictive skill varies from model to model and from one area to the other. Therefore, it is crucial to assess the ability of each model to predict the parameters of interest over the area(s) of interest before such a model can be used operationally.

The purpose of this paper is to assess the ability of one such model, CCAM (conformal-cubic atmospheric model), to reproduce three of the major (and relatively well-observed) meteorological input parameters to air quality models. Specifically, the current paper focuses on temperature, wind speed and rainfall. The significance of these parameters in the dispersion and fate of air pollutants is well-documented in the literature (e.g. Fisher, 1983; van Jaarsveld and de Leeuw, 1993; Stevenson *et al.*, 1998). For instance, warmer temperatures can accelerate production and increase concentrations of

photochemical oxidants such as tropospheric ozone (see e.g. Lee *et al.*, 2014). Wind speed determines how quickly air pollutants are transported away from their original sources. In addition, wind speed is the most important factor affecting emissions from sources such as wind-blown dust and sea spray (see e.g. Sullivan and Ajwa, 2011). Rainfall significantly contributes to the removal of air pollutants from the atmosphere (i.e. wet deposition) (e.g. Josipovic *et al.*, 2011).

The area of interest is the Waterberg-Bojanala Air Quality Priority Area (see Figure 1). This area is set

for major coal-fired power generation and mining development. This has prompted the South African government to declare this region an air quality priority area in line with the above-mentioned regulation (DEA, 2012). This was done because air pollution levels are anticipated to increase in the near future. In order to accomplish the objective of this study, CCAM is verified against meteorological observations obtained from a variety of sources at eight locations within the study area as shown in Figure 1 below.

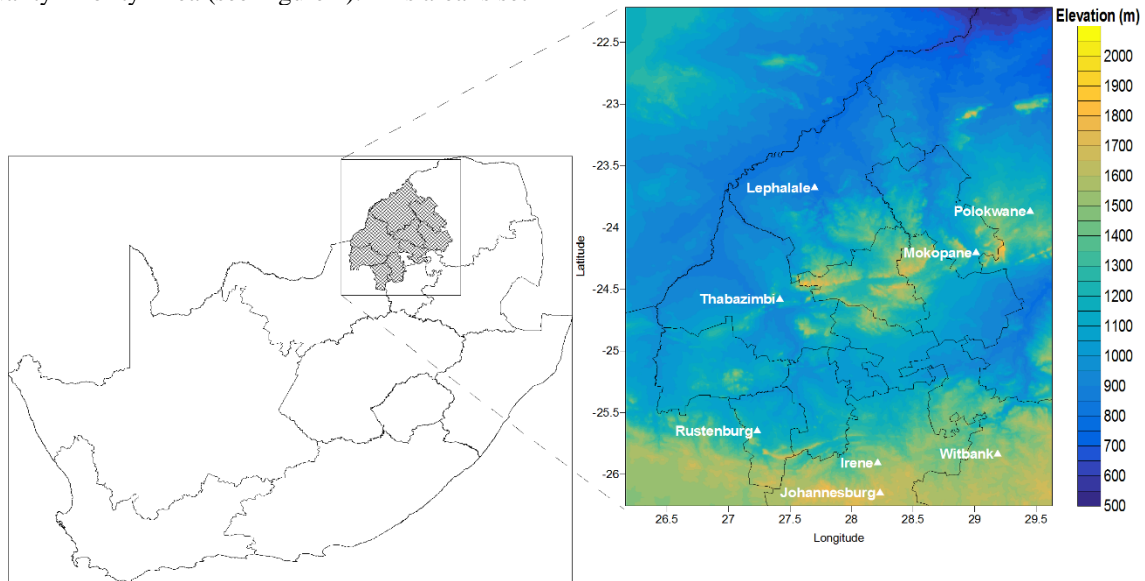


Figure 1: Location of the Waterberg-Bojanala Air Quality Priority Area and weather stations from which the observations used in this study were obtained. Also shown are the elevations in meters above mean sea level within the study area.

Experimental design of the CCAM simulations and observed data

Observations

Three different data sets are used for verification purposes. The simulated rainfall is verified against the Climatic Research Unit (CRU; $0.5^\circ \times 0.5^\circ$; New *et al.*, 1999) and the Famine Early Warning System daily precipitation estimates (FEWS; $0.1^\circ \times 0.1^\circ$; Love *et al.*, 2004). The station data (i.e. rainfall, temperature and wind speed) were obtained from eight of the South African Weather Service (SAWS) weather stations located within the study area. Due to limited data records at these measurement stations, only 12 years of simultaneous data records at all these stations were used for model verification purposes.

The CCAM Simulations

CCAM is a general circulation model (GCM) which may be used in a variable resolution mode to function as a regional climate model (RCM). That is, the model may be integrated with high horizontal resolution over the area of interest, with the resolution gradually decreasing as one moves away from the area of interest. Compared to the more traditional nested limited-area modelling approach (e.g. McGregor, 1997), variable-resolution modelling provides great flexibility for dynamic downscaling from any global model, essentially requiring only sea-surface temperatures and optionally, far-field winds from the host model (McGregor & Dix, 2001; Wang *et al.*, 2004). It also avoids other problems that may occur with limited-area models, such as reflections at lateral boundaries. For the CCAM regional climate simulations presented here, CCAM was integrated in stretched-grid mode over the study region, at a

resolution of about 8 km (0.08° degrees in latitude and longitude). The model domain was about 1300 x 1300 km² in size. The model was forced at hourly

intervals with ERA reanalysis data to obtain a downscaling for the period 1979-2015.

Results and discussion

Model simulations

Monthly variation in rainfall

The seasonal cycle in rainfall as observed and simulated at 8 different locations across the area of interest is displayed in Fig. 2. For each location, weather station (black line), CRU (green line), FEWS (blue line) and CCAM (red line) data is shown. Note that this analysis is valid only for the period 2003-2014, as determined by the availability of weather station data. It is clear that the area of interest is a pronounced summer rainfall region, with the model correctly portraying this cycle. Rainfall totals are overestimated by the model across all months of the year. For the five stations in the Limpopo Province, the CRU data exhibits more

monthly rainfall totals than the FEWS and station data. Generally, there is a closer correspondence between the FEWS and point data than between the CRU and point data. It is interesting to note that for the southern stations (Irene, Johannesburg and Witbank), there are indications of a local rainfall maxima in May. This is not evident in longer term time-series at these locations (see e.g. Engelbrecht *et al.*, 2009), and is probably the result of one or more cut-off low events occurring over these regions in May during the 2003-2014 period. There are also indications of this May rainfall peak in the CRU and FEWS data, but not in the model simulations.

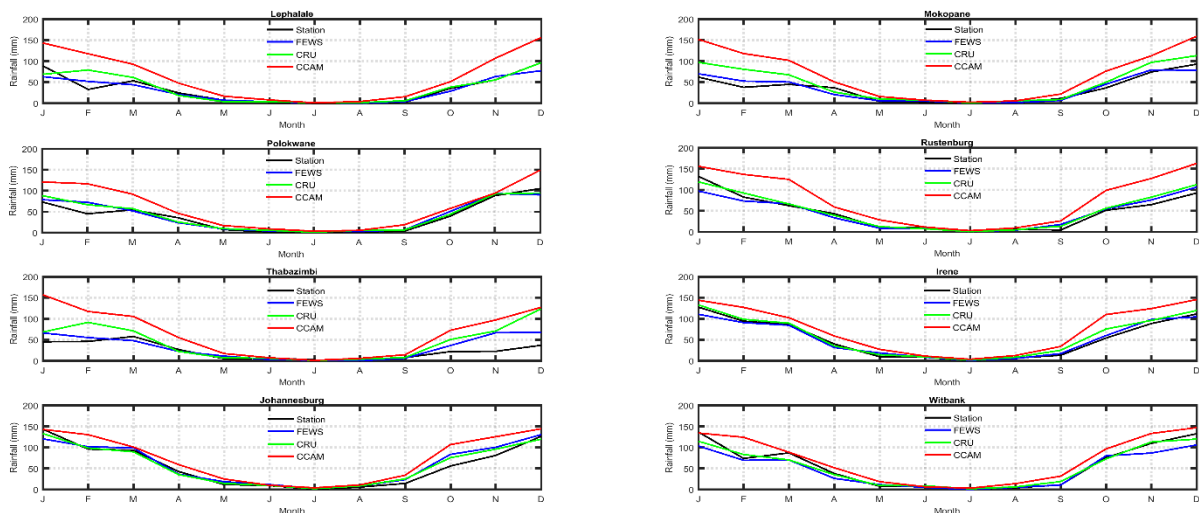


Figure 2: Monthly variation in rainfall at eight different locations over the study area for the period 2003-2014.

Diurnal variation in DJF surface temperature

Fig. 3 shows the diurnal variation in surface temperature for the middle austral summer season (i.e. December-January-February) at eight different stations over the study region. The surface temperatures at all the stations peak at 15:00. The surface temperatures show a very similar temporal pattern across all the stations. Lowest surface temperatures occur in the early hours of the morning, while the highest temperatures occur in the

afternoon after sunrise. The temperatures start increasing at 06:00 at all the stations. This increase continues until it peaks at 15:00, after which a gradual decrease occurs until the minimum in the early morning. The diurnal cycle in temperature is very realistically simulated by CCAM, both in terms of amplitude and timing. At some stations the model slightly overestimates temperatures, but not to the extent in amplitude or space that this overestimation can explain the wet bias (that is, the model is not simulating too intense convection in response to an

overestimation of surface temperatures). At a number of stations, the minimum temperature is simulated to occur an hour earlier than observed, implying that day-time warming sets in earlier than

observed. This bias may well contribute to the model's convective rainfall peak occurring earlier in the afternoon than is observed.

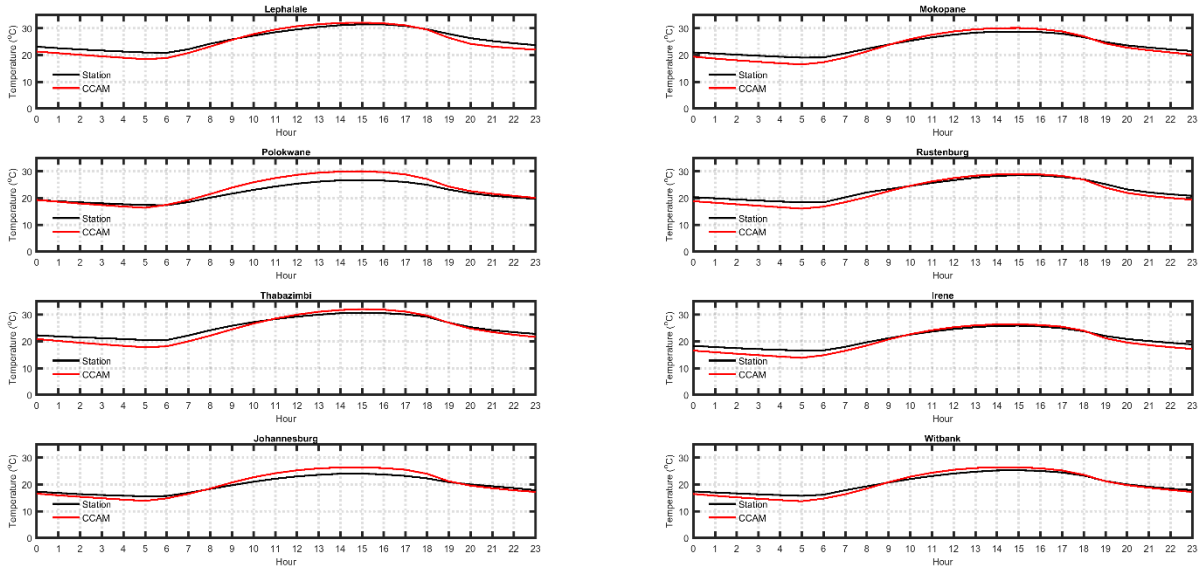


Figure 3: Diurnal cycle in DJF temperature at eight different locations over the study area for the period 2003-2014.

Monthly variation in wind speed

Fig. 4 presents the monthly variation in wind speed at the eight different locations over the region of interest in this study. It can be seen that the wind speed peaks in October at most of the locations

considered here. The model generally correctly simulates both the month-to-month variation in wind speed as well as the occurrence of peaks in October.

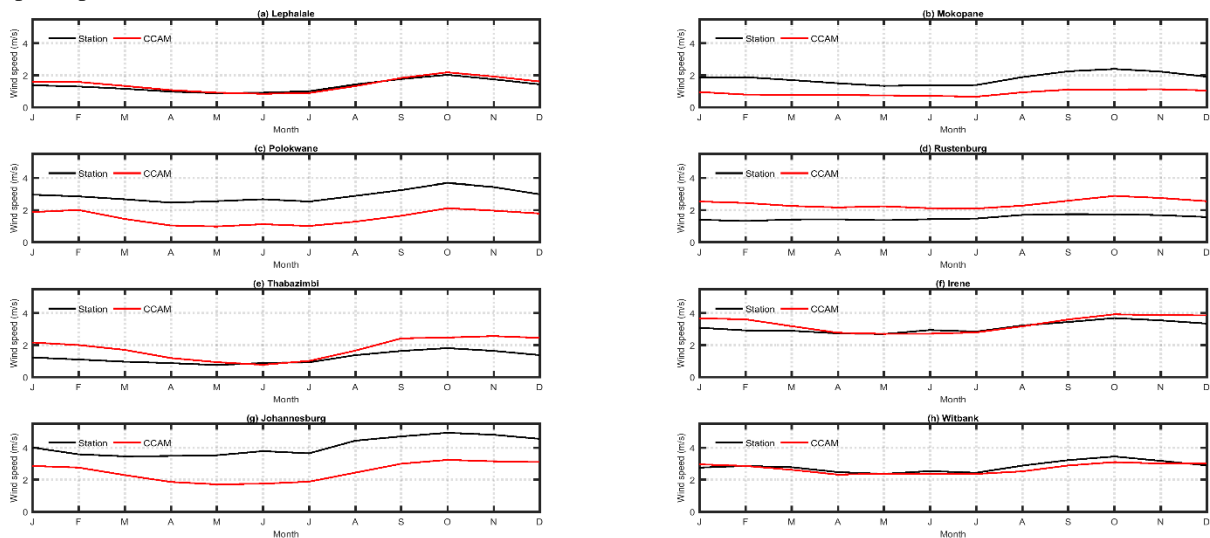


Figure 4: Monthly variation in wind speed at eight different locations over the study area for the period 2003-2014.

Conclusions

The ability of the CCAM variable-resolution atmospheric general circulation model to simulate meteorological variables that are relevant to air quality studies has been assessed in this study. The verification of the model simulations of the seasonal rainfall cycle against month-to-month variation in rainfall at the eight weather stations provide confidence in the ability of the model to simulate the seasonal cycle in rainfall over northeastern South Africa. At some stations, the model slightly overestimates temperatures. Generally, CCAM

Acknowledgements

This research was funded by the Applied Centre for Climate and Earth Systems Science (ACCESS) in South Africa. The views expressed herein are those of the authors and do not necessarily reflect the views of ACCESS. The meteorological observational data were obtained from the South

References

DEA, 2010: National Environmental Management: Air Quality Act (39/2004): List of activities which result in atmospheric emissions which have or may have a significant detrimental effect on the environment, including health, social conditions, economic conditions, ecological conditions or cultural heritage. Government Gazette: 33064, 3-36.

DEA, 2012: Declaration of the Waterberg Priority Area, Notice 494 of 2012, 15 June 2012, Government Gazette, 35435.

Engelbrecht, F.A., Rautenbach, C.J.deW., McGregor, J.L. and Katzfey, J.J., 2002: January and July climate simulations over the SADC region using the limited-area model DARLAM, Water SA, **28**, 361–374.

Fisher, B.E.A., 1983: A review of the processes and models of long-range transport of air pollutants, *Atmospheric Environment*, **17**, 1865-1880.

Josipovic, M., Annegarn, H.J., Kneen, M.A., Pienaar, J.J. and Piketh, S.J., 2011: Atmospheric dry and wet deposition of sulphur and nitrogen species and assessment of critical loads of acidic deposition exceedance in South Africa, *South African Journal of Science*, **107**, 1-10.

Lee, Y.C., Shindell, D.T., Faluvegi, G., Wenig, M., Lam, Y.F., Ning, Z., Hao, S. and Lai, C.S., 2014: Increase of Ozone concentrations, its temperature sensitivity and the precursor factor in South China, *Tellus*, **66**, 1-16.

Love, T.B., Kumar, V., Xie, P. and Thiaw, W., 2004: A 20-year daily Africa precipitation climatology using satellite and gauge data. In: *Proceeding of the 84th AMS annual meeting*, Seattle, WA

overestimates rainfall totals. This study presents promising results for regional-scale atmospheric research studies over the Waterberg-Bojanala Air Quality Priority Area, which, like many other areas in developing countries, has limited meteorological stations observing variables of interest to different research areas, including air quality.

African Weather Service. The utilization of computer clusters of the Centre for High Performance Computing (CHPC) of the Meraka Institute of the Council for Scientific and Industrial Research (CSIR) is acknowledged with gratitude.

Lyons, W.A., Pielke, R.A., Tremback, C.J. and Walko, R.L., 1995: Modelling impacts of mesoscale vertical motions upon coastal zone air pollution dispersion, *Atmospheric Environment*, **29**, 283-301.

New, M., Hulme, M. and Jones, P., 1999: Representing twentieth-century space-time climate variability. Part I: development of a 1961–90 mean monthly terrestrial climatology, *Journal of Climate*, **12**, 829–856.

Segal, M., McNider, R.T., Pielke, R.A. and McDougal, D.S., 1982: A numerical model simulation of the regional air pollution meteorology of the greater Chesapeake Bay area-Summer day case study, *Atmospheric Environment*, **16**, 1381-1397.

Segal, M., Mahrer, Y. and Pielke, R., 1982: A numerical model study of plume fumigation during nocturnal inversion break-up, *atmospheric environment*, **16**, 513-519.

Stevenson, D.S., Collins, W.J., Johnson, C.E. and Derwent, R.G., 1998: Intercomparison and evaluation of atmospheric transport in a Lagrangian model (STOCHEM), and an Eulerian model (UM), using ²²²Rn as a short-lived tracer, *Quarterly Journal of Royal Meteorological Society*, **124**, 2477-2491.

Sullivan, D.A. and Ajwa, H.A., 2011: Evaluation of wind erosion emissions factors for air quality modeling, *Soil Physics*, **75**, 1285-1294.

Van Jaarsveld, J.A. and de Leeuw, F.A.A.M., 1993: OPS: an operational atmospheric transport model for priority substances, *Environmental Software*, **8**, 91-100.

Impacts of spectral nudging on the simulation of present-day rainfall patterns over southern Africa

Mavhungu S Muthige^{1,2} and Francois A Englebrecht^{1,2}

1. Climate Studies, Modelling and Environmental Health, CSIR Natural Resources and the Environment, Pretoria, South Africa, 0001
2. School of Geography, Archaeology and Environmental Studies, University of the Witwatersrand, Johannesburg, 2050

Abstract

Regional climate models (RCMs) provide finer-scale simulations than those of Global climate models (GCMs), whilst being forced by the output of the host GCMs. In this study, we examine the influence of various strengths of spectral nudging on the simulation rainfall patterns in Southern Africa. We use the Conformal-Cubic Atmospheric Model (CCAM) as RCM to downscale ERA-interim reanalysis data to a resolution of 50 km in the horizontal over the globe. A scale-selective filter (spectral nudging technique) is used for nudging the CCAM simulations. The filter is applied at length scales of 9000 km, and 4500 km. The model simulations of rainfall are compared against CRUTS3.2. Both the experiments realistically simulate the present day rainfall patterns.

Keywords: Regional climate models, Rainfall, Spectral nudging

Introduction

Regional Climate Models (RCMs) are used to obtain detailed simulations of present-day or future climate by dynamically downscaling large-scale atmospheric circulation from Global Climate Models (GCMs), or reanalysis data. RCMs are expected to provide finer scales that are absent in the course resolution driving field, but with the condition of maintaining the large scale circulation of the driving field over the high-resolution domain (Jones et al 1995). Traditionally the way to downscale reanalyses datasets or GCM outputs has been through the application of limited-area models (LAMs), with forcing of the host simulation applied at the lateral boundaries of the LAM (Davies 1976). Such methods make use of relaxing the model variables to the driving fields in a buffer zone several points wide along the borders of the high-resolution domain, effectively damping numerical noise and physical inconsistencies that accumulate in the vicinity of the lateral boundaries. LAMs forced by host models/reanalysis following this procedure are sometimes referred to as nested RCMS. However, numerous studies have demonstrated that lateral boundary conditions as described above are associated with a number of problems. These include the spurious reflection of atmospheric waves leaving/entering the high-resolution domain of the LAM, and the occurrence of spurious precipitation in the vicinity of the lateral boundaries. These problems are sufficiently large to cause spurious

small-scale variability in ⁸the LAM simulation thereby limiting the downscaling applicability of the nesting technique. For example, Miguez Macho et al (2004) investigated the ability of an RCM to simulate precipitation and established that the simulations were distorted by misrepresentations of the large scale atmospheric circulation produced by the interaction of RCM simulations with the imposed lateral boundary conditions of the nested domain. Consequently, the spatial distribution of precipitation generated by their RCM varied unrealistically across the domain. There are several studies of the view that large scale atmospheric fields are not realistically communicated to the downscaling RCM. To maintain coherence of the large scale between the host GCM and the LAM, another method known as grid point nudging was developed. It relies on nudging each and every grid cell for example, Castro et al (2005) established that nudging the entire domain interior helps in retaining the value of the atmospheric large scales, which happens to lose variability during the specific period they studied.

Another nudging technique that has gained interest is spectral nudging (Von Storch et al, 2000). In this technique a nudging term is introduced in both the meridional and zonal direction and a selective filtering is done to select only the waves under the selected wave number. Through the process of selective filtering, Miguez-Macho (2005) has outlined that by keeping long scale waves in the

⁸ Email: muthigems@gmail.com

Tel :0128414258

nudging term large scale precipitation bias is eliminated, hence while the small scale features are maintained. In order to maintain the balance between the large scale forcing from the GCM and the change brought by smaller scale features introduced by the RCM appropriate wave numbers need to be selected appropriately through the use of sensitivity tests (Liu et al, 2012). For the southern African region, it is important to specify the nudging appropriately for the key synoptic-scale forcings to be communicated appropriately over the high-resolution region. However, simultaneously, the RCM should be left with sufficient degrees of freedom to simulate deep convection and internal model-domain dynamics. It is the aim of this study to determine the appropriate filter which improves the model's ability to simulate rainfall patterns over Southern Africa.

Methodology

The model

The Conformal Cubic Atmospheric Model (CCAM) is a variable-resolution global atmospheric model, developed by the Commonwealth Scientific and Industrial Research Organization (CSIRO) (McGregor, 1996, 2005; McGregor and Dix, 2001). It employs a semi-implicit semi-Lagrangian method to solve the hydrostatic primitive equations. The model includes a fairly comprehensive set of physical parameterizations. The GFDL parameterizations for long-wave and short-wave radiation are employed, with interactive cloud distributions determined by the liquid and ice-water scheme of Rotstajn (1997). A stability-dependent boundary layer scheme based on Monin Obukhov similarity theory is employed (McGregor, 2005). A canopy scheme is included, and it has six layers for soil temperatures, six layers for soil moisture (solving Richard's equation) and three layers of snow. The cumulus convection scheme uses a mass-flux closure, as which includes downdrafts, entrainment and detrainment.

Experiment design

We use the Conformal-Cubic Atmospheric Model (CCAM) as RCM to downscale ERA-interim reanalysis data at a resolution of 50 km in the horizontal over the globe. The simulations are performed for the period 1979-2012. A scale-selective filter (spectral nudging technique) is used for nudging the CCAM simulations (Thatcher and McGregor, 2009, 2010). The filter is applied at length scales of 9000 km, 4500 km. The filter is applied at six-hourly intervals and from 900 hPa upwards. Use of this spectral-nudging technique ensures that observed synoptic-scale circulation

patterns are represented with increasing realism as the length-scale at which the filter is applied decreases. The model simulations of rainfall are compared against CRUTS3.2 observed data set.

Results and discussions

The seasonal Raifall patterns and monthly rainfall of selected areas over southern Africa are depicted on figures 1 and 2. The simulated CCAM_ERA-interim downscaling realistically represents the movement of the Intertropical Convergence zone. Both the experiments captures the south ward shift of the ITCZ during the DJF season and its northward shift during JJA season. Many regional features such as the west-east moisture gradient (rainfall gradient) across South Africa and the dry slot over the Limpopo basin are also well captured by the model. The decrease in the selective

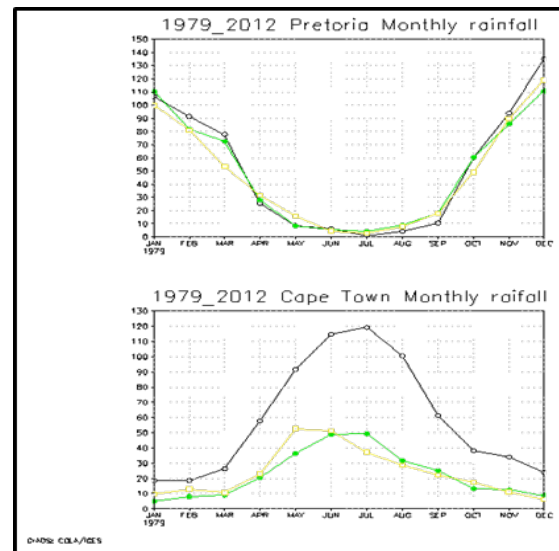


Figure 1: monthly rainfall (mm/day) in Pretoria and Cape Town as simulated by CCAM (yellow-9000 km, green -4500 km) and black line indicating CRU data.

Length scale of spatial filtering somewhat improves the model performance. The downscalings simulate the amplitude of montly rainfall totals well over the interior, but over coastal areas such as Cape Town the amplitude of the monthly totals are underestimated. Both the experiments indicate a pronounced rainfall during the DJF season of the mountainous eastern escarpment of South Africa and Lesotho. It should also be noted that CRU data may not realistically represent the present-day climate in areas with less monitoring stations. The rainfall spring onset period is well captured in Pretoria as well as the winter rainfall onset period in Cape Town. The Taylor diagram in figure 3 indicates how closely the two simulations represent the present-day rainfall pattern across southern

Africa. The 4500 km length-scale spatial filtering (indicated by the black symbols) generally exhibits higher pattern correlations than in the case of the 9000 km length-scale spatial filtering. The standard

deviations of both the simulations for all seasons and annually are larger than 1 (mostly below 1.5) indicating that there is great variability in space in the simulated compared to the observed climates.

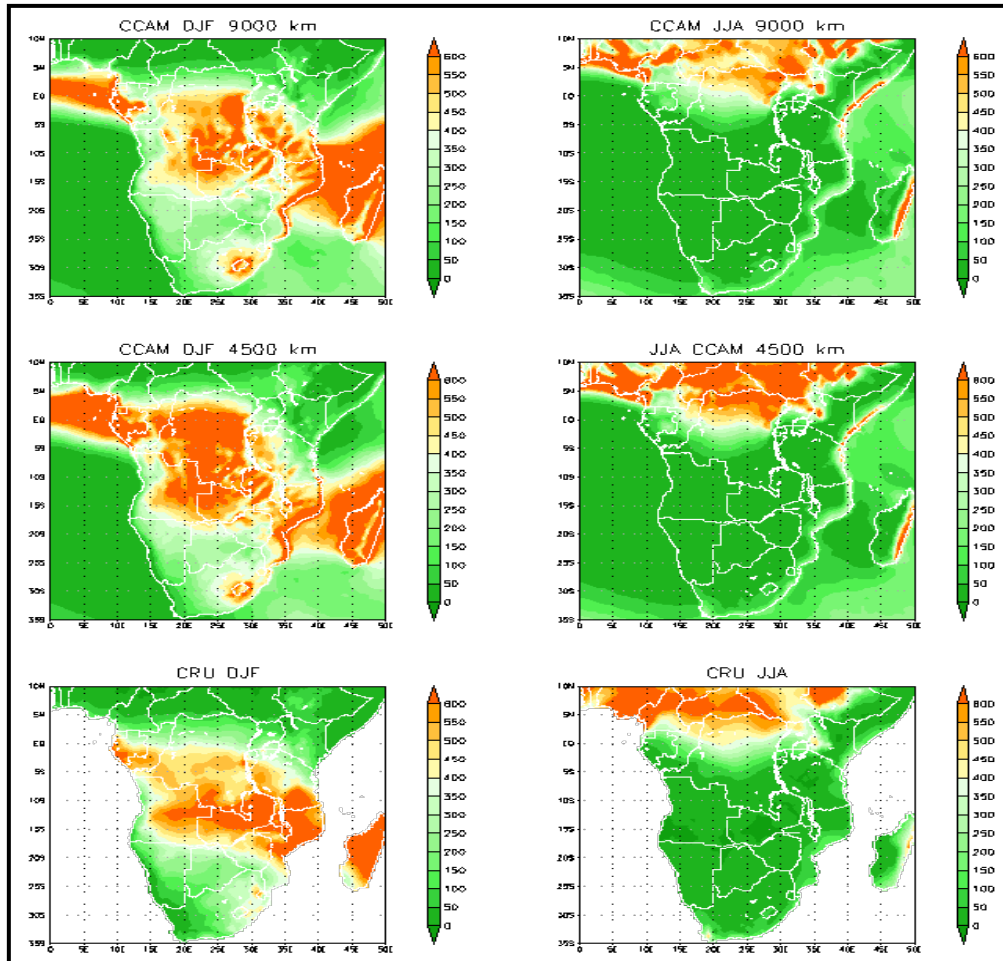


Figure 2: seasonal rainfall (mm/day) over Southern Africa as simulated by CCAM ERA-Interim downscaling (900km and 4500 spatial filtering length scale) compared against CRUTS 3.2 rainfall data.

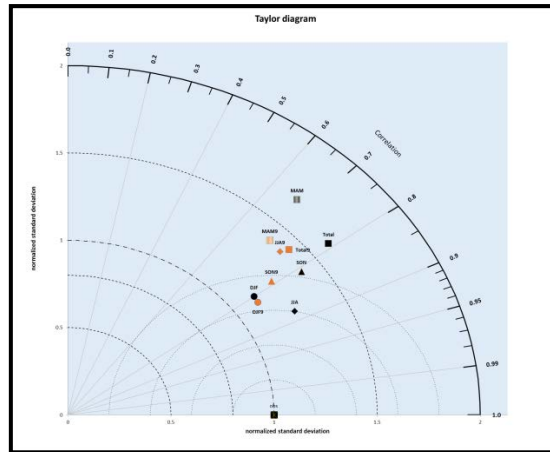


Figure 3 Taylor diagram depicting pattern correlation, normalized standard deviation and normalized root mean square error of the two CCAM-ERA downscalings and observations (cross on the x-axis) for southern Africa. The 4500 km length-scale spatial filtering is indicated by the orange symbols and the 9000 km length-scale spatial filtering is indicated by the black symbols.

Conclusions

Most of the southern Africa regional rainfall features are well captured by the model. A reduction in spatial filtering length scale somewhat improves model performance and further experiments need to be conducted for even shorter length scales of the forcing, in order to determine the most optimum spatial filtering length scale.

References

- Castro, C.L., Pielke Sr, R.A. and Leoncini, G. (2005). Dynamical downscaling: Assessment of value retained and added using the Regional Atmospheric Modeling system (RAMS). *J.Geophys.Res.* 110: D05108.
- Davies, H.C. (1976). A lateral Boundary formulation for multi-level prediction models. *Q.J Roy.Meteor.Soc.* 102:405-418.
- Miguez-macho, G., Stenchikov, G.L. and Robock, A. (2008). Spectral nudging to eliminate the effects of domain position and geometry in regional climate model simulations. *J.Geophys.Res.* 109: D13104.
- McGregor, J.L. (1996). Semi-Lagrangian advection on conformal-cubic grids. *Mon.Weather Rev.* 124: 1311-1322.
- McGregor, J.L. (2005). *C-CAM: geometric aspects and dynamical formulation*. CSIRO Atmospheric research. Dickson ACT. Australia.
- McGregor, J.L. and Dix, M.R., The CSIRO conformal-cubic atmospheric GCM. In: IUTAM symposium on advances in mathematical modelling of atmosphere and ocean dynamics 2001, Kluwer, Dordrecht, p. 197-202.
- Liu, P., Tsimpidi, A.P., Hu, Y., Stone, B., Russell, A.G., and Nenes, A. (2012). Differences between downscaling with spectral and grid nudging using WRF. *Atmos.Chem.Phys.* 12: 3601-3610.
- Rotstayn, L.D. (1997). A physical based scheme for the treatment of stratiform clouds and precipitation in large scale models. I: Description and evaluation of the microphysical process. *Q.J.R. Meteorol.Soc.* 123:1227-1282.
- Thatcher, M. and McGregor, J.L. (2009). Using a scale selective filter for dynamically downscaling with the conformal cubic atmospheric model. *Mon.Weather Rev.* 137: 1742-52.
- Thatcher, M., and McGregor, J.L. (2010). A technique for dynamically daily –averaged GCM datasets over Australia using the conformal-Cubic atmospheric model. *Mon.Weather Rev.* 139: 79-95.
- Von Storch, H., Langenberg, H. and Feser, F.(2000). A spectral Nudging technique for dynamical downscaling purposes. *Mon.WeaRev.* 128:3664-367

Summer circulation trends over southern Africa and its adjacent oceans.

Teboho Nchaba^a, Chris Lennard^{a*}, and Moeketsi Mpholo^{b,c}

^a*Climate System Analysis Group, University of Cape Town, Rondebosch 7701, South Africa*

^b*Materials Research and Engineering Center, Univ. of Pennsylvania, 3231 Walnut Street, Philadelphia, PA 19104-6202, USA*

^c*National University of Lesotho, Dept. of Physics and Electronics, Roma 180, Lesotho*

Abstract

The study detects and determines wind speed trends and their drivers between 1980 and 2015 at 10-m and 850 hPa. Trends are detected in the CFSR, MERRA and ERA-Interim data using Theil-Sen and Mann-Kendall methods. Circulation types and their occurrence frequencies are determined using self organising maps. Negative trends dominate in space and magnitude and average -0.19 and -0.36 m s^{-1} /decade at 10-m and 850 hPa respectively. The trends are moderately linearly associated with the Antarctic and southern oscillation indices and linked to reduced subsidence at 500 hPa and a poleward migration of the subtropical south Atlantic anticyclone.

Keywords: Subtropical Anticyclone, Southern Annular Mode, Intertropical Convergence Zone, Wind speed trends, Angolan low

Introduction

A host of industries require a thorough understanding of wind speed characteristics over different short and long-term time periods. These include marine, aviation, renewable electrical energy, climate and weather research, prediction and/ or forecasting institutes and industries. Studies on long-term wind speed trends and variability are few, relative to those of rainfall and temperature, and confined mainly within data rich northern hemisphere regions including Australia. In a review by Vautard et al. (2010), a large majority of these local, country, and regional studies show a downward trend, termed a global stilling, in historical wind speeds.

Over southern Africa wind speed trends are only discussed briefly for completeness in studies whose focus are other climate variables (Vizy & Cook, 2015). This study fills this gap by providing an analysis of near surface wind speed trends in austral summer (December to January: DJF) over southern Africa and the surrounding Atlantic and Indian oceans (10-40°S, 10°W-50°E) using the most advanced, 3rd generation, reanalyses. Much of the subcontinent is a summer rainfall area and its west and south coasts experience the strongest winds in the summer and hence the omission of the other seasons in the study. The analysis extends from the subcontinent over the two oceans because of their importance to land circulation primarily effected through the tropical high pressure and the midlatitude low pressure belts (Jury & Nkosi, 2000; Reason *et al.*, 2006). The Climate Forecast System Reanalyses versions 1 and 2 (CFSR), the Modern Era Retrospective-Analysis for Research and* Applications version 2 (MERRA2), and the ERA-Interim, are used due to the scarcity of temporal and spatially homogeneous observational data. Three reanalyses, instead of one, are

used to evaluate confidence in the absence of observations for verification.

Summer circulation over the domain is driven by pressure gradients, subtropical anticyclones, midlatitude and continental (Angolan and Kalahari) cyclones, and to a much less extend topographical features. The anticyclones sit above the south east Atlantic and south west Indian oceans and at times ridge over the subcontinent. Flow is mainly south easterly and easterly over the subcontinent, diverges from the anticyclones, and converges over the Intertropical Convergence Zone (ITCZ) and Congo Air Boundary (CAB). In the midlatitudes, cyclones induce a predominant westerly flow. Tyson and Preston-Whyte (2000) have provided detailed descriptions and discussions of these features and their interactions. Large scale circulation regimes, the Southern Annular Mode (SAM) and the El Niño Southern Oscillation (ENSO) have also been associated with fluctuations and variability in flow characteristics over southern Africa (Philander, 1983). Trends in wind speeds are a response to sustained changes in these physical mechanisms.

Methods

Trends in wind speeds and some of its drivers, geopotential height and surface skin temperature, are determined using the Theil-Sen slope estimator (Theil, 1950; Sen, 1968) and their statistical significance with the Mann-Kendall method (Mann, 1945; Kendall, 1975). These are robust non-parametric methods that are insensitive to outliers. The classification and inter-annual changes of the summer weather types are determined using self organising maps (Hewitson & Crane, 2002). The linear association of the SAM and the ENSO are determined by regressing the Marshall (2003)

*Email: lennard@csag.uct.ac.za, Tel: (021) 650 2684, Fax: (021) 650 5773

Southern Annular Mode Index (SAMI) and Southern Oscillation Index (SOI) to the wind speeds time series over the study domain.

Results and Discussion

Figs. 1(a)-(c) show wind speed trends at 850 hPa significant at 95% confidence level. Negative trends dominate and average 1.62, 1.35, and 0.98 m s^{-1} over the

study period for the CFSR, MERRA2, and ERA-Interim respectively. At 10-m (results not shown), the negative trends average 0.76, 0.66, and 0.68 m s^{-1} . Figs. 1(d)-(f) show time series reanalyses for grid cells area averaged within $2.5^\circ \times 2.5^\circ$ centred around the letters A, B, C, D, and E in Fig. 1(a). The time series show that the trends are not superficial step changes as a result of, for example, changes in the reanalyses assimilation systems and/or errors in observations.

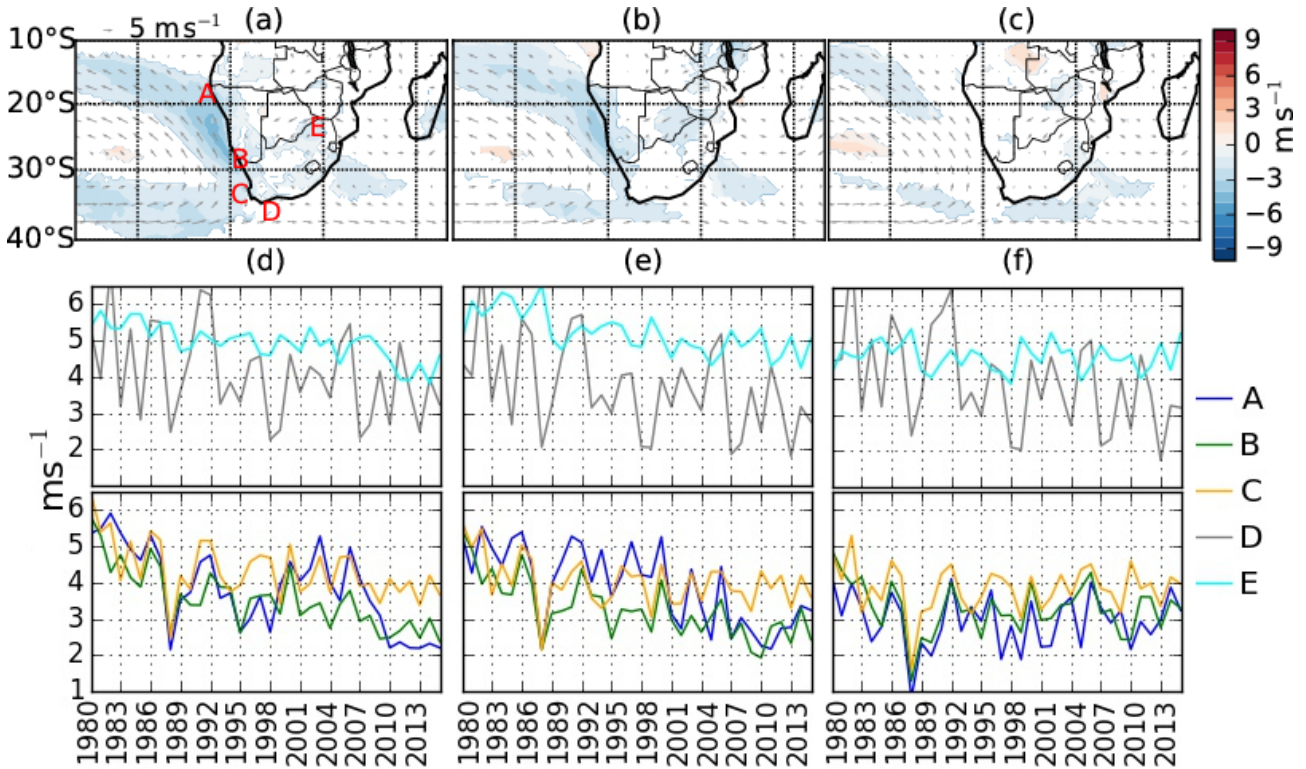


Figure 12: Wind speed trends, significant at 95% confidence level, at 850 hPa (a)-(c) and time series (d)-(g) for grid cells marked with letters A, B, C, D, and E in (a) for the CFSR, MERRA2 and ERA-Interim respectively.

At 10-m (results not shown), wind speeds trends show little agreement between the reanalyses and with their counterparts at 850 hPa. Topographic features are represented uniformly between the reanalyses (results not shown) and therefore cannot be ascribed to the inconsistencies across reanalyses. The differences are associated in part to different computation methods for 10-m and 850 hPa winds. The former are derived using parameterised land surface schemes and the latter through solutions to classical equations (Decker *et al.*, 2012). Trends may also be lower, at 10-m and over land, due to higher frictional drag relative to 850 hPa and over the ocean. The inconsistencies in the trends within and

across reanalyses highlight qualitatively the level of uncertainty in the results.

To establish the relationship between near surface wind speed trends in Fig. 1 and upper level winds, 500 hPa wind speed trends are shown in Figs. 2(a)-(c). Reduction in flow north of 20°S and south of 25°S in south easterly and westerly winds over the Atlantic at 850 hPa is linked to reduced subsidence from 500 hPa towards the surface. The absence of trends at 500 hPa along the west coast, and its adjacent interior, suggest that the trends observed over this area are induced from surface conditions such as changes in surface skin temperature.

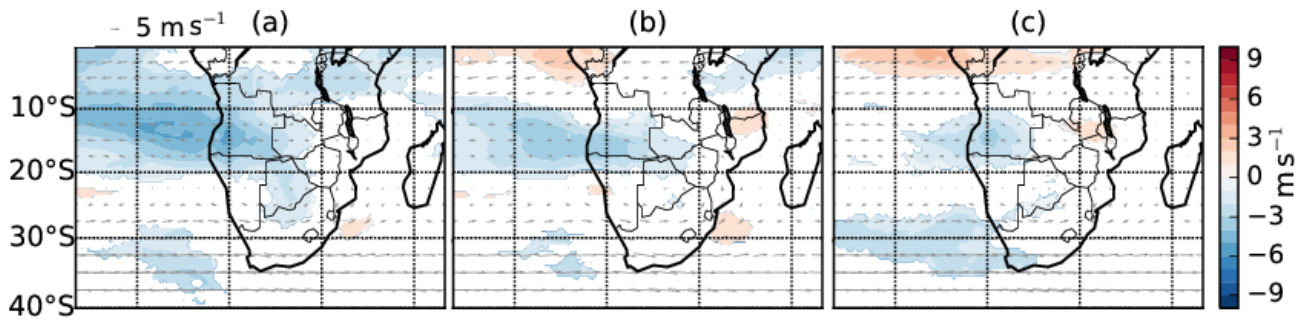


Figure 13: Wind speed trends, significant at 95% confidence level, at 500 hPa for the CFSR (a), MERRA2 (b), and ERA-Interim (c).

Trends in 850 hPa geopotential height Figs. 3(a)-(c) are consistent with wind speeds trends in Figs. 1(a)-(c). They show a southward migration of the south Atlantic high pressure system (SAH) and the weakening of continental lows. The SAH shift is likely induced by a poleward shift in the descending limb of the Hadley cell. The weakening of the continental lows is likely due to increased subsidence over the area in response to a stronger Hadley circulation. The trends in the intensity

of the pressure systems have induced a reduction in the land-ocean pressure gradient and a corresponding reduction in flow straddling the west coast and around the SAH. A SOMs classification of the daily 850 hPa geopotential height fields (not shown) also indicates a progressive increase in the frequency of occurrence of fields with low land-ocean pressure gradients that are associated with low wind speeds.

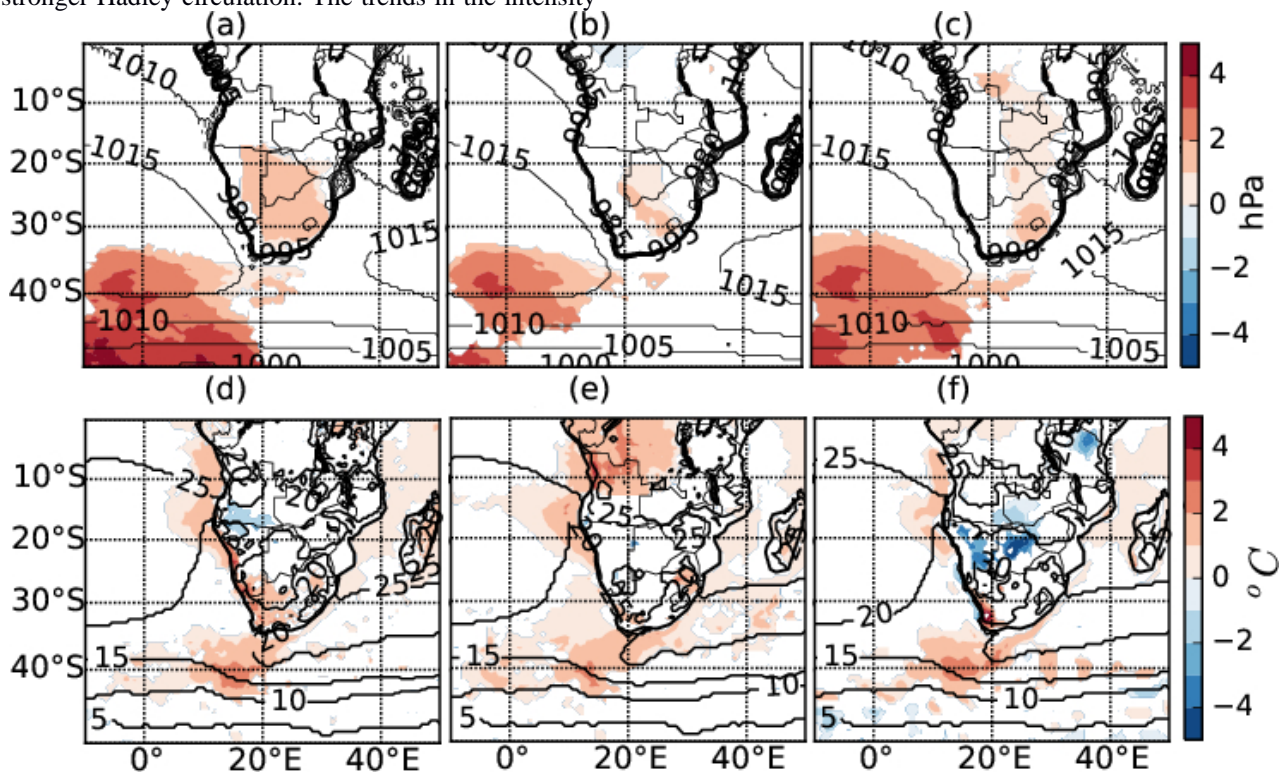


Figure 14: Trends, significant at 95% confidence level, in 850 hPa geopotential height (a)-(c) and surface skin temperature (d)-(e) for the CFSR, MERRA2 and ERA-Interim respectively.

Along the west coast, over the Benguella upwelling system, the negative trends in wind speeds at 850 hPa are also a response to increases in surface skin temperatures over the area (Figs. 3(d)-(f)). The temperature trends are strongest over the Angola Benguella Frontal Zone (ABFZ) and are associated with the shift in the SAH and an ocean wind curl weakened ocean front.

The moderate correlations of the SAM (Figs. 4 (a)-(c)) and ENSO (Figs. 4 (d)-(f)) with 850 hPa wind speeds

have spatial distributions largely consistent with wind speed trends at 850 hPa (Fig. 1), indicating that the trends are partly driven by the SAM and ENSO. The tendency of the SAM towards its positive polarity, also associated with the expansion of the Hadley, is linked to weak westerly winds consistent with findings in this study. The positive polarity of the SAM indicates stratospheric cooling which is induced by ozone depletion and is associated with a poleward migration of the eddy-driven jet (Mathole *et al.*, 2014).

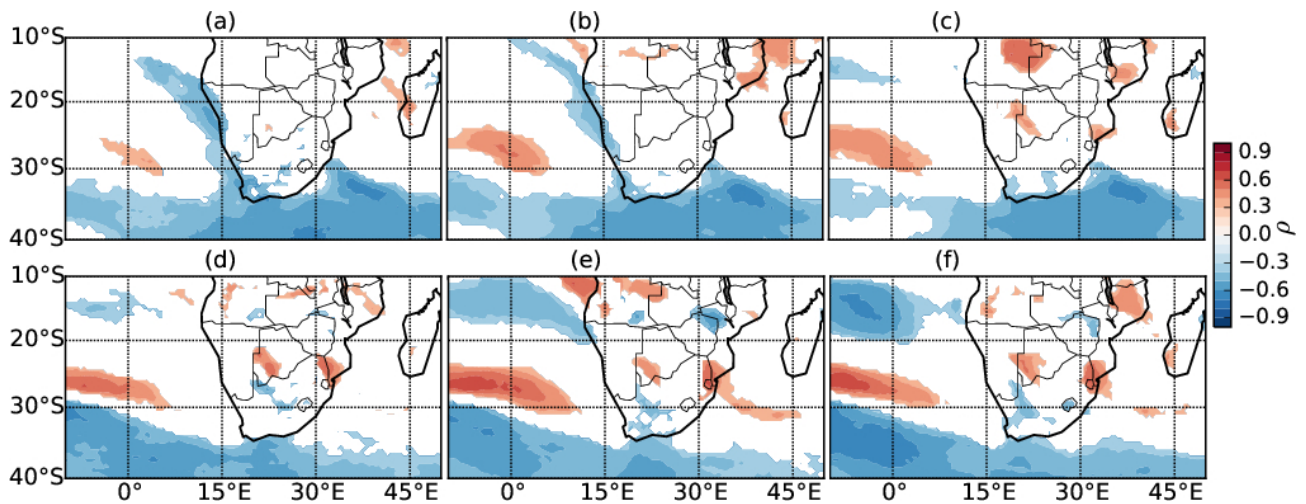


Figure 15: Correlations of the SAM (a)-(c) to the ENSO (d)-(f) to wind speeds at 850 hPa winds for the CFSR, MERRA2, and ERA-Interim respectively.

Conclusions

Results show an overall decrease in wind speeds mainly over the south east Atlantic and the west coast adjacent interior. These findings are largely consistent across the reanalyses, especially between the CFSR and MERRA2. However, the results should be interpreted with caution considering the reanalyses caveats and that the results have not been verified against observations.

Acknowledgements

The Alliance for Collaboration on Climate and Earth Systems Science (ACCESS), the Climate System Analysis Group at UCT, and MRSEC at the University of Pennsylvania (Grant No. DMR-1120901), are thanked their financial support. Sabina Abba Omar, Brendan Argent, and Phillip Mukwenha are thanked for their meaningful discussions and technical support. The NCEP, NASA, and ECMWF are also thanked for providing the reanalyses data used in the study.

References

Decker, M., Brunke, M., Wang, Z., Sakaguchi, K., Zeng, X., Bosilovich, M.G. (2012). Evaluation of the reanalysis products from GSFC, NCEP, and ECMWF using flux tower observations. *Journal of Climate*.25: 1916–1944.

Jury, M.R., Nkosi, S.E. (2000). Easterly flow in the tropical Indian Ocean and climate variability over south-east Africa. *Water SA*.26: 147–152.

Hewitson, B.C., Crane, R.G. (2002). Self-organizing maps, Application to synoptic climatology. *Climate Research*22: 13–26.

Marshall, G.J. (2003). Trends in the Southern Annular

Mode from Observations and Reanalyses. *Journal of Climate*16: 4134–4143.

Mathole, K., Ndarana T., Beraki, A., Landman, A.W. (2014). Impact of lower stratospheric ozone on seasonal prediction systems. *South African Journal of Sciences*. 110: 1–8.

Philander, S.G.H. (1983). El Nino Southern Oscillation phenomena. *Nature*. 302: 295–301.

Reason, C.J.C., Landman, W., Tennant, W. (2006). Seasonal to decadal prediction of southern African climate and its links with variability of the Atlantic Ocean. *Bulletin of the American Meteorological Society*.87: 941–955.

Sen, P.K. (1968). Estimates of the Regression Coefficient Based on Kendall's Tau. *Journal of the American Statistical Association*. 63: 1379–1389.

Theil, H. A rank-invariant method of linear and polynomial regression analysis, I. In Proceedings of the Koninklijke Nederlandse Academie van Wetenschappen, 1950. pp. 386–392.

Tyson, P.D., Preston-Whyte R.A. (2000). *The Weather and Climate of Southern Africa*, Oxford University Press, Cape Town.

Vautard R, Cattiaux J, Yiou P, Thépaut J-N, Ciais P. 2010. Northern Hemisphere atmospheric stilling partly attributed to an increase in surface roughness. *Nature Geoscience*3: 756–761. doi:10.1038/ngeo979.

Vizy, E.K., Cook, K.H. (2015). Understanding long-term (1982–2013) multi-decadal change in the equatorial and subtropical South Atlantic climate. *Climate Dynamics*.46: 2087–211

Comparison of summer and spring carbon dioxide vertical and spatial distribution over the Southwest Indian Ocean Islands using TES data

Xolile G. Ncipha^{1,2}, Venkataraman Sivakumar², Rakotondraompiana Solofo³, Hassan Bencherif⁴

¹South African Weather Service, Private Bag X097, Pretoria, South Africa, 0001, xolile.ncipha@weathersa.co.za

²School of Chemistry and Physics, University of KwaZulu-Natal, Durban 4000, South Africa

³Remote Sensing and Environmental Geophysics Laboratory, Institute & Observatory of Geophysics, Antananarivo (IOGA),
University of Antananarivo, P.O. Box 3843, 101, Antananarivo, Madagascar

⁴Laboratoire de l'Atmosphère et des Cyclones UMR, 8105, 15 Avenue René Cassin, Université de la Réunion, CS 92003, 97744
Saint—Denis, Cedex, Réunion, France

ABSTRACT

Southwest Indian Ocean (SWIO) Islands States are vulnerable to environmental hazards, caused by pressure on the environment to satisfy the socio-economic needs of growing human population. The forests of these tropical islands are rich in biodiversity and they are large carbon sinks. Rapid population growth in these islands is identified as one of the main factors responsible for deforestation, which in turn is the main source of carbon dioxide (CO₂) emissions. This study is born from the Agence Universitaire de la Francophonie (AUF) programme called *observation des Risques naturels en Milieux Insulaires (RAMI)*. In this study we contrast the CO₂ 3-dimensional atmospheric loading between the wet austral summer and dry spring seasons, and compare the relative CO₂ loading over the Comoros, Madagascar, Reunion and Mauritius islands. We found there is a general shift to higher concentrations from summer to spring season and the CO₂ concentration is highest at the southern part of Madagascar in both seasons. This study also illustrates the influence of source strength and meteorology.

Keywords: Tropical forest deforestation, carbon dioxide

Introduction

The Southwest Indian Ocean (SWIO) islands states are vulnerable to natural hazards, these environmental threats are intensified by the changing climate caused by pressure on the environment to satisfy the socio-economic needs of growing human population (AUF, 2015). One of the important natural terrestrial ecosystems that are affected by this anthropogenic pressure in this region is its tropical forests. The human pressure on the tropical forests leads to their removal and degradation. Tropical forests provide various ecosystem services and social benefits (Vieilledent *et al.*, 2013). Tropical forests of SWIO islands states provide natural habitat to diverse fauna and flora and they are regarded as global biodiversity hotspots (Hansen *et al.*, 2013; Vieilledent *et al.*, 2013).

Forests cover approximately 28% of global land surface and contain 77% of all terrestrial above ground carbon (Goodman and Herold, 2014; Baccini *et al.*, 2012). They play a crucial role in the global carbon cycle by exchanging trace gases between the atmosphere and biosphere and they are large carbon sinks. They sequester about a third of the total anthropogenic emissions (Rodda *et al.*, 2016; Vieilledent *et al.*, 2013; Pan *et*

al., 2011). Tropical forests are the biggest with the largest carbon density and they are most diverse forests on Earth. Intact tropical forests store more carbon per unit area than forests in temperate or boreal zones (Goodman and Herold, 2014). Forest clearing particularly in the tropics is a key source of carbon dioxide (CO₂) to the atmosphere (Baccini *et al.*, 2012).

As tropical forest deforestation and degradation is an important source of atmospheric CO₂ over the SWIO islands, however there are other contributing emitters of this greenhouse gas with varied relative strength in each island. Reunion and Mauritius islands are net sources of CO₂, whose emission is dominated by the energy sector. While Madagascar and Comoros islands are net sinks of CO₂, in these islands CO₂ emissions are dominated by land use and land change sector (Praene *et al.*, 2016; Praene *et al.*, 2011; Ministry of Environments and Forests (MEF), 2010; Ministry of Environment and Sustainable Development (MESD), 2010). In this study we are comparing the CO₂ 3-dimensional atmospheric loading between the wet austral summer and dry spring seasons, and compare the relative CO₂ loading over the Comoros, Madagascar, Reunion

and Mauritius islands. This study is part of the Agence Universitaire de la Francophonie (AUF) programme called *observation des Risques naturels en Milieux Insulaires (RAMI)*.

Instrumentation and Method

The data used in this study were collected from the Tropospheric Emission Spectrometer (TES) instrument on-board the Aura satellite. TES is an infrared, high resolution Fourier transform spectrometer (FTS) and it operates in both nadir (downward view) and limb (side view) modes to measure atmospheric profiles. It covers the spectral range 650–3050 cm (3.3–15.4 μm) at a spectral resolution of 0.1 cm (nadir viewing) or 0.025 cm (limb viewing) (Beer, 2006).

We analysed TES nadir view data over the SWIO region bounded by (42.04°- 60.13°) E longitude and (9.04°-26.93°) S latitude. Five areas of interest over the SWIO region were chosen to characterize the austral summer and spring season vertical distribution of CO₂. Table 1 shows these areas and their demarcations. Averaged CO₂ vertical profiles over the areas of interest (Table 1) were constructed by averaging atmospheric CO₂ horizontally at different altitudes up to 18 km altitude during the summer (DJF) 2004-2009 and spring (SON) 2005-2009 seasons. Geographic Information System (GIS) was used to plot all five year surface seasonal spatial distribution maps. The CO₂ data was collected from a column representing the boundary layer with the top at 700 hPa (approximately 3400 m) the level of the first semi-permanent stable layer (Garstang *et al.*, 1996). The CO₂ column data was averaged vertically from the surface to 700 hPa first and the averaged data at different locations was mapped and the spatial data gaps were filled by interpolation. We used the inverse distance weighted (IDW) tool with its default setting for interpolation.

Table 1: SWIO study areas spatial demarcations

Area	Latitude (°S)	Longitude (°E)
Comoros (C)	10.90-13.02	42.81-46.21
North Madagascar (NM)	11.75-17.96	48.88-49.75
Central Madagascar (CM)	15.55-20.12	44.12-51.36
South Madagascar (SM)	21.27-25.46	43.51-48.56
Reunion-Mauritius (RM)	19.82-21.914	54.39-58.40

Results and Discussion

Figures 1(a) and 1(b) show the vertical distribution of CO₂ in austral summer, and spring seasons, over selected study areas over SWIO islands. Between the two seasons there is a clear shift to higher surface concentrations from summer to spring.

This is due to that the peak fire occurrence season in SWIO islands is in spring (van der Werf *et al.*, 2003). There is no particular order in the relative CO₂ surface loading among the study areas in the two seasons, except for SM which has the highest concentrations in both seasons (Figure 1). In both seasons there is a clear influence of the semi-permanent stable layers at about 3400m (700 hPa) and 5500 m (500 hPa) on the vertical tropospheric loading of CO₂ over the SWIO islands (Figure 1). These stable layers separate the tropospheric CO₂ into three bands of layers of different loading, the one between the surface and 700 hPa stable layer, the one between the 700 hPa and 500 hPa stable layers and the layer above 500 hpa.

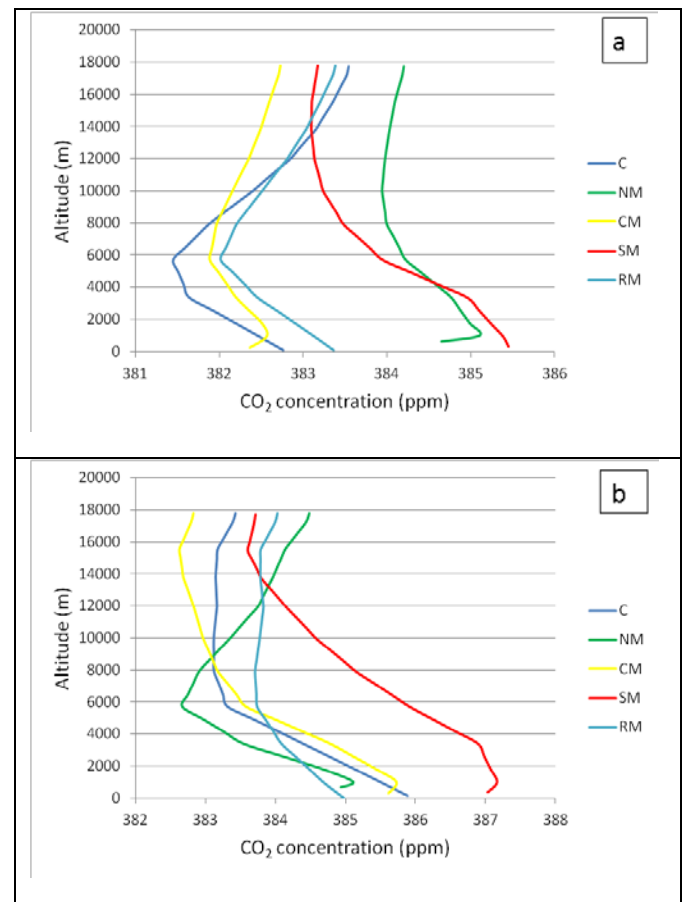


Figure 1. Seasonal CO₂ vertical profiles over selected areas over SWIO islands: Figures 1(a) to (b) are profiles during the summer and spring seasons respectively.

Trajectory analysis (not included in this article) in both seasons, indicate the transport of air from South America and southern Africa over SWIO at the free troposphere level, explaining the increase of CO₂ with altitude above 5500 m altitude. Figures 2(a) and 2(b) show the surface spatial distribution of CO₂ over the SWIO islands in austral summer and spring respectively. Mauritius and Reunion islands show a weak gradient of the spatial concentration distribution, with the concentrations decreasing from the northwest to southwest parts of the islands.

There is no clear difference in the spatial distribution of CO₂ concentration in Comoros islands. In Madagascar there is a clear spatial concentration variation over the island. There are several CO₂ hotspots over the island, with the southern part (SM) having the most and then followed by the central part (CM). These hotspots coincide with the locations of gemstones

and gold mines reported by Cook and Healy, (2012). The spatial extent of high CO₂ levels in spring is wider than in summer, this should be due to the contribution of biomass burning which is at its peak in this season (van der Werf *et al.*, 2003).

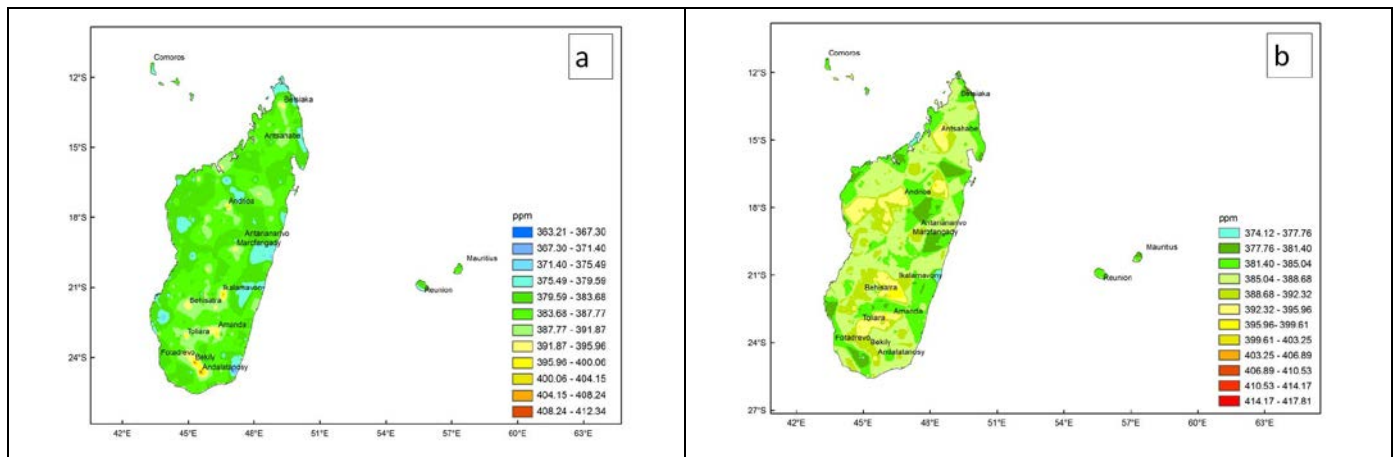


Figure 1. Seasonal CO₂ surface spatial distribution over the SWIO islands: Figures 2(a) and 2(b) are spatial distributions during the austral summer and spring seasons respectively.

Conclusions

The results show that the semi-permanent stable layers at about 3400 m (700 hPa) and 5500 m (500 hPa) play important roles in the vertical tropospheric loading of CO₂ over the SWIO region. The stable layers at 700 hPa and 500 hPa separate the troposphere into three bands of CO₂ layers of different loading. They exert control on the vertical motion of air by inhibiting mixing of air parcels between them. The free troposphere long range air transport from South America and southern Africa is responsible for the increase of CO₂ with altitude above 5500 m altitude over the SWIO region.

There is a clear shift to higher surface concentrations from summer to spring. This is due to the peak fire occurrence season in the SWIO islands in spring. There is no particular order in the relative CO₂ surface loading among the study areas in the two seasons, except for SM which has the highest concentrations in both seasons.

The surface CO₂ foot print in Madagascar resembles the spatial distribution of reported mining activities, especially during the summer season when the background CO₂ surface loading is relatively low. During the summer season the impact of industrial CO₂ emissions stands out, as there are several occurrences of localised high surface CO₂

concentration places surrounded by large areas of low background concentrations. In the spring season the surface CO₂ foot prints are spatially expanded as a result of contributions of emissions from biomass and domestic fuel-wood combustion. The wide CO₂ signatures are prevalent in the south and the west part of Madagascar particularly in the spring season, as a result of the burning of dry forests that are growing in limestone grounds.

Acknowledgements

The authors wish to thank the following organisations for supporting the study in different capacities: University of KwaZulu-Natal School of Chemistry and Physics, the Bureau Océan Indien of the Agence Universitaire de la Francophonie (AUF) and South African Weather Service (SAWS).

References

Agence Universitaire de la Francophonie, (2015). *Observation des Risques Naturels en Milieux Insulaires (RAMI)*. <https://translate.google.com/translate?hl=en&sl=fr&u=https://www.auf.org/bureau/bureau-ocean-indien/actions-regionales/formation/college-doctoral-rami-observation-des-risques-naturels-en-milieu/&prev=search>

- Baccini, A., Goetz, S.J., Walker, W.S., Laporte, N.T., Sun, M., Sulla-Menashe, D., Hackler, J., Beck, P.S.A., Dubayah, R., Friedl, M.A., Samanta, S. and Houghton, R.A. (2012). Estimated carbon dioxide emissions from tropical deforestation improved by carbon-density maps. *Nature Climate Change*. DOI:10.1038/NCLIMATE1354
- Beer, R., 2006. TES on the Aura Mission: Scientific Objectives, Measurements, and Analysis Overview. *IEEE Transactions on Geoscience and Remote Sensing*, 44, 5, 1102-1105.
- Cook, R., and Healy, T. (2012). Madagascar Case Study: Artisanal Mining Rushes in Protected Areas and Response Toolkit. *World Wildlife Fund. Estelle Levin Ltd.* <https://portals.iucn.org/library/sites/library/files/documents/Bios-Cons-Nat-Pro-691-008.pdf>
- Garstang M., Tyson, P.D., Swap, R., Edwards, M., Källberg, P. and Lindesay, J.A., (1996). Horizontal and vertical transport of air over southern Africa. *Journal of Geophysical Research*, 101, D19, 23,721-23,736.
- Goodman, R.C., and Herold, M. (2014). Why Maintaining Tropical Forests is Essential and Urgent for a Stable Climate. *Centre for Global Development*. <http://www.cgdev.org/publication/why-maintaining-tropical-forests-essential-and-urgent-stable-climate-working-paper-385>
- Hansen, M.C., Potapov, P.V., Moore, R., Hancher, M., Turubanova, S.A., Tyukavina, A., Thau, D., Stehman, S.V., Goetz, S.J., Loveland, T.R., Kommareddy, A., Egorov, A., Chini, L., Justice, C.O. and Townshend, J.R.G. (2013). High-Resolution Global Maps of 21st-Century Forest Cover Change. *Science*. 342,850-853, DOI:10.1126/science.1244693.
- Pan, Y., Birdsey, R.A., Fang, J., Houghton, R., Kauppi, P.E., Kurz, W.A., Phillips, O.L., Shvindenko, A., Lewis, S.L., Canadell, J.G., Cias, P., Jackson, R.B., Pacala, S.W., McGuire, A.D., Piao, S., Rautiainen, A., Stich, S. and Hayes, D. (2011). A Large and Persistent Carbon Sink in the World's Forests. *Science*. 333, 988-993, DOI:10.1126/science.1201609.
- Praene, J-P., Radanielina, H. and Rakotondramiarana, H.T. (2016). Dish Stirling System Potential Assessment for Eight Main Sites in Madagascar. *Journal of Heat and Mass Transfer*, 13(1), 119-141. <10.17654/HM013010119>. <hal-0117730>
- Praene, J-P., David, M., Sinama, F., Morau, D. and Marc, O. (2011). Renewable energy: Progressing towards a net zero energy island, the case of Reunion island. *Renewable and Sustainable Energy Reviews*, doi:10.1016/j.rser.2011.08.007
- Rodda, S.R., Thumaty, K.C., Jha, C.S. and Dadhwal, V.K. (2016). Seasonal Variations of Carbon Dioxide, Water Vapor and Energy Fluxes in Tropical Indian Mangroves. *Forests*, 7, 35;doi:10.3390/f7020035.
- van der Werf, G.R., Randerson, J.T., Collatz, G.J. and Giglioli, L. (2003). Carbon emissions from fires in tropical and subtropical ecosystems. *Global Change Biology*, 9, 547-562.
- Vieilledent, G., Grinand, C. and Vaudry, R. (2013). Forecasting deforestation and carbon emissions in tropical developing countries facing demographic expansion: a case study in Madagascar. *Ecology and Evolution*, 3(6):1702-1716.
- Ministry of Environments and Forests, (2010). Madagascar. Second national communication on climate change submitted under the United Nations Framework Convention on Climate Change. Executive summary. <http://unfccc.int/resource/docs/natc/mdgnc2exsume.pdf>
- Ministry of Environment and Sustainable Development, (2010). Second National Communication of the Republic of Mauritius under the United Nations Framework Convention on Climate Change (UNFCCC). <http://unfccc.int/resource/docs/natc/musnc2.pdf>

Anthropogenic Heat Flux in South African Cities: Initial Estimates from the LUCY model

Yerdashin Padayachi¹ and Tirusha Thambiran¹

¹ CSIR Natural Resources and the Environment
Climate Studies, Modelling & Environmental
Health; P O Box 17001, Congella, 4013, Durban, South Africa

Abstract

The anthropogenic heat fluxes (AHF) from buildings, transport and people are an essential component of the urban climate within cities. Presently limited information on the AHF in South African cities exists. This study quantifies the AHF in South African cities using the LUCY (Large scale Urban Consumption of energy) model. This initial work provides an important baseline to support developing an improved characterisation of urban heat islands under a changing climate in South African cities.

Key words: Urban Climate; Cities; Urban Heat Island; Climate Change

1. Introduction

The anthropogenic heat flux (AHF) modifies local atmospheric circulation and surface temperature within cities (Chen *et al.* 2016). Quantifying the AHF can contribute to a better understanding of the links between urban environments and the local climate in cities through improvements in the parameterisation of the surface energy balance within urban canopy models (UCMs) (Loridan and Grimmond, 2012) that are used to simulate the urban heat island effect within cities. Using the information derived from UCM simulations to inform cityscale climate change policy is key to identifying mitigation measures that have synergies for simultaneously improving a city's resilience to climate change impacts, whilst improving air quality. There is to date, limited information on the AHF in South Africa. In this paper, the LUCY (Large scale Urban Consumption of energy), a global to neighbourhood scale AHF model, is used to estimate the AHF in South African cities. The main objectives of the study include the identification of the main area emission sources of the AHF distinguished by settlement type and the analysis of the mean AHF in the three most populated cities in South Africa. The case studies are used to highlight the need to quantify the AHF in South African cities which is becoming more pronounced due to greater development and urbanisation.

2. Instrumentation and Method

2.1. Background

The LUCY model takes into account waste heat emissions from human metabolism, vehicles and buildings (Eq. 1). When the model calculates the AHF across a geographic area, the spatial resolution of the outputs is 2.5×2.5 arc-minutes.

The AHF (Q_F) is calculated:

$$Q_F = Q_m + Q_v + Q_b \quad (1)$$

Where (Q_m) is the waste heat emissions from human metabolism, (Q_v) is the waste heat emissions from traffic and (Q_b) is the waste heat emissions from buildings. Further information about the data used in the LUCY and the assumptions made in the calculations can be found in Allen *et al.* 2011.

2.2. Applying the LUCY model to South Africa

2.2.1. Parameterising the LUCY model

LUCY was parameterised for South Africa by using country level temperature, population, transport and primary energy consumption data for 2011 (Table 1).

Population density data was obtained from the Centre for International Earth Science Information Network (CIESIN) for the year 2010 and 2015. Population density for 2011 was interpolated using the 2010 and 2015 data in ArcGIS 10.3 using the raster calculator

tool. Primary energy consumption data were acquired from the Department of Energy (DoE).

Vehicle population data were sourced from the Electronic National Administration Traffic Information System (e-NATIS) database for the year 2011 and mid-year population data from Statistics South Africa (Stats SA) was used to calculate vehicle density. The vehicle fraction of 0.8 was calculated by dividing the modelled vehicle population from Merven *et al.* (2012) with the live vehicle population statistics from eNATIS. The modelled vehicle population was assumed to be representative of the actual vehicle population due to the inclusion of scrapping factors and vehicle deterioration rates. Merven *et al.* (2012) determined that the average speed for a private motor vehicle in South Africa was 34 km/h for urban areas. However LUCY only provides pre-selected options for average vehicle speed. An average vehicle speed of 32 km/h was assumed to calculate the AHF across South Africa.

Table 1: Data sources used in this study

Heat Source	Input	Source	Spatial Unit
Metabolic Heat	Population Density	CIESIN	Global 2.5 arcminute grid
Vehicle heat	Live vehicles population	e-NATIS	South Africa
		Stats SA	South Africa
	Average Vehicle Speed	Merven <i>et al.</i> (2012)	South Africa
	Vehicle population modelled	Merven <i>et al.</i> (2012)	South Africa
Building heat	Primary energy consumption Temperature data	DoE	South Africa
		Willmot and Matsuura (2016)	Global 0.5° × 0.5° grid

2.2.2. Running the LUCY model

LUCY is best suited to provide a rough estimate of the AHF at a global to regional scale (Yang *et al.* 2013). Model runs for the whole year in 2011 were completed and it was found that the day to day variations in the AHF were comparable to the annual mean AHF. Examples are provided for Johannesburg, eThekweni and Cape Town in the results and discussion section. However it was found that LUCY could not readily produce spatial maps of the mean AHF over many days, weeks, months or years. Spatial analysis of the mean AHF in South African cities was an important component of this study in order to identify ‘hot-spots’ of AHF in the country. Previous studies including Allen *et al.* (2011) and Lindberg and Grimmond

(2013) have run the LUCY model for selected days during the year. A similar approach was taken in this study. LUCY was run for two selected days in 2011 with spatial surfaces of the mean AHF produced at a spatial resolution of 2.5 x 2.5 arc minutes as an initial run of the model to provide a first estimate of AHF.

The mean AHF for two days, namely the 17 January 2011 and the 15 August 2011 are presented with August representing normal mean monthly temperatures across South Africa for 2011 and January representing warmer mean monthly temperatures across South Africa for 2011. Mean monthly temperature data was provided by Willmot and Matsuura (2016). The mean monthly temperature for South Africa in August was 17°C and the mean monthly temperature in January was 22°C. LUCY assigns the mean monthly temperature for each day in the month when monthly mean temperature is used instead of mean daily temperature. As such the mean daily temperature data used in the calculations of the AHF by LUCY are equal to the mean monthly temperature

Comparative analysis was used to select the case study cities based on population, total surface area and total primary energy consumption which are the three primary drivers of the AHF (Sailor, 2011). As such the cities of Johannesburg, Cape Town and eThekweni were selected as case studies. Spatial analysis in ARC GIS was done using the zonal statistics tool to determine the spatial mean AHF for 17 January 2011 and 15 August 2011 across different settlement typologies using the Council for Scientific and Industrial Research/South African Cities Network (CSIR/SACN) typology and for the three case study cities used in the study.

3. Results and Discussion

The AHF was compared for both days across the major cities and smaller settlements within South Africa to provide an indication of AHF ‘hot spots’ (Table 2). The mean AHF was found to be greater on the 15 January 2011 compared to the 15 August 2011. The City Region represented by Gauteng has the largest mean AHF in South Africa which is about five times larger relative to other settlement types. Cities in general have a high mean AHF. Population density and energy consumption per land use type are likely drivers in the spatial distribution of the AHF (Sailor, 2011) across South Africa.

In **Table 3**, the high population, total surface area and total primary energy consumption contributed by different land use activities within the major cities in South Africa are compared. Total surface area, population and total primary energy consumption are not always proportional, for example Tshwane is quite large in area, has a large population but the city's energy consumption is much lower than that of Cape Town. Cape Town, eThekweni and Johannesburg have the largest populations in South Africa.

Table 2: The mean AHF by settlement type for South Africa for 17 January 2011 and 15 August 2011.

Settlement type	AHF mean for 17 January 2011 (W.m ⁻²)	AHF mean for 15 August 2011 (W.m ⁻²)
Sparse Rural	0.03±0.21	0.02±0.18
Service Town	0.68±1.13	0.60±0.99
Dense Rural	0.27±0.24	0.24±0.21
High Density Rural	0.34±0.44	0.30±0.38
Local or Niche Town	0.27±0.53	0.24±0.46
Regional Centre 2	1.16±2.09	1.04±1.86
Regional Centre 1	1.22±2.27	1.06±1.95
City	1.30±2.65	1.13±2.29
Regional Centre 3	1.02±2.21	0.89±1.94
City Region	3.25±6.46	2.83±5.63
Homeland	0.03±0.05	0.03±0.05
Non-Homeland	0.00±0.00	0.00±0.00

The City of Johannesburg has the greatest mean AHF relative to eThekweni and Cape Town which is about 6.9 W.m⁻² on 17 January and 6.3 W.m⁻² on 15 August (**Table 4**). The mean annual AHF is provided for comparability. While the mean AHF on both days are within the deviations of the mean annual AHF, the mean AHF on 17 January is larger, relative to the mean AHF on 15 August. The results do indicate that the AHF mean on a 'hot day' is higher relative to a 'normal day'.

Table 3: Population, total surface area and primary energy consumption of South African metropolitan municipalities in 2011.

City	Population ¹ (million)	Total Area ² (km ²)	Primary Energy Consumption ³ (PJ)
Cape Town	3.74	816	159
eThekweni	3.42	1062	210
Johannesburg	4.40	1645	176
Mangaung	0.74	176	15
Buffalo City	0.76	168	23
Nelson Mandela Bay	1.16	389	31

Tshwane	2.91	1230	93
Ekurhuleni	3.17	1975	127

1. Data source: Stats SA; 2. Data source: Municipal Demarcation Board; 3. Data source: Sustainable Energy Africa (SEA, 2015)

When the mean AHF in Johannesburg for 2011 is compared to other cities (**Table 5**), the AHF in Johannesburg is shown to be significantly smaller due to the city's relatively smaller population. The mean AHF in London, for example, is almost twice that of Johannesburg with a population two times larger than Johannesburg.

Table 4: The mean AHF for Johannesburg, eThekweni and Cape Town on 17 January 2011 and 15 August 2011.

City	Annual AHF mean (W.m ⁻²)	AHF mean for 17 January 2011 (W.m ⁻²)	AHF mean for 15 August 2011 (W.m ⁻²)
Johannesburg	4.52±7.87	6.92±9.93	6.34±8.98
eThekweni	3.40±5.93	4.23±7.25	3.67±6.23
Cape Town	2.65±4.92	3.24±6.57	2.70±5.51

Table 5: Comparative analysis of AHF mean for different cities

City	Population (millions)	Total Area (km ²)	Year of estimate	AHF Mean	Citation
Johannesburg	4.4	1645	2011	4.5	This study
Beijing	19.61	3937	2010	17	Yang <i>et al.</i> (2014)
Shanghai	23.02	3885	2010	19	Yang <i>et al.</i> (2014)
Guangzhou	12.7	3820	2010	7.8	Yang <i>et al.</i> (2014)
Taiwan	23.20	1140	2010	9.6	Koralegedara <i>a et al.</i> (2016)
London	7.56	1738	2005-2008	10.9	Iamarino <i>et al.</i> (2012)
Sao Paul	10.89	2707	2007	13.2	Ferreira <i>et al.</i> (2011)

By 2030, the UN population division predicts that Johannesburg will be one of six megacities in Africa. The production of waste heat may not be a problem at present while energy consumption levels remain relatively low. However, accelerated population growth and energy consumption in the future will contribute to greater waste heat production. The effect of the AHF on urban temperature will become even more pronounced in the future. This will be additional to the climate change impacts on warming patterns in the city.

Conclusions

The LUCY model has been used in this study to provide an initial estimate of the AHF in South African settlements. The results indicate that cities in South Africa are important sources of waste heat emissions. The inclusion of the comparison between the AHF mean on a 'hot day' versus a 'normal day' highlights the sensitivity of the AHF to temperature change. Waste heat emissions in cities contribute to increasing urban temperatures and in turn higher urban temperatures contribute to increasing waste heat production. Waste heat is an unwanted product of energy consumption and under future scenarios of development and climate change in South African cities, the AHF within South African cities will grow. The AHF will contribute much more to urban temperature change in the future. As a consequence, waste heat emissions will become an important tradeoff for cities to account for in climate change policy.

AHF is an essential factor in city-scale atmospheric circulation and surface temperature and as such, there is a need to improve our ability to quantify the AHF in South African cities. Future work towards improving the parameterisation of building, transport and human sources of waste heat emissions within these cities is envisaged. The input of such data into UCMs will help support research into urban heat island effects in South African cities under a changing climate.

References

- Allen, L., Lindberg, F., & Grimmond, C. S. B. (2011). Global to city scale urban anthropogenic heat flux: model and variability. *International Journal of Climatology*, 31(13), 1990-2005.
- Chen, B., Dong, L., Liu, X., Shi, G. Y., Chen, L., Nakajima, T., & Habib, A. (2016). Exploring the possible effect of anthropogenic heat release due to global energy consumption upon global climate: a climate model study. *International Journal of Climatology*.
- Ferreira, M. J., de Oliveira, A. P., & Soares, J. (2011). Anthropogenic heat in the city of São Paulo, Brazil. *Theoretical and applied climatology*, 104(1-2), 43-56.
- Iamarino, M., Beevers, S., & Grimmond, C. S. B. (2012). High-resolution (space, time) anthropogenic heat emissions: London 1970– 2025. *International Journal of Climatology*, 32(11), 1754-1767.
- Lindberg, F., Grimmond, C. S. B., Yogeswaran, N., Kotthaus, S., & Allen, L. (2013). Impact of city changes and weather on anthropogenic heat flux in Europe 1995–2015. *Urban Climate*, 4, 115.
- Loridan, T., & Grimmond, C. S. B. (2012). Characterization of energy flux partitioning in urban environments: links with surface seasonal properties. *Journal of Applied Meteorology and Climatology*, 51(2), 219-241.
- Merven, B., Stone, A., Hughes, A., & Cohen, B. (2012). Quantifying the energy needs of the transport sector for South Africa: A bottom-up model. University of Cape Town, Cape Town, RSA.
- Koralegedara, S. B., Lin, C. Y., Sheng, Y. F., & Kuo, C. H. (2016). Estimation of anthropogenic heat emissions in urban Taiwan and their spatial patterns. *Environmental Pollution*, 215, 84-95.
- Kušnerová, M., Valíček, J., Harničárová, M., & Tozan, H. (2016). Prediction of Optimal Load and Performance of Thermal Batteries. In *Applied Mechanics and Materials* (Vol. 821, pp. 641-648). Trans Tech Publications.
- Sailor, D. J. (2011). A review of methods for estimating anthropogenic heat and moisture emissions in the urban environment. *International Journal of Climatology*, 31(2), 189-199.
- Sustainable Energy Africa (2015). State of Energy in South African Cities 2015, Sustainable Energy Africa, Cape Town, RSA.
- Willmott, C. J. and K. Matsuura (2016) Terrestrial Air Temperature: 1900-2014 Gridded Monthly Time Series, Retrieved from http://climate.geog.udel.edu/~climate/html_pages/Global2014/README.GlobalTsT2014.html. Accessed 02 April 2016.
- Yang, Y., Endreny, T. A., & Nowak, D. J. (2013). A physically based analytical spatial air temperature and humidity model. *Journal of Geophysical Research: Atmospheres*, 118(18).
- Yang, W., Chen, B., & Cui, X. (2014). High-resolution mapping of anthropogenic heat in China from 1992 to 2010. *International journal of environmental research and public health*, 11(4), 4066-4077.

Evaluation of the Convective Scale Configurations of the Unified Model

Elelwani Phaduli

South African Weather Service, 012 367-6200, elelwani.phaduli@weathersa.co.za

Abstract

The addition of two convective scale configurations of the Unified Model at the South African Weather Service has led to improvement in both model forecasts and downstream products. Verification statistics of the 1.5 km convective scale model (SA1p5) and 4km convective scale model (SA4) convective scale models has shown that the two models performs better than the 12km model(SA12) . The SA4 configuration performs better than SA1p5 and SA12 when forecasting 2m temperatures. The Contingency Table Statistics shows that the SA4 and SA1p5 configuration has a better skill when forecasting heavy precipitation events compared to SA12. The Gilbert Skill Score shows that SA12 has less or no skill at all for higher precipitation amounts.

Keywords Verification, Numerical Weather Prediction, Unified Model, Spatial Verification

Introduction

Numerical Weather Prediction Models (NWP) are improved, by increasing model resolution and improving model physics and dynamics. High resolution NWP models tend to give more realistic simulation of large scale convective systems such as thunderstorms and Mesoscale Convective Systems like squall lines Done *et al.* (1997).

The South African Weather Service (SAWS) is currently using the Unified Model (UM) as the main for NWP purposes. The UM is run at SAWS under the license agreement between SAWS and the United Kingdom Meteorological Office (MO, hereafter). SAWS started using the UM with 12km horizontal grid spacing (SA12 hereafter) in 2006, SA12 has been run once a day at 00:00UTC over the Southern African domain.

Currently with the commissioning of the high performance supercomputer, SAWS is able to run two high resolution convective scale models over South Africa one with 4km horizontal grid spacing (SA4) and the other with 1.5 km horizontal grid spacing (SA1p5). Both the convective scale models are run four times daily at (00:00UTC, 06:00UTC, 12:00, 18:00UTC) with initial and boundary conditions derived from MO's global model forecasts. Numerous studies have shown that decreasing the horizontal resolution of an NWP model can bring more benefits to the skill of the model forecasts.

Weismann *et al* (1997), used the non-hydrostatic cloud model to simulate the squall lines using 1-12 km resolution models, they found that the squall lines became more realistic as the horizontal grid spacing was decreased to 4km. A study by Davis et al 1999, showed that decreasing the grid spacing of the MM5 model to 1.5km led to the improved diurnal circulations produced by the topography and varying land surface conditions over West central Utah. Another study done at the UK Met Office using the high resolution configurations of the UM indicated that the 4km and the 1km grid spacing models often give more realistic looking precipitation fields because convection is not parameterized but is represented explicitly Learn *et al.* (2008).

Though increasing horizontal resolution of NWP models can be more beneficial to the forecasters and other model users, improved verification strategies are still required. There are drawbacks that are associated with using traditional verification statistics to verify high resolution NWP models.

For verification of rainfall cases spatial verification techniques such as neighborhood methods Ebert (2009), scale separation/decomposition, Roberts and Learn (2008), feature/object based, Davis *et al* (2006) and field deformation methods can be used.

Evaluation and comparison of the three configurations of the UM will be done using both traditional verification approaches and spatial verification techniques

There are limited studies on verification of NWP models over South Africa. This focuses on using

different verification methods to assess the skill of the convective scale models in forecasting temperature and rainfall over South Africa.

Instrumentation and Method

Observations

Observed rainfall forecast were obtained by combining 24 hour total rainfall from both Automated Weather Station (AWS) and Automated Rain Stations (ARS).

Model data

Currently the South African Weather Service is running the Unified Model at different horizontal resolutions on a daily basis. The SA12 configuration is run over the Southern African domain (0-44S; 0-56E) with 48hr lead time and grid spacing of about 0.11 degrees. The SA4 configuration is run over the Southern African domain (0-38S; 5-54E) with 72hr lead time and grid spacing of about 0.038 degrees.

The SA1p5 configuration is run over the South African domain (36-22S; 15-34E) with 36hr lead time and grid spacing of about 0.013 degrees. For verification purposes all the models configurations were gridded to the common grid (i.e. 0.5 x0.5 degree resolutions) using bilinear interpolation methods.

Two spatial verification methods were used to evaluate two heavy rainfall case. The first method used was the Method for Object-Based Diagnostic Evaluation (MODE) which provides an object-based verification for comparing gridded observations with gridded forecasts. Davis *et al.*, (2006).

Another method used was the Wavelet-based Intensity Scale decomposition Casati (2010). Here the binary forecasts and observations are decomposed into sum of components on different spatial scales by using haar wavelet transforms. Two statistics namely the Intensity Scale Skill Score (ISS) as well as the Mean Squared Error (MSE) are calculated for the three configurations of the UM. The perfect score for MSE=0, whereas the perfect score for the ISS=1.

Results and Discussion

Eyeball verification

For all the three cases the spatial maps of the rainfall were used to compare the rainfall intensity and the spatial distribution of rainfall using all configurations of the UM (see fig 1, 2 and 4).

Case 1: 20160310

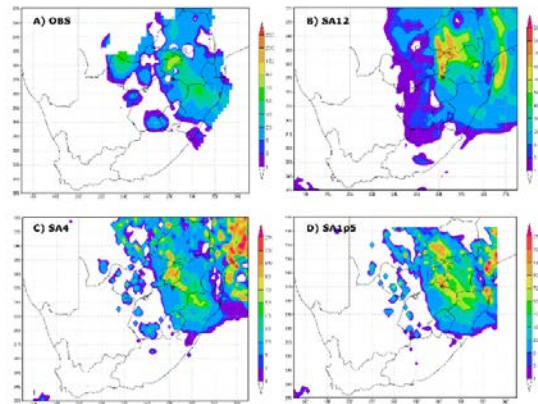


Figure 1: Spatial distribution of 24 total rainfall from three configurations of the UM compared with the observations on 10th March 2016.

From fig 1 it is evident from the maps showing the distribution of the rainfall that both models differ in terms of rainfall intensities and locating the heavy rainfall areas. Both models overestimates the amount of rainfall on the day. The SA4 (fig1(C)) model predicted heavy rainfall over the North Eastern parts of the country, but the observations did not agree with the model. Both models slightly overestimated the rainfall over the central interior of the country (i.e. Gauteng), but the spatial distribution was fairly well.

Wavelet-based intensity scale decomposition

Further analysis of the above case study was done using the Wavelet-based intensity scale decomposition method. The 24hr rainfall totals were decomposed scales into different scales and the Mean Square Error and the Intensity Skill Score were calculated for the three configurations of the UM(see Table 1).

Table 3: Shows the Means Square Error and the Intensity Skill Score for the three configuration of the UM.

Score	SA1p5	SA4	SA12
MSE	0.10547	0.091	0.1035
ISS	0.405	0.501	-0.001

The ISS in Table 1, shows that the SA12 models is worse than the two convective configurations of the UM. The SA4 model performs better than the two configurations.

Case 2: 20160315

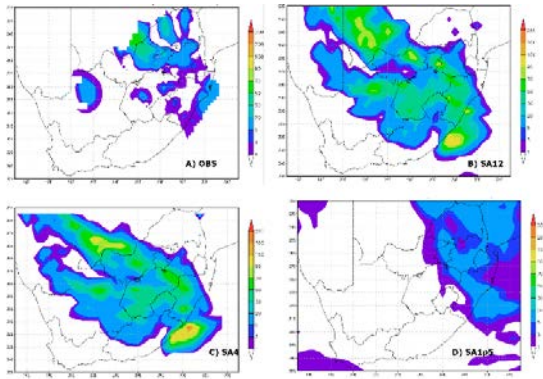


Figure 2: Spatial distribution of 24 total rainfall from three configurations of the UM compared with the observations on 15th March 2016.

The spatial comparison of the 24 total rainfall from three configurations shows that the distribution of rainfall from the two convective scale models is comparable. From fig 2, it is shown that the SA12 model underestimates the amount of rainfall compared to the other two configurations. The SA12 model also misplaced the rainfall, it is showing some rainfall over the North Eastern parts of the country whereas in the other models and the observations it is not shown.

Further analysis of the above case study was done using Method for Object based verification.

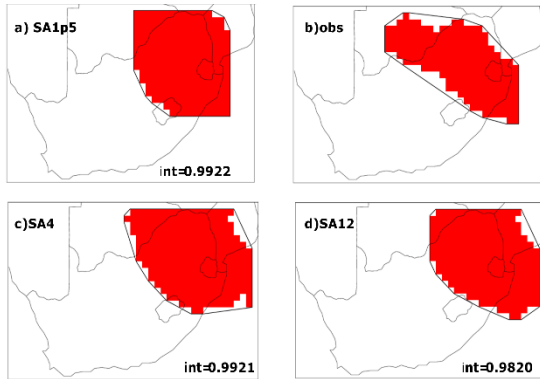


Figure 16: Results for MODE showing the fraction of the area common to both model forecasts and observations on 15th March 2016. 10mm rainfall threshold was used for comparison.

According to fig 3, the total interest or the fraction of the area common to both objects is highest for the convective scale models as compared to the SA12 model. This is consistent with the analysis obtained from subjective or eyeball verification. The difference

of interest between the convective scale models is very small.

Case 3: 20160318

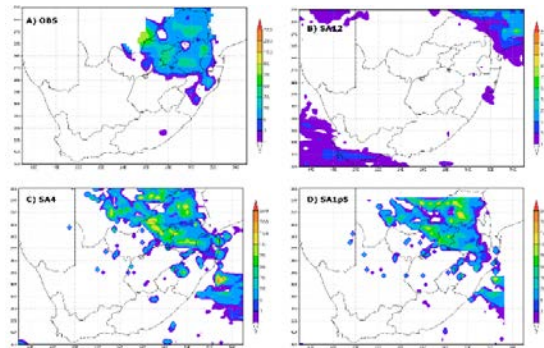


Figure 4: Spatial distribution of 24 total rainfall from three configurations of the UM compared with the observations on 18th March 2016.

The spatial comparison of the 24 total rainfall from three configurations shows that the distribution of rainfall from the two convective scale models is comparable. From fig 4, it is shown that the SA12 model underestimates the amount of rainfall compared to the other two configurations. The SA12 model also misplaced the location of the heavy rainfall.

Method for Object based verification

Spatial comparison of the three configurations of the UM is shown in (fig5), together with the interest or correlations in the bottom of the figure. The interests shown in the bottom of the fig.5 shows a slight difference between Sa4 and SA1p5, the SA12 model missed the rainfall completely.

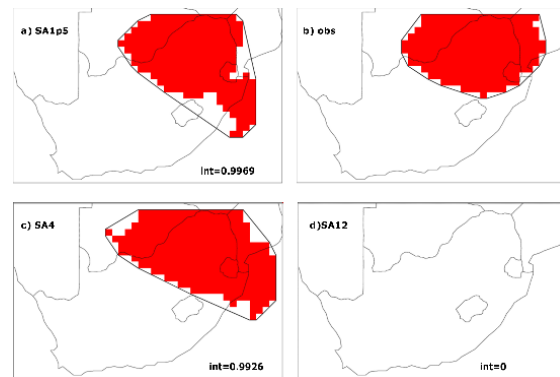


Figure 5: Results for MODE showing the fraction of the area common to both model forecasts and observations on 18th March 2016. 10mm rainfall threshold was used for comparison.

According to fig 5, the total interest or the fraction of the area common to both objects is zero for SA12 model. This implies that there are no common features available between the SA12 model and the observed rainfall. The highest interest was found SA1p5 model. This is consistent with the analysis obtained from subjective or eyeball verification. The difference of interest between the convective scale models is very small also in this case study

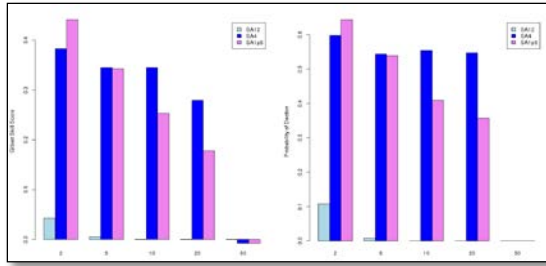


Figure 6: Contingency Table Statistics comparing the three configurations of the UM using different rainfall thresholds.

The Contingency Table Statistics in fig6, shows a major improvement in the skill of the rainfall forecast by adding the convective scale models. The SA12 configuration of the UM has the least skill compared to the two convective scale configurations. Statistics obtained from other rainfall cases also showed similar results.

Wavelet-based Intensity Scale decomposition

Table 4: Shows the Means Square Error and the Intensity Skill Score for the three configuration of the UM.

Score	SA1p5	SA4	SA12
MSE	0.10547	0.091	0.1035
ISS	0.405	0.501	-0.0002

The scores in table 2&3 above shows that the convective scale models gives score that are very close to each other both for MSE and ISS.

Conclusion

Both subjective and objective verification methods used in this study showing increasing the horizontal resolution of the NWP model increases the skill of the rainfall forecasts. In all the three case studies, the SA12 model seems to have less skill as compared to the convective scale models. The improvements in the models will also lead to the improvements of the downstream products produced from the SA4 and SA1p5 models. Future work will consider how data

assimilation and bias correction methods will further improve the skill of convective scale models as SAWS.

Acknowledgements

I would like to acknowledge South African Weather service for funding the trip to attend the SASAS conference.

References

Davis, C., Brown, B. and Bullock, R. (2006). Object-based verification of precipitation forecasts. Part I: Methodology and application to mesoscale rain areas. *Monthly. Weather. Review.* 134:1772–1784.

Davis, C, and Carr, F.(1999), Summary of the 1998 workshop on mesoscale model verification. *Bulletin of American Society.* 81. 809-819

Casati, B. (2010). New developments of the intensity scale technique within the spatial verification methods inter-comparison projects. *Spatial verification methods collection*, 4:113-143

Ebert, E. E. (2008). Fuzzy verification of high resolution gridded forecasts: A review and proposed framework. *Meteorological. Applications.* 15: 51–64.

Jolliffe, I. T. and D. B. Stephenson, D.B. (2003). *Forecast Verification. A Practitioner’s Guide in Atmospheric Science.* Wiley and Sons.

Learn, H.W, Clark, P.A, Dixon, M, Roberts, N,M, Fitch A, Forbes, R, Halliwell C, 2008, Characteristics of high resolution versions of the Met Office Unified Model for forecasting convection over the United Kingdom.

Roberts, N. M., and Lean, H.W. (2008). Scale-selective verification of rainfall accumulations from high-resolution forecasts of convective events. *Monthly Weather. Review.* 136:78–97.

Weismann, ML, Klempad, J.B. and Rotunno R, (1998), Structure and evolution of numerically simulated squall lines, *Journal of Atmospheric Sciences*, 45, 1990-2013.

Preliminary investigation into the impacts of assimilating SST and SLA on the surface velocities in a HYCOM of the Agulhas Current

Tharone Rapeti¹ and Dr Björn Backeberg^{1,2,3}

Nansen-Tutu Centre for Marine Environmental Research, Department of Oceanography, University of Cape Town, South Africa

*Coastal Systems Research Group, Council for Scientific and Industrial Research, South Africa²
Nansen Environmental and Remote Sensing Center, Norway³*

Abstract

Data assimilative ocean models play crucial roles in furthering the understanding, and providing forecasts of the Agulhas Current system. This study investigates the impact that assimilating sea surface temperatures (SST) combined with sea level anomalies (SLA) has on the simulated surface velocities of the Agulhas Current in a Hybrid Coordinate Ocean Model. A preliminary comparison of a free running simulation (FREE) and two assimilation experiments, (1) SLA only assimilation (ASSIM_{SLA}) and (2) combined SLA and SST assimilation (ASSIM_{combined}), indicates that the impact is sensitive to the observed/simulated velocity magnitude in the Agulhas Current, while the mean velocities are overestimated compared to drifter observations.

Keywords

Forecasts, Agulhas Current, data assimilation, SST, SLA, surface velocities

Introduction

The Agulhas Current system, one of the world's most dynamic and energetic western boundary currents, plays a vital role in the resources and ecosystem of the regional marine environment, as well as impacting local weather and global climate (Lutjeharms, 2006).

Recent studies by Rouault et al., (2009) and Backeberg et al., (2012) have indicated that the Agulhas system is undergoing climate related changes. Rouault et al., (2009) noted a decadal warming trend in the region associated with an intensified Agulhas Current, while Backeberg et al., (2012) found that the mesoscale variability in the region has intensified. It has also been hypothesised that the Agulhas leakage, a process of inter-ocean exchange south of Africa, has increased over the past few decades, supplying more warm and saline waters to the Atlantic Meridional Overturning Circulation. This has the potential to counteract the North Atlantic freshening from melting ice-sheets and glaciers due to the anthropogenic warming of the global climate (Biastoch et al., 2008, 2009). A lack of data in the Agulhas systems hinders our ability to quantify the extent to which the Agulhas Leakage has changed, including its potential impact on the global ocean circulation and climate.

Due to the Agulhas' influence on the regional and global climate, it is crucial that these changes are understood, mapped and monitored accurately. The ability to predict these changes on scales of days to decades would enable stakeholders (governments,

environmental agencies etc.), to plan for changes as well as implement mitigation strategies.

This study builds on Backeberg et al., (2014) where the impacts of assimilating along-track SLA into a Hybrid Coordinate Ocean Model (HYCOM) of the Agulhas region were assessed. This study presents a preliminary investigation into how Agulhas Current surface velocities are affected by the combined assimilation of along-track SLA and SST data.

Method

Ocean forecasting and reanalysis systems are dependent on a dynamical numerical ocean model, a data assimilation scheme, and access to regularly available observational data (Backeberg et al., 2014). Using such systems in forecast mode requires that observational data is available in near-real time.

A regional implementation of HYCOM was used in this study. It has been shown to recreate the dynamics in the region to an acceptable degree of accuracy (Backeberg et al., 2008; 2009; 2014). The regional model is set up in a nested configuration, consisting of a 1/10th of a degree resolution HYCOM of the Agulhas System, nested within a basin-scale HYCOM of the Indian and Southern Ocean (George et al., 2010) providing boundary conditions every 6 hours (Backeberg et al., 2014). The model forcing fields and configurations are described in detail in Backeberg et al., (2014).

The Ensemble Optimal Interpolation (EnOI) data assimilation scheme was used to assimilate along-

track SLA only and along-track SLA combined with SST. The EnOI is 3-dimensional and multivariate, and updates the model at an efficient computational cost (Backeberg et al., 2014). This scheme had been previously used in regions with similar dynamics to the Agulhas Current, including the East Australia Current region (Oke et al., 2007), the Gulf of Mexico (Counillon and Bertino, 2009; Srinivasan et al., 2011) and the South China Sea (Xie et al., 2011).

The static ensemble is derived from an unassimilated simulation of the Agulhas HYCOM sampled every 5-days for the period 1998–2007. The model was spun-up prior to the sampling period in order to avoid model drift, which can produce artificial erroneous correlations during the assimilation (Backeberg et al. 2014). The static ensemble is important to the EnOI because it represents the forecast error of the model.

Observations are generally sparse and sporadic in space and time. To assimilate sparse observations it would be impractical to stop the model at random intervals whenever an observation becomes available. Therefore observations are collected over a weekly cycle and assimilated as one batch once a week.

To constrain the model with such a limited number of observations, the multivariate covariance between one observation and the model grid, needs to be calculated. At each point the model is projected into the observational space, a covariance matrix between the model and the observation is then constructed and weighted against the total error covariance, which is the sum of the model error covariance and the observation error covariance.

This is then multiplied by the innovation factor, defined as the difference between the model and the observation. In determining the innovation factor, a first-guess approach is employed, where the analysis model forecast and the collected observations are then compared for the same day in the weekly cycle. The resultant analysis is then projected back into the model space and the model is moved forward in time. A full explanation of the method can be found in Counillon and Bertino, (2009) and Backeberg et al., (2014).

For this study three model simulations were run; FREE, the unassimilated numerical model; ASSIM_{SLA}, only along-track SLA was assimilated; and ASSIM_{combined}, both SST and along-track SLA were assimilated.

Data

Assimilated data

All satellite altimetry data used in the study was produced by Ssalto/Duacs and distributed by Aviso (Archiving, Validation and Interpretation of Satellite Oceanographic), supported by CNES. The delayed time unfiltered along-track SLA from satellite altimeters was used and assimilated into the model (Backeberg et al. 2014).

The SST data assimilated was obtained from the Operational Sea Surface Temperature and Sea Ice Analysis (OSTIA). OSTIA analysis uses satellite data from sensors that include the Advanced Very High Resolution Radiometer (AVHRR), Advanced Along Track Scanning Radiometer (AATSR), Spinning Enhanced Visible and Infrared Imager (SEVIRI), Advanced Microwave Scanning

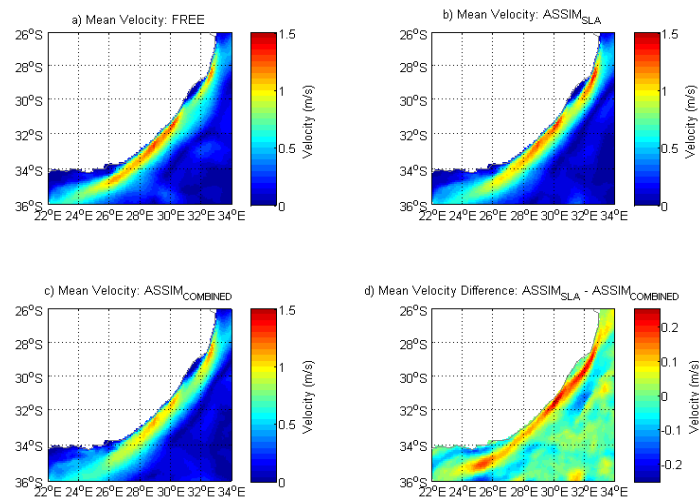


Figure 1. a) 2008 – 2009 mean velocity map from the FREE; b) mean velocity map from ASSIM_{SLA}; c) mean velocity map from ASSIM_{combined}; d) Difference map, of mean velocities, ASSIM_{SLA} minus ASSIM_{combined}. Red colours indicate where ASSIM_{SLA} has higher velocities than ASSIM_{SST}, while blue indicates the opposite.

Radiometer-EOS (AMSRE), and the Tropical Rainfall Measuring Mission Microwave Imager (TMI). The data set has a global coverage, with a grid resolution of 0.054° , and a temporal resolution of one day. OSTIA is produced by the Group for High Resolution Sea Surface Temperature (GHRSSST) project. The OSTIA SST data was specifically produced to support SST data assimilation into Numerical Weather Prediction (NWP) models.

Validation data

To determine the accuracy of the assimilation system against independent (unassimilated) observations, surface velocity data from satellite tracked surface drifting buoys (drifters) were used. These drifters consist of a surface buoy and a 15m deep subsurface drogue. The surface buoy measures temperature and records its position, which is then transmitted to a satellite. The raw drifter data is interpolated to 6 hourly positions, with surface u and v velocities and surface temperatures provided for each corresponding position. The drifter data are managed and distributed by the Global Drifter Program (GDP).

Results and discussion

To allow for the comparison between the simulated surface velocities and the *in situ* drifter data, daily surface velocities from all drifters entering the region $26-36^\circ\text{S}$ $22-34^\circ\text{E}$, between 2008 and 2009 are first calculated. The model fields are then interpolated to the median latitudinal and longitudinal positions of the daily averaged drifter velocities, using the nearest neighbour method of interpolation. Median positions of the drifters were used to ensure that the daily position fell on the drifter track; as opposed to using the mean position, where the position may fall outside the drifter's daily track, thereby representing incorrect dynamics.

From fig.1 (a-c) the impact of the various assimilations on FREE is evident. FREE maintains high velocities along the Agulhas Current, extending further south, compared to both assimilations. This only differs north of the Natal Bight, where the velocities are reduced, similar to that seen in ASSIM_{combined}. FREE and ASSIM_{SLA} show velocities up to 1.4 m.s^{-1} along the Agulhas Current, while ASSIM_{combined} only contains velocities up to 1.2 m.s^{-1} . FREE produces a narrower Agulhas Current as compared to ASSIM_{SLA} and ASSIM_{combined}, with ASSIM_{combined} simulating the widest current.

Fig.1d illustrates the difference the additional assimilation of SST has had on ASSIM_{SLA}. The most notable difference is in the core of the Agulhas

Current. Here the surface velocities in ASSIM_{SLA} are up to 0.25 m.s^{-1} higher than in ASSIM_{combined}. There are also areas, adjacent to the current and inshore of the current south of Port Elizabeth, where ASSIM_{SLA} is around 0.2 m.s^{-1} lower than ASSIM_{combined}.

To better quantify these differences a quantile-quantile analysis was performed (fig.2). This compares *in situ* drifter derived velocities against the corresponding simulated velocities. Simulated velocities that lie closer to the drifter magnitudes are more accurate than those further away. From fig.2 it is visible that the FREE and ASSIM_{SLA} are more accurate at producing surface velocities when they are below 1 m.s^{-1} , with FREE being the most accurate.

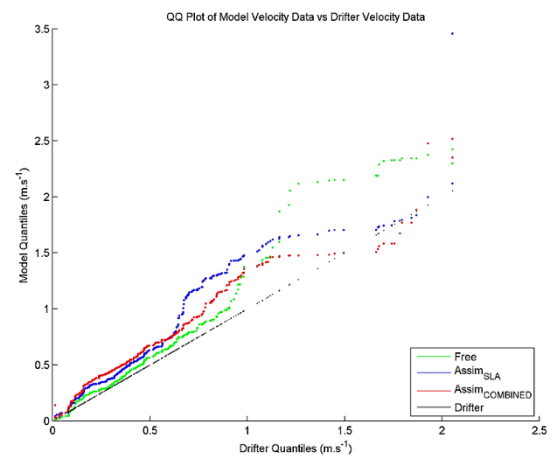


Figure 2. Quantile-quantile (QQ) plot of the *in situ* drifter derived velocities compared to the modelled corresponding velocities. Illustrates how the modelled velocities compare to the *in situ* measurements.

While ASSIM_{combined} is shown to be more accurate when velocities are above 1 m.s^{-1} . ASSIM_{SST} over-estimates velocities below 1 m.s^{-1} , while ASSIM_{SLA} over-estimates velocities over 1 m.s^{-1} (fig.1c).

What these preliminary analyses suggest is that the assimilation of SST benefits regions in the Agulhas Current, where SSTs are high and their gradients are strong. In regions outside the Agulhas Current where SSTs are lower and the gradients are weaker, the combined SLA-SST assimilation has led to an exaggeration of surface velocities. This may be due to incorrect correlations between SST and SSH in the static ensemble used in the EnOI, similar to the finding by Backeberg et al., (2014) in the Agulhas Return Current.

A correlation between the simulated (FREE, ASSIM_{SLA} and ASSIM_{combined}) and drifter-derived u and v component velocities was used as a proxy for

the placement and timing of mesoscale features as in Backeberg et al., (2014); in the region 26-36°S 22-34°E. An improvement in the correlation of $ASSIM_{combined}$ (0.41) over $ASSIM_{SLA}$ (0.36) and FREE (0.06) is noted, suggesting that the combined SST-SLA assimilation has improved the models ability to correctly place mesoscale features in space and time. Comparing the root mean squared error (RMSE), a statistical measure of accuracy, showed an improvement in $ASSIM_{combined}$ (0.46) over $ASSIM_{SLA}$ (0.53) and FREE (0.63).

Conclusions

This preliminary investigation into the impact of combined SST-SLA assimilation in an eddy resolving model of the Agulhas Current has revealed promising results. The initial analysis suggests that the inclusion of SST in the assimilation scheme has improved upon HYCOM's overall accuracy in simulating surface velocities in the core of the Agulhas Current, while also improving the placement and timing of mesoscale features.

Further research is needed to understand the reasons behind $ASSIM_{combined}$ over-estimating surface velocities in the Agulhas Current less than $0.5 \text{ m}\cdot\text{s}^{-1}$, compared to both $ASSIM_{SLA}$ and FREE, whilst markedly improving upon $ASSIM_{SLA}$ in the velocity range $0.6\text{-}1.5 \text{ m}\cdot\text{s}^{-1}$, and FREE where velocities exceed $1.2 \text{ m}\cdot\text{s}^{-1}$.

This preliminary analysis indicates that the assimilation of SST appears to improve the simulated surface velocities in core of the Agulhas Current.

References

- Backeberg BC, Johannessen JA, Bertino L, Reason CJ (2008). The greater Agulhas Current system: an integrated study of its mesoscale variability. *J Oper Oceanogr* 1(1):29–44.
- Backeberg BC, Bertino L, Johannessen JA (2009). Evaluating two numerical advection schemes in HYCOM for eddy-resolving modelling of the Agulhas Current. *Ocean Sci* 5:173–190.
- Backeberg BC, Penven P, Rouault M (2012). Impact of intensified Indian Ocean winds on mesoscale variability in the Agulhas system. *Nat Clim Chang* 2:608–612.
- Backeberg BC, Counillon F, Johannessen JA, Pujol MI (2014). Assimilating Along-track SLA data using the EnOI in an eddy resolving model of the Agulhas system. *Ocean Dyn* 64: 1121-1136. DOI 10.1007/s10236-014-0717-6

Biastoch A, Boning CW, Lutjeharms JRE (2008). Agulhas leakage dynamics affects decadal variability in Atlantic overturning circulation. *Nat* 456:489492.

Biastoch A, Boning CW, Schwarzkopf FU, Lutjeharms JRE (2009). Increase in Agulhas leakage due to poleward shift of Southern Hemisphere westerlies. *Nat* 462:495–498.

Counillon F, Bertino L (2009). Ensemble Optimal Interpolation: Multivariate properties in the Gulf of Mexico. *Tellus* 61:296308.

George MS, Bertino L, Johannessen OM, Samuelsen A (2010). Validation of a hybrid coordinate ocean model for the Indian Ocean. *J Oper Oceanogr* 3(2):25–38.

Lutjeharms JRE (2006). *The Agulhas Current*. Springer-Praxis Books.

Oke P, Sakov P, Corney S (2007). Impacts of localisation in the EnKF and EnOI: Experiments with a small model. *Ocean Dyn* 57: 32–45.

Rouault M, Penven P, Pohl B (2009). Warming in the Agulhas Current system since the 1980s. *Geophys Res Lett* L12:602.

Srinivasan A, Chassignet E, Bertino L, Brankart J, Brasseur P, Chin T, Counillon F, Cummings J, Mariano A, Smedstad O, Thacker W (2011). A comparison of sequential assimilation schemes for ocean prediction with the HYbrid Coordinate Ocean Model (HYCOM): Twin experiments with static forecast error covariances. *Ocean Mod* 37:85–111.

Xie J, Counillon F, Zhu J, Bertino L, (2011). An eddy resolving tidal driven model of the South China Sea assimilating along-track SLA data using the EnOI. *Ocean Sci* 7:609–627.

Acknowledgments

This work has been jointly supported by the Nansen-Tutu Centre for Marine Environmental Research, Cape Town, South Africa, the South African National Research Foundation (grant 87698), the Nansen Environmental and Remote Sensing Centre, Bergen, Norway. A grant for computing time from the Norwegian Program for supercomputing (NOTUR) was received through project number nn2993k.

Wind changes above warm Agulhas Current eddies

M. Rouault^{1,2} and B. Backeberg^{2,3,4}

¹*Department of Oceanography, Mare Institute, University of Cape Town, South Africa.*

²*Nansen-Tutu Center for Marine Environmental Research, University of Cape Town, South Africa*

³*Nansen Environmental and Remote Sensing Centre, Bergen, Norway*

⁴*CSIR, Stellenbosch, South Africa.*

Sea-surface temperature (SST), altimetry derived sea-level anomalies (SLA) and surface current are used south of the Agulhas Current to identify warm core mesoscale ocean eddies presenting a distinct SST perturbation superior to 1°C to the surrounding ocean. The analysis of 960 twice daily instantaneous charts of equivalent stability neutral wind speed estimates from the SeaWinds scatterometer onboard the QuikScat satellite collocated with SST during the lifespan of six warm eddies show stronger wind speed above those warm eddies than surrounding water for half of the cases. For cases where the wind is stronger above warm eddies, there is no relationship between the increase in surface wind speed and the SST perturbation. Mean wind increase is about 15 % at 1.8 m.s⁻¹. Wind speed increase of 4 to 7 m.s⁻¹ above warm eddies is not uncommon. Average eddy radius is 100 km and SST perturbations range from 1°C to 6°C

1 Introduction

Microwave radiometry and altimetry allow making observations in the Southern Ocean with unprecedented spatial and temporal resolution. This is a real advantage in the latitudes between 35°S to 50°S south of Africa where persistent cloud cover previously was a perennial problem in this regard. In addition, equivalent stability neutral instantaneous wind speed estimates from the SeaWinds scatterometer onboard the QuikScat satellite is available from July 1999 (Chelton et al., 2004) to November 2009 at a quarter of a degree resolution along a wide swath. Chelton et al. (2004) used 4 years of filtered QuikScat data to show a ubiquitous picture of mesoscale ocean atmosphere interaction linked to SST heterogeneity such as fronts, western boundary currents and tropical instability waves. In general, using satellite estimates of wind speed, wind stress and SST and moorings, there is a linear relationship between SST perturbation and wind speed or wind stress especially evident for SST perturbation from the surrounding ocean between -1 °C and 1 °C (Chelton et al., 2004, O'Neill et al, 2005).

Several mechanisms can explain the phenomena that encompass a high range of SST and wind speed wind speed. It is thought that the increase or decrease of surface wind speed along SST gradient is due to the change in the latent and sensible turbulent heat fluxes and associated change in surface atmospheric stability. Consequently there is a substantial modification of the constant flux layer and of the height and structure of the marine atmospheric boundary layer above the surface layer.

2 Data

SST was derived from the AMSR-E, launched in 2002 by NASA. It is a passive microwave radiometer. In this investigation, we use weekly

data at a resolution of 56 km. We used twice daily equivalent stability neutral surface instantaneous wind speed and direction estimated by the SeaWinds scatterometer on the QuikScat satellite. It is available in 25 Km Swath Grid. Weekly sea-level anomalies (SLA) were obtained from Centre national d'études spatiales (CNES) and surface current were obtained from Globcurrent. Globcurrent product is an optimal analysis of surface current at two different depth (surface and 15 m depth) at 1/4° resolution three hourly.

3 Wind speed acceleration above eddies

We looked for eddies with SLA of +15 cm and SST perturbation > 1°C. The selected eddies shed from the Agulhas Retroflexion and the Agulhas Return Current, were identified in an area ranging from 35°S to 45°S latitude and 15°E to 25°E longitude. Most eddies that we are studying stayed quite close to the Agulhas Return Current for a few months and were re-absorbed by the Agulhas Retroflexion or the Agulhas Return Current. AMSR-E SST was therefore instrumental in corroborating the location of warm eddies and their trajectories. Our period of study was July 2002-June 2004. Using SST and altimetry data in this region, we selected six warm eddies that had a significantly different thermal expression at the sea surface compared to ambient waters. The record represents a total of 22 months of clear-cut, identifiable eddies. We have cases for all seasons with a variety of SST (19°C to 12°C) and SST perturbations of up to 6 °C. Figure 1 shows four examples of cases showing high wind acceleration above warm eddies of up to 10 m/s and deceleration downstream. We note that the warm Agulhas Current is found to the north of the domain. In the four selected cases, the wind speed increase is superior to 5 m.s⁻¹ and relatively homogeneous eddies.

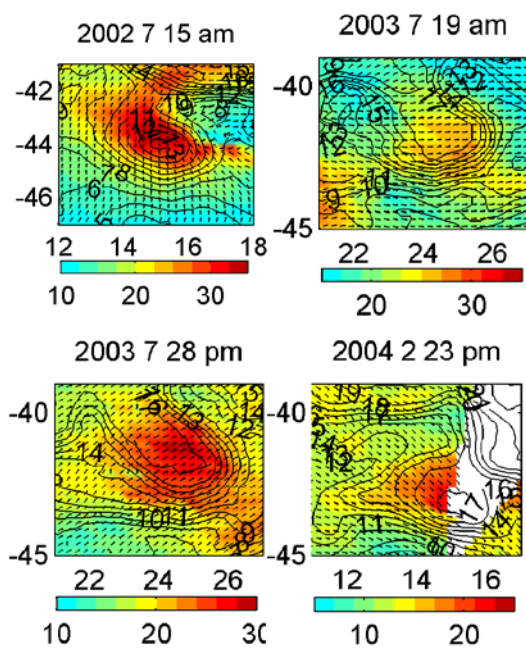


Figure 1: Clockwise from top left, Instantaneous estimate of QuikScat wind speed in m.s^{-1} (color) and directions (arrows) and AMSR microwave sea-surface temperature in $^{\circ}\text{C}$ (contours) south of the Agulhas Current system in the “Roaring forties” on the 15 07 2002 (morning path) 19 07 2003 (morning path), 23 02 2004 (evening path) and 28 07 2003 (evening path) showing strong and homogeneous increase and decrease in wind speed collocated with increases and decrease of sea surface temperature.

Not all instantaneous morning and evening paths display a clear increase above eddies but eddies have a strong imprint on the wind field when averaging the wind field data for at least a week at the spatial scales of the eddies. We then systematically plotted the instantaneous SeaWinds wind speed and direction for morning and evening passes with corresponding interpolated SST and SLA for a period of two years and examined those images. We selected 904 cases. However 20 % of the scenes had no data above eddies mainly because the satellite path does not cover the all globe or due to rainfall contamination. This left us with 711 cases.

Increase in wind speed above warm eddies and decrease downstream were a clear feature for 340 cases, about 50% of all. Wind speed, SST and SLA were also digitally saved in a common latitude longitude matrix format. To quantify the relationship between SST perturbation, wind speed increase above eddies and wind speed decrease downstream, we looked at the statistics of the merged dataset of cases that presented a wind speed increase above eddies and a decrease downstream and cases that did not. We considered only SST perturbation $> 1^{\circ}\text{C}$. For each case, we extracted SST, SLA, and wind speed at three positions along the

wind flow: a) just before the border (large SST gradient) of the eddy upstream of the center b) in the middle of the eddy c) downstream of the eddy border. In order to have robust results, we used a stretch of 4 points encompassing 100 km just before and around the eddy, 4 points at the eddy center in the direction of the wind and a stretch of 4 points just after and around the eddy border downstream of the eddy center. SST, wind speed and direction and SLA for those 3 locations were then averaged and stored with time and date. The eddy SST centers ranged from 19°C to 12°C with SST perturbation of up to 6°C for a mean gradient of 2.5°C per 100 km. Altogether, the average SST at the center of the eddies is 15.9°C while average SST at the eddy border is 13.2°C upstream and 13.3°C downstream. This leads to a mean perturbation of 2.65°C . Increase in wind speed above warm eddies and decrease downstream were a clear feature for 340 cases, about 50% of all cases with available data. 180 cases did not show an increase above the warm eddies and 191 cases did not show a decrease downstream of the eddies center.

Figure 2 presents a scatter plot of the instantaneous wind speed increase versus the SST perturbation. Figure 2 does not show any clear linear relation between those parameters for SST perturbation > 1 . This seems to contradict a number of similar studies. Wind speed increase of 4 to 7 m.s^{-1} above warm eddies is not uncommon.

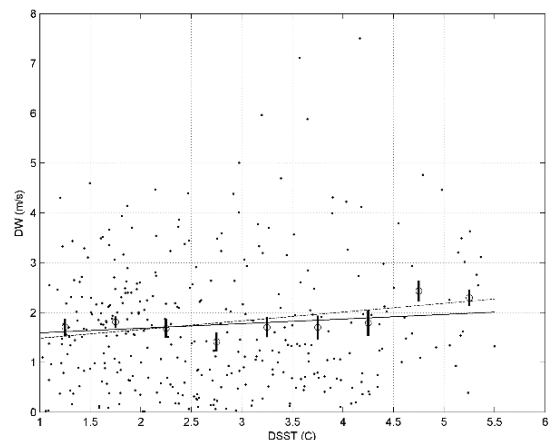


Figure 2: scatter plot of SST perturbation (DSST) versus wind speed increase (DW) in m.s^{-1} for the 340 cases when the wind increased above warm core eddies and decrease downstream and for SST perturbation from the surrounding ocean $> 1^{\circ}\text{C}$. Solid line is a linear fit. The circle represent the means within each 1°C bin and the error bars represent ± 1 standard deviation of the wind differences within each bin divided by the square root of the number of sample within each bin. The dashed line is a linear fit of the means within the bins.

4 Conclusions

Our study provides instantaneous values of wind changes above warm core eddies for the first time because we did not filter or average the data. Wind speed, increase substantially above warm SST perturbations by about 20 %. With increases of more than 4 m.s⁻¹ in eddies not uncommon, the warning should be taken seriously when sailing in the “Roaring Forties”. At last, this study questions the hypothesis that there is a ubiquitous linear relationship between SST perturbation and wind speed modification for large SST perturbation > 1 °C as we did not find a linear relationship between SST perturbation and wind increase across warm eddy.

Acknowledgements

Mathieu Rouault wishes to thank ESA GlobCurrent project, NRF, the Nansen-Tutu Center Globcurrent products are made freely available thanks to ESA funding under Globcurrent DUE project AO/1-7472/13/I-LG.

References

- Chelton, D.B., Schlax, M.G., Freilich, M.H., Milliff, R.F., 2004. Satellite measurements reveal persistent small-scale features in ocean winds. *Science* 303, 978-983.
- Davidson, K.L., Boyle, P.J., Gautier, C., Hanson, H.P., and Khalsa, S.J.S., 1991. Medium- to large-scale atmospheric variability during the Frontal Air-Sea Interaction Experiment. *Journal of Geophysical Research* 96, 8531-8551.
- O'Neill, L.W., Chelton, D.B., Esbensen, S.K., Wentz, F.J., 2005. High-resolution satellite observations of SST modification of the marine atmospheric boundary layer over the Agulhas Return Current. *Journal of Climate* 18, 2706-2723.
- Rouault, M., Lutjeharms, J.R.E., 2000. Air-sea exchange over an Agulhas eddy at the Subtropical Convergence. *The Global Atmosphere and Ocean System* 7, 125-150.
- Rouault, M., Lee-Thorp, A.M., Lutjeharms, J.R.E. 2000. Observations of the atmospheric boundary layer above the Agulhas Current during alongcurrent winds. *Journal of Physical Oceanography* 30, 70-85.

Comparative study of OMI BRD and PCA algorithm retrievals in relation to ground based measurements over a South African Site

S.K. Sangeetha¹, V. Sivakumar², M. Josipovic³, M. Gebreslasie¹ and C.Y. Wright^{4, 5}

¹ School of Agriculture, Earth and Environmental Science, College of Agriculture Engineering and Science, Westville Campus, Private Bag X5400, Westville, Durban 4000, South Africa

² School of Chemistry and Physics, College of Agriculture Engineering and Science, Westville Campus, Private Bag X5400, Westville, Durban 4000, South Africa

³ Unit for Environmental Sciences and Management, North-West University, Potchefstroom Campus, Private Bag X6001, Potchefstroom 2520, South Africa

⁴ South African Medical Research Council, Private Bag x385, Pretoria, 0001, South Africa

⁵ Department of Geography, Geoinformatics and Meteorology, University of Pretoria, Private Bag X20, Hatfield, 0028, South Africa.

Abstract

The Ozone Monitoring Instrument (OMI) on board the National Aeronautics and Space Administration's (NASA) Aura satellite plays a vital role in observing global emissions of ozone and other trace gases since its launch in 2004. Here, a comparative study of two OMI planetary boundary layer (PBL) sulphur dioxide (SO₂) products with Band Residual Difference (BRD) and Principal Component Analysis (PCA) techniques have been studied by estimating their monthly and seasonal variations in relation to their corresponding ground-based (GB) instrument variations located at Sharpeville (27.86 °E; 26.68 °S), Gauteng Province, South Africa during the time period from 2007 to 2013. The results showed that PCA retrievals followed similar trend and overestimated GB SO₂ values, whereas BRD retrievals underestimated them throughout the entire period. The SO₂ overall monthly variations measured by the GB instrument showed maximum values during winter. The daily, monthly regression analysis and seasonal correlation studies have also indicated that PCA technique performed better than BRD algorithm.

Keywords: SO₂ measurements, Satellite, Ground based, Climatology and Comparison

Introduction

Satellite-based monitoring of sulphur dioxide (SO₂) provides essential information on its atmospheric chemistry, annual emission estimates, and tracks the SO₂ clouds during intensive volcanic activity. Some of them are nadir UV-based, while others are thermal Infrared (IR) based sensors. The Ozone Monitoring Instrument (OMI) is onboard NASA'S Earth Observing System's (EOS) Aura Satellite that was launched on 15th July 2004 (OMI Data User's Guide, 2012). It is a near UV/ Visible spectrometer, with two unique features of daily global coverage and high spatial resolution which is more advanced in comparison with GOME and SCIAMACHY. This is feasible because of 2 dimensional charge coupled device (CCD) detector, where one dimension collects the spectral information and the other gathers spatial information (Levelt *et al.*, 2006).

There are two types of OMI Planetary Boundary Layer (PBL) SO₂ data products. The former product was produced using BRD algorithm and after October 2014, a newly developed product was available which relies on PCA algorithm (OMSO2 README File, 2008). The BRD algorithm uses differential residuals at the following 3 wavelength pairs: 310.8 nm – 311.9 nm, 311.9 nm – 313.2 nm, 313.2 nm – 314.4 nm. Each pair residual is converted to SO₂ slant column density (SCD). The resulting SCD's of three pairs are averaged and converted into total SO₂ vertical column density (VCD) with the help of air mass factor (AMF) of 0.36 (Krotkov *et al.*, 2006). The BRD algorithm

* Corresponding author:

Email Address: trijashan@yahoo.com.

Telephone: 031 260 8276

depends on the instrument specific correction factor for radiance data set in order to decrease the noise and systemic biases on SO₂ retrieval (Li *et al.*, 2013). The newly developed PCA algorithm, instead of depending on the above said correction factors, directly applies PCA technique (a statistical procedure of inputting large set of correlated variables into small set of uncorrelated variables) to OMI level 1b radiance and irradiance data in the full spectra from 310.5- 340 nm, with the strongest SO₂ absorption band at 310.8 nm (Li *et al.*, 2013). The retrieval noise is almost reduced by a factor of 2 when compared to BRD algorithm (see..OMSO2 README File, 2008).

The goal for this study was to interpret the performance of the earlier OMSO₂ PBL product with BRD algorithm and the newly launched PCA algorithm OMSO₂ PBL product and check their agreement with GB data. This was done by performing a comparative study between the two OMI data products in relation to the ground-based (GB) data collated at Sharpeville station, over Sharpeville (27.86 °E; 26.68 °S), Gauteng Province, South Africa for a time period between 2007 and 2013.

Instrumentation and Methods

Ground Based Data: The *in-situ* instrument used at the Sharpeville station is the Thermo electron 43i SO₂ analyser. The instrument was routinely calibrated and maintained on biweekly basis. More details on its principal and working performance are described in detail in the Instruction Manual (Model 43i, Instruction Manual). The hourly averaged SO₂ data (23 March 2007 to 31 January 2014) was provided by the South African Air Quality Information System (SAAQIS). About 70% data completeness based on daily, monthly and annual basis was pursued, where the data gaps and anomalies were filtered out.

OMI Data: A sampling grid of 0.125 × 0.125 degrees was selected over the GB station and both the OMI data products from 2004 to 2013 (i.e., PCA and BRD algorithms) in Dobson Units (DU) were converted to surface level volume mixing ratios (VMR) by applying the methods referred to in Josipovic (2009) and Josipovic *et al.*, 2013 as adjusted from Ziemke *et al.*, (2001 and 2006). A well mixed boundary layer (BL) throughout its complete vertical extent was assumed in this adjustment method and hence the VMR from *in situ* based methods were representative of the standard VMR throughout the vertical column of BL from OMI. Such conversions were required in order to perform a valid comparative study between the ground based and its concurrent BL VMR.

Results

Inter-annual Variations:

Annual averages based on monthly means of GB data, PCA and BRD algorithms for each year were calculated and are given in Fig. 1. It is to be noted that OMI data from 2004 was considered for trend analysis. It was found that GB values showed a steady decreasing trend between 2010 and 2012, where 15% reduction was found. The same trend was followed by both PCA and BRD algorithms, however BRD algorithm showed only a moderate annual variation while PCA showed a well defined annual variation where year 2006 had the highest SO₂ value of 10 ppbv, followed by 2010 of 9 ppbv, but after 2010 showed a decreasing trend of 16% similar to GB data. However, BRD algorithm showed the highest value of only 5.4 ppbv in 2004, but between 2010 and 2012 a 12 % decreasing trend was shown. Thus all the three measurements resembled each other by showing a decline in SO₂ after 2010.

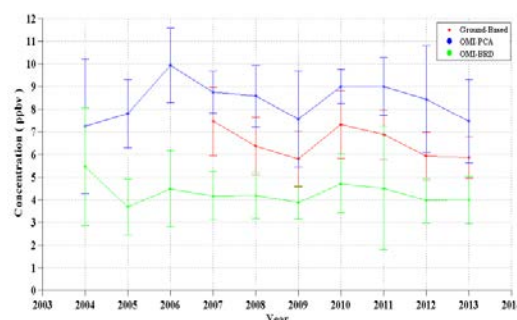


Figure 1: Inter-annual average values of GB data, OMI PCA & BRD algorithm retrievals. The vertical line represents 1 standard deviation.

Seasonal Variations:

Seasonal variations of GB values, PCA and BRD algorithm retrievals for the time period were estimated by calculating the overall monthly mean values and is displayed in figure-2. It is noted that there is no satellite overpass data for the month of June. The GB data showed a well marked seasonal difference where it started to increase from March (entire period) and reached a peak value of 9 ppbv in July (entire period), but later on showed a decreasing trend until it reached a minimum value of 3.5 ppbv during December. The comparative study of the three methods showed that PCA algorithm overestimated, whereas BRD algorithm underestimated GB values. The underestimation of BRD algorithm might be due to the errors caused by non-linear relationship between the band residual differences of three wavelength pairs selected in the BRD algorithm and high ozone residuals during high SO₂ events, which limit the retrieval capacity of BRD algorithm (Yang *et al.*,

2007 and 2009). It showed lower ranges between 3 and 5 ppbv throughout the entire season, GB data ranged between 4 and 9 ppbv and PCA algorithm showed slightly higher ranges between 6 and 10 ppbv. Hence, the overall mean for the entire period for PCA algorithm was almost twice as that of BRD algorithm (8.6 ppbv for PCA and 4.1 ppbv for BRD) and the GB data had medium range levels of 6.4 ppbv. PCA algorithm showed better seasonal variation similar to GB data, with higher values until winter, but later on started to decline in spring where lower levels were maintained during this season. Contrary to this, BRD algorithm did not exhibit clear seasonal changes and measurements remained below 5 ppbv all throughout the entire period. The absolute overall relative percentage differences for PCA and BRD algorithms with GB data was almost the same at 35%, but in summer the relative percentage of differences between GB data and PCA algorithm was higher when it reached almost -80%. Besides this, PCA algorithm had higher standard deviations of almost double than that of BRD algorithm.

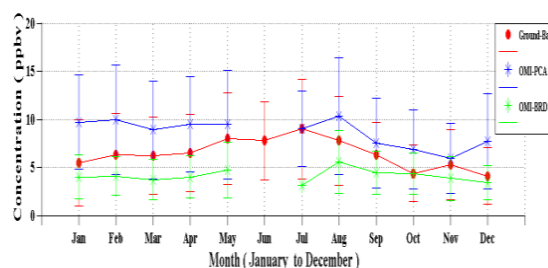


Figure 2: Overall seasonal variations of GB values, OMI PCA & BRD algorithm retrievals. The vertical line represents 1 standard deviation.

Relationship between GB values and OMI PCA and BRD algorithm retrievals

The correlation studies were conducted between GB values and PCA algorithm, and GB data and BRD algorithm for each season based on their daily mean values. Table 1 lists the correlation coefficient value (R) of PCA and BRD algorithms with GB values for each season. The table shows that PCA algorithm showed a better correlation result with GB values in comparison to BRD algorithm. However, only a moderate relationship was seen in PCA algorithm for all the seasons. The reason is also due to the daily mean values of GB data and a single overpass data from satellite data considered for this study. The background atmospheric conditions (such as pressure, humidity, wind speed, temperature), PBL dynamics (including turbulence, buoyancy, height) varies and various other parameters play an important role. The scatter plots of daily mean values between GB

data and PCA algorithm, and GB data and BRD algorithm in Figs. 3(a) and (b) also showed that PCA algorithm agreed with GB data better than BRD algorithm, where the slope of the regression line was 0.47 which was in contradiction with BRD algorithm where the slope was only 0.067. The monthly mean scatter plots (figure not shown) also supported this finding where the PCA algorithm had a slope of 0.42 and BRD algorithm had only 0.11. However, equivalent correlation coefficient values of 0.7 and 0.67 for PCA and BRD algorithms, respectively, between annual averages were found.

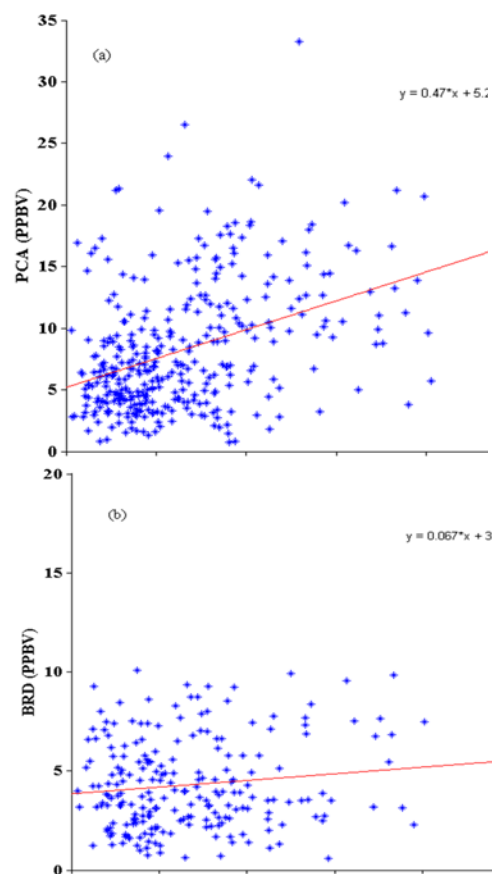


Figure 3: Scatter plots (Daily Mean): GB values & PCA (a); GB & BRD (b) algorithm retrievals

Table 1: Correlation Coefficient between GB values & PCA algorithm retrievals and GB values & BRD algorithm retrievals over different seasons

Season	Summer	Autumn	Winter	Spring
PCA	0.34	0.37	0.38	0.39
BRD	0.25	0.22	-0.04	0.07

Conclusions

A comparative study was carried out between OMI SO₂ PBL products derived from BRD and PCA algorithms in relation to *in situ* GB measurements in Sharpeville from 2007 to 2013. The results

showed that PCA algorithm overestimated GB data whereas BRD, which always had lower ranges thus underestimated GB data. A strong inter-annual variation was seen in both GB data and PCA algorithm than BRD algorithm. Nonetheless, the three measurements proved that SO₂ levels reduced eventually after 2010. Similarly, clear seasonal changes were shown by both GB data and PCA algorithm whereas BRD algorithm showed fair variations. Besides this, the daily, monthly mean values further indicated that PCA values are correlated better with GB data than BRD values.

The overall results thus proved that the newly developed PCA algorithm retrievals were in better agreement with GB values than BRD algorithm retrievals and could identify increase in SO₂ values both on seasonal and yearly time scales. Thus the newly developed OMI PCA algorithm could be used as a surrogate for remote areas with no ground based stations, in examining SO₂ variations in such areas on long time basis qualitatively. However, multivariate analysis between meteorological parameters, GB data and OMI data need to be carried out in order to study the inter-relationship between them. Hence, further research is necessary in order to rely on satellite based remote sensing retrievals better quantitatively.

Acknowledgements

The authors sincerely thank SAAQIS for providing the ground instrument data and SANSA for the financial support to one of the author (SKS).

References:

Josipovic, M. (2009), Acid deposition emanating from the South African Highveld-a critical levels and critical loads assessment (Ph.D. thesis). University of Johannesburg, Johannesburg, South Africa.

Josipovic, M., R.P. Burger, H.J. Annegarn, J.J. Pienaar, S.J. Piketh, M.A. Kneen (2013), Atmospheric boundary layer reduction enabled comparison of remotely sensed and surface measured trace gas concentrations over South Africa, 29th Annual conference of South African Society for Atmospheric Sciences (SASAS) 2013, Salt Rock Hotel, Kwa-Zulu Natal, 26/09/2013 - 27/09/2013, ISBN 978-0-620-56626-1: 91-94.

Krotkov, N. A., Carn, S. A., Krueger, A. J., Bhartia, P. K. and Yang, K. (2006). Band residual difference algorithm for retrieval of SO₂ from the Aura Ozone Monitoring Instrument (OMI). *Geoscience and Remote Sensing, IEEE Transactions on*. 44(5):1259-1266.

Levelt, P. F., van den Oord, G. H., Dobber, M. R., Malkki, A., Visser, H., de Vries, J., Stammes, P., Lundell, J.O.V. and Saari, H. (2006). The ozone monitoring instrument. *Geoscience and Remote Sensing, IEEE Transactions on*. 44(5):1093-1101.

Li, C., Joiner, J., Krotkov, N.A. and Bhartia, P.K. (2013). A fast and sensitive new satellite SO₂ retrieval algorithm based on principal component analysis: Application to the ozone monitoring instrument. *Geophys. Res. Lett.*, 40(23):6314-6318.

Model 43i Instruction Manual Pulsed Fluorescence SO₂ Analyzer Part Number 101589-00 16May2015 <https://tools.thermofisher.com/content/sfs/manuals/EPM-manual-Model%2043i.pdf> [Accessed: 03/5/2015]

OMSO2 README File v1.2.0 Released Feb 26, 2008 Updated: September 26, 2014.

Ozone Monitoring Instrument (OMI) Data User's Guide, 2012. http://disc.sci.gsfc.nasa.gov/Aura/dataholdings/additional/documentation/README_OMI_DUG.pdf, [Accessed: 19/8/2014].

Yang, K., Krotkov, N.A., Krueger, A.J., Carn, S.A., Bhartia, P.K. and Levelt, P.F. (2007). Retrieval of large volcanic SO₂ columns from the Aura Ozone Monitoring Instrument: Comparison and limitations, *J. Geophys. Res.*, 112(D24):DOI: 10.1029/2007JD008825.

Yang, K., Krotkov, N.A., Krueger, A.J., Carn, S.A., Bhartia, P.K. and Levelt, P.F. (2009). Improving retrieval of volcanic sulfur dioxide from backscattered UV satellite observations. *Geophys. Res. Lett.*, 36(3): DOI: 10.1029/2008GL036036.

Ziemke, J.R., Chandra, S. and Bhartia, P.K. (2001). Cloud slicing"- A new technique to derive upper tropospheric ozone from satellite measurements. *J. Geophys. Res.* 106(D9):9-853.

Ziemke, J.R., Chandra, S., Duncan, B.N., Froidevaux, L., Bhartia, P.K., Levelt, P.F. and Waters, J.W. (2006). Tropospheric ozone determined from Aura OMI and MLS: Evaluation of measurements and comparison with the Global Modeling Initiative's Chemical Transport Model. *J. Geophys. Res.* 111(D19):DOI: 10.1029/2006JD007089.

Open water evaporation – quo vadis?

Michael J. Savage¹

School of Agricultural, Earth and Environmental Sciences, Agrometeorology Discipline, Soil-Plant-Atmosphere Continuum Research Unit, University of KwaZulu-Natal, Pietermaritzburg, South Africa

Abstract

Evaporation estimation is still a challenge for the atmospheric, agricultural and environmental sciences, particularly in the face of climate change. How can evaporation, an important component of the water balance, be measured or estimated routinely with reliable accuracy and precision? Different methods for measuring or estimating evaporation are reviewed. Remote sensing modelling methods have good spatial but poor temporal resolution compared to most other methods that have poor spatial but good temporal resolution. The Monin-Obukhov Similarity Theory (MOST) is applied to open water evaporation and the impact of climate change for differing scenarios is presented using a long-term dataset.

Keywords

Climate change, Eddy covariance, Monin-Obukhov similarity theory, Open water evaporation, Penman-Monteith.

Introduction

“The 1998 Republic of South Africa National Water Act refers to the possible prescription, by government, of methods for making a volumetric determination of water for purposes of water allocation and charges in the case of activities resulting in stream flow reduction. Given this scenario and the demand on water resources (*and the widespread 2015/6 drought*) it is important to consider how evaporation, one of the main components of the water balance, is to be measured or estimated with reliable accuracy and precision. Determination of reliable and representative evaporation data is an important issue of atmospheric research with respect to applications in agriculture, catchment hydrology and the environmental sciences, not only in South Africa. Long-term measurements of evaporation at different time scales and from different climate regions are not yet readily available” (Savage *et al.* 2004, Savage 2009).

The field-measurement of total evaporation (mainly soil evaporation and transpiration) is of paramount hydro-meteorological importance in determining the water use of vegetation, and open water evaporation. In general, studies on total evaporation measurement are limited due to the high cost of instrumentation and sensors, instrumentation battery power requirements and the difficulty in obtaining real-time measurements in, for example, remote areas. Furthermore, many micrometeorological measurement methods require site homogeneity, adequate fetch, neglect of advection influences and application of the Monin-Obukhov similarity theory (MOST) (Foken 2006).

Point (single-level such as eddy covariance), profile and line-averaged (such as Bowen ratio, other profile methods and scintillometry) atmospheric measurements have been used to measure sensible heat. Sensible heat is driven by vertical temperature differences between the canopy or soil surface and overlying air. By contrast, latent energy (*LE*) (evaporation) is driven by vertical water vapour pressure differences between those just above the canopy or soil surface and that of overlying air.

Eddy covariance is widely regarded as the standard method for the determination of fluxes above a surface. The method is however expensive and requires many corrections and high skill. In addition, the method has a high power requirement that is problematic for measurements above water. Near real-time estimates are not possible, until recently. Platforms or other methods for supporting the eddy covariance instruments are subject to vibration with potential measurement error.

Remote sensing methods, while having good spatial resolution, have poor temporal resolution and are impacted on by clouds particularly for summer rainfall areas.

There have been very few investigations of open-water evaporation that have used the MOST method. MOST semi-empirical theory has stood the test of time and has been used for the estimation of entity fluxes in many different systems under a variety of atmospheric conditions and climates (Savage *et al.* 2004, Foken 2006, Savage 2009, 2010a).

Open water evaporation estimation using the surface energy balance and methods such as surface renewal (Mengistu and Savage 2010b, temperature variance or Penman-Monteith requires measurements or algorithms to obtain the available flux from the surface net irradiance and the water-stored heat flux. Both measurements and estimations are much more difficult for water bodies. In particular, sub-hourly stored heat fluxes are variable to the extent that smoothing when using the energy balance equation (Mengistu and Savage 2010a) is not sufficiently accurate for reliable results.

The aim of this work is to very briefly review the status of open evaporation estimation and to give two examples, viz., MOST and the reference evaporation (*ET_o*) methods applied to open water evaporation estimation over Midmar Dam, South Africa using normal micrometeorological measurements but with the addition of water-surface temperature for the MOST method. The MOST method requires the relevant flux equations to be solved iteratively

by varying the surface roughness parameter to minimise the differences between MOST-modelled and measured momentum, sensible heat and/or latent energy fluxes. In addition to this main aim, the impact of climate change on open water evaporation was investigated using a 25-year weather dataset and a 50-year stochastically generated set of daily weather data.

Instrumentation and Method

Apart from the climate change investigation using reference evaporation, measurements used in this study are shown in Table 1. The measurement height was 2 m above the water

Method	Measurement
Monin-Obukhov similarity theory	Air temperature, water vapour pressure, wind speed and surface water temperature
ETo	Solar irradiance, air temperature, water vapour pressure and wind speed

surface. The following assumptions for application of MOST to open water, implemented in a spreadsheet, were made in respect of the surface boundary conditions of a water surface and above-surface atmosphere:

1. due to the friction imparted by the water surface to the overlying air, it is assumed that wind speed $U_o = 0$ m s⁻¹ at roughness height z_o (m) above the surface;
2. the surface temperature T_o is estimated using an infrared thermometer suspended 2 m above the water surface. Infrared radiation absorption by the water surface, within even a few millimetres, would invalidate thermocouple surface temperature measurements;
3. the specific humidity just above the water surface is the saturated value at the temperature T_o – viz., $q_o = q_s(T_o)$. This assumption would be invalid in the case for sea water or other highly saline waters;
4. other inputs include the measurement height and the roughness lengths z_o , z_{oT} and z_{ow} for momentum, sensible heat and latent energy fluxes respectively. Blanc (1983) recommended $z_o = z_{oT} = z_{ow} = 0.0002$ m and this was confirmed using eddy covariance (EC) measurements of sensible heat flux (data not shown). The various MOST functions used for the iterative evaluation of the various fluxes are shown in Table 2 – mostly based on Högström (1996).

The Climgen (v4.2) software (Stöckle *et al.* 2001), based on Richardson and Wright (1984), was used to generate a 50-

year daily data set of maximum and minimum air temperatures using measured daily temperatures for Cedara for the period 1990 to 2015. The generated daily values were adjusted according the following climate scenarios:

scenario A: no adjustments (baseline conditions);

scenario B: an increment of 2 °C to the daily average air temperature weighted according to daylength and nightlength;

scenario C: an increment of 4 °C to the daily average air temperature weighted as in scenario B.

These temperature scenarios assume that they result from increased concentration in carbon dioxide with scenario B within the IPCC (2013) temperature ranges of 1.1 to 2.6 °C (scenario RCP4.5) and 1.4 to 3.1 °C (RCP6.0) and scenario C within the temperature range 2.6 to 4.8 °C (RCP8.5).

A 25-year dataset consisting of daily maximum and minimum air temperatures for Cedara, South Africa, was used to generate a 50-year dataset that was manipulated to reflect the various climate change scenarios. The generated daily minimum and maximum air temperatures were used to determine daily ETo and hence open water evaporation for each scenario from which annual totals were compute

Table 2 The various fluxes and corresponding universal semi-empirical MOST functions applicable for a wide range of surfaces from forests to water for unstable and stable conditions where ζ is a dimensionless stability parameter determined through iteration

Fluxes	Momentum φ_m	Sensible heat φ_h	Latent energy φ_w
Univer- sal func- tion (un- stable)	$(1 - 19 \zeta)^{-1/4}$ $-2 < \zeta < 0$	$0.95 (1 - 11.6 \zeta)^{-1/2}$ $-2 < \zeta < 0$	$(1 - 16 \zeta)^{-1/2}$ $-1 < \zeta < -0.1$ Dyer and Hicks (1970)
Univer- sal func- tion (stable)	$1 + 5.3 \zeta$ $0 < \zeta < 0.5$	$1 + 8.0 \zeta$ $0 < \zeta < 0.5$	$1 + 8.0 \zeta$ $0 \leq \zeta \leq 0.5$

Table 3 Instrumentation details, including sensor accuracy (adapted from manufacturer specifications)

Measurement	Instrument model	Supplier	Comment(s)
Air temperature T_z at height $z = 2$ m ($^{\circ}\text{C}$)	HC2S3	Rotronic AG (Bassersdorf Switzerland)	Accuracy at 23°C : $\pm 0.1^{\circ}\text{C}$ with standard configuration settings. Due to the optical properties of water in efficiently reflecting solar irradiance at low solar angles, a 10-plate Gill radiation shield was required for air temperature and relative humidity measurements
Relative humidity (%) for determining q_z (kg kg^{-1})	HC2S3	Rotronic	Accuracy between 10 and 30°C : $\pm 0.8\%$ RH with standard configuration settings
Sonic anemometer U_z (m s^{-1})	CSAT3	Campbell Scientific (Logan, UT, USA)	Wind speed: accuracy ± 0.08 m s^{-1} ; resolution 0.001 m s^{-1} ; range 0 to 30 m s^{-1}
Water-surface temperature T_o ($^{\circ}\text{C}$) and for determining $q_o = q_s(T_o)$ (kg kg^{-1})	Model SI-111, SI-121	Apogee Instruments (Logan, UT, USA)	Model SI-111 field of view (FOV) = 22.0° ; model SI-121 FOV = 18.0° . For target temperature within 20°C of sensor body temperature: accuracy $\pm 0.2^{\circ}\text{C}$ (SI-111, SI-121); uniformity $\pm 0.1^{\circ}\text{C}$; repeatability $\pm 0.05^{\circ}\text{C}$

Results and Discussion

The MOST and eddy covariance (EC) methods for estimating open water evaporation were compared. The EC data quality assurance protocols followed for data rejection resulted in an EC rejection rate of about 59 % for daytime hours and 69 % for nighttime. It was therefore not possible to obtain reliable estimates of daily evaporation LE using the EC method. At times, there was very good comparison between the EC and MOST methods for estimating LE (R^2 of 0.64 and a slope of 0.89 for LE_{MOST} (y) and LE_{EC} (x) for 30-min quality-assured data for the period 12th February to 24th March 2016). The MOST method yielded the most consistent estimates of sensible heat flux H and LE and allowed the 30-min estimates to be scaled to a daily timescale and compared with the daily estimates obtained using a Penman-Monteith (PM) model implementation using equilibrium temperature ((Edinger *et al.* 1968) as further developed by Keijman and Koopmans (1973) and de Bruin (1982)) for the period 14th February to 25th May 2016. Daily Penman-Monteith open water estimates were within 9.2 % of MOST evaporation measurements with the former being lower.

Correction to the water surface temperature T_o for water-surface emissivity and reflected backward infrared irradiance resulted in a consistent bias of 0.037°C . This increase resulted in an increase of all LE_{MOST} estimates by 1.72 %. Applying this correction allowed MOST to be used without the need for measurement of the reflected background infrared irradiance and resulted in PM and MOST estimates of daily evaporation agreeing to within 10.7 %. The mean PM daily estimate of evaporation for the study period 14th February to 25th May 2016 was 2.88 mm compared to 3.26 mm for the mean corrected MOST method.

MOST estimates of evaporation using land-based wind speed measurements resulted in poor agreement with previous estimates obtained using the above-water wind speed (data not shown). The nighttime MOST evaporation represented 43.5 % of the total (24-hour) evaporation over the 101 days of the measurement study with the daytime evaporation

therefore representing 56.4 %. The influencing factor or driving force for this significant amount of evaporation during the nighttime appeared to be wind speed – the total cumulated nighttime hours wind run was 41.7 % of the total wind run and 58.3 % for the daytime.

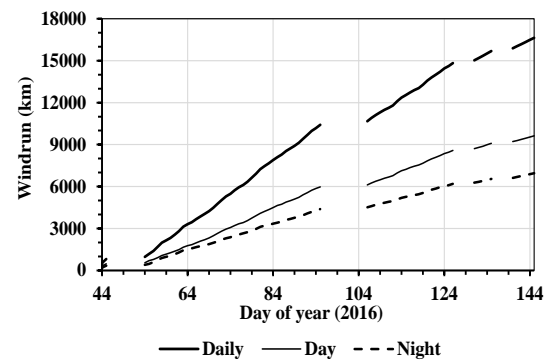


Fig. 1. Wind run for the day, daytime and nighttime hours for 14th February 2016 (day 44) to 25th May (day 145)

Using the MOST method, the dominant term of the energy balance, the evaporative flux, was 86 % of the available energy flux (Fig. 2). Sensible heat flux was the smallest component of the energy balance, slightly less than the estimated water-stored heat flux S , and about 12 % of net irradiance R_{net} .

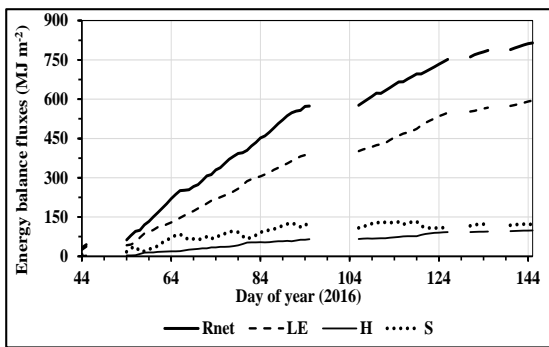


Fig. 2. Cumulated energy balance fluxes (MJ m^{-2}) from MOST H and LE estimates and measurements of net irradiance R_{net} with stored heat flux S calculated as a residual of the energy balance for the study period

Open water evaporation was estimated using a daily Penman-Monteith approach (Allen *et al.*, 1998) using a “crop” factor of 1.05. The Hargreaves and Samani (1982, 1985) approach was used to calculate daily solar radiation from the daily range in air temperature and the extraterrestrial solar radiation. The results of these calculations are shown in Table 4. There is a slight increase in the 50-year total annual evaporation for scenarios B from 952.9 to 065.8 mm (1.4 %) and C from 952.9 to 977.7 mm (2.6 %). The increases in maximum and minimum air temperatures did not change the daily range in air temperature and therefore the calculated daily solar radiation remained much the same. If the daily maximum and minimum temperatures were increased asymmetrically (Karl *et al.*, 1993), the solar radiation would have decreased with likely decreases in open water evaporation estimates.

Table 4 Total annual open water evaporation for the three climate change scenarios A, B and C, using the stochastically-generated 50-year dataset, using the Penman-Monteith approach and a “crop” factor of 1.05

	Scenario A (baseline)	Scenario B (+ 2 °C)	Scenario C (+ 4 °C)
Total	952.9	965.8	977.7
Minimum	907.0	920.5	933.2
Maximum	982.3	995.8	1008.3

Conclusions

There was a high rejection of eddy covariance (EC) estimates of evaporation and therefore it was not possible to estimate daily evaporation using the EC method. The energy balance components for open water were determined using the MOST method. Climate change impacts on evaporation were relatively minor assuming symmetric nighttime and daytime air temperature increases.

Acknowledgements

Financial support from the Water Research Commission, National Research Foundation and the University of KwaZulu-Natal is gratefully acknowledged. Dr A.D. Clulow, Mr J.M. Pasi and L. Myeni assisted with data collection. Mr S. Strydom provided the stochastically-generated 50-year

dataset. The Agricultural Research Council provided the 25-year daily air temperature dataset.

References

- Allen, R.G., Pereira, L.S., Raes, D. and Smith, M. (1998). Crop Evapotranspiration - Guidelines for Computing Crop Water Requirements. *FAO Irrigation and Drainage Paper 56* FAO. Food and Agriculture Organization of the United Nations Rome, Italy. 315 pp.
- Blanc, T.V. (1983). An Error Analysis of Profile Flux, Stability, and Roughness Length Measurements Made in the Marine Atmospheric Surface Layer. *Boundary-Layer Meteorology*, 26: 243–267.
- de Bruin, H.A.R., 1982. Temperature and energy balance of a water reservoir determined from standard weather data of a land station. *Journal of Hydrology*, 59: 261–274.
- Dyer, A.J. and Hicks, B.B. (1970). Flux-Gradient Relationships in the Constant Flux Layer. *Quarterly Journal of Royal Meteorological Society*, 96: 715–721.
- Edinger, J.E., Duttweiler, D.W. and Geyer, J.C. (1968). The Response of Water Temperatures to Meteorological Conditions. *Water Resources Research*, 45: 1137–1143.
- Foken, T. (2006). 50 years of the Monin-Obukhov Similarity Theory. *Boundary-Layer Meteorology*, 119: 431–447.
- Hargreaves, G.H. and Samani, Z.A. (1982). Estimation of Potential Evapotranspiration. *Journal of Irrigation and Drainage Division, Proceedings of the American Society of Civil Engineers* 108, 223–230.
- Hargreaves, G.H. and Samani, Z.A. (1985). Reference Crop Evapotranspiration from Temperature. *Applied Engineering in Agriculture*, 1: 96–99.
- Högström, U. (1996). Review of Some Basic Characteristics of The Atmospheric Surface Layer. *Boundary-Layer Meteorology*, 78: 215–246.
- IPCC, 2013: Climate Change 2013: The Physical Science Basis. Contribution of Working Group I to the Fifth Assessment Report of the Intergovernmental Panel on Climate Change [Stocker, T.F., Qin, D., Plattner, G.-K., Tignor, M., Allen, S.K., Boschung, J., Nauels, A., Xia, Y., Bex, V. and Midgley P.M. (eds.)]. Cambridge University Press, Cambridge, United Kingdom and New York, NY, USA, 1535 pp.
- Karl, T.R., Jones, P.D., Knight, R.W., Kukla, G., Plummer, N., Razuvayev, V., Gallo, K.P., Lindseay, J., Charlson, R.J., and Peterson, T.C. (1993). Asymmetric Trends of Daily Maximum and Minimum Temperature. *Bulletin of the American Meteorological Society*, 74: 1007–1023.
- Keijman, J. and Koopmans, R. (1973). A Comparison of Several Methods of Estimating the Evaporation of Lake

Flevo. Proc. Int. Assoc. Hydrol. Sciences, Helsinki, Finland. Symp. Hydrol. Lakes, pp. 225–232.

Mengistu, M.G. and Savage, M.J. (2010a). Open Water Evaporation for a Small Shallow Dam in Winter Using Surface Renewal and Eddy Covariance Methods. *Journal of Hydrology*, 380: 27–35.

Mengistu, M.G. and Savage, M.J. (2010b). Surface Renewal Method for Estimating Sensible Heat Flux. *Water SA*, 36: 9–17.

Richardson, C.W. and Wright, D.A. (1984) WGEN: A Model for Generating Weather Variables. US Department of Agriculture, Agricultural Research Service, ARS-8.

Savage, M.J. (2009). Estimation of Evaporation Using a Dual-Beam Surface Layer Scintillometer and Component Energy Balance Measurements. *Agricultural and Forest Meteorology*, 149: 501–517.

Savage, M.J. (2010). Sensible Heat Flux for Estimating Evaporation. D.Sc.Agric. thesis, University of KwaZulu-Natal, South Africa. 343pp.

Savage, M.J., Everson, C.S., Odhiambo, G.O., Mengistu, M.G. and Jarman, C. (2004). Theory and Practice of Evaporation Measurement, With Special Focus on Surface Layer Scintillometry as an Operational Tool for the Estimation of Spatially Averaged Evaporation. Water Research Commission Report No. 1335/1/04, p204, ISBN 1-77005-247-X.

Stöckle, C.O., Nelson, R., Donatelli, M., and Castellvi, F. (2001). ClimGen: A Flexible Weather Generation Program 2001, 2nd Int. Symp. Modelling Cropping Systems, Florence, Italy

Comparison between Aerosol Optical Depth acquired from Sun Photometer and MODIS satellite over Durban

Priyanka Singh^{1,2*}, V. Sivakumar¹, Michael Gebreslasie²

¹*Discipline of Environmental Science, School of Agriculture Earth and Environmental Science, College of Agriculture, Engineering and Science, Westville Campus, University of KwaZulu-Natal, Durban 4000, South Africa.*

²*Discipline of Physics, School of Chemistry and Physics, College of Agriculture, Engineering and Science, Westville Campus, University of KwaZulu-Natal, Durban 4000, South Africa.*

*corresponding author: priysingh91@gmail.com

Abstract

Due to the ubiquitous and inconsistent nature of aerosol loads, multiple instrumentation are required to measure their loads. Long-term, detailed measurements from satellites, ground-based instruments and weather data are required to adequately measure aerosols for a given area. This study uses the preliminary results from the ground-based Durban sun photometer (part of the AERONET federated group) to compare aerosol optical depth at 550 nm (AOD) to the satellite Moderate Resolution Imaging Spectroradiometer (MODIS) for the Aqua, Terra plus Aqua and Terra combined (average of both) datasets for the dark target (DT) and deep blue (DB) retrieval algorithms to validate satellite retrievals. The results show moderate correlations between MODIS Terra and AERONET for both DB ($R^2 = 0.70$) and DT ($R^2 = 0.60$), and between MODIS Aqua and AERONET for DB (0.68). Good correlations were noted for MODIS Terra and Aqua merged for both DB (0.79) and DT (0.74). It was concluded that for certain seasons MODIS predicted AOD better than other seasons and that usage of MODIS sensors and recommendations are quite complicated and specific to certain regions.

Key Words: Aerosols, Aerosol Optical Depth, AERONET, MODIS radiometry, dark target, deep blue

I. Introduction

Recently, Adesina, et al., (2014), Kumar, et al., (2013) and Sivakumar, et al., (2010) used AERONET stations operational around South Africa, in Pretoria, Skukuza, Bethlehem and Johannesburg to study aerosol optical properties and compared the measurements with satellite instrumentation. Additionally, the Southern African Regional Science Initiative (SAFARI 2000) followed SAFARI 92 and 94 was also a major surface, airborne and space-borne field campaign undertaken in southern Africa in 2000 and 2001. These campaigns covered extensive phenomena relating to atmosphere interactions and the biogeochemical functioning of the southern African climate (Swap, et al., 2003). However despite the aforementioned studies, there still exist inconsistencies in understanding aerosol properties in many parts of the world, especially in Southern Africa due to the significant lack of ground-based monitoring stations (Sivakumar, et al., 2009). There are not enough monitoring stations to gauge aerosol climatology of the whole country, therefore there is a requirement for satellite validation studies in South Africa. This is especially true for Durban, due to the lack of continuous ground based monitoring in Durban and the presence of industrial activity and agricultural activity which can potentially generate varying aerosol species. Aerosol optical depth (AOD) is an important parameter to determine the climate forcing of aerosols. AOD is a measure of the degree to which aerosols inhibit the transmission of

light by absorption or scattering of light (Kaufman, et al., 2002). This study will compare AOD derived from the Moderate Resolution Imaging Spectroradiometer (MODIS) dark target (DT) and deep blue (DB) retrieval algorithms for both the Aqua and Terra sensors also one merged Terra and Aqua (the average of Terra and Aqua) with sun photometer derived AOD from January – September 2014, using correlation statistical analysis. The DT algorithm has specific algorithms for land and ocean and covers dark vegetated surfaces. The deep blue algorithm is a land retrieval only, in particular, DB has been expanded to cover vegetated land surfaces as well as brighter desert/urban areas (Sayer, et al., 2014). Both algorithms were compared in order to determine, which algorithm better suits Durban. The DT algorithm is expected to work better for Durban than DB, due to Durban being a coastal city and due to the prevalence of dark vegetation (Mucina & Rutherford, 2006).

II. Dataset

This study made use of area averaged, C6, level 3 data, at the nominal 10 km spatial scale, MODIS Terra and MODIS Aqua gridded atmospheric daily product which contained daily 1 x 1 degree grid average values of atmospheric parameters, for both the DT and DB algorithms. Area averaged MODIS AOD at 550 nm were extracted for Durban and daily average AOD was downloaded from the Durban sun photometer located at the University of KwaZulu – Natal was also used. MODIS AOD₅₅₀ properties

were downloaded from <http://giovanni.gsfc.nasa.gov/giovanni/>. AOD derived from MODIS Terra, MODIS Aqua and MODIS Terra and Aqua combined (averaged) for both the DT and DB retrieval algorithms were compared with the sun photometer derived AOD. Statistics were generated for MODIS derived AOD and the sun photometer derived AOD for Durban. Only days where measurements were available for both instrumentation were included in the analysis. The means and the standard deviations of MODIS and sun photometer derived AOD were also compared for Durban. MODIS measurements were compared against the sun photometer for Durban by using regression statistical analysis and determining the R^2 correlation coefficient. R^2 is one measure of how well a model can predict the data, and falls between 0 and 1. The higher the value of R^2 , the better the model is at predicting the data. Where \hat{y} represents the calculated values of y and \bar{y} is the mean of y , R^2 is defined as:

$$R^2 = 1 - \frac{\sum_{i=1}^n (y_i - \hat{y})^2}{\sum_{i=1}^n (y_i - \bar{y})^2}$$

For the analysis, it is important to interpolate the AOD values from each sensor to a common wavelength. The sun-photometer AOD wavelength was, therefore, converted to the MODIS AOD wavelength using the power law:

$$AOD_a = AOD_b \left(\frac{a}{b}\right)^{-AE}$$

Where $a = 550$ nm for MODIS, $b = 500$ nm for AERONET, and AE is the Ångström exponent ($\alpha_{440-870}$) (Kumar, et al., 2015).

III. Results and Discussion

a. Comparison between different MODIS retrieval algorithms and AERONET

Table 1. depicts the R^2 (square of the correlation coefficient) between sun photometer and MODIS observations. From Table 1 it can be noted that for Durban, DB has a higher R^2 (0.70) for the Terra sensor than DT (0.60), however, DT performed better for the Aqua sensor with a higher R^2 (0.78) than the value for DB ($R^2 = 0.68$). The Terra and Aqua sensors correlated better using the DT algorithm ($R^2 = 0.65$) than the DB algorithm ($R^2 = 0.55$). Due to the varying correlations, aqua and terra values were averaged and the merged dataset was used to perform correlations. DB performed better for the merged dataset with a higher R^2 (0.79) value than DT (0.74). The low correlation observed between MODIS Terra and the sun photometer for Durban, using DT and DB, was also noted for Durban by Kumar et al., (2015), who have studied AOD from 2005 to 2011, using sun photometer observations from Skukuza to validate results.

Numerous researchers have been performing inter comparisons between retrievals from AERONET sun photometers and MODIS for several years. Sun, et al., 2008, showed a moderate correlation between MODIS Terra and sun photometer derived AOD over seas around China ($R^2 = 0.68$), however, better results were noted during certain seasons such as spring ($R^2 = 0.77$). More, et al., (2013) also noticed strong correlations on the seasonal scale between MODIS and sun photometer derived AOD over Pune, India with seasonal R^2 values ranging from 0.62 – 0.93 (More, et al., 2013). For South Africa in particular, the Multi-angle Imaging Spectro Radiometer (MISR) satellite performs better than MODIS, when comparing with AERONET retrievals (Diner, et al., 2001, Kumar, et al., 2015). There are many parameters that should be considered when using different sensor sources such as retrieval algorithms, consistency, revisit times, instrument calibration, cloud screening, data availability, algorithm assumptions regarding aerosol microphysical properties and surface boundary environments (Kahn, et al., 2009).

Table 1. R^2 value obtained by linear and 2nd degree interpolation for the different retrieval algorithms on common days from January – December 2014.

Algorit hm	AERON ET vs. Terra	AERON ET vs. Aqua	Ter ra vs. Aq ua	Terra and AERON ET
	R^2	R^2	R^2	R^2
Deep	0.70	0.68	0.5	0.79
Blue			5	
Dark	0.60	0.78	0.6	0.74
Target			5	

b. Monthly AOD trends from AERONET and MODIS sensors

Fig. 1 and Fig. 2, depicts the monthly averaged AOD values at 550 nm obtained from MODIS Aqua and Terra sensors and the sun photometer over Durban from January to December 2014 (for MODIS sensors) and from January to September 2014 (for the sun photometer), using the DT and DB algorithm respectively. From Fig. 1 for the DT algorithm, it can be ascertained that MODIS Aqua and Terra merged derived AOD is closer to the sun photometer values than MODIS Terra and MODIS aqua derived AOD, whereas for the DB algorithm, MODIS Aqua AOD appears closer to the sun photometer derived AOD. The MODIS sensors, for both algorithms (DT and DB), depict a rise in AOD from February to March, whereas the sun photometer depicts a drop in AOD values during this time. AOD values decreased from

March to April, for both the sun photometer and MODIS sensors. From April to July, both the sun photometer and MODIS derived AOD remained at low values and quite constant (<0.2). For all instruments and sensors, and for both algorithms, AOD increase from July to August. AOD then decreased drastically for the sun photometer from August to September. AOD was still high for both the MODIS sensors and algorithms from August to September and then decreased from September to October. AOD derived from the MODIS sensors from October to December remained relatively low. Fig. 1 (DT algorithm) displays some seasonal variation, with maximum values depicted during August (sun photometer) with AOD means greater than 0.2 for both sensors, for Durban. From Fig. 2 (DB algorithm), MODIS derived AOD is <0.2 and always less than sun photometer derived AOD, for all sensors, including Terra and Aqua merged, this means that the DB algorithm underestimated AOD during all months studied. The underestimation of AOD could be due to sensor calibration error or an unsuitable assumption about the ground surface reflection (Chin, et al., 2002; Sayer, et al., 2014). This points towards inconsistencies between the aerosol microphysical and optical properties used in the retrieval algorithm and in the real situation thus suggesting an underestimation of AOD by MODIS with regards to AOD retrieval (Tripathi, et al., 2005). From February of 2014, the MODIS DT algorithm

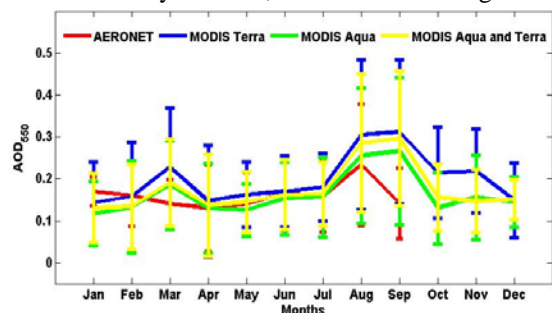


Figure 1 Monthly averaged AOD at 550 nm wavelength over Durban during the year 2014 retrieved from MODIS (DT) and AERONET. The error bars represent the standard deviation of AOD

derived AOD was greater than the sun photometer derived AOD, thus suggesting an overestimation of AOD by the DT algorithm. This supports findings from Sayer, et al., (2014), a study that has validated MODIS Aqua sensor DB and DT algorithms using 111 AERONET sites, suggesting that while one algorithm does perform better than the other on occasion, performance of retrieval algorithms are region specific and complicated.

IV. Summary

This study made use of data from MODIS sensors and the sun photometer located in Durban. Moderate

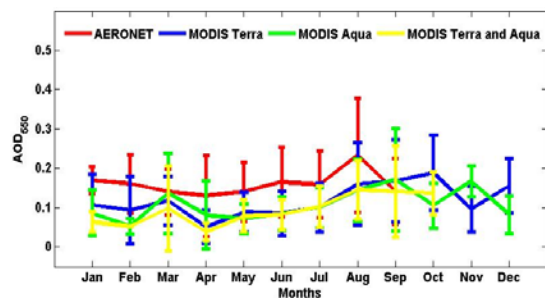


Figure 2 Monthly averaged AOD at 550 nm wavelength over Durban during the year 2014 retrieved from MODIS (DB) and AERONET. The error bars represent the standard deviation of AOD

correlations can be observed when using both retrieval algorithms (DT and DB) during certain months. Similar to the results in this study, low to moderate correlations, with higher seasonal correlations were found between MODIS and AERONET for various studies over India, China and Illinois and southern Africa (More, et al., 2013, Bibi, et al., 2015, Sun, et al., 2008, Khan, et al., 2009, Diner, et al., 2003, Kumar, et al., 2015). Therefore, when using satellite measurements to obtain aerosol characteristics it is important to consider the time of year, retrieval algorithms, consistency, revisit times, instrument calibration, cloud screening, data availability and algorithm assumptions.

Acknowledgement

The authors are thankful to NASA for providing MODIS satellite data from the Giovanni website (<http://disc.sci.gsfc.nasa.gov/>) and AERONET for the sun photometer data (<http://aeronet.gsfc.nasa.gov/>).

References

- Adesina, A. J., Kumar, K. R., Sivakumar, V. & Griffith, D., 2014. Direct radiative forcing of urban aerosols over Pretoria (25.75° S, 28.28° E) using AERONET Sunphotometer data: First scientific results and environmental impact. *Journal of Environmental Sciences*, 26(12), pp. 2459 - 2474.
- Bibi, H. et al., 2015. Intercomparison of MODIS, MISR, OMI, and CALIPSO aerosol optical depth retrievals for four locations on the Indo-Gangetic plain and validation against AERONET data. *Atmospheric Environment*, Volume 111, pp. 113 - 126.
- Chin, M. et al., 2002. Tropospheric Aerosol Optical Thickness from the GOCART model and Comparisons with Sun photometer Measurements. *American Meteorological Society*, Volume 59, pp. 461 - 482.

Diner, D. J. et al., 2001. MISR aerosol optical depth retrievals over southern Africa during the SAFARI-2000 dry season campaign. *Geophysical Research Letters*, Volume 28, pp. 3127 - 3130.

Kaufman, Y. J., Tanre, D. & Boucher, O., 2002. A satellite view of aerosols in the climate system. *Nature*, 419(6903), pp. 215 - 223.

Khan, R. A. et al., 2009. MISR aerosol product attributes and statistical comparisons with MODIS. *IEEE Transactions on Geoscience and Remote Sensing*, 47(12), pp. 4095 - 4114.

Kumar, K. R. et al., 2013. Inferring Wavelength Dependence of Angstrom Exponent over a subtropical Station in South Africa Using AERONET data: Influence of Meteorology, Long range Transport and Curvature Effect. *Science of the Total Environment*, Volume 461 - 462, pp. 397 - 408.

Kumar, K. R. et al., 2015. Aerosol climatology and discrimination of aerosol types retrieved from MODIS, MISR and OMI over Durban (29.88° S, 31.02° E), South Africa.. *Atmospheric Environment*, Volume 117, pp. 9 - 18.

More, S. et al., 2013. Comparison of aerosol products retrieved from AERONET, MICROTOPS and MODIS over a tropical urban city, Pune, India. *Aerosol and Air Quality Research*, 13(1), pp. 107 - 121 .

Sayer, A. M. et al., 2014. MODIS Collection 6 aerosol products: Comparison between Aqua's e-Deep Blue, Dark Target and "merged" datasets, and usage recommendations.. *Journal of Geophysical Research: Atmospheres*, 119(24), pp. 13 - 26.

Sivakumar, V. et al., 2010. Aerosol measurements over South Africa using satellite, sun photometer and LIDAR.. *Advanced Geoscience*, Volume 16, pp. 253 - 262.

Sivakumar, V. et al., 2009. CSIR South Africa mobile LIDAR—First scientific results: comparison with satellite, sunphotometer and model simulations. *South African Journal of Science*, 105(11-12), pp. 449 - 455.

Sun, L., Li, X. & Guo, M., 2008. Validation of MODIS aerosol optical thickness product distributed by NSMC over seas around China and its adjacent area. *The International Archives of the Photogrammetry, Remote Sensing and Spatial Information Sciences*, 34(1), pp. 95 - 98.

Swap, R. J. et al., 2003. Africa burning: A thematic analysis of the Southern African Regional Science Initiative (SAFARI 2000). *Journal of Geophysical Research*, Volume 108, pp. 1 - 15.

Tripathi, S. N. et al., 2005. Comparison of MODIS and AERONET derives aerosol optical depth over the Ganga Basin, India.

An Analysis of the Air Dispersion Potential over Uubvlei, Oranjemund, Namibia.

Anzel Swart and Prof. George Djolov

Department of Geography, Geoinformatics and Meteorology, University of Pretoria.

The 800 MW Kudu power project in south-west Namibia is a Combined Cycle Gas Turbine (CCGT) that will use natural gas from the Kudu gas field located in the Atlantic Ocean, 170km off-shore. The Kudu Project aims to respond to the increased power demand in the southern African region and to limit Namibia's importation of energy from South Africa. The proposed site for the CCGT power plant is located at Uubvlei (~25 km north of Oranjemund town). The proximity of the ocean to the proposed site means that it will significantly influence the meteorological factors that have an effect on pollution dispersion in the atmosphere. The overall aim of this paper is to analyse the air pollution characteristics of the study region on the basis of an integral Air Dispersion Potential (ADP) index. This index combines the parameters responsible for the spreading of pollutants in the atmosphere and indicates if the conditions are unfavourable, moderate or favourable for the dispersion of pollutants. The period with the most favourable ADP values is summer during daytime and the most unfavourable conditions for pollution dispersion are found in winter during the night. It was found that overall, the biggest contributor to favourable dispersion of air pollution in the region is the Monin-Obukhov Length. Wind speed mostly contributes moderately to ADP while mixing height is predominantly unfavourable.

Keywords – Air Quality, Wind Velocity, Monin-Obukhov Length, Atmospheric Stability

Introduction

Meteorological science is becoming an important tool in economic development projects, agricultural practices, environmental protection, air pollution dispersion, solar and wind power developments, urban planning, forensic investigations, insurance, weather and climate predictions, health exposure studies and many more. In particular, the energy sector, which plays a major role in the development of any country and in the eradication of poverty, demands meteorological information. Theoretical and modelling results can be utilized for assessing the background climatic and air quality conditions needed for planning and design in many fields of human activities.

The meteorology of an area, together with the technological characteristics of an emission source are two of the most important factors in determining the way in which pollutants disperse in the Planetary Boundary Layer (PBL) and plays a role in determining the diluting effects of the atmosphere (Kanevce et al, 2006). The information on the type and emission rate of pollutant sources, observed concentrations and air pollution modelling results are all tools for making policy and planning decisions, developing and updating air quality regulations and management plans at national, provincial, district and local levels.

The atmosphere is the medium in which emitted pollutants from various natural and man-made sources are transported by winds and dispersed by numerous processes. The ever present atmospheric boundary layer turbulence is a major role player in the diffusion process. The air pollution phenomenon is further determined and complicated by the interaction of pollutants with underlying surfaces (land, vegetation, water bodies) and precipitation events, all of which are associated with different physical and chemical processes.

The characterization of the ability of the atmosphere to adequately dilute and disperse any admixture is often referred

as Air Pollution Potential (Holzworth, 1967) or in this paper as Air Dispersion Potential (ADP). The PBL processes which contribute to the dispersal potential of any area are turbulent eddy movement and advection due to the motion of air masses by the wind (Stokie, 2011). Therefore, the PBL parameters chosen to represent the ADP in this paper are the horizontal wind velocity, the PBL height and the atmospheric stability.

Wind Velocity

Horizontal winds, measured in meters per second ($m \cdot s^{-1}$), have a significant effect on the dispersion of pollution in the atmosphere. Increased wind speed means an increase in the volume of air being transported in a period of time (Liu, 2000). As described by the Gaussian equation (Eq. 1), if the emission rate of a pollutant is kept constant, a doubling in wind speed will cause the concentration of the pollutant to halve (Cimorelli et al., 2004).

$$C(x, y, z) = \frac{Q}{2\pi\sigma_y^2\sigma_z U} \exp\left(\frac{-y^2}{2\sigma_y^2}\right) \left(\exp\left(\frac{-(z-h)^2}{2\sigma_z^2}\right) + \exp\left(\frac{-(z+h)^2}{2\sigma_z^2}\right) \right) \quad (1)$$

In the Gaussian equation (Eq.1), C is the concentration of pollution at the location x, y, z . Q is the rate at which emissions exit the source and U is the average wind speed measured at stack height. σ_y is the standard deviation of concentration distribution in the horizontal and σ_z is in the vertical, both parameters are stability dependant.

H represents the combination of the physical height of the stack and the rise of the plume as it exits the stack, x is the distance downwind from the stack, y is the crosswind distance from the plume centreline and z is the vertical distance from the surface of the earth (Stokie, 2011).

Planetary Boundary Layer (PBL) height

The mixing height, also known as the height of the PBL, is measured in meters (m), and can be defined as the height above the surface of the earth where turbulent air-flow is present. Mixing height is a key parameter when characterizing the air pollution climate of a region because it controls the extent of the vertical mixing process. Theoretical studies have shown that key factors which determine its growth are the mechanical turbulent flux and the atmospheric stability.

Atmospheric Stability

Atmospheric stability is the tendency of the atmosphere to increase or suppress vertical movement and it affects the concentration of pollutants. A stable atmosphere will cause higher pollutant concentrations and inhibit dispersion while in an unstable atmosphere, pollutant concentration will be less and dispersion will increase (Faiz, 1990). In this paper, Monin-Obukhov Length (MOL), measured in meters (m), is used in order to describe atmospheric stability.

Methodology & Data

In this research paper, Air Dispersion Potential (ADP) is implemented. This is a novel, comprehensive and contemporary representation of the characteristics of air pollution. ADP is a joint probability distribution which takes into account the combined effect of all relevant dynamic, thermodynamic and turbulence processes which determine the conditions of air pollutant dispersion in the atmosphere. Modelled meteorological data is analyzed on the basis of contemporary statistical and time-space series techniques in order to produce the ADP index for the region. The ADP index uses the input information required to run contemporary dispersion models which includes the dynamic factors wind velocity ($|\vec{V}|$), preferably at several levels in the atmosphere, appropriate atmospheric stability information (Monin-Obukhov length (L)), height of the planetary boundary layer (H) and/or inversion height ($H_{inversion}$) and turbulence parameters.

The ADP index is based on the conditional probability distribution of these parameters which allows constructing the relevant probability tree. This means that the probability of the comprehensive ADP index is the multiple of probabilities for wind speed $P(|\vec{V}|)$, height of the planetary boundary layer $P(H)$ and stability $P(L)$. Therefore, the probability tree for individual realization of the parameters will be:

$$P(ADP) = P(|\vec{V}|)P(H)P(L) \quad (2)$$

Eq. (2) is used to calculate the individual ADP values using outputs from a chosen weather forecast model. The equation describes the calculation of ADP and reveals its atmospheric physics correctness by applying a dimensional analysis. The dimension of the ADP is m^3/s multiplied by the stability factor $P(L)$. Therefore, ADP index gives how many cubic

meters of air is passing through a certain point per second (ventilation rate) and what the conditions are for the pollutants to diffuse.

The individual values of ADP can be used to obtain average daily, monthly, seasonal and annual statistics. These values can also be used to create the joint distribution of wind direction and ADP, i.e. ADP rose.

Further, if the intervals for the wind speed, planetary boundary layer height and stability are quantified by proxy for favourable, moderate and unfavourable, the ADP index will have value that describe the combined effect of the meteorological variables which determine the air quality potential for a region. The coefficients for favourable, moderate and unfavourable (Table 1) are chosen in such a way that the ADP value will be in the range 100 to 25 (value 100 gives absolutely favourable air dispersion conditions, 50 moderate, while 25 very unfavourable).

Table 1: Parameters and limits used in ADP calculation.

	Unfavourable	Moderate	Favourable
Wind speed	0-2 m/s	2-5 m/s	>5 m/s
Mixing height	0-400 m	400-1000 m	>1000 m
MOL	0 to 200 m	>1000 m	0 to -200 m

The Air Pollution Model (TAPM) is an air pollution model which is comprised of a meteorological and an air pollution component. The meteorological component of TAPM was used to produce the hourly meteorological parameters at points on a grid over the study region.

The meteorological component of TAPM is a primitive equation, three-dimensional model. It contains a terrain-following vertical coordinate system and includes parameterizations for the micro-physical processes associated with cloud and precipitation, turbulence, radiative fluxes, urban/vegetative canopy and soil (Hurley, 2008). The model equations disregard time zones, the curvature of the earth and also assumes a uniform distance grid across the domain.

In the case of the study site (Uubvlei), the study region is covered by 81 points which are approximately 20 km apart (Fig. 1). TAPM was used to model all necessary meteorological information needed to develop the research methodology for the year of 2014 on an hourly basis.

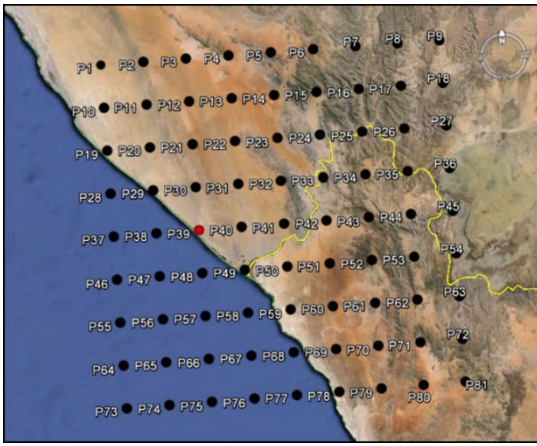


Figure 1: 81-point grid with a space step of 20km for producing the TAPM modelled data over the study region. P39 (red) is located at the proposed site for the CCGT power station (Google earth pro, 2016).

Results and Discussion

ADP was calculated and plotted on an 81-point grid located over the study region using one year of meteorological data. A combination of modelled wind speed, mixing height and MOL data is used to describe the ADP for the region for different periods. Average ADP values for summer, summer during the day and night were calculated and plotted in Figs. 2 and 3. Figs. 4 and 5 describe the components used to calculate ADP for summer during the day and night.

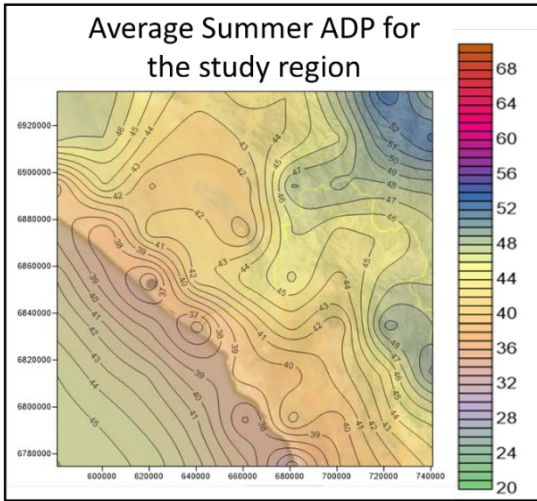


Figure 2: Average ADP during summer (Dec, Jan, Feb) over the study region.

Average ADP values during summer (Fig. 2) varies from 34 to 54. The potential for air dispersion is better over land than over ocean. ADP values drop approaching the coast. The unfavourable conditions near the coast can be attributed to lower mixing heights, lower wind speeds and conditions of stability.

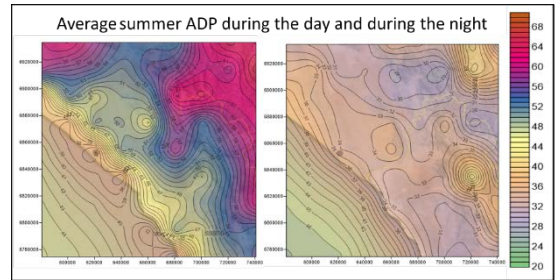


Figure 3: Average summer ADP during the day (left) and during the night (right).

Comparing the ADP values for summer during the day and summer during the night (Fig. 3), it is clear that conditions for air dispersion are much more favourable during the day. This is because of larger mixing heights and greater instability during daytime. At night, as the earth cools, mixing heights become smaller and stable conditions prevail.

Both summer day and night ADP values show a similar pattern, conditions are more favourable inland, deteriorates towards the coast and picks up again over the ocean. The preferred site is located very close to the coast and consequently in an area of lower ADP during summer days and nights.

It is useful to analyze the contribution of the separate meteorological parameters to the average ADP. In Figs. 5 and 6 below, the color blue indicates an unfavourable contribution to average ADP, yellow indicates a moderate contribution and pink a favourable one.

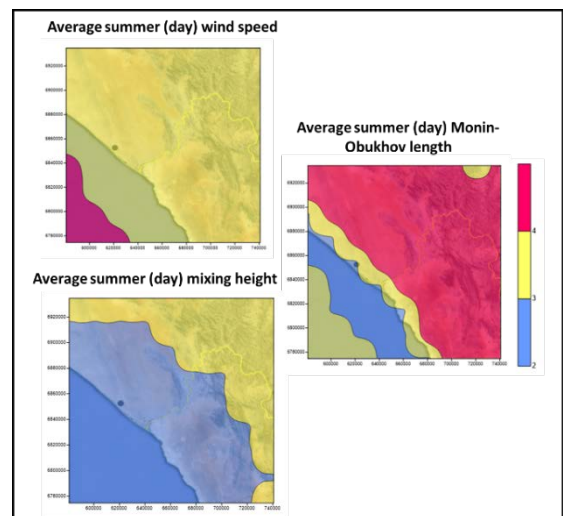


Figure 4: Average of the components of ADP (wind speed, mixing height and MOL) for summer during the day.

In Fig. 4, the components of ADP for summer during the day and the night are presented. High ADP values during the day in the summer are driven by favourable MOL's over land and favourable wind speed over the ocean. Also, the moderately favourable wind speeds and mixing heights over land contribute to relatively favourable ADP conditions in Fig. 3.

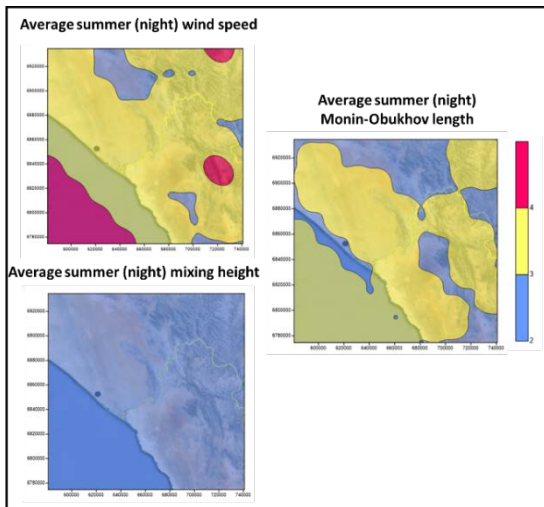


Figure 5: Average of the components of ADP (wind speed, mixing height and MOL) for summer during the night.

In Fig. 5, the average of the components of ADP for summer during the night are presented. Relatively high ADP values over the ocean for summer nights are due to the favourable contribution of wind speeds and moderately favourable contribution of MOL's. In this case, mixing height is constant throughout the study region and contributes unfavourably to ADP in Fig. 3.

Conclusions

The analysis of the transport and diffusion of pollutants in the atmosphere indicates that the wind velocity affects the ground level concentration in inverse proportionality. This means that low wind speeds lead to increased pollutant concentration while high wind speeds lead to decreased concentration levels. The same inverse proportionality is characteristic for the height of the PBL (H) where low values of H lead to higher pollutant concentration. The reverse is true for larger values of H which leads to lower pollutant concentration levels. Unstable stratification ($L < 0$) leads to good mixing of pollutants while stable stratification ($L > 0$) inhibits the diffusion process. This analysis leads to the conclusion that wind speed distribution (wind roses) is far from sufficient to allow wide-ranging air quality management.

Annual average ADP for the study region is moderate with values only reaching 51. The period with the most favourable ADP values is summer day and the most unfavourable conditions for pollution dispersion are found in winter during the night. It was found that overall, the biggest contributor to favourable dispersion of air pollution in the region is the

Monin-Obukhov Length. Wind speed mostly contributes moderately to ADP while mixing height is predominantly unfavourable.

Applying ADP with an appropriate weather forecasting model can see the development of an air dispersion potential forecasting tool. Using the forecasted values for the needed parameters and the methodology to calculate ADP over a region can be of value in the forecasting of air dispersion conditions over this, and any other region.

Knowledge of the ADP of the region for a certain period could influence the operation of the CCGT power station. The power station operator will have the option to plan high-emission activities for a period when the ADP of the region is predicted to be favourable and to slow down production when ADP is predicted to be unfavourable. An ADP prediction tool, when used in conjunction with operational activities at the CCGT power station could lower the influence of the pollutants on the closely located populations like Oranjemund. The ADP index may also be used for health impact studies as proxy of weather condition in deriving air pollution exposure models.

References

Cimorelli, A. J., S.G. Perry, A. Venkatram, J. C. Weil, R. J. Paine, R. B. Wilson, R. F. Lee, W. D. Peters, R. W. Brode, and J. O. Paumier. 2004. AERMOD: Description of Model Formulation, EPA-454/R-03-004. U.S. Environmental Protection Agency, Research Triangle Park, NC.

Faiz, A. 1990. Automotive air pollution. Washington, DC (1818 H St. NW, Washington 20433): Infrastructure and Urban Development Dept., World Bank.

Google Earth Pro. 2016. "TAPM Grid" Lat -28.424604 and Lon 16.246414. September 4, 2013. Accessed: May 2016.

Hurley, P. 2008. TAPM V4. Part 1: Technical Description. CSIRO Marine and Atmospheric Research paper, no. 25. Aspendale, Vic.: CSIRO Marine and Atmospheric Research, pp.4 - 23.

Holzworth, G. 1967. "Mixing Depths, Wind Speeds and Air Pollution Potential for Selected Locations in the United States", J.Appl.Meteorol., 6, 1039-1044.

Kanevce, G., & Kanevce, L. 2006. "Dispersion modelling for regulatory applications." Thermal Science 10 (2), 141-154.

Liu, D. and Lipták, B. 2000. Air pollution. Boca Raton: Lewis Publishers.

Stokie, J. M. 2011. "The mathematics of atmospheric dispersion modelling." Siam Review, Vol 53 (2), 349-372.

Acknowledgements

Dr. Gerhard Fourie for supplying the modelled meteorological data.

Climate change related impact on avocado production areas in South Africa

Harold L Weepener^{***}, ARC-Institute for Soil, Climate and Water, Private Bag X79, Pretoria, 0001, South Africa

Christien J Engelbrecht, ARC-Institute for Soil, Climate and Water, Private Bag X79, Pretoria, 0001, South Africa

Zelda Bijzet, ARC-Institute for Tropical and Subtropical Crops, Private Bag X11208, Nelspruit, 1200, South Africa

Potential changes in avocado production areas over South Africa under future climate change are investigated using six high-resolution projections of a regional climate model. Apart from the climate, the soil also determines whether an area can be suitable for crop production. Here, the national land type database, developed and hosted at the Agricultural Research Council, is employed to complement the climate criteria in delineating avocado production areas under climate change. Southward shifts along the eastern coastal board of the country as well as towards the eastern higher lying areas are projected to be the new areas suitable for avocado production.

Keywords: Climate projections; Crop suitability; GIS; *Persea americana* MILLS

Introduction

Avocado is an important crop in South Africa. It contributed 32% (R1.1 billion) to total gross value of subtropical fruits (R3.4 billion) during the 2013/14 season (Mogala, 2015).

This study analysed simulations of present day and future climate over South Africa, with the emphasis on identifying the impact of future climate change on avocado production areas.

Instrumentation and Method

Environmental suitability criteria for avocado production were applied to dynamically downscaled climate projections of a regional climate model, together with land type data. The projections were obtained through the dynamic downscaling of six different Coupled Global Climate Model (CGCM) projections of future climate change to high resolution over southern Africa. The regional model used is the Conformal-Cubic Atmospheric Model (CCAM), a variable resolution global atmospheric model of the Commonwealth Scientific and Industrial Research Organization (CSIRO) in Australia (McGregor, 2005). The model was applied in stretched-grid mode over

southern and tropical Africa, to obtain simulations at a resolution of approximately 0.5° in longitude and latitude. A detailed description of the downscaling procedure is provided by Engelbrecht *et al.* (2011). All the CGCM simulations are for the A2 Special Report on Emissions Scenario (SRES) and were downscaled for the period 1961-2100. The CGCMs that were downscaled are:

- GFDL-CM2.0 from the National Oceanic and Atmospheric Administration (NOAA);
- GFDL-CM2.1 from NOAA;
- ECHAM5/MPI-Ocean Model from Germany;
- UKMO-hadCM3 from the United Kingdom;
- MIROC3.2-medres from the Japanese Agency for Marine-Earth Science and Technology (JAMSTEC); and
- CSIRO Mark3.5 from Australia.

South Africa is fortunate in having a national soil database in the form of land types. Land types are described in the land type memoirs (Land Type Survey Staff, 1972-2006) as comprising:

- the delineation of areas, known as land types, at 1:250 000 scale such that each land type displays

^{***} Corresponding author:

Fax: +27 12 3231157

Tel: +27 12 3102505

E-mail: weepenerh@arc.agric.za

a marked degree of uniformity with regard to terrain form, soil pattern and climate;

- the definition of each land type in terms of terrain, soil and climate parameters; and
- an in-depth analysis of a number of soil profiles, termed modal profiles, selected to represent the range of soils encountered during the survey.

The land type dataset was developed through a country-wide inventory (1972-2002). Each 1:250 000 map sheet is accompanied by a memoir describing the soil patterns per land type on a probability basis. The percentage distribution of various soil attributes is linked to the following terrain units: crests, scarps, mid-slopes, foot slopes and valley bottoms. The percentage distributions can be used to determine the percentage of area in an entire land type unit that adheres to certain criteria. For example, it is possible to determine the area of a land type unit where the soil depth is deeper than a specific threshold, or the percentage area with a clay percentage lower than a specified clay threshold.

Environmental suitability criteria were defined for avocado production (Table 1). The criteria table was used to prepare a time series of maps to show potential shifts in avocado production areas. The climate criteria of avocado crops were applied to six CGCM projections of future climate while land type data has been used for the soil criteria, which were assumed not to change. To simplify the interpretation of maps, soil suitability was only classified into two classes, namely suitable and unsuitable. Areas unsuitable due to soil criteria are masked out in the maps and are kept as a constant over time. A land type unit was considered unsuitable if less than 10% of the soils in the unit were suitable.

Fig. 1 illustrates the potential shifts in avocado production areas from 2015 to 2090. Current production areas of avocado are projected to become marginal or unsuitable in future, while large areas in KwaZulu-Natal and Eastern Cape provinces are projected to become suitable. The southward shift of avocado production areas corresponds with shifts of the Tropical, Savannah zone from Köppen-Geiger climate types (Engelbrecht and Engelbrecht, 2016).

Results and Discussion

Table 1: Environmental suitability criteria for avocado production under supplementary irrigation (adapted from Wolstenholme, 2011)

Suitability class	Optimal	Sub-optimal	Marginal	Unsuited
Land Attribute				
Climate requirements				
Annual rainfall (mm) ¹	≥600			<600
Frost occurrence ² : heavy frost	None (Aug-Sept)	None (Aug-Sept)	None (Aug-Sept)	Other
Frost occurrence: T _{min} July	≥7	5-7	3-5	<3
T _{ave} annual (°C) ³	17-21	21-22	22-23	<17 and >23
T _{ave} Aug-Sept (°C) ⁴	≥17			<17
T _{max} Nov-Feb (°C) ⁵	≤34	34-35	35-36	>36
Soil requirements				
Soil depth (mm)				<700
Topsoil clay (%) ⁶				<12 and >50
Soil pH (water)				<4; >7

¹At least 1000 mm is required, with a dry period in winter. Additional water is also required during fruit set in Sept, when rainfall is still low. THUS supplementary irrigation is required. For irrigation to be regarded as supplementary, an annual rainfall of at least 600 mm is suggested as a rule of thumb.

²Heavy frost not tolerated, particularly during flowering (Aug-Sept) and fruit set (Sept-Oct).

³Parameter for demarcating a cool to warm subtropical climate (Wolstenholme, 2011).

⁴Critical period of flowering and fruit set: low temperatures to be avoided.

⁵Second critical period: onset of second vegetative growth flush: very high temperatures to be avoided.

⁶Sandy soils to be avoided due to low water-holding capacity.

Suitability for avocado production (supplementary irrigation)

Criteria: rainfall, minimum temperature, maximum temperature and soil
Median of six climate projections for 2015, 2030, 2060 and 2090

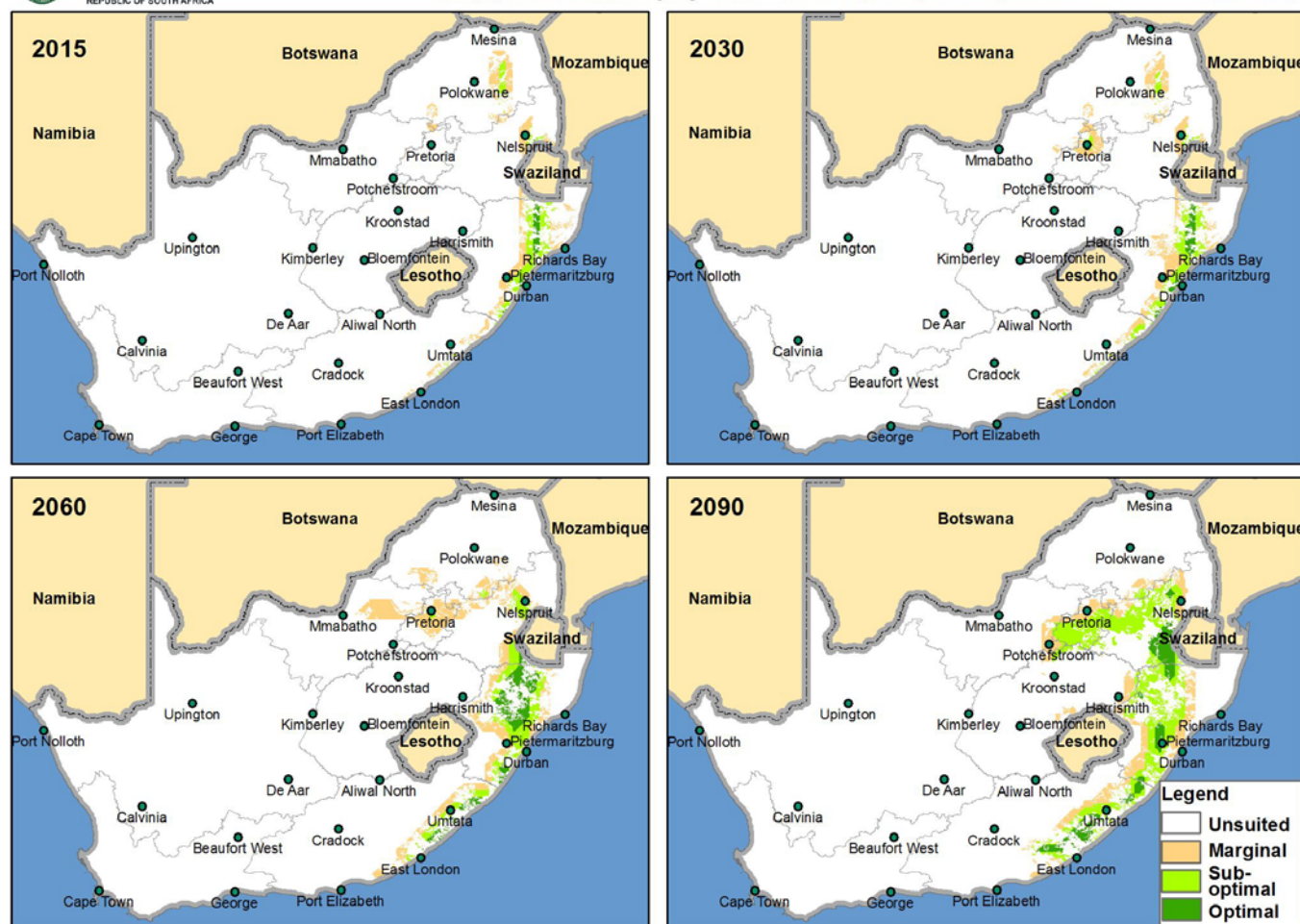


Figure 1: Shifts in avocado production areas from 2015 to 2090.

The crop suitability maps are based on environmental criteria only and do not consider the following:

- **New cultivars:** Development of new cultivars could make it possible to cultivate under higher temperature regimes, which could change the production areas correspondingly (Bitu, and Gerats, 2013; Mathur et al., 2012)
- **Diseases and pests:** Climate change will affect the fecundity, dispersal and distribution of plant diseases and pests (Van der Waals et al., 2013). Higher temperatures will increase overwintering of pathogens and pests, modify host susceptibility to infection, accelerate pathogen and vector life cycles and increase the sporulation and infectiousness of fungi (Harvell et al., 2002; Schaap et al., 2011). As the number of extreme rainfall events increases, soil

- conditions will favour the establishment and reproduction of soil borne pathogens such as *Phytophthora cinnamomi* in avocado.
- **Effect of increased CO₂:** Increased CO₂ levels are likely to have a positive effect on potential water use efficiency and crop productivity (Haverkort et al., 2013). However, large variations have been found across a range of horticultural commodities. Avocado was found amongst other crops such as citrus, potato, cotton, wheat, soybeans and lettuce to benefit substantially from additional atmospheric CO₂, where increasing temperatures may offset increased productivity (Oosterhuis, 2013).

Conclusions

According to Mogala (2015), Limpopo province represented 61% of the national avocado production in 2012. Most of the avocado plantings in Limpopo are found in the Letaba district while the other main production area is Soutpansberg. Currently, the second and third largest producers of avocados are Mpumalanga and KwaZulu-Natal provinces with 30% (4 554 ha) and 8% (1 319 ha) respectively. South Africa has exported 52,000 tonnes of avocado worldwide in 2015, with an additional 500 ha developed during 2015 to bring the total production area across the country to 15,500 ha (McShane, 2015).

The current area planted to commercial avocado corresponds to the areas as per the 2015 map in Fig. 1. The commercial avocado industry originated in Limpopo due to the establishment of imported enhanced Californian cultivars in 1938. Upon expansion of the industry, other commodities such as cattle and sugarcane competed for land in the also suitable KwaZulu-Natal region. Another factor that supports expansion in an area is already established infrastructure such as pack-houses, transport and support such as vendors and extension services.

Changes in climatic suitability for tropical fruit such as avocado will result in a gradual southward shift or a shift towards higher lying areas during the 21st century, according to current projections. Producers will have to adapt accordingly to be in a better position to provide for the demand.

Acknowledgements

Department of Agriculture, Forestry and Fisheries (DAFF) Directorate: Climate Change and Disaster Management (CCDM) for funding the research project.

Climate Studies, Modelling and Environmental Health, CSIR Natural Resources and Environment for providing the climate change projections used in this study.

References

- Bitu, C. E., and Gerats, T. (2013). Plant tolerance to high temperature in a changing environment: scientific fundamentals and production of heat stress-tolerant crops. *Front. Plant Sci.* 4:273.
- Engelbrecht, C.J. and Engelbrecht, F.A. (2016). Shifts in Köppen-Geiger climate zones over southern Africa in relation to key global temperature goals. *Theoretical and Applied Climatology*. 123: 247-261.
- Engelbrecht, F.A., Landman, W.A., Engelbrecht, C.J., Landman, S., Bopape, M.M., Roux, B., McGregor, J.L. and Thatcher, M. (2011). Multi-scale climate modeling over Southern Africa using a variable-resolution global model. *Water SA*. 37: 647-658.
- Harvell, C.D., Mitchell, C.E., Ward, J.R., Altizer, S., Dobson, A.P., Ostfeld, R.S. and Samuel, M.D. (2002). Climate warming and disease risks for terrestrial and marine biota. *Science*. 296: 2158-2162.
- Haverkort, A.J., Franke, A.C., Engelbrecht, F.A. and Steyn, J.M. (2013). Climate change and potato production in contrasting South African agro-ecosystems 1. Effects on land and water use efficiencies. *Potato Research*. 56: 31-50.
- Land Type Survey Staff (1972-2006). Land Types of South Africa: Maps (69 sheets) and Memoirs (39 books). ARC-Institute for Soil, Climate and Water, Pretoria.
- Mogala, M. (2015). A profile of the South African avocado market value chain 2015. Available at <http://www.nda.agric.za/doiDev/sideMenu/Marketing/Annual%20Publications/Commodity%20Profiles/FRUITS%20AND%20VEGETABLES/Avocado%20market%20value%20chain%20profile%202015.pdf> [Accessed 29 July 2016].
- McGregor, J.L. (2005). *C-CAM: Geometric aspects and dynamical formulation*. CSIRO Atmospheric Research Tech. Paper no 70, p. 43.
- McShane, G. (2015). South Africa zones in on year-round avocados with new varieties. In: *Produce Business UK – The online publication for buyers of fresh fruit and vegetables*. Available at <http://www.producebusinessuk.com/supply/stories/2015/12/22/south-africa-zones-in-on-year-round-avocados-with-new-varieties#sthash.fe56ESC7.dpuf> [Accessed 29 July 2016].
- Mathur, P.N., Ramirez-Villegas, J. and Jarvis, A. (2012). The impacts of climate change on tropical and subtropical horticultural production. IN: Sthapit B.R., Ramanatha Rao V and Sthapit S.R. (Eds.) *Tropical Fruit Tree Species and Climate Change*. Bioversity International, New Delhi, India. pp. 27-44.
- Oosterhuis, D.M. (2013). Global warming and cotton productivity. *ICAC 72nd Plenary Meeting*, September 29 - October 4, 2013. Cartagena, Colombia.
- Schaap, B.F., Blom-Zandstra, M., Hermans, C.M.L., Meerburg, B.G. and Verhagen, J. (2011). Impact changes of climatic extremes on arable farming in the north of the Netherlands. *Reg. Environ. Change*. 11: 731-741
- Van der Waals, J.E., Krüger, K., Franke, A.C., Haverkort A.J. and Steyn J.M. (2013). Climate change and potato production in contrasting South African agro-ecosystems 3. Effects on relative development rates of selected pathogens and pests. *Potato Research*. 56: 67-84.
- Wolstenholme, B.N. (2011). Climatic and soil requirements. In: De Villiers, E.A. and Joubert, P.H. (Eds.) *The cultivation of avocado*. ARC-Institute for Tropical and Subtropical Crops, Nelspruit. pp. 13-34.

Improving visualizations of climate projection information

Piotr Wolski*, Chris Jack, Anna Steynor, Lisa Coop

Climate System Analysis Group, University of Cape Town

Abstract

In the complex landscape of climate projections creating meaningful graphical presentations of data is not a trivial task. In the RSA context, the presentations in the most of high profile documents focused on presenting aspects of spatial heterogeneity of the signal, at the expense of the nuanced information on its uncertainty and significance. Here, we present an alternative way of visualizing climate projections that stresses multi-model ensemble agreement and the magnitude of projected change, offers ability to capture the time of emergence, and maintains the ability to discern regional differences in signal.

Keywords: Climate change, visualization, communication, uncertainty

*Introduction**

Climate projections are complex and multi-dimensional, with “dimensions” spanning such aspect as space (location, region), seasonal cycle (year, season, month), variable (e.g. rainfall, temperature), variable’s attributes (e.g. maximum, frequency), time (future period, e.g. near future or far future) and application (combination of climate variables as in hydrological, ecological or disease responses). Additional “dimensions” are added by the aspects of uncertainty involved in the process of simulating future climates that are a consequence of emission scenarios and model uncertainty. The latter is generally being expressed through multi-model ensemble data. Yet another level of uncertainty arises from natural variability of climate that manifests at a range of temporal scales, from interannual to multidecadal.

In view of the above, it is not surprising that communicating climate projections is an extremely challenging process. Recently, much attention has been given to creating frameworks enabling a meaningful engagement of climate scientists with broadly defined “end-users” (practitioners, managers, decision-makers the public etc.) around the concepts of uncertainty both in climate projections as well as in the broader decision-making context. In that, the emerging concept of knowledge co-production (Lemos & Morehouse, 2005) built around climate change narratives is gaining traction in climate services practitioner circles.

At the base of the evolving communication paradigms, graphic representation of climate projection data

remains a key medium of conveying quantitative aspects of climate information (e.g. van der Linden et al., 2014), and the proverbial statement that “a picture is worth a thousand words” is as valid as ever. To complement the new ways of communicating climate change information, here we propose a new, nuanced way of visualizing climate change projection data.

Visual presentation of climate change projections

The usability of visualizations in the context of conveying climate change information has often been investigated. Some research focuses on the perceptual and cognitive aspects, i.e. what particular visualization attributes such as color schemes or graphical elements are employed to present a given set of numbers so that the underlying information is not distorted (e.g. Daron et al., 2015; Lorenz et al., 2015; Kaye et al., 2012). Other research targets the information content of the presentation, i.e. what data and information are presented (e.g. MacLeod & Morse, 2014, Pappenberger et al., 2013). To our knowledge, no clear recommendations for the latter exist, although some framing is provided by IPCC’s guidance on uncertainty concepts and related language (Mastrandrea et al., 2011) and other guidelines for graphical presentation of weather forecast data (WMO, 2001).

Obviously, which aspects of climate projections are presented is determined by the context - what sort of information is needed by the “end-user”. This is increasingly determined through the interaction of the data “producers” and “end-users”. However, it is also limited by several aspects: the primary 2-dimensionality of the medium, and the human brain’s

*wolski@csag.uct.ac.za, tel: +27216502999

ability to distinguish colors, sizes and patterns in graphics. For example, maps can effectively convey two types of information concurrently - through color intensity and pattern. Adding a third layer, overlay is possible, but the readability may be dependent on a particular interplay of the patterns (e.g. Böttinger et al., 2015). Additionally, the contents of the graphics are framed by the ability of the quite often generic “end-users” to assimilate complex, multi-dimensional aspects of climate projections. The simplification of the complexity is in general justified - humans seem to prefer short and clear messages to complex and nuanced ones (e.g. van der Linden et al., 2014). These aspects, in combination with the very practical limits of the medium (e.g. length of the document such as report or paper), quite often reduce the data presented to that which directly answer the question “how strongly different will variable X be in Y-years time at location Z compared to current (or recent) conditions”.

The most common visual presentation of climate projections seems to be threefold:

1. Representing temporal evolution of a climate variable for a location using a time series plot (line plot), which in a multi-model context becomes the so-called “spaghetti” plot with individual lines representing individual models, and possibly with a median of the multi-model ensemble superimposed.
2. Representing spatial distribution (on a map) of a climate variable (or its anomaly) for a particular future period. Individual model projections may be visualized on individual maps, or alternatively, a map showing an ensemble median and/or percentiles may be used. An expression of uncertainty may be added through a superimposed pattern/hatching.
3. Representing relationship between climate variables for a particular location and a particular future period on a scatterplot that often depicts relative change in rainfall (ΔP) versus relative change in air temperature (ΔT) - the so called ΔP - ΔT plot. That plot represents projection uncertainty directly through the spread of individual points and can include “whiskers” to represent uncertainty.

Each of these approaches has their peculiarities in what message they convey. For example, the map-based representation does indeed convey detailed spatial patterns of mean change with possibly uncertainty aspects such as model agreement, but it does not allow for a clear appreciation of neither the magnitude of mapped values as compared to the level

of natural variability, nor the temporal evolution of the climate. The time-series based approaches are, obviously location-specific and are not able to convey spatial information in any nuanced manner. It is possible, of course, to present temporal evolution of a regional mean signal instead of a point signal, but that, if averaging is done across areas with divergent signal, can possibly lead to misrepresenting the magnitude of local responses.

Climate projection visualizations in generic climate change documents in RSA

In the context of South Africa, three general, high-level documents summarizing the climate projections at the country level, i.e. the Second National Communication (SNC) to UNCCC (DEA, 2011) the South African Risk and Vulnerability Atlas (SARVA, DST, 2009) and the Long-Term Adaptation Scenarios (LTAS) Flagship Research Programme (DEA, 2013) were clearly focused on presenting spatial patterns of change. All three contain maps representing spatial distribution of median and two percentiles of ensemble range in seasonal rainfall and mean temperature originating from two approaches (statistical and dynamical downscaling) for a selected future period. The LTAS document additionally contains ΔP - ΔT plots that contain time-stratified data from an ensemble of dynamically downscaled projections. Neither of the graphical presentations contains any expression of significance of the visualized signal compared to the levels of natural variability. The maps resolution suggests similar resolution of the visualized information.

The alternative approach

Here we present an alternative, nuanced approach to visualizing climate projections that simultaneously represents aspects of model uncertainty, signal strength compared to natural variability, timing of the emergence of significant signal and allows for implicit representation of spatial heterogeneity within a broader region. We believe it is strongly applicable in a range of contexts such as National Communication and initiatives such as SARVA or LTAS.

The approach is based on the visualization of temporal evolution of projected climate for climate regions rather than for administrative regions. The regions are established on the basis of similarity of temporal evolution of past climate (Fig. 1). The temporal evolution of projected (modelled) climate is visualized in the form of so called “plume” plots (Fig. 2).

Plume plots

These depict the temporal evolution of individual members of the multi-model ensemble. Each model's projection is shown as a moving average of the deviation of a particular variable's attribute - e.g. mean seasonal rainfall from the mean value of that attribute over the reference period. In addition, a 95% confidence interval (CI) of the difference between each of the moving window periods and the reference period is presented as a shaded band for each model's projection. The band representing CI is semi-transparent, so that agreement between the members of the ensemble is easily discernible by the increase in colour intensity. Also, the colour of the CI band changes as the individual member's signal becomes statistically significant as compared to the level of natural variability in the reference period. This allows for an easy representation of the "time of emergence" of the signal.

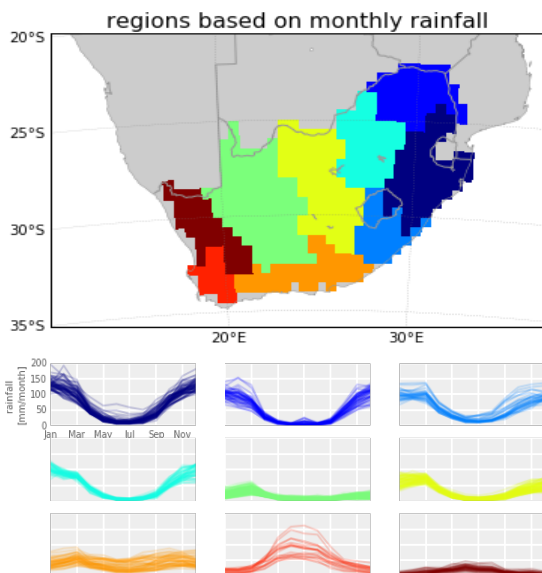


Figure 1 Climate regions based on hierarchical clustering of CRU 3.23 monthly rainfall. Bottom figures represent rainfall climatology for each of the given regions (color coordinated) grid points.
Plume plots for climate projections for RSA

The example of plume plots presented below is based on CMIP5 multimodel ensemble projections under RCP 8.5 emission scenario. Segmentation of the RSA into climate zones is based on hierarchical clustering of CRU 3.23 gridded rainfall dataset (Fig. 1). GCM fields of total annual rainfall and mean annual temperature were space-averaged for each of the climate zones. The plots (Fig. 2) are based on a 20-year moving average for the 1986-2005 reference

period. Each individual GCM time series was bias-corrected in mean (by applying an additive factor for temperature, and multiplicative factor for rainfall) so that its mean in the reference period is equal to the raw ensemble mean. The CI was calculated for each position of the moving average window through bootstrapping as the 2.5-97.5th percentile range of the bootstrap distribution of differences in mean between a given moving window period and that of the reference period. For cases where the reference period and the moving window period overlap, the bootstrap sample data for the reference period's overlap were substituted by the moving window period's bootstrap sample. In this way, the resultant CI accounts for the lack of independence in between the two periods. Bootstrapping was performed using a randomized block bootstrap procedure - as this is robust with respect to eventual serial correlation in data.

Discussion and conclusions

In the complex landscape of climate projections creating meaningful graphical presentations of data is not a trivial task. In the RSA context, the presentations in most of the high profile documents focused on aspects of spatial heterogeneity of the signal, at the expense of the nuanced information on its uncertainty and significance. The alternative way of visualizing climate projections proposed here stresses multimodel ensemble agreement and the significance of projected change. Additionally, it provides information on the time of emergence of a signal. In the meantime, the approach maintains the ability to discern regional differences in climate change signals.

In developing the plume plots for RSA's climate regions we took numerous arbitrary decisions that are perhaps debatable, and need to be adjusted for a particular application context. Notably, the definition of climate regions based on temporal similarity of temporal evolution of rainfall in a generic gridded rainfall dataset offers room for further improvement. Our motivation was to derive regions that are more relevant than administrative boundaries often used for summarizing climate trends and projections. Perhaps a better alternative to regions based on past rainfall evolution would be regions based on the similarity of the evolution of future climate, but the advantage of such a solution remains to be further investigated. Another important decision was the level of significance of the signal that is the basis for visual highlighting. The 5% significance level is obviously relevant from a statistical point of view, but not necessarily from a user's perspective. Lower levels of significance can be used should user's impact

threshold be more sensitive to the level of a given climate variable.

The approach presented here was implemented in a recent project updating climate projections for the City of Cape Town, as well as in the development of materials for RSA Third National Communication to UNCCC. Furthermore, we plan to conduct a rigorous study of South African user's perceptions of this way of presenting climate change information in the future.

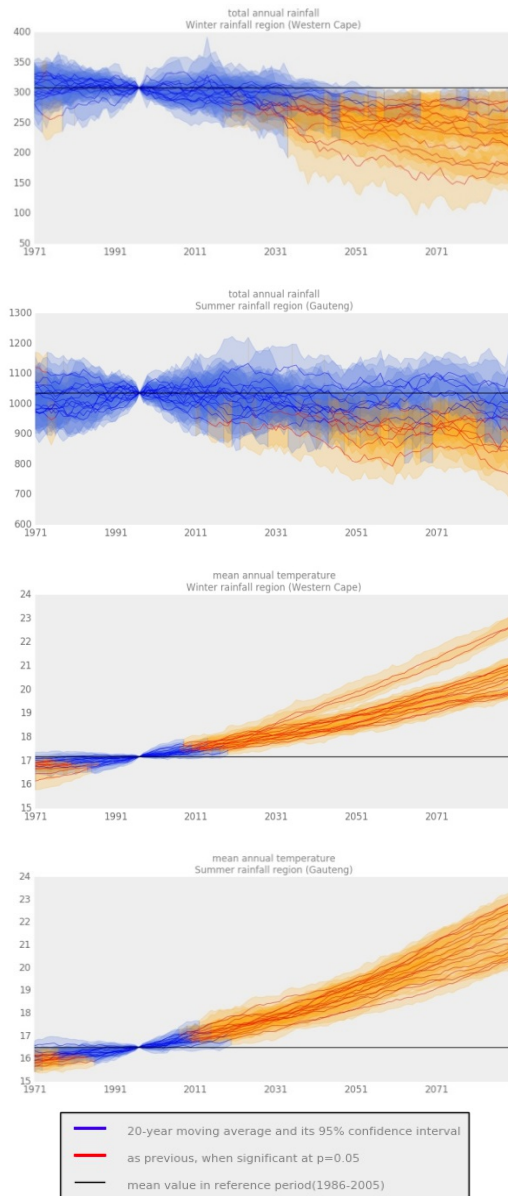


Figure 2 Plume plots of two projected variables (total annual rainfall and mean annual temperature) for two selected regions - winter rainfall region roughly corresponding to the Western Cape (in red in Fig. 1)

and summer rainfall region encompassing the Gauteng province (in light blue in Fig. 1).

References

- Böttiger M., Pohlmann H., et al. (2015). Visualization of 2D uncertainty in decadal climate predictions. Workshop on Visualisation in Environmental Sciences (EnvirVis), Cagliari, Italy.
- Daron J.D., Lorenz S., Wolski P., Blamey R.C., Jack C. (2015). Interpreting climate data visualisations to inform adaptation decisions. *Clim. Risk Manag.* 10, 17–26.
- DEA (Department of Environmental Affairs). 2011. *South Africa's Second National Communication under the United Nations Framework Convention on Climate Change*. Pretoria. South Africa.
- DEA (Department of Environmental Affairs). 2013. *Climate Trends and Scenarios for South Africa. Long-Term Adaptation Scenarios Flagship Research Programme (LTAS) for South Africa*. Pretoria, South Africa.
- DST (Department of Science and Technology). 2009. *South African Risk and Vulnerability Atlas*. Pretoria. South Africa. <http://sarva.dirisa.org>.
- Kaye N.R., Hartley A., Hemming D. (2012). Mapping the climate: guidance on appropriate techniques to map climate variables and their uncertainty. *Geosci. Model Dev.* 5, 245–256.
- Lemos M.C. & Morehouse B.J. (2005). The co-production of science and policy in integrated climate assessments. *Global Env. Change*, 15(1), 57-68.
- Lorenz S., Dessai S., Forster P.M., Paavola J. (2015). Tailoring the visual communication of climate projections for local adaptation practitioners in Germany and the UK. *Philos. Trans. R. Soc. A Math. Phys. Eng. Sci.* 373, 20140457.
- MacLeod D.A., Morse A.P. (2014). Visualizing the uncertainty in the relationship between seasonal average climate and malaria risk. *Sci. Rep.* 4, 7264.
- Mastrandrea M.D., Mach K.J. et al. (2011). The IPCC AR5 guidance note on consistent treatment of uncertainties: a common approach across the working groups. *Clim. Change* 108, 675–691.

Pappenberger F., Stephens E., et al. (2013). Visualizing probabilistic flood forecast information: expert preferences and perceptions of best practice in uncertainty communication. *Hydrol. Process.* 27, 132–146.

Van der Linden S., Leiserowitz A., Feinberg G., Maibach E. (2014). How to communicate the scientific consensus on climate change: plain facts, pie charts or metaphors? *Clim. Change* 126, 255–262.

WMO (World Meteorological Organization) (2001). *Guidelines on graphical presentation of public weather services products*. WMO/TD No. 1080. Geneva, Switzerland.